UNIVERSITA' DEGLI STUDI DI ROMA
"TOR VERGATA"

FACOLTA' DI INGEGNERIA

DOTTORATO DI RICERCA IN INGEGNERIA AMBIENTALE

CICLO XXII

Landslide Tsunamis

Emiliano Renzi

A.A. 2009/2010

Tutor: prof. P. Sammarco

Coordinatore: prof. R. Gavasci

Abstract

This study concerns several aspects of the generation and propagation of landslide tsunamis in different oceanographic topographies, i.e. an indefinite plane beach, a plane beach connecting to a flat continental platform and a conical island.

A forced two-horizontal dimension (2HD) analytical model is developed to investigate the distinguishing physical features of landslide induced tsunamis generated and propagating on a plane beach. The method of separation of variables and the Fourier transform are employed to obtain the solution in the form of an eigenfunction expansion. The resulting wave field is made by a fast-decaying component propagating offshore and a system of transient edge waves travelling along the shoreline. Parametric analysis highlights the influence of the landslide initial position and velocity on the amplitude of the generated wave field. Results are satisfactorily compared with available experimental data. Discussion about the validity of non-forced numerical models is also made.

A forced 2HD analytical model is developed to investigate the main characteristics of landslide tsunamis propagating on a semi-plane beach. All the eigensolutions are perfectly trapped along the shoreline, as it happens in the limit case of the indefinite plane beach. Parametric discussion shows that the finite length of the incline does not modify the nature of the eigensolutions, but is responsible of a more moderate decay of the propagating wave field in the offshore direction.

Finally, an analytical forced two-horizontal-dimension model is derived to investigate landslide tsunamis propagating around a conical island lying on a flat continental platform. Separation of variables and Laplace transform are used to obtain the free-surface elevation in the whole domain and the runup at the shoreline in terms of confluent Heun functions. The main properties of these functions and their asymptotic behaviour for large parameters are investigated. The generated wave field is made by a system of transient waves propagating to infinity and transient local waves almost trapped. Expression of the transient leading wave travelling offshore is also derived. The distinguishing physical features of landslide tsunamis propagating in a round geometry are then pointed out and compared with those of landslide tsunamis propagating along a straight coast. Analytical results satisfactorily agree with available experimental data.

Sommario

Lo studio riguarda vari aspetti della generazione e propagazione di tsunami generati da frane su diverse topografie oceanografiche, quali una spiaggia piana indefinita, una spiaggia semipiana connessa ad una piattaforma continentale ed un'isola conica.

Un modello analitico forzato tridimensionale è sviluppato per studiare la propagazione di tsunami generati da frane lungo una spiaggia piana. Il metodo della separazione delle variabili e la trasformata di Fourier vengono impiegati per ottenere la soluzione in forma di serie di autofunzioni. Il campo d'onde risultante è costituito da una componente evanescente propagantesi ortogonalmente alla spiaggia e da un sistema di onde di bordo transitorie lungo la spiaggia. L'analisi parametrica del sistema evidenzia l'influenza della posizione e velocità iniziali della frana nel determinare l'ampiezza del campo d'onde generato. I risultati sono confrontati con successo con dati sperimentali. Lo studio termina con la discussione sulla validità di modelli numerici non forzati.

Un modello analitico tridimensionale è sviluppato per studiare la propagazione lungo una spiaggia semipiana di tsunami generati da frane. Le soluzioni proprie del sistema sono perfettamente intrappolate lungo la linea di riva, come accade nel caso limite della spiaggia piana indefinita. L' analisi parametrica del sistema mostra che la lunghezza finita del pendio non modifica la natura delle soluzioni, ma è responsabile di una più moderata attenuazione del campo d'onde nella direzione ortogonale alla linea di riva.

Un modello analitico forzato tridimensionale è sviluppato per studiare la propagazione intorno ad un'isola conica di tsunami generati da frane. La separazione delle variabili e la trasformata di Laplace vengono impiegate per ottenere l'elevazione della superficie libera nell'intero dominio e il runup sulla linea di riva, in termini delle funzioni confluenti di Heun. Si studiano le proprietà principali di queste funzioni ed il loro comportamento asintotico. Il campo d'onde è formato da un sistema di onde transitorie che si propagano radialmente rispetto all'isola e da onde transitorie quasi intrappolate localmente. Si deriva inoltre l'espressione della leading wave transitoria. Le caratteristiche fisiche distintive degli tsunami che si propagano in geometrie a simmetria polare sono quindi confrontate con quelle degli tsunami propagantesi su spiaggia piana. I risultati analitici vengono confrontati con successo con i dati sperimentali a disposizione.

Acknowledgements

I wish to thank prof. Paolo Sammarco for his patient and outstanding guide through all the three years of PhD. He is exactly that kind of person for whom you could say there's a "before" and an "after" you meet him. My gratitude is not only due to his great academic teaching on how to perform research the right way, but especially for all the times he could accept my errors with patience and encourage me to overcome the "brick walls" I found in my academic and personal path.

Great thanks to prof. Giulia Viggiani, for her interest in my personal and professional achievements. Our talks on the "sacred fire of research" are stored in my personal luggage.

Many thanks to prof. Alberto Noli, prof. Leopoldo Franco and prof. Paolo de Girolamo. Other than being outstanding professionals, these people got a plus... they do things stylishly.

Thanks to Dr. Giorgio Bellotti, Dr. Marcello Di Risio, Dr. Andrea Panizzo and all the people I met from Roma Tre and La Sapienza. I spent very nice days with them.

I am grateful to prof. Philip L.-F. Liu and prof. Patrick Lynett for having accepted to review this work. I am very honoured that they could add their precious views to improve it.

A special thought is for prof. Chiang Mei. His unbelievable knowledge in Hydraulics and Ocean Engineering is known worldwide. I hope people also know how much kindness and attention he always offers to his students.

Finally, thanks to myself... I knew there was something good in this guy.

Contents

List of Figures

List of Tables

List of recurring symbols

γ	Euler's constant $= 0.577\ldots$ / Inverse of landlisde characteristic angle
ϵ	Nonlinearity parameter
ϵ_n	Jacobi's epsilon
$\zeta(x, y, t)$	Non-dimensional free-surface elevation
ζ^e	Evanescent component of the free-surface elevation
ζ^o	Oscillatory component of the free-surface elevation
$\zeta'(x', y', t')$	Free-surface elevation in m
η	Landslide maximum vertical height
$\eta(x, y, t)$	Non-dimensional Spatial component of the free-surface elevation
θ	Angular coordinate
θ_0	Landslide characteristic angle
λ	Wavelength / Landslide characteristic width
μ	Dispersion parameter
π	3.14159
ρ	Frobenius expansion index
σ	Landslide characteristic length
Φ	Velocity potential
ω	Non-dimensional wave frequency / Laplace integral transform parameter
ω_n	n-th modal eigenfrequency
A	Wave amplitude
A_n	Wave amplitude coefficient
b	Non-dimensional beach horizontal length / Island bottom radius
b'	Beach horizontal length / Island bottom radius in m
B_n	Wave amplitude coefficient
$\mathbb{C}$	Complex numbers set
c	Speed of a moving observer / Landslide shape parameter
C_g	Wave group velocity
C_n	Wave amplitude coefficient
g	Acceleration due to gravity $= 9.80665$ m/s^2
h	Non-dimensional water depth
h'	Water depth in m
H_n	Hankel function of the first kind and order n
$Hc_n^{(1)}$	Confuent Heun function of the first kind and order n
$Hc_n^{(2)}$	Confuent Heun function of the second kind and order n
i	Imaginary unit $= \sqrt{-1}$
I_n	Modified Bessel function of the first kind and order n
J_n	Bessel function of the first kind and order n
k	Wavenumber / Fourier integral transform parameter

k_n^*	Points of stationary phase
K_n	Modified Bessel function of the second kind and order n
L_n	Laguerre polynomial of order n
M	Kummer function of the first kind
$\mathbb{N}$	Natural numbers set
n	Integer number
$\mathbb{R}$	Real numbers set
r	Non-dimensional radial coordinate
r'	Radial coordinate in m
r_0	Non-dimensional island wet-contour radius
r'_0	Island wet-contour radius in m
r_s	Non-dimensional landslide centroid initial position along the flank of the island
r'_s	Landslide centroid initial position along the flank of the island in m
s	Incline slope
$s(y)$	Landslide lateral spreading function
t	Non-dimensional time
t'	Time in s
$\mathbf{u}(x, y, z, t)$	Velocity vector
U	Kummer function of the second kind
u_0	Non-dimensional landslide characteristic horizontal velocity
u'_0	Landslide characteristic horizontal velocity in m
U_r	Ursell number
U'_s	Landslide velocity along the incline in m/s
W	Wronsikan
w_n	Phase function
x, y, z	Non-dimensional spatial coordinates
x', y', z'	Spatial coordinates in m
x_0	Non-dimensional landslide initial position along the incline
x'_0	Landslide initial position along the incline in m
X'_s	Landslide release distance in m

Chapter 1

Introduction

The dramatic tsunamis - a Japanese word meaning "harbour waves" - that occurred in the last century fostered and increased the interest in understanding such destructive events. Very harmful tsunamis like the slump-induced one of Papua New Guinea (1998) or the devastating earthquake-generated one of the Indian Ocean (2004) have made again topical the necessity of predicting the generated wave runup and rundown, in order to assess the risks for the environment and the urbanised areas. Indeed these devastating effects are strongly dependent on the tsunami generation mechanism and its length scale (see Synolakis et al., 2008).

Tsunamis generated by distant earthquakes, occurring in the ocean floor far from the coast, spread over a very large area with a characteristic length scale $O(100\,\mathrm{Km})$. When a tilting of the bottom occurs in the middle of the ocean, an elevation surface wave starts propagating on the uplifting side of the fracture, while a depression wave travels in the opposite direction on the other side. When the perturbation attacks the coast, the shoaling and refraction effects due to the irregular coastal profiles increase the wave height dramatically, as shown in figure 1.1.

In the United States, in the last sixty years, earthquake-generated tsunamis have killed more people than earthquakes within the USA (Bardet et al., 2003). The renowned Pacific Tsunami Warning Center has been established after the 1946 Aleutian tsunami to protect the coastline and people from tsunami attacking from the ocean.

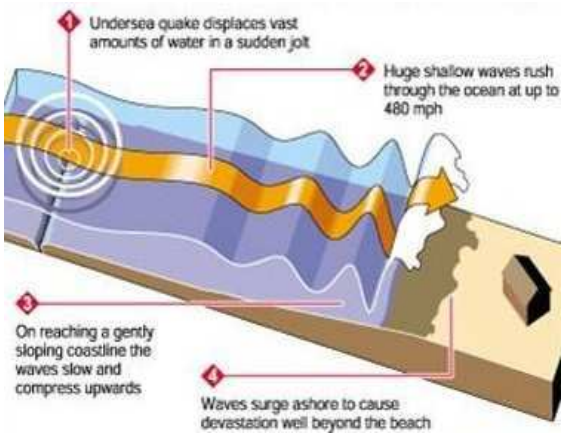

FIGURE 1.1: How earthquake tsunamis form. Source: Longman, Physical Geography in Diagrams, www.tsunami.org.

A fundamental task of the PTWC is to issue early warnings to evacuate coastal regions which may be stroke by an incoming tsunami. The activities promoted by the PTWC injected interest into the scientific community in investigating such catastrophic events, so that by 1990 the problems of tsunami propagation and coastal inundation were thought to be well understood (Bardet et al., 2003). However, successive events like the 1992 Flores island tsunami in Indonesia (see Yeh et al., 1994) or the devastating inundation of Papua New Guinea in 1998 (see Tappin et al., 2002), could not be explained and interpreted with the tools developed till that time. These tsunamis were characterised by three distinctive features, i.e. (1) unpredicted large wave amplitude, (2) delayed time of wave crest arrival and (3) limited extent of coastal inundation (see Bardet et al., 2003). These anomalies, usually not observed for earthquake-generated tsunamis, have been recognised as proper of landslide-generated tsunamis. During a seismic event, in fact, the vertical deformation of the seafloor is up to several metres, while the fault extends laterally up to 1000 km. On the other hand, the vertical deformation of the seafloor induced by a landslide depends on the slide dimensions and the distance travelled by its center of mass, usually both in the order of 100 m. However, the lateral spreading of the slide does not exceed few kilometres. Differences in these orders of magnitude explain why earthquake-generated tsunamis have greater wavelength and longer period and can travel huge distances, while landslide-generated tsunamis are localised around the source, but can reach higher amplitudes locally (this argument has been proposed by Bardet et al., 2003).

As far as Europe is concerned, Mediterranean nations are still far to develop a tsunami early warning system, despite tsunamis occur in the Mediterranean as frequently as in the Indian Ocean (see Synolakis, 2008). Only in Italy 19 tsunamis occurred during the last century, as reported in the Italian Tsunami Catalogue prompted by the National Institute of Geophysics and Volcanology (INGV) (see table 1.1). Among these, the recent landslide tsunami of the Stromboli island (2002, South Mediterranean, Italy) (see Tinti et al., 2005) has again pointed out the necessity of establishing an effective tsunami warning center, following the PTWC model.

While excellent advancements have been made in understanding earthquake tsunamis, knowledge of the generation and propagation of landslide tsunamis is instead still fragmentary (see Liu et al., 2005). The most challenging issue is that landslide tsunamis are not generated instantaneously as earthquake tsunamis, but strongly depend on the time-history of the seafloor deformation. As a consequence, these events cannot be investigated by transferring a "hot-start" initial condition, due to the impulsive ground movement, to the free-surface. Indeed at the state of the art, the main gap in modelling such events seems to be the absence of analytical three-dimensional models which take into account the interaction between landslide and water (see Lynett and Liu, 2005). This work aims to give a contribution in filling this gap, with a specific insight on modelling the coupled dynamics of landslide motion and wave field generation.

When a landslide occurs near the shoreline, a depression wave is usually generated in the immediate surroundings, while an elevation wave propagates outwards, as shown in figure 1.2. The nature of the generated waves strongly depends on the geometry of the beach (see Meyer, 1971; Mei et al., 2005). In the following we shall consider two typical oceanographic topographies: a plane beach and a conical island. Due to refraction, a straight plane beach is able to trap all the energy transferred to the fluid inside a narrow belt near the shoreline. As a result, after few instants following the generation, the waves start travelling along the shore, while in the offshore direction

Year	Month	Day	Location	Description
1905	9	8	Tyrrhenian Calabria	Extended flooding
1906	4	4	Campania	Sea oscillations in Naples gulf
1907	10	23	Ionian Calabria	Sea flooding
1908	12	28	Messina Strait	Destructions, hundreds of victims
1916	7	3	Aeolian Islands	Inundation at Stromboli
1916	8	16	Central Adriatic	Tsunami waves observed at Tavollo
1919	5	22	Aeolian Islands	Sea retreat / flooding at Stromboli
1926	8	17	Aeolian Islands	Anomalous sea retreat at Salina
1930	9	11	Aeolian Islands	Flood at Stromboli. Two victims
1930	10	30	Central Adriatic	Sudden high tide at Ancona
1940	1	15	Northern Sicily	Waves in gulf of Palermo
1944	8	20	Aeolian Islands	Flooding. Houses destroyed
1954	2	NA	Aeolian Islands	Tsunami at Stromboli
1968	4	18	Liguria	Flooding at Alassio
1978	6	21	Central Adriatic	Extended flooding and damage
1979	10	16	Liguria-Cote d'Azur	3m high waves at Antibes
1988	4	20	Aeolian Islands	Waves in Vulcano and Lipari
1990	12	13	Eastern Sicily	Anomalous wave at Augusta
2002	12	30	Aeolian Islands	Heavy damage at Stromboli

TABLE 1.1: Tsunami occurrences in Italy in the last century. Font: Italian Tsunami Catalogue, National Institute of Geophysics and Volcanology (INGV), Italy.

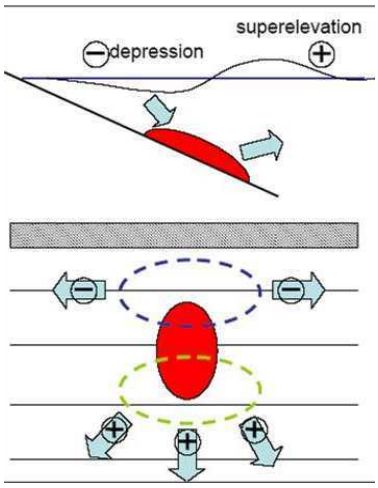

FIGURE 1.2: Landslide tsunami generation and propagation. After the mass falls into water, a leading elevation wave starts propagating offshore, while a deep depression wave travels alongshore backwards of the slide.

the perturbation rapidly decays in time (see Lynett and Liu, 2005). Since these waves reach their maximum amplitude near the coast, they are called *edge waves*. For a conical island, refraction is sensitively reduced and waves are no more trapped along the shoreline (see Meyer, 1971). Energy radiates outwards from the island and waves are expected to propagate also in the offshore direction.

The work is organized as follows. In chapter 2 the general theory of transient surface waves propagating on flat bottoms is recalled, both in shallow and intermediate waters, as an introduction to the more complex problems investigated in the subsequent sections. In chapter 3 landslide generated tsunamis propagating along an indefinite plane beach are investigated. In chapter 4 the topography is made slightly more approximated by considering a semi-plane beach, consisting of a sloping part connected to a flat continental platform. Finally, in chapter 5 landslide tsunamis propagating around a conical island are studied, emphasizing the analytical complexities and the physical novelties introduced when considering a round geometry.

Chapter 2

3D transient surface waves propagating on flat bottoms

In this section we investigate on transient disturbances generated by either an impulsive movement of the bottom or a sudden bump of the free surface and propagating in all horizontal directions. Due to the dispersive nature of free-surface waves, the propagation of transient water waves is more complex than many similar phenomena occurring in different media. To clearly understand the role of dispersion we shall consider two different cases. In section §2.1 we will focus on transient waves generated by a sudden bottom disturbance and propagating in intermediate waters. Here dispersion plays a fundamental role in separating the wave packets travelling away from the source. Then in section §2.2 we will analyse transient waves propagating in shallow waters. Here the non-dispersive nature of the medium is responsible of the generation of solitary oscillations travelling away from the source.

2.1 3D transient dispersive waves generated by bottom disturbances

Within the linearised approximation for small-amplitude waves (see Mei et al., 2005), the governing equation for an irrotational flow in an ocean of constant depth h can be expressed in terms of the velocity $\mathbf{u}(x, y, z, t)$ and its potential $\Phi(x, y, z, t)$ as

$$\mathbf{u}(x, y, z, t) = \nabla\Phi(x, y, z, t), \quad -h < z < 0. \tag{2.1.1}$$

In the latter expression, $\nabla(\cdot) = (\partial\cdot/\partial x, \partial\cdot/\partial y, \partial\cdot/\partial z)$ is the 3D nabla operator. As shown in figure 2.1, (x, y) are the coordinates of a point on the horizontal plane representing the unperturbed free surface, z is the vertical elevation from the (x, y) plane and t is time. If the fluid is inviscid too, conservation of mass requires

$$\nabla \cdot \mathbf{u} = 0, \quad -h < z < 0. \tag{2.1.2}$$

Then equations (2.1.1) and (2.1.2) can be combined into the Laplace equation

$$\nabla^2\Phi(x, y, z, t) = 0, \quad -h < z < 0. \tag{2.1.3}$$

The govering equation (2.1.3) is to be solved together with the linearised kinematic boundary condition on the free-surface

$$\zeta_t(x, y, t) = \Phi_z(x, y, z, t), \quad z = 0, \tag{2.1.4}$$

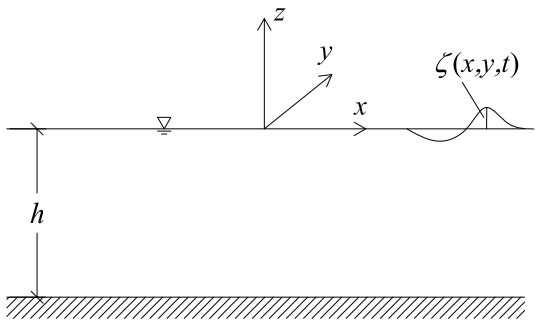

FIGURE 2.1: Geometry of the fluid domain.

and the linearised dynamic boundary condition

$$\Phi_t + g\zeta(x, y, t) = 0, \quad z = 0. \tag{2.1.5}$$

In the latter equations, $\zeta(x, y, t)$ denotes the free-surface elevation from the undisturbed water plane (see figure 2.1), g is the gravity acceleration and subscripts denote differentiation with respect to the relevant variable. Differentiating (2.1.5) with respect to time and substituting into (2.1.4) we derive a combined form of the kinematic and dynamic boundary conditions on the free surface

$$\Phi_{tt} + g\Phi_z = 0, \quad z = 0. \tag{2.1.6}$$

Finally, an appropriate no-flux condition at the bottom needs to be applied. Let us introduce a displacement of the bottom with vertical velocity $W(x, y, t)$; the no-flux condition on the sea floor is then

$$\Phi_z = W, \quad z = -h. \tag{2.1.7}$$

The boundary value problem governed by equation (2.1.3) with boundary conditions (2.1.6) and (2.1.7) will be solved by employing an efficient method based on Green functions following Mei et al. (2005). First, consider an impulsive disturbance concentrated at the origin

$$W(x, y, t) = \delta(x)\delta(y)\delta(t - 0^+) \tag{2.1.8}$$

at time $t = 0^+$, $\delta(x)\delta(y)$ being the $2D$ delta function, and denote the solution of this transient problem as $G(x, y, z, t)$. Once $G(x, y, z, t)$ is known, thanks to linearity, the potential induced by a generic disturbance $W(x, y, t)$ can be obtained as

$$\Phi(x, y, z, t) = \int_0^t \int_{-\infty}^{\infty} \int_{-\infty}^{\infty} W(x', y', \tau)\, G(x - x', y - y', t - \tau)\, \mathrm{d}x'\mathrm{d}y'\mathrm{d}\tau \tag{2.1.9}$$

i.e. the superposition of transient waves generated by infinitesimal impulsive sources whose magnitude at $(x, y, t) = (x', y', \tau)$ is $W(x', y', \tau)\mathrm{d}x'\mathrm{d}y'\mathrm{d}\tau$. Let us now find the solution $G(x, y, z, t)$ of the boundary-value problem generated by the impulsive disturbance W (2.1.8).

2.1.1 Impulsive bottom disturbance concentrated at the origin

In order to study the wave propagation in all the horizontal directions, let us introduce a system of polar coordinates r, θ in the horizontal plane, such that

$$x = r\cos\theta, \quad y = r\sin\theta.$$

Then require the unknown wave potential $G(r,\theta,z,t)$ to satisfy the Laplace equation (2.1.3), i.e.

$$\nabla^2 G = 0, \quad -h < z < 0, \tag{2.1.10}$$

where

$$\nabla^2 = \frac{1}{r}\frac{\partial}{\partial r}\left(r\frac{\partial}{\partial r}\right) + \frac{1}{r^2}\frac{\partial^2}{\partial\theta^2} + \frac{\partial^2}{\partial z^2}$$

is the Laplacian in cylindrical polar coordinates. Let us now introduce the boundary and the initial conditions. The kinematic and dynamic b.c.'s on the free surface in the combined form (2.1.6) applied to the impulsive potential G require

$$G_{tt} + g\,G_z = 0, \quad z = 0. \tag{2.1.11}$$

The impulsive disturbance on the bottom (2.1.8) can be also written as

$$W(r,\theta,t) = \frac{\delta(r)}{2\pi r}\,\delta(t-0^+), \tag{2.1.12}$$

where $\delta(r)/2\pi r$ is the $2D$ delta function in polar coordinates (see Mei et al., 2005), which satisfies

$$\int_0^{2\pi}\int_0^{\infty} \frac{r\delta(r)\mathrm{d}r}{2\pi r}\,\mathrm{d}\theta = 1.$$

Having defined W by (2.1.12), the no-flux condition on the bottom (2.1.7) applied to G becomes then

$$G_z = \frac{\delta(r)}{2\pi r}\,\delta(t-0^+), \quad z = -h. \tag{2.1.13}$$

Furthermore we require that the potential G and its radial derivative G_r both vanish at large distance from the origin

$$G, G_r \to 0 \quad \text{as } r \to \infty. \tag{2.1.14}$$

Finally let us prescribe the initial conditions at rest

$$G = G_t = 0, \quad t = 0. \tag{2.1.15}$$

Condition (2.1.13) applies an impulsive disturbance on the vertical velocity G_z at the seafloor, concentrated at the origin $r = 0$ and independent of θ. Since the bottom disturbance is isotropic with respect to θ, we assume the potential to be isotropic, i.e. $G = G(r,z,t)$. The governing equation (2.1.10) becomes then

$$\frac{1}{r}\frac{\partial}{\partial r}\left(r\frac{\partial G}{\partial r}\right) + \frac{\partial^2 G}{\partial z^2} = 0. \tag{2.1.16}$$

To solve the latter equation together with the boundary conditions (2.1.11), (2.1.13) and (2.1.14) let us employ the Hankel integral transform

$$\hat{G}(z,t;k) = \int_0^{\infty} r J_0(kr)\,G(r,z,t)\;\mathrm{d}r, \quad G(r,z,t) = \int_0^{\infty} k J_0(kr)\hat{G}(z,t;k)\,\mathrm{d}k, \tag{2.1.17}$$

where J_0 is the Bessel function of first kind and order 0. Now apply the Hankel transform (2.1.17) to the first term of the governing equation (2.1.16). Integrating twice by parts and employing the boundary conditions at infinity (2.1.14) we obtain

$$\begin{aligned}&\int_0^{\infty} r J_0(kr)\left[\frac{1}{r}\frac{\partial}{\partial r}\left(r\frac{\partial G}{\partial r}\right)\right]\mathrm{d}r = \\ &= -\int_0^{\infty}\left[kJ_{0,rr}(kr)r + J_{0,r}(kr)\right]kG(r,z,t)\mathrm{d}r = -k^2\hat{G}(z,t;k),\end{aligned} \tag{2.1.18}$$

since $J_0(kr)$ satisfies the Bessel equation

$$krJ_{0,rr}(kr) + J_{0,r}(kr) + krJ_0(kr) = 0.$$

With (2.1.18), the Hankel transform of the whole governing equation (2.1.16) becomes then

$$\hat{G}_{zz} - k^2\hat{G} = 0, \tag{2.1.19}$$

while the boundary conditions (2.1.11) and (2.1.13) become respectively

$$\hat{G}_{tt} + g\hat{G}_z = 0, \quad z = 0, \tag{2.1.20}$$

$$\hat{G}_z = \tfrac{1}{2\pi}\,\delta\left(t - 0^+\right), \quad z = -h. \tag{2.1.21}$$

Finally, the Hankel transform of the initial conditions (2.1.15) gives

$$\hat{G} = \hat{G}_t = 0, \quad t = 0. \tag{2.1.22}$$

The boundary-value problem defined by (2.1.19)–(2.1.22) can be solved by further employing the Laplace trasform of $\hat{G}$

$$\hat{\bar{G}}(z;k,s) = \int_0^\infty \hat{G}(z,t;k)\mathrm{e}^{-st}\mathrm{d}t, \tag{2.1.23}$$

being s the complex transform parameter, together with the initial conditions (2.1.22). Applying the Laplace transform (2.1.23) to the governing equation (2.1.19) gives

$$\hat{\bar{G}}_{zz} - k^2\hat{\bar{G}} = 0, \quad -h < z < 0, \tag{2.1.24}$$

while the Laplace transforms of the boundary conditions (2.1.20) and (2.1.21) are respectively

$$\hat{\bar{G}}_z + \frac{s^2}{g}\,\hat{\bar{G}} = 0, \quad z = 0, \tag{2.1.25}$$

$$\hat{\bar{G}}_z = \frac{1}{2\pi}, \quad z = -h. \tag{2.1.26}$$

The general solution of the governing equation (2.1.24) is simply

$$\hat{\bar{G}}(z) = A\cosh kz + B\sinh kz, \tag{2.1.27}$$

where A and B are integration constants to be found via the boundary contitions (2.1.25) and (2.1.26). Applying these b.c.'s to (2.1.27) yields the values of the integration constants

$$A = -\frac{\omega^2}{\omega^2 + s^2}\frac{1}{2\pi\sinh kh}, \quad B = \frac{\omega^2}{2\pi gk^2\sinh kh}\frac{s^2}{\omega^2 + s^2},$$

where

$$\omega^2 = gk\tanh kh. \tag{2.1.28}$$

Substituting the above values of the integration constants A and B into (2.1.27) and simplifying the algebra, we obtain the solution of the boundary-value problem (2.1.24)–(2.1.26)

$$\hat{\bar{G}}(z) = \frac{1}{2\pi}\frac{s^2\sinh kz - gk\cosh kz}{k\cosh kh}\frac{1}{\omega^2 + s^2}. \tag{2.1.29}$$

Finally, performing the inverse Hankel transform of (2.1.29) we get

$$\bar{G}(r,z;s) = \int_0^\infty kJ_0(kr)\hat{\bar{G}}(z;k,s)\mathrm{d}k. \tag{2.1.30}$$

Expression (2.1.30) is then the Laplace transform of the velocity potential relevant to an impulsive disturbance of the sea floor concentrated at the origin.

2.1.2 Tsunami generated by a sudden movement of the bottom

As anticipated before, if the velocity disturbance on the bottom $W(r,t)$ is generic, linearity of the problem allows us to apply relation (2.1.9), which in polar coordinates writes as

$$\Phi(r,\theta,z,t) = \int_0^\infty \int_0^{2\pi} \int_0^t r' W(r',\theta',\tau) G(|\mathbf{r}-\mathbf{r}'|, z, t-\tau)\, \mathrm{d}\tau\, \mathrm{d}\theta'\, \mathrm{d}r', \tag{2.1.31}$$

where

$$|\mathbf{r}-\mathbf{r}'| = \left[\left(x-x'\right)^2 + \left(y-y'\right)^2\right]^{1/2} = \left[r^2 + r'^2 - 2rr'\cos(\theta-\theta')\right]^{1/2}$$

and Φ is the velocity potential generated by the bottom movement. Following the procedure outlined above, let us now apply the Laplace transform (2.1.23) to (2.1.31)

$$\bar{\Phi}(r,\theta,z;s) = \int_0^\infty r' \int_0^{2\pi} \int_0^\infty \int_0^t W(r',\theta',\tau) G(|\mathbf{r}-\mathbf{r}'|, z, t-\tau)\, e^{-st}\, \mathrm{d}\tau\, \mathrm{d}t\, \mathrm{d}\theta'\, \mathrm{d}r'. \tag{2.1.32}$$

By making use of the convolution theorem (see Mei, 1997)

$$\bar{W}(r',\theta';s)\bar{G}(|\mathbf{r}-\mathbf{r}'|, z; s) = \int_0^\infty \int_0^t W(r',\theta',\tau) G(|\mathbf{r}-\mathbf{r}'|, z, t-\tau)\, \mathrm{e}^{-st}\, \mathrm{d}\tau\, \mathrm{d}t$$

the two inner integrals of (2.1.32) have a strong simplification and the Laplace transform of the velocity potential Φ (2.1.31) simplifies to

$$\bar{\Phi}(r,\theta,z;s) = \int_0^\infty r' \int_0^{2\pi} \bar{W}(r',\theta',s)\bar{G}(|\mathbf{r}-\mathbf{r}'|, z; s)\, \mathrm{d}\theta' \mathrm{d}r'. \tag{2.1.33}$$

Since our final goal is to obtain the expression for the free-surface elevation $\zeta(r,\theta,t)$, let us consider the only condition we haven't applied yet, namely the dynamic boundary condition on the free-surface (2.1.5). Laplace transform of (2.1.5) is

$$\bar{\zeta}(r,\theta;s) = -\frac{s}{g}\, \bar{\Phi}\big|_{z=0}\,.$$

Substituting expression (2.1.33) for the transformed potential $\bar{\Phi}$, the latter equation becomes

$$\bar{\zeta}(r,\theta;s) = -\frac{s}{g} \int_0^\infty r' \int_0^{2\pi} \bar{W}(r',\theta';s)\bar{G}(|\mathbf{r}-\mathbf{r}'|, 0; s) \mathrm{d}\theta'\, \mathrm{d}r'. \tag{2.1.34}$$

Finally, by making use of (2.1.29) and (2.1.30) for the transformed impulsive potential $\bar{G}$, we get the expression for the Laplace transform of the free-surface elevation

$$\bar{\zeta}(r,\theta;s) = \frac{1}{2\pi} \int_0^\infty r' \int_0^{2\pi} \bar{W}(r',\theta',s) \int_0^\infty k J_0(k|\mathbf{r}-\mathbf{r}'|) \frac{s}{\omega^2+s^2} \frac{\mathrm{d}k\, \mathrm{d}\theta' \mathrm{d}r'}{\cosh kh}. \tag{2.1.35}$$

The free-surface elevation $\zeta(r,\theta,t)$ can be determined by inverse-transforming the latter expression, once the form of W is known.

Let us consider an impulsive displacement of the bottom, i.e.

$$W(r,\theta,t) = w(r,\theta)\delta\left(t-0^+\right),$$

such that $\bar{W}(r,\theta;s) = w(r,\theta)$. With this position, the Laplace transform of the free-surface elevation (2.1.35) becomes

$$\bar{\zeta}(r,\theta;s) = \frac{1}{2\pi}\int_0^\infty r' \int_0^{2\pi} w(r',\theta') \int_0^\infty kJ_0(k|\mathbf{r}-\mathbf{r}'|)\frac{\overline{\cos\omega t}}{\cosh kh}\,\mathrm{d}k\,\mathrm{d}\theta'\mathrm{d}r',$$

being

$$\overline{\cos\omega t} = \int_0^\infty \cos\omega t\,\mathrm{e}^{-st}\mathrm{d}s = \frac{s}{\omega^2+s^2}.$$

Therefore the free-surface elevation in the time domain is

$$\zeta(r,\theta,t) = \frac{1}{2\pi}\int_0^\infty r' \int_0^{2\pi} w(r',\theta') \int_0^\infty kJ_0(k|\mathbf{r}-\mathbf{r}'|)\frac{\cos\omega t}{\cosh kh}\,\mathrm{d}k\,\mathrm{d}\theta'\mathrm{d}r'. \tag{2.1.36}$$

The latter expression can be further simplified by applying the addition theorem of Bessel functions

$$J_0(k|\mathbf{r}-\mathbf{r}'|) = \sum_{n=0}^{\infty}\epsilon_n J_n(kr)J_n(kr')\cos n(\theta-\theta'), \tag{2.1.37}$$

where

$$\epsilon_n = \begin{cases} 1 & \text{if } n=0 \\ 2 & \text{if } n=1,2,\ldots \end{cases}$$

is the Jacobi epsilon. By substituting (2.1.37) into (2.1.36) and developing some simple algebra, we obtain the final expression for the free-surface elevation:

$$\zeta(r,\theta,t) = \sum_{n=0}^{\infty}\epsilon_n \int_0^\infty kJ_n(kr)\frac{\cos\omega t}{\cos kh}\left(W_n^c\cos n\theta + W_n^s\sin n\theta\right)\mathrm{d}k, \tag{2.1.38}$$

where the amplitude coefficients $W_n^{c,s}$ are given by

$$W_n^{c,s}(k) = \frac{1}{2\pi}\int_0^\infty r' \int_0^{2\pi} w(r',\theta')J_n(kr')(\cos n\theta', \sin n\theta')\mathrm{d}\theta'\mathrm{d}r'. \tag{2.1.39}$$

The free-surface elevation (2.1.38) is the sum of all the even ($\cos n\theta$) and odd ($\sin n\theta$) angular modes, whose amplitudes are respectivley W_n^c and W_n^s, depending on the shape of the disturbance $w(r,\theta)$.

In the following, consider as a practical application

$$w(r,\theta) = A\mathrm{e}^{-r^2/\alpha^2}, \tag{2.1.40}$$

where A is the amplitude at the origin, measured in metres, and take $\alpha = 1\,\mathrm{m}$ for simplicity. Expression (2.1.40) describes a perturbation centred at the origin and attenuating exponentially in the radial direction, not depending on the angle θ. Since w represents a zero-th modal perturbation, substitution of (2.1.40) into (2.1.39) gives

$$\begin{aligned} W_0^c(k) &= \tfrac{A}{2}\,\mathrm{e}^{-k^2/4} \\ W_n^c(k) &= 0 \quad \text{for } n=1,2,\ldots \\ W_n^s(k) &= 0 \quad \text{for } n=0,1,\ldots \end{aligned} \tag{2.1.41}$$

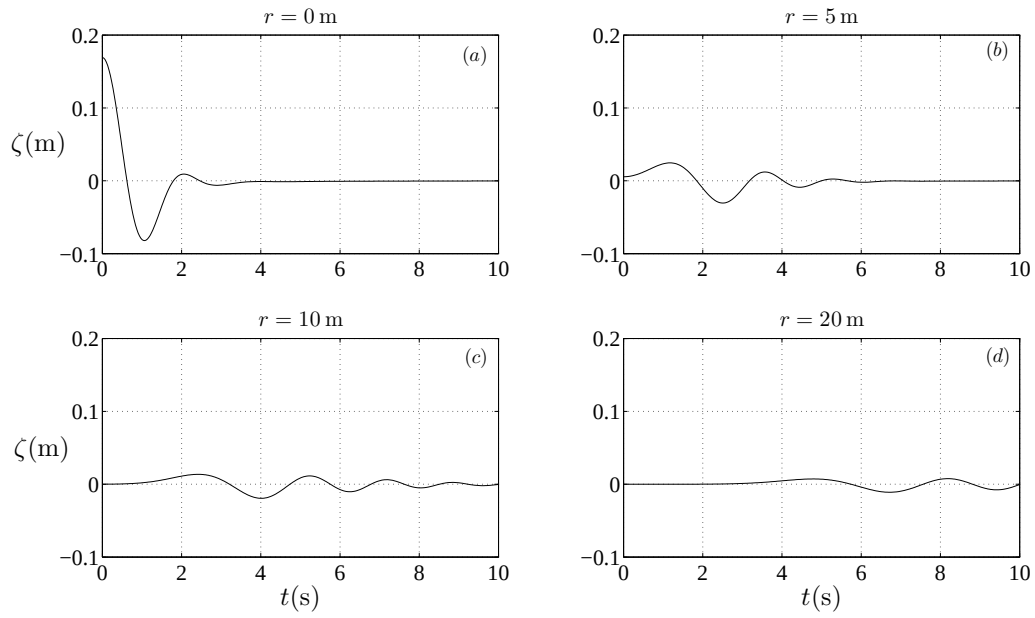

FIGURE 2.2: Radial propagation of a tsunami induced by the bottom disturbance (2.1.40) centred at the origin in intermediate waters, with $A = 1\,\mathrm{m}$. Time series at points: (a) $r = 0\,\mathrm{m}$, (b) $r = 5\,\mathrm{m}$, (c) $r = 10\,\mathrm{m}$, (d) $r = 20\,\mathrm{m}$.

and the free-surface elevation (2.1.38) becomes

$$\zeta(r,t) = \frac{A}{2}\int_0^\infty k\,\mathrm{e}^{-k^2/4}\frac{\cos\omega t}{\cosh kh}J_0(kr)\mathrm{d}k, \tag{2.1.42}$$

where

$$\omega = (gk\tanh kh)^{1/2} \tag{2.1.43}$$

from the dispersion relation (2.1.28). Since the bottom disturbance is isotropic, the generated perturbation ζ (2.1.42) does not depend on θ. Figure 2.2(a–d) shows the time series of the free-surface elevation (2.1.42) at four different points, respectively $r = 0\,\mathrm{m}$ (figure 2.2a), $r = 5\,\mathrm{m}$ (figure 2.2b), $r = 10\,\mathrm{m}$ (figure 2.2c) and finally $r = 20\,\mathrm{m}$ (figure 2.2d), for unit amplitude $A = 1\,\mathrm{m}$. As the wave motion propagates away from the origin $r = 0$, the different wave components start to unpack, due to the dispersive nature of water. Far from the source, longer waves come first and are followed by a tail of shorter waves. Since energy leaks towards infinity, the wave amplitude decreases while travelling away from the origin. Finally, note also that near the origin the first crest is always larger than the first trough (see figure 2.2a), while far from the origin the amplitude of the first incoming crest becomes smaller than the amplitude of the first trough (see figure 2.2c, d). We next turn to the analysis of the leading wave at large distance from the source of the perturbation.

The leading wave

Consider again the expression of the free-surface elevation (2.1.42). For large r, the asymptotic expansion of the Bessel function

$$J_0(kr) \simeq \sqrt{\frac{2}{\pi kr}}\cos\left(kr - \frac{\pi}{4}\right) \tag{2.1.44}$$

can be used (see Mei, 1997). Substitution of the latter expansion into (2.1.42) yields

$$\zeta(r,\theta,t) \simeq \frac{A}{\sqrt{2\pi r}} \int_0^\infty \frac{\sqrt{k}\,\mathrm{e}^{-k^2/4}}{\cosh kh} \cos\omega t \cos\left(kr - \frac{\pi}{4}\right) \mathrm{d}k, \tag{2.1.45}$$

for large t. Let us transform the product between the two cosines of (2.1.45) in the exponential form to obtain

$$\zeta(r,t) \simeq \frac{A}{2\sqrt{2\pi r}} \int_0^\infty \frac{\sqrt{k}\,\mathrm{e}^{-k^2/4}}{\cosh kh} \Re\left\{\mathrm{e}^{\mathrm{i}(kr-\omega t-\pi/4)} + \mathrm{e}^{\mathrm{i}(kr+\omega t-\pi/4)}\right\} \mathrm{d}k,$$

where $\Re\{z\}$ is the real part of the complex number z and $\mathrm{i} = \sqrt{-1}$ is the imaginary unit. After some elementary algebraic manipulations, the latter expression can be finally re-written as

$$\zeta(r,t) \simeq \frac{A}{2\sqrt{2\pi r}} \Re\left\{\int_0^\infty \frac{\sqrt{k}\mathrm{e}^{-k^2/4}}{\cosh kh} \left[\mathrm{e}^{\mathrm{i}t(kr/t-\omega-\pi/4t)} + \mathrm{e}^{\mathrm{i}(kr/t+\omega-\pi/4t)}\right] \mathrm{d}k\right\}, \tag{2.1.46}$$

where the exponential terms represent respectively an outgoing wave and an incoming wave. The behaviour of these two waves at large times can be analysed with the method of *stationary phase* (see Mei et al., 2005), that we quicky review in the following paragraph.

Let us consider an integral of the form

$$I = \int_0^\infty f(k)\,\mathrm{e}^{\mathrm{i}tg(k)}\mathrm{d}k. \tag{2.1.47}$$

For large t, the complex exponential functions of phase $g(k)$ oscillate very quickly with varying k, sweeping a very small net area, and so determining the integral (2.1.47) to be approximately null. However, if there is a point k^* where the phase is stationary, i.e.

$$\left.\frac{\mathrm{d}g(k)}{\mathrm{d}k}\right|_{k=k^*} = 0,$$

the exponential function $\mathrm{e}^{\mathrm{i}tg(k)}$ varies very slowly in a neighbourhood of k^*, covering a larger net area. The contribution to the integral (2.1.47) coming from this stationary point k^* is therefore significant. In a neighbourhood of the stationary point k^*, we approximate

$$f(k) \simeq f(k^*) \tag{2.1.48}$$

$$g(k) \simeq g(k^*) + \frac{1}{2}\left.\frac{\mathrm{d}^2 g}{\mathrm{d}k^2}\right|_{k=k*} \cdot (k-k^*)^2, \tag{2.1.49}$$

such that (2.1.47) becomes

$$I \simeq f(k^*)\mathrm{e}^{\mathrm{i}tg(k^*)} \int_0^\infty \mathrm{e}^{\,\mathrm{i}\ddot{g}(k^*)\cdot(k-k^*)^2/2}\,\mathrm{d}k, \tag{2.1.50}$$

where $\dot{()} = \mathrm{d}/\mathrm{d}k$ for brevity. Solving the last integral finally gives the stationary-phase approximation of I (2.1.47) at large times:

$$I \simeq f(k^*)\mathrm{e}^{\mathrm{i}tg(k^*)} \sqrt{\frac{2\pi}{t\,|\ddot{g}(k^*)|}}\,\mathrm{e}^{\pm\mathrm{i}\pi/4}, \tag{2.1.51}$$

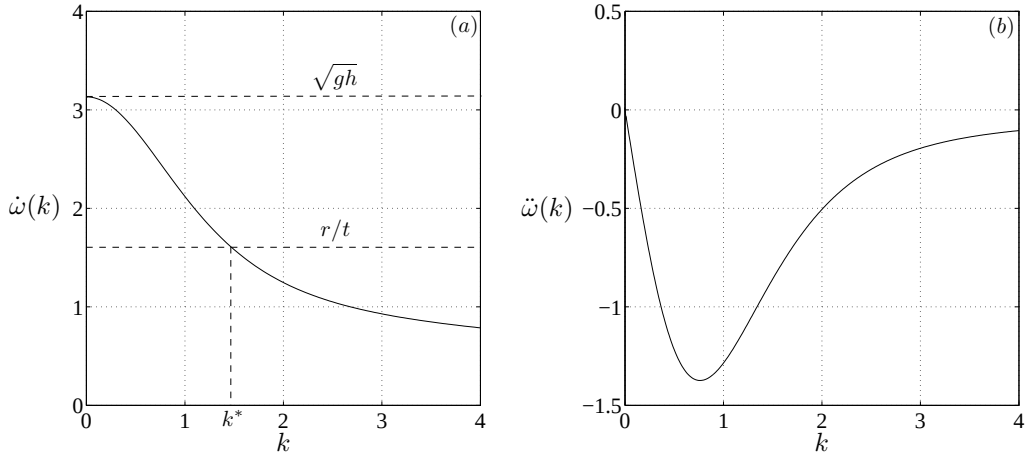

FIGURE 2.3: Behaviour of (a) $\dot{\omega}$ and (b) $\ddot{\omega}$ versus the wavenumber k for $h = 1\,\mathrm{m}$. The stationary point k^* satisfies $\dot{\omega}(k^*) = r/t$.

where the $\pm$ sign has to be taken if $\ddot{g}(k^*) \gtrless 0$.

Now let us go back to our original problem (2.1.46); the phase functions of the complex exponentials are

$$g(k) = k\frac{r}{t} \mp \omega(k) - \frac{\pi}{4t} \tag{2.1.52}$$

respectively for the outgoing wave $(-)$ and the incoming wave $(+)$. Therefore the stationary points for the outgoing wave occur at

$$\dot{g}(k^*) = \frac{r}{t} - \dot{\omega}(k^*) = 0,$$

which gives

$$\frac{r}{t} = \dot{\omega}(k^*) = C_g(k^*) \tag{2.1.53}$$

for the stationary point k^*, where

$$C_g(k) = \dot{\omega}(k) = \frac{1}{2}\frac{\omega(k)}{k}\left(1 + \frac{2kh}{\sinh 2kh}\right) \tag{2.1.54}$$

is the group celerity and $\omega(k)$ is still given by (2.1.43). Numerical inspection of (2.1.53) shows that stationary points for the right-going wave can occur only if

$$\frac{r}{t} < \sqrt{gh}, \tag{2.1.55}$$

as illustrated in figure 2.3(a). Note also that the second derivative $\ddot{\omega}(k) \leq 0$ as shown in figure 2.3(b). On the other hand, for the incoming wave there are no stationary points and its contribution to the integral (2.1.46) is negligible at large times. By applying the stationary-phase approximation (2.1.51) with

$$\begin{aligned} g(k) &= k\frac{r}{t} - \omega(k) - \frac{\pi}{4t}, \\ \ddot{g}(k) &= -\ddot{\omega}(k) \geq 0, \\ f(k) &= \frac{\sqrt{k}\mathrm{e}^{-k^2/4}}{\cosh kh}, \end{aligned} \tag{2.1.56}$$

the free surface elevation at large t and r (2.1.46) can be finally approximated by

$$\zeta(r,t) \simeq \frac{A}{2\sqrt{r}} \frac{\sqrt{k^*}\,\mathrm{e}^{-{k^*}^2/4}}{\cosh k^* h} \mathrm{e}^{\mathrm{i}tg(k^*)} \sqrt{\frac{1}{t\,|\ddot{\omega}(k^*)|}}\,\mathrm{e}^{\mathrm{i}\pi/4} \tag{2.1.57}$$

where the stationary point k^* is the solution of (2.1.53) (see figure 2.3), provided the existence condition (2.1.55). Expression (2.1.57) is therefore the stationary-phase approximation of the free-surface elevation at large times and far from the origin $r = 0$. According to (2.1.57), an observer travelling at constant speed $r/t = c < \sqrt{gh}$, for which the stationary point k^* satisfies $C_g(k^*) = c$, sees a wavetrain whose amplitude

$$\zeta(r = ct, t) \simeq \frac{A}{2t\sqrt{c}} \frac{\sqrt{k^*}\,\mathrm{e}^{-{k^*}^2/4}}{\cosh k^* h} \mathrm{e}^{\mathrm{i}tg(k^*)} \sqrt{\frac{1}{|\ddot{\omega}(k^*)|}}\,\mathrm{e}^{\mathrm{i}\pi/4} \tag{2.1.58}$$

decays with time as $O\left(t^{-1}\right)$. Due to the radial spreading of two-dimensional waves, this rate of decay is larger than that of a transient one-dimensional disturbance propagating along a flat bottom, $O\left(t^{-1/2}\right)$.

What about the leading wave? To follow the wave front, an observer must travel at a speed near to the maximum group celerity, i.e. $r/t \to \sqrt{gh}$. At this speed, $k^* \to 0$ and $\ddot{\omega} \to 0$ (see figure 2.3). As a consequence, the free-surface elevation (2.1.57) tends to infinity and the stationary phase approximation fails. To obtain a better approximation for the leading wave, we need to go back to the general expression (2.1.45) of the free-surface elevation and expand $\omega(k)$ (2.1.43) near the stationary point $k^* = 0$ to the third order (see Mei et al., 2005):

$$\omega(k) \simeq \sqrt{gh}\left(k - \frac{k^3 h^3}{6}\right).$$

With this approximation, (2.1.46) becomes

$$\zeta(r,t) \simeq \frac{A}{2\sqrt{2\pi r}} \Re\left\{\int_0^\infty \sqrt{k}\mathrm{e}^{\mathrm{i}\left[k(r-\sqrt{gh}t)+k^3h^2/6t\sqrt{gh}-\pi/4\right]}\mathrm{d}k\right\}, \tag{2.1.59}$$

having neglected the contribution of the incoming wave at large times. Unlike transient one-dimensional waves, where the leading wave could be expressed in terms of Airy functions of the spatial variable (see Mei et al., 2005, for further details), the integral (2.1.59) cannot be further simplified in terms of known analytical functions of r. However, since the wave front moves at the fastest speed possible, i.e. $c = \sqrt{gh}$, its position at a given time is described by $r = \sqrt{gh}t$. Substituting the latter relation into (2.1.59) yields

$$\zeta(r,t) \simeq \frac{A}{4}\sqrt{\frac{2}{\pi\sqrt{gh}t}}\,\Re\left\{\mathrm{e}^{-\mathrm{i}\pi/4}\int_0^\infty \sqrt{k}\,\mathrm{e}^{\mathrm{i}k^3h^2/6\,t\sqrt{gh}}\mathrm{d}k\right\}. \tag{2.1.60}$$

Since

$$\int_0^\infty \sqrt{k}\,\mathrm{e}^{\mathrm{i}k^3\alpha}\mathrm{d}k = \frac{(1+\mathrm{i})\sqrt{2\pi}}{6\sqrt{\alpha}},$$

(2.1.60) can be further simplified to obtain the final expression of the leading wave ζ_l

$$\zeta_l(t) \simeq \frac{\sqrt{3}}{6\sqrt{gh}}\frac{A}{ht}. \tag{2.1.61}$$

Note that the leading wave decays as $O(t^{-1})$ in the three-dimensional domain, i.e. it vanishes faster than the leading Airy wave, $O(t^{-1/3})$, generated by a transient disturbance in a two-dimensional ocean of constant depth (see Mei et al., 2005).

2.2 3D transient long waves generated by surface disturbances

In the geometric scheme of section §2.1 (see figure 2.1), let us consider the shallow-water limit $kh \ll 1$. Within this approximation, it is more convenient to consider directly the free-surface elevation $\zeta(r,\theta,t)$ rather than the velocity potential, as this procedure will ease the calculations. The long-wave governing equation for $\zeta(r,\theta,t)$ in polar coordinates writes

$$\zeta_{tt} - gh\left(\frac{1}{r}\,\zeta_r + \zeta_{rr} + \frac{1}{r^2}\,\zeta_{\theta\theta}\right) = 0. \tag{2.2.1}$$

Furthermore, instead of applying an initial disturbance at the bottom, in this section we shall follow a different approach, based on the so-called "hot-start" condition. As anticipated in §1, when a tsunami is triggered by an impulsive bottom movement, the time-history of the seafloor motion is negligible and the initial bottom deformation can be transferred directly on the free surface. The validity of this simplifying assumption will be confirmed later on.

Let us apply to the present problem the procedure we already used to find the velocity potential in §2.1. First analyse the response $\eta(r,\theta,t)$ to a sudden bump of the free-surface concentrated at the origin

$$F(r,t) = \frac{\delta(r)}{2\pi r}\,\delta\left(t-0^+\right).$$

Once η is known, linearity of the problem allows to write again

$$\zeta(r,\theta,t) = \int_0^t \int_0^{2\pi} \int_0^{\infty} F(r',\theta',\tau)\,\eta\left(\left|\mathbf{r}-\mathbf{r}'\right|, t-\tau\right) r'\mathrm{d}r'\mathrm{d}\theta'\mathrm{d}\tau \tag{2.2.2}$$

for the response to a generic initial disturbance of the free-surface $F(r,\theta,t)$. The governing equation (2.2.1) for the response η generated by a sudden bump of the free-surface concentrated at the origin becomes

$$\eta_{tt} - gh\left(\frac{1}{r}\,\eta_r + \eta_{rr}\right) = 0, \tag{2.2.3}$$

since η does not depend on the angle θ. The initial conditions are

$$\eta = \frac{\delta(r)}{2\pi r}, \quad t = 0, \tag{2.2.4}$$

$$\eta_t = 0, \quad t = 0 \tag{2.2.5}$$

and the boundary conditions at infinity prescribe

$$\eta,\ \eta_r \to 0 \quad \text{as } r \to \infty. \tag{2.2.6}$$

Note that (2.2.6) only require the free surface and the velocity to vanish at infinity. No radiation condition can be applied, since the disturbance is impulsive and does not imply a steady-state propagation of energy to infinity. In order to solve the problem, let us first rewrite (2.2.3) as

$$\eta_{tt} - gh\frac{1}{r}\frac{\partial}{\partial r}\left(r\eta_r\right) = 0. \tag{2.2.7}$$

Then apply the Hankel transform

$$\hat{\eta}(t;k) = \int_0^\infty rJ_0(kr)\eta(r,t)\,\mathrm{d}r$$

to the governing equation (2.2.7) and obtain

$$\hat{\eta}_{tt} + ghk^2\hat{\eta} = 0, \tag{2.2.8}$$

while the transforms of the initial conditions (2.2.4) and (2.2.5) become respectively

$$\hat{\eta}(t;k) = \frac{1}{2\pi}, \quad t = 0 \tag{2.2.9}$$

$$\hat{\eta}_t(t;k) = 0, \quad t = 0. \tag{2.2.10}$$

Hence application of the Laplace transform

$$\hat{\bar{\eta}}(k,s) = \int_0^\infty \hat{\eta}(t;k)\mathrm{e}^{-st}\,\mathrm{d}t$$

to the initial value problem (2.2.8)-(2.2.10) yields a simply algebraic equation for $\hat{\bar{\eta}}$ in the space of parameters (k,s):

$$\hat{\bar{\eta}}(k,s) = \frac{1}{2\pi}\frac{s}{s^2+\omega^2}, \tag{2.2.11}$$

where

$$\omega = \sqrt{gh}k \tag{2.2.12}$$

is the new dispersion relation in the transformed space. Since the ratio ω/k is constant, shallow water waves are non-dispersive. Recalling that

$$\frac{s}{s^2+\omega^2} = \overline{\cos\omega t},$$

(2.2.11) can be re-written as

$$\hat{\eta}(t;k) = \frac{1}{2\pi}\cos\omega t.$$

Finally, inverse Hankel transform of $\hat{\eta}$

$$\eta(r,t) = \int_0^\infty kJ_0(kr)\hat{\eta}(t;k)\,\mathrm{d}k$$

gives the expression of free-surface elevation induced by a sudden bump concentrated at the origin

$$\eta(r,t) = \frac{1}{2\pi}\int_0^\infty kJ_0(kr)\cos\omega t\,\mathrm{d}k. \tag{2.2.13}$$

If the initial disturbance is described by a generic impulsive function $F(r,\theta,t) = f(r,\theta)\delta\left(t-0^+\right)$, linearity of the problem allows us to use relation (2.2.2), which together with (2.2.13) gives

$$\zeta(r,\theta,t) = \frac{1}{2\pi}\int_0^\infty r'\int_0^{2\pi} f(r',\theta')\int_0^\infty kJ_0\left(k\left|\mathrm{r}-\mathrm{r}'\right|\right)\cos\omega t\,\mathrm{d}r'\mathrm{d}\theta'\mathrm{d}k. \tag{2.2.14}$$

Applying again the addition theorem for Bessel functions (2.1.37) to the latter equation yields the expression of the free-surface elevation

$$\zeta(r,\theta,t) = \sum_{n=0}^{\infty} \epsilon_n \int_0^{\infty} kJ_n(kr)\cos\omega t\,(W_n^c \cos n\theta + W_n^s \sin n\theta)\,\mathrm{d}k, \tag{2.2.15}$$

where the amplitude coefficients $W_n^{c,s}$ are given respectively by

$$W_n^{c,s}(k) = \frac{1}{2\pi}\int_0^{\infty} r' \int_0^{2\pi} f(r',\theta')J_n(kr)\left(\cos n\theta', \sin n\theta'\right)\mathrm{d}\theta'\mathrm{d}r'. \tag{2.2.16}$$

Note that the perturbation (2.2.15) induced by a sudden bump on the free-surface in shallow waters is formally similar to the response (2.1.38) to a sudden displacement of the bottom in intermediate waters. In other words, (2.2.15) can be interpreted as the shallow-water limit of (2.1.38) and the validity of the "hot-start" initial condition is proven.

In the following we will consider as a practical application

$$f(r,\theta) = A\mathrm{e}^{-r^2/\alpha^2}$$

and take again $\alpha = 1\,\mathrm{m}$ for simplicity. Substituting the latter form for the inital bump of the free-surface into (2.2.15) and making the same passages of section §2.1, we finally obtain

$$\zeta(r,t) = \frac{A}{2}\int_0^{\infty} k\,\mathrm{e}^{-k^2/2}J_0(kr)\cos\omega t\,\mathrm{d}k, \tag{2.2.17}$$

with $\omega = k\sqrt{gh}$, as the shallow-water limit of the analogous expression (2.1.42). Figure 2.4(*a–d*) shows the time series of the free-surface elevation (2.2.17) at four different points, respectively $r = 0\,\mathrm{m}$, $r = 5\,\mathrm{m}$, $r = 10\,\mathrm{m}$ and $r = 20\,\mathrm{m}$ far from the origin, for $A = 1\,\mathrm{m}$. Since the different components of the transient wavetrain (2.2.17) move at the same velocity $c = \sqrt{gh}$, they do not separate. The resulting wave profile is that of a solitary-type wave propagating away from the origin, made by a leading elevation wave followed by a smaller trough, whose amplitude attenuates as r increases. Let us now investigate on the leading wave propagating at large distance from the origin.

The leading wave

For large r the Bessel function J_0 in (2.2.17) can be expanded according to expression (2.1.44). Hence the free-surface elevation (2.2.17) can be approximated at large r as

$$\zeta(r,t) \simeq A\sqrt{\frac{2}{\pi r}}\int_0^{\infty} \frac{\sqrt{k}}{2}\,\mathrm{e}^{-k^2/4}\cos\omega t\cos\left(kr - \frac{\pi}{4}\right)\mathrm{d}k. \tag{2.2.18}$$

Transforming again the cosine product into the complex exponential form and neglecting the incoming wave at large times (see section §2.1.2), we obtain

$$\zeta(r,t) \simeq A\sqrt{\frac{2}{\pi r}}\,\Re\int_0^{\infty} \frac{\sqrt{k}}{4}\,\mathrm{e}^{-k^2/4}\,\mathrm{e}^{\mathrm{i}(kr-\omega t-\pi/4)}\mathrm{d}k. \tag{2.2.19}$$

for large r and t. In shallow waters, the position of the leading wave front at a given time t is given by $r = \sqrt{gh}t$. Substituting the latter relation into (2.2.19) yields

$$\zeta(r,t) \simeq \frac{A}{2}\sqrt{\frac{2}{\pi\sqrt{gh}t}}\int_0^{\infty} \frac{\sqrt{k}}{2}\,\mathrm{e}^{-k^2/4}\,\mathrm{d}k\,\Re\mathrm{e}^{-\mathrm{i}\pi/4}. \tag{2.2.20}$$

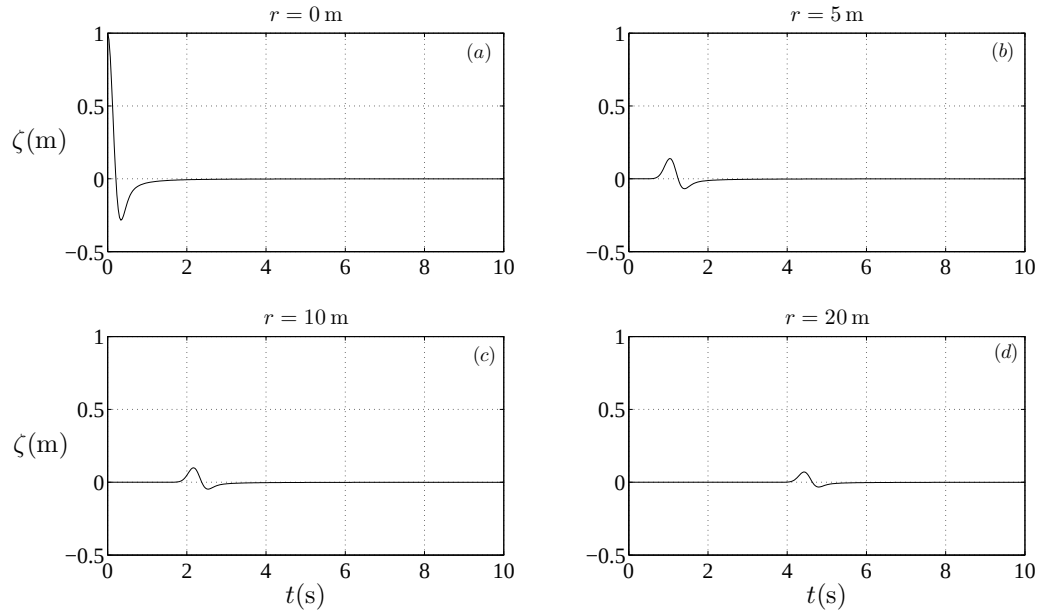

FIGURE 2.4: Radial propagation of a tsunami induced by the surface disturbance (2.2.17) centred at the origin in shallow waters, $A = 1\,\mathrm{m}$. Time series at points: (a) $r = 0\,\mathrm{m}$, (b) $r = 5\,\mathrm{m}$, (c) $r = 10\,\mathrm{m}$, (d) $r = 20\,\mathrm{m}$.

Since

$$\int_0^\infty \frac{\sqrt{k}}{2}\,\mathrm{e}^{-k^2/4}\,\mathrm{d}k = \frac{\sqrt{2}}{2}\,\Gamma\left(\frac{3}{4}\right),$$

Γ being the gamma function, (2.2.20) can be further simplified to obtain the expression of the leading wave ζ_l generated by a sudden bump of the free-surface in shallow waters:

$$\zeta_l = A\frac{\Gamma\,(3/4)}{4\sqrt{gh}}\sqrt{\frac{2}{\pi t}}\,. \tag{2.2.21}$$

Note that the leading wave (2.2.21) decays as $O(t^{-1/2})$ in the three-dimensional shallow-water domain, i.e. it vanishes slower than the leading wave of a transient 3D disturbance in intermediate waters (2.1.61), $O(t^{-1})$. This is due to the absence of dispersion in the shallow-water limit, for which the energy does not "unpack" following the different components of the frequency spectrum as it happens in intermediate waters. As a result, in shallow waters the energy moves together with the impulsive perturbation of the free-surface and energy leakage is reduced.

In table 2.1, the behaviour of the leading wave with time is summarized for the two-dimensional case of Mei et al. (2005) (table 2.1, 1st row) and the three-dimensional geometry of the present review, respectively for both dispersive and non-dispersive media (table 2.1, 2nd and 3rd rows).

Domain	**Medium**	**Leading wave**	**Notes**
2D	Dispersive	$O\left(t^{-1/3}\right)$	Airy wave (see Mei et al., 2005)
3D	Dispersive	$O\left(t^{-1}\right)$	Fast decay due to geometry/dispersion
3D	Non-dispersive	$O\left(t^{-1/2}\right)$	Slow decay due to absence of dispersion

TABLE 2.1: Behaviour of the leading wave in different geometries (2D/3D) and media (dispersive/non-dispersive).

Chapter 3

Landslide tsunamis propagating along a plane beach

Landslide tsunamis occur as a consequence of local events, and are characterized by a length scale $O(1$ Km$)$, much smaller than that of earthquake-generated tsunamis, $O(100$ Km$)$, though the maximum induced runup can be still significant. The first systematic experiments on landslide tsunami generation, made by Wiegel (1955) with sliding blocks down an incline, showed that the induced wave height increases with increasing the slope, while decreasing with increasing submergence of the sliding mass. More recently, Watts (1997) performed a series of similar tests on a smaller scale with sliding blocks, though concentrating on the block terminal velocity and not measuring wave runup. Large-scale experiments of Liu et al. (2005) investigated the correlation between the maximum runup and the initial elevation of the slide, showing that larger runup occurs for subaerial slides compared to submerged ones. The experimental work of Panizzo et al. (2005) showed that the time of underwater landslide motion and the landslide front shape have a major role in determining the maximum wave height. Various numerical studies on the behaviour of tsunamis generated by a three-dimensional sliding mass on a plane beach have been also undertaken (see Liu et al., 2005; Lynett and Liu, 2005). By studying the free surface elevation time series for a wide set of numerical simulations for both subaerial and submerged landslides, Lynett and Liu (2005) observed the occurrence of two different wave fields. At the earliest times following the landslide generation, two dimensional wave motion occurs with high amplitudes only in a small region near the slide. As time passes, these waves then radiate out by fast decaying, while a shoreline motion starts to become significant; later, edge waves propagating along the coastline become predominant, while wave amplitudes near the slide annihilate. Therefore, since both a shoreline movement and an outgoing wave field are usually induced by the landslide interaction with the water, the study of such transients requires the development of an appropriate two-horizontal dimension (2HD) model. However, even though Liu et al. (2003) developed a one-dimensional (1HD) analytical model, to date very few analytical studies of landslide tsunamis include 2HD effects, as already pointed out by Lynett and Liu (2005).

In the following, an analytical two-horizontal dimension model of landslide tsunamis propagating along a plane beach is developed based on the forced linear long wave equation of motion. The above mentioned numerical observations of Lynett and Liu (2005) are then confirmed analytically. Furthermore, the application of the method of stationary phase enables us to derive a simplified expression for the free surface elevation

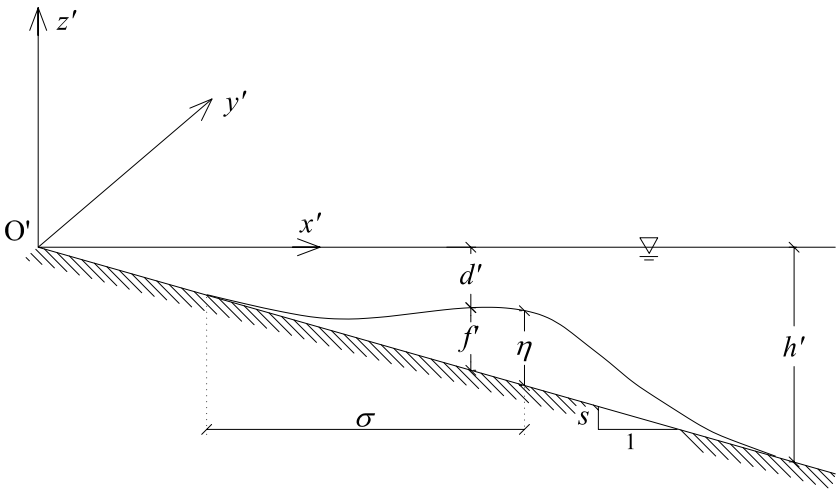

FIGURE 3.1: The fluid domain in physical coordinates. η and σ are respectively the slide maximum vertical thickness and characteristic horizontal length, depending on the shape of the landslide (see §3.2).

at larger times, which consists of propagating transient edge waves. Comparisons with the transient waves due to a displacement of the free surface over a constant depth is made in order to further appreciate the peculiar nature of landslide generated tsunamis along a sloping beach, which is the absence of a leading wave at large times. Results are discussed with emphasis on the parametric dependence of the generated wave field upon the slide parameters, such as slide dimensions, centroid initial position and slide velocity. The free-surface elevation time series are analysed and compared to available experimental data. Finally the validity of homogeneous models currently used in numerical analysis is discussed.

3.1 Position of the problem

Referring to figure 3.1, let us consider a straight beach with constant slope s, and define a plane reference system of coordinates (O', x', y'), with the y'-axis along the mean shoreline; water is in the region $x' > 0$. We assume that the landslide originates in a neighbourhood of the origin O', and its shape is symmetric with respect to the y'-axis; the induced wave field is also symmetric in y', allowing us to solve the equation of motion in $y' > 0$ only.

3.1.1 Governing equations

Within the shallow-water limit, consider the governing equations for long waves on a uniformly sloping beach, namely the mass conservation law

$$\frac{\partial}{\partial t}\left(\zeta' + d'\right) + \nabla \cdot \left[\mathbf{u}'\left(\zeta' + d'\right)\right] = 0 \tag{3.1.1}$$

and the momentum equation

$$\frac{\partial \mathbf{u}'}{\partial t} + \mathbf{u}' \cdot \nabla \mathbf{u}' = -g \nabla \zeta'. \tag{3.1.2}$$

In (3.1.1) and (3.1.2) $\nabla(\cdot) = [\partial(\cdot)/\partial x', \partial(\cdot)/\partial y']$ is the nabla operator, $\zeta'(x', y', t')$ the free surface elevation, $\mathbf{u}(x, y, t)$ the flow velocity; g is the gravity acceleration, t' denotes time and

$$d' = h' - f'(x', y', t')$$

the bottom depth, measured with respect to the mean water level $z' = 0$. In the previous expression $h' = sx'$ is the undisturbed bottom depth, while $f'(x', y', t')$ is a time-dependent perturbation of the sea floor, representing the landslide moving on the plane beach, as sketched in figure 3.1. Let us assume that the landslide generates small amplitude waves, i.e.

$$\frac{f'}{h'} \ll 1 \text{ and } \frac{\zeta'}{h'} \ll 1,$$

such that (3.1.1) and (3.1.2) can be linearised into

$$\frac{\partial \zeta'}{\partial t'} + \nabla \cdot \left(\mathbf{u}' h'\right) = \frac{\partial f'}{\partial t'} \tag{3.1.3}$$

and

$$\frac{\partial \mathbf{u}'}{\partial t'} = -g \nabla \zeta' \tag{3.1.4}$$

respectively (see Mei, 1997; Mei et al., 2005). Now, expressions (3.1.3) and (3.1.4) can be combined into a single expression. First take the derivative of (3.1.3) with respect to t', then take the divergence of the product between (3.1.4) and h'; finally subtract these two intermediate results and obtain

$$\frac{\partial^2 \zeta'}{\partial t'^2} - gs\nabla \cdot \left(x' \nabla \zeta'\right) = \frac{\partial^2 f'}{\partial t'^2}. \tag{3.1.5}$$

The latter is the governing equation for forced linear long waves on a uniformly sloping beach. Let η and σ be respectively the maximum vertical height and the characteristic horizontal length of the landslide. To investigate the range of validity of the linearised long-wave equation (3.1.5), let us consider the Ursell number, which measures the ratio of nonlinearity versus dispersion

$$\mathrm{U_r} = \frac{\text{nonlin.}}{\text{disp.}} = \frac{A}{h}\left(\frac{2\pi}{\lambda}h\right)^{-2}. \tag{3.1.6}$$

In the latter expression, A is the wave amplitude, λ the wavelength and h is the bottom depth. With the physical scales

$$A = \eta\,, \quad \lambda = \sigma\,, \quad h = \sigma s,$$

the Ursell number (3.1.6) becomes

$$\mathrm{U_r} = \frac{\eta}{\sigma s}\frac{1}{4\pi^2 s^2} = \frac{\epsilon}{\mu^2}, \tag{3.1.7}$$

having defined

$$\epsilon = \frac{\eta}{\sigma s} = \frac{A}{h}\,, \quad \mu = 2\pi s = \frac{2\pi}{\lambda}h. \tag{3.1.8}$$

With this position, ϵ and μ^2 give a measure of nonlinear and dispersive effects respectively (see Mei et al., 2005). In order for (3.1.5) to be applied, nonlinear and dispersive effects must be negligible, i.e. we must require both $\epsilon \ll 1$ and $\mu^2 \ll 1$:

$$\frac{\eta}{\sigma s} \ll 1\,, \quad s \ll \frac{1}{2\pi}, \tag{3.1.9}$$

and $\epsilon = O\left(\mu^2\right)$, so that $\mathrm{U_r} = O(1)$. Now, the first of (3.1.9) requires the ratio between the landslide maximum vertical height η and characteristic length σ to be much smaller than the given slope s. This is the so-called hypothesis of *thin slide* (see Liu et al., 2003). Finally, the second of (3.1.9) requires the incline to be of *mild slope*. Within the hypotheses of thin slide and mild slope, let us introduce the following non-dimensional variables:

$$(x, y) = (x', y')/\sigma, \quad t = \sqrt{gs/\sigma}t', \quad (\zeta, f) = \left(\zeta', f'\right)/\eta, \tag{3.1.10}$$

so that the equation of motion (3.1.5) becomes:

$$x\zeta_{xx} + \zeta_x + x\zeta_{yy} = \zeta_{tt} - f_{tt}. \tag{3.1.11}$$

The subscripts denote derivation with respect to the relevant variable. We require the free surface elevation $\zeta(x, y, t)$ to be bounded at the shoreline $x = 0$, and to decay as x tends to infinity for all positive y and t. Since the spatial domain is the quadrant $x > 0, y > 0$, and the free surface elevation is expected to be an even function of y, the cosine Fourier transform pair of ζ

$$\hat{\zeta}(x, k, t) = \int_0^\infty \zeta(x, y, t) \cos ky \, \mathrm{d}y, \quad \zeta(x, y, t) = \frac{2}{\pi} \int_0^\infty \hat{\zeta}(x, k, t) \cos ky \, \mathrm{d}k \tag{3.1.12}$$

can be employed, k being the non-dimensional transform parameter. Equation of motion (3.1.11) is then transformed into

$$x\hat{\zeta}_{xx} + \hat{\zeta}_x - xk^2\hat{\zeta} = \hat{\zeta}_{tt} - \hat{f}_{tt}. \tag{3.1.13}$$

By introducing the further transformations

$$\xi = 2kx, \quad \hat{\zeta} = \mathrm{e}^{-\xi/2} Z(\xi, k, t), \tag{3.1.14a, b}$$

equation (3.1.13) becomes finally

$$2k \left[\xi Z_{\xi\xi} + (1 - \xi) Z_\xi - \tfrac{1}{2} Z\right] - Z_{tt} = -\Phi_{tt}(\xi, k, t), \tag{3.1.15}$$

where

$$\Phi(\xi, k, t) = \hat{f}(\xi/2k, k, t) \, \mathrm{e}^{\xi/2} \tag{3.1.16}$$

is a forcing factor, depending on the shape of the landslide.

3.1.2 Solution

The transformed equation of motion (3.1.15) is a non-homogeneous partial differential equation of the second order in the domain $\xi > 0, t > 0$. To obtain its solution, let us first consider the associated homogeneous equation

$$2k \left[\xi Z_{\xi\xi} + (1 - \xi) Z_\xi - \tfrac{1}{2} Z\right] - Z_{tt} = 0. \tag{3.1.17}$$

The solution Z_h of (3.1.17) can be obtained by means of separation of variables:

$$Z_h = X(\xi) U(k, t). \tag{3.1.18}$$

Substituting the latter expression into (3.1.13) we obtain two separate equations for $X(\xi)$ and $U(t)$ respectively

$$\xi X_{\xi\xi} + (1 - \xi) X_\xi - \tfrac{1}{2} \left(1 - \tfrac{\omega^2}{k}\right) X = 0, \tag{3.1.19}$$

$$U_{tt} + \omega^2 U = 0. \tag{3.1.20}$$

Furthermore, boundedness of the free surface requires

$$|X(0)| < +\infty, \quad \lim_{x\to\infty} \mathrm{e}^{-\xi/2} X(\xi) = 0. \tag{3.1.21}$$

Equation (3.1.19) is a particular form of the confluent hypergeometric equation, i.e. the Kummer equation (see Abramowitz and Stegun, 1972). Nontrivial solutions which satisfy the boundary conditions (3.1.21) can be found by applying the Frobenius method of power series, as shown in appendix A. The relevant eigenfunctions are proportional to the Laguerre polynomials of order (0) and degree $n \in \mathbb{N}$

$$X(\xi) = L_n(\xi) = \sum_{m=0}^{n} (-1)^m \left(\begin{array}{c} n \\ n-m \end{array} \right) \frac{\xi^m}{m!},$$

where $\left(\begin{array}{c} p \\ q \end{array} \right)$ is the binomial coefficient between two integers p and q (see Appendix A). Recall that the Laguerre polynomials $L_n^{(a)}$ of order (a) are orthonormal functions with respect to the weighting function $\mathrm{e}^{-\xi}\xi^a$ in $\xi \in [0, \infty)$:

$$\int_0^\infty \mathrm{e}^{-\xi} \xi^a L_n^{(a)}(\xi) L_m^{(a)}(\xi)\, \mathrm{d}\xi = \frac{\Gamma(n+a+1)}{n!}\, \delta_{nm}, \tag{3.1.22}$$

δ_{nm} being the Kronecker's operator and a a positive real number. In the case of (3.1.19) therefore

$$\int_0^\infty \mathrm{e}^{-\xi} L_n(\xi) L_m(\xi)\, \mathrm{d}\xi = \delta_{nm}. \tag{3.1.23}$$

The associated eigenvalues are given by

$$\omega_n = \sqrt{k\,(2n+1)}, \quad n = 0, 1, 2, \ldots \tag{3.1.24}$$

which defines the motion eigenfrequencies (see appendix A.2 for details). Note that (3.1.24) is a weakly nonlinear relation between the wave frequency ω and the wavenumber k in the transformed domain. As a result, dispersive phenomena can be still taken into account by the analytical model employed, even if at a low order of approximation. Equation (3.1.20) is instead an ordinary differential equation of the second order whose independent solutions are simply

$$U_n(t) = \left\{ \begin{array}{c} \cos \omega_n t \\ \sin \omega_n t \end{array} \right\}.$$

Therefore, solution of the separated problems for $X(\xi)$ and $U(t)$ yields

$$Z_h(\xi, t) = \sum_{n=0}^{\infty} Z_{h_n}(\xi, t) = \sum_{n=0}^{\infty} L_n(\xi) \left[c_n \cos \omega_n t + d_n \sin \omega_n t \right], \tag{3.1.25}$$

c_n and d_n are integration constants to be determined from initial conditions.

The method of *variation of parameters* can be employed to find the solution of the inhomogeneous problem (3.1.15) with boundedness conditions (3.1.21). We assume for $Z(\xi, k, t)$ the same algebraic expression of Z_h, i.e.

$$Z(\xi, k, t) = \sum_{n=0}^{\infty} L_n(\xi) T_n(k, t), \tag{3.1.26}$$

with T_n unknown functions required to satisfy (3.1.15). Now multiply both sides of (3.1.26) by $\mathrm{e}^{-\xi}L_m(\xi)$, $m \in \mathbb{N}$, and apply the orthogonality property (3.1.23) to obtain

$$T_n(t) = \int_0^\infty \mathrm{e}^{-\xi} L_n(\xi) Z(\xi, t)\, \mathrm{d}\xi.$$

Differentiating the latter expression twice with respect to time and then using (3.1.15) for Z_{tt} yield the following differential equation for T_n

$$T_{n,tt}(t) = \int_0^\infty \mathrm{e}^{-\xi} L_n(\xi) \left\{2k \left[\xi Z_{\xi\xi} + (1-\xi)Z_\xi - \tfrac{1}{2}Z\right] + \Phi_{tt}\right\} \mathrm{d}\xi. \tag{3.1.27}$$

Now integrate the addends of (3.1.27) by parts, thus obtaining

$$T_{n,tt}(t) = -2k \int_0^\infty \mathrm{e}^{-\xi} \xi L_{n,\xi} Z_\xi \,\mathrm{d}\xi - k \int_0^\infty \mathrm{e}^{-\xi} L_n(\xi) Z \,\mathrm{d}\xi + \int_0^\infty \mathrm{e}^{-\xi} L_n(\xi) \Phi_{tt}(\xi, k, t)\, \mathrm{d}\xi, \tag{3.1.28}$$

where

$$L_{n,\xi}(\xi) = -L^{(1)}_{n-1,\xi}$$

(see Abramowitz and Stegun, 1972). In (3.1.28) express the unknown functions $Z(k,t)$ in terms of T_n with the series expression (3.1.26) and apply the orthogonality property (3.1.23) to simplify the integrals, thus getting the following differential equation for T_n:

$$T_{n,tt} + \omega_n^2 T_n = \int_0^\infty \mathrm{e}^{-\xi} L_n(\xi) \Phi_{tt}(\xi, k, t)\, \mathrm{d}\xi, \tag{3.1.29}$$

where the forcing factor $\Phi(\xi, k, t)$ is still given by (3.1.16) and the ω_ns are defined by (3.1.24). The general solution of (3.1.29) can be found via the method of variation of parameters (see for example Mei, 1997)

$$\begin{aligned} T_n(k,t) = c_n^{(1)} \mathrm{e}^{-\mathrm{i}\omega_n t} + c_n^{(2)} \mathrm{e}^{\mathrm{i}\omega_n t} + \\ + \int_0^t \int_0^\infty \mathrm{e}^{-\xi} L_n(\xi) \Phi_{\tau\tau}(\xi, k, \tau)\, \mathrm{d}\xi \frac{1}{W(\tau)} \left[\mathrm{e}^{\mathrm{i}\omega_n(t-\tau)} + \mathrm{e}^{-\mathrm{i}\omega_n(t-\tau)}\right] \mathrm{d}\tau. \end{aligned} \tag{3.1.30}$$

In the latter expression,

$$W(t) = \mathrm{e}^{-\mathrm{i}\omega_n t} \frac{\mathrm{d}}{\mathrm{d}t} \mathrm{e}^{\mathrm{i}\omega_n t} - \frac{\mathrm{d}}{\mathrm{d}t} \mathrm{e}^{-\mathrm{i}\omega_n t} \mathrm{e}^{\mathrm{i}\omega_n t} = 2\mathrm{i}\omega_n$$

is the Wronskian between the two homogeneous solutions $\mathrm{e}^{\mp \mathrm{i}\omega t}$, while $c_n^{(1,2)}$ are two integration constants to be found by applying the initial conditions. We require that at $t = 0$ both the free surface elevation ζ and velocity $\partial\zeta/\partial t$ are zero, hence

$$T_n(k,0) = 0, \quad T_{n,t}(k,0) = 0.$$

Solution of this initial-value problem gives $c_n^{(1,2)} = 0$, so that (3.1.30) simplifies

$$T_n(k,t) = \frac{2k}{\omega_n} \int_0^\infty \mathrm{e}^{-k\alpha} L_n(2k\alpha) I_n(\alpha, k, t)\, \mathrm{d}\alpha, \tag{3.1.31}$$

with

$$I_n(\alpha, k, t) = \int_0^t \hat{f}_{\tau\tau}(\alpha, k, \tau) \sin\left[\omega_n(t-\tau)\right] \mathrm{d}\tau\,, \tag{3.1.32}$$

having posed

$$\alpha = \frac{\xi}{2k}.$$

Without loss of generality, the integral form (3.1.32) can be solved by parts to obtain

$$\begin{aligned} I_n(\alpha,k,t) &= -\hat{f}_\tau(\alpha,k,0)\sin\omega_n t + \omega_n \hat{f}(\alpha,k,t) - \omega_n \hat{f}(\alpha,k,0)\cos\omega_n t + \\ &- \omega_n^2 \int_0^t \hat{f}(\alpha,k,\tau)\sin\omega_n\,(t-\tau)\,\mathrm{d}\tau. \end{aligned} \tag{3.1.33}$$

Note that the I_n (3.1.33) can be determined only after having chosen the shape of the slide and its law of motion by imposing an analytical form for the forcing term $f(x,y,t)$. Finally, inverse transform of (3.1.26), together with the substitutions dictated by (3.1.14), yields the free-surface elevation

$$\zeta(x,y,t) = \frac{2}{\pi}\sum_{n=0}^{\infty}\int_0^\infty \mathrm{e}^{-kx} L_n(2kx) T_n(k,t)\cos ky\,\mathrm{d}k, \tag{3.1.34}$$

where the T_n are given by (3.1.31) and the I_n by (3.1.33). Further analysis can be made only once the forcing function $f(x,y,t)$ is specified.

3.2 Landslide shape

In this section we shall determine the analytical form of the forcing term $f(x,y,t)$ starting from some basic assumptions on the shape of the landslide and its law of motion. We consider two different landslide shapes: i) a double Gaussian ii) a rectangular wedge.

3.2.1 Double Gaussian

Let us now go back to physical variables in the reference system (x',y',z') (see figure 3.1). Referring to figure 3.2, define a local reference system on the incline (X',Y',Z') such that

$$X' = x'/\cos\alpha, \quad Y' = y', \quad Z' = z'/\cos\alpha \tag{3.2.1}$$

and introduce the following quantities

$$H = \eta\cos\alpha, \quad \Sigma = \sigma/\cos\alpha, \tag{3.2.2}$$

where α is the angle between the incline and the horizontal, i.e. $s = \tan\alpha$. With this notation, H denotes the maximum landslide height measured along the Z' axis. Let $F'(X',Y')$ measure the landslide thickness along the Z' axis at a point (X',Y') on the incline, and finally let Σ be the projection of the landslide characteristic length σ along the X' axis. Let C' be the abscissa of the centroid at a given time t' in the (X',Y',Z') reference system, then the law of motion $C' = C'(t)$ depends on several factors such as the initial position and velocity of the landslide, the landslide weight, the friction between the slide and the incline (see Di Risio et al., 2009a). In our work we make the symplifying assumption that the slide moves as a rigid body along the incline, starting from an initial position

$$C'_0 = X'_0 - \eta\sin\alpha,$$

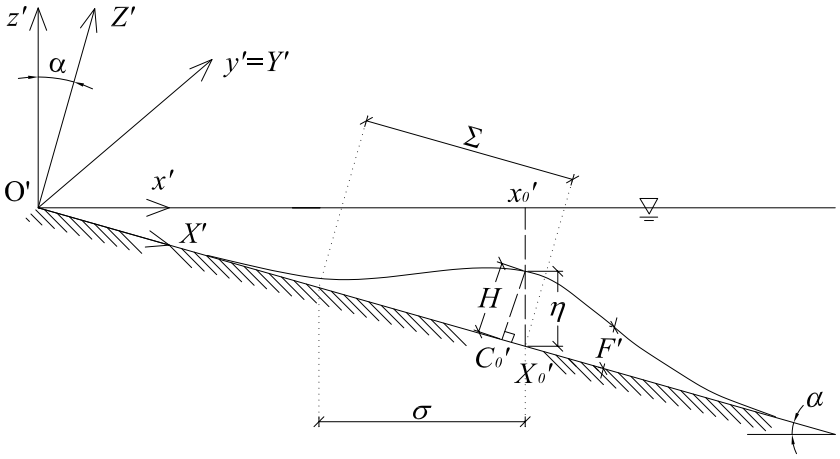

FIGURE 3.2: Local reference system on the incline (X', Y', Z') and landslide at starting position. C'_0 represents the initial position of the landslide centroid in the local reference system, and H the landslide maximum thickness along the Z' direction.

where $X'_0 = x'_0/\cos\alpha$ (see figure 3.2). In the latter expression, x'_0 represents the initial position of the landslide centroid in the original reference system. Conventionally, we define a landslide to be 'subaerial' when $x'_0 < 0$, while 'submerged' when $x'_0 > 0$. Let us also assume the slide velocity to be uniform along the X' direction and always equal to its initial value U_0, i.e. $U'(t) = U'(0) = U_0$. Then the law of motion of the centroid is

$$C'(t) = C'_0 + U'_0 t' = X'_0 - \eta\sin\alpha + U'_0 t'. \tag{3.2.3}$$

Now let the landslide shape function be of the form

$$F'(X', Y', t') = H\,\exp\left\{-\left[X' - C'(t)\right]^2/\Sigma^2\right\}\exp\left[-\left(Y'/\lambda\right)^2\right], \tag{3.2.4}$$

i.e. a double Gaussian where the second exponential is a lateral spreading function, and λ is the characteristic landslide width in the $Y'(y')$ direction. Note that F' is infinitely differentiable with contiuous derivatives on the real set $(X', Y') \in \mathbb{R}^2$, i.e. it is a very smooth function. Substituting the law of motion (3.2.3) into (3.2.4) yields

$$\begin{aligned} F'(X', Y', t') &= H\,\exp\left\{-\left[X' - X'_0 - U'_0 t' + \eta\sin\alpha\right]^2/\Sigma^2\right\} \times \\ &\times \exp\left[-\left(Y'/\lambda\right)^2\right]. \end{aligned} \tag{3.2.5}$$

Now the latter expression needs to be transformed into the original reference system (x', y', z'). First, in order to determine the relation between the shape functions $F'(X', Y', t')$ and $f'(x', y', t')$, let us consider the following Taylor expansion of F'

$$F'(X', Y', t') \simeq F'(X' - f'\sin\alpha, Y', t') + \left.\frac{\partial F'}{\partial X'}\right|_{X' - f'\sin\alpha} \cdot \left(f'\sin\alpha\right), \tag{3.2.6}$$

where

$$F'(X' - f'\sin\alpha, Y', t') = f'(x', y', t')\cos\alpha \tag{3.2.7}$$

as shown in figure 3.3. The physical scales of the terms in (3.2.6) are respectively

$$F' \propto H = \eta\cos\alpha\,, \quad \frac{\partial F'}{\partial X'}\,f'\sin\alpha \propto \frac{H}{\Sigma}\eta\sin\alpha = \left(\frac{\eta}{\sigma}\right)\eta\cos^2\alpha\sin\alpha.$$

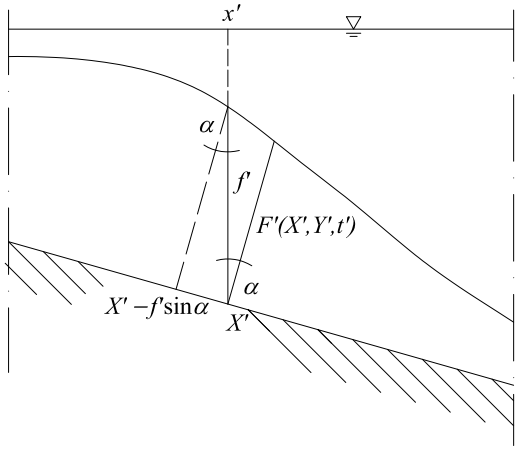

FIGURE 3.3: Geometrical construction used to determine the relationship between f' and F' (3.2.6).

Under the hypotheses of thin slide $\eta/\sigma s \ll 1$ and mild slope $s^2 \ll 1$, the second term of the above expression becomes

$$\frac{\partial F'}{\partial X'} f' \sin\alpha \propto \left[\left(\frac{\eta}{\sigma s}\right) s^2 \cos^3\alpha\right] \eta \ll \eta.$$

Therefore retaining only terms proportional to $O(\eta)$ in (3.2.6), the latter becomes

$$F'(X', Y', t') \simeq F'(X' - f'\sin\alpha, Y', t') = f'(x', y', t')\cos\alpha,$$

where (3.2.7) has also been employed. By substituting the latter expression into (3.2.5) and applying the transforms (3.2.2), we obtain the analytical form of the forcing term in the original reference system (x', y', z')

$$\begin{aligned} f'(x', y', t') &= \eta \exp\left\{-\left[\frac{(x' - x'_0)}{\sigma} - \frac{U'_0}{\sigma}\cos\alpha\, t' + \frac{\eta}{\sigma s} s^2 \cos\alpha\right]^2\right\} \times \\ &\times \exp\left[-\left(y'/\lambda\right)^2\right]. \end{aligned} \tag{3.2.8}$$

Thanks to the hypotheses of thin slide and mild slope, the third argument of the first exponential in (3.2.8) can be neglected, and the forcing term becomes in non-dimensional variables (3.1.10)

$$f(x, y, t) = \exp\left[-\left(x - x_0 - u_0 t\right)^2\right] \exp\left[-\left(cy\right)^2\right]. \tag{3.2.9}$$

In the latter expression $c = \sigma/\lambda$ is a lateral spreading factor, while

$$u_0 = \frac{U'_0 \cos\alpha}{\sqrt{\sigma g s}} \tag{3.2.10}$$

is the non-dimensional velocity of the slide along the horizontal x direction. Relation (3.2.10) allows also to express the velocity of the slide along the x'-direction in physical variables

$$u'_0 = U'_0 \cos\alpha = u_0 \sqrt{\sigma g s}, \tag{3.2.11}$$

where $\sqrt{\sigma g s}$ is the physical scale of velocity.

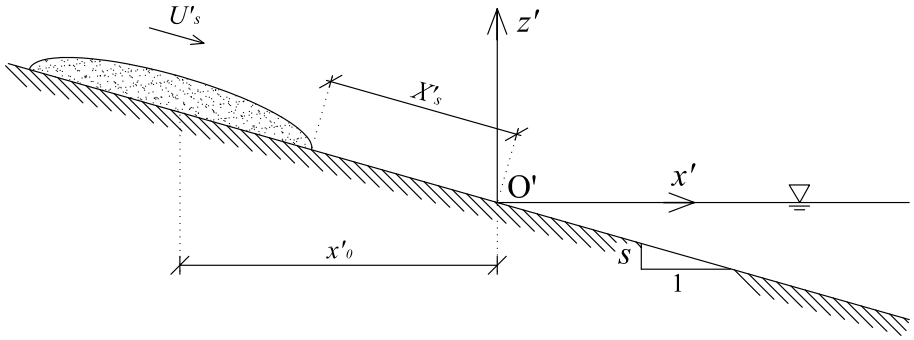

FIGURE 3.4: ellipsoidal slide used in the experiments of Di Risio et al. (2009a). X'_s represents the landslide release distance, while U'_s is the slide velocity along the incline.

Property	**Value**
Shape	ellipsoidal
Length	0.8 m
Width	0.4 m
Max. height	0.05 m
Total volume	$V' = 0.084\,\mathrm{m}^3$

TABLE 3.1: Properties of the experimental landslide of ellipsoidal shape used by Di Risio et al. (2009a)

Further considerations on the landslide velocity

The landslide horizontal velocity u'_0 (3.2.11) depends on the landslide shape, weight and dimensions, and also on the centroid initial position x'_0. With a simplifying hypothesis, first we neglect the influence of x'_0 and relate u'_0 to the asymptotic velocity of underwater motion introduced by Lynett and Liu (2005)

$$u'_0 = \sqrt{g \frac{\sigma}{\cos\alpha} \frac{\pi\,(\gamma - 1)}{2C_d} \sin\alpha \cos\alpha}, \tag{3.2.12}$$

where $\sigma/\cos\alpha = \Sigma$ is the slope-parallel slide length, γ is the specific gravity of the slide material and C_d is the drag coefficient. The latter depends on several parameters such as the friction between the body and the incline, the slide shape and dimensions and the slope of the incline. Finally (3.2.12) can be rewritten in non-dimensional variables (3.1.10)

$$u_0 = 1.25 \sqrt{\frac{\gamma - 1}{C_d}} \cos\alpha, \tag{3.2.13}$$

which is a simplified expression of the non-dimensional horizontal slide velocity u_0. As an example, assuming $C_d = 1$ (see Lynett and Liu, 2005), $\gamma = 1.8$ and $\alpha = 18°$ (corresponding to $s = \tan\alpha = 1/3$) gives $u_0 \simeq 1$.

A more accurate expression for $u'_0 = u'_0\,(x'_0, \sigma, \lambda, s, \gamma, C_d)$ can be obtained by employing the experimental results of Di Risio et al. (2009a) relevant to a ellipsoidal slide (see figure 3.4), whose dimensions are reported in table 3.1. This slide can be approximated by an equivalent double-gaussian shaped landslide of similar total volume (see figure 3.6), whose characteristic parameters are reported in table 3.2. By measuring the

Property	**Value**
Shape	Double Gaussian
Characteristic length	$\sigma = 0.37\,\mathrm{m}$
Characteristic width	$\lambda = 0.185\,\mathrm{m}$
Max. vertical height	$\eta = 0.045\,\mathrm{m}$
Total volume	$V' = 0.09\,\mathrm{m}^3$

TABLE 3.2: Properties of the analytical double-Gaussian shaped landslide equivalent to the experimental landslide of ellipsoidal shape used by Di Risio et al. (2009a)

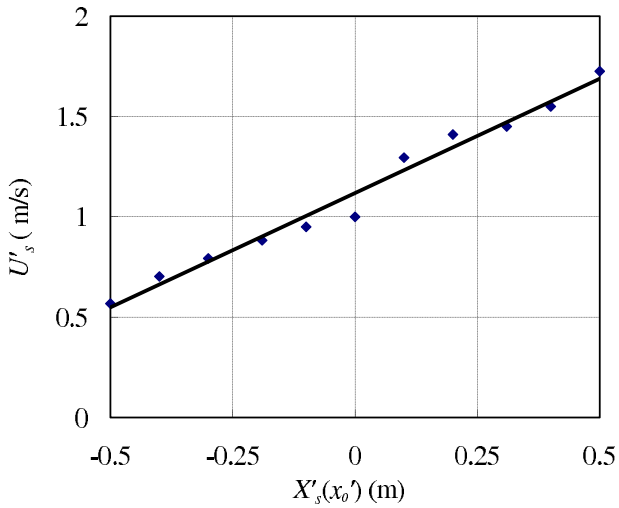

FIGURE 3.5: Experimental relationship between the mean underwater velocity U_s' and the release distance X_s' obtained by Di Risio et al. (2009a) for a ellipsoidal landslide. Diamonds show experimental measures, the bold line the relevant linear regression (3.2.14). Note that $U_s' \approx 1$ for $X_s' = 0$.

mean velocity of the slide U_s' during the underwater motion for various release distances X_s' (see figure 3.4), Di Risio et al. (2009a) obtained the empirical linear relationship

$$U_s' = 1.119 + 1.139 X_s'. \tag{3.2.14}$$

The dimensional coefficients $1.119\,\mathrm{m/s}$ and $1.139\,\mathrm{s}^{-1}$ of the latter expression have been derived via the linear regression of the experimental data as shown in figure 3.5. Expresion (3.2.14) is of course a specific law valid only for the geometry of Di Risio et al. (2009a) experimental setup. We now express (3.2.14) in terms of the non-dimensional variables u_0 and x_0. First we assume that U_s' coincides with our average velocity along the incline U_0', so that the velocity u_0' in the x' direction (3.2.11) can be derived

$$u_0' = \left(1.119 + 1.139 X_s'\right) \cos\alpha, \tag{3.2.15}$$

where α is still the angle between the incline and the horizontal (see figure 3.2). Furthermore, simple geometric considerations (see figure 3.6) lead to the relation

$$x_0' = -\sigma - X_s' \cos\alpha \tag{3.2.16}$$

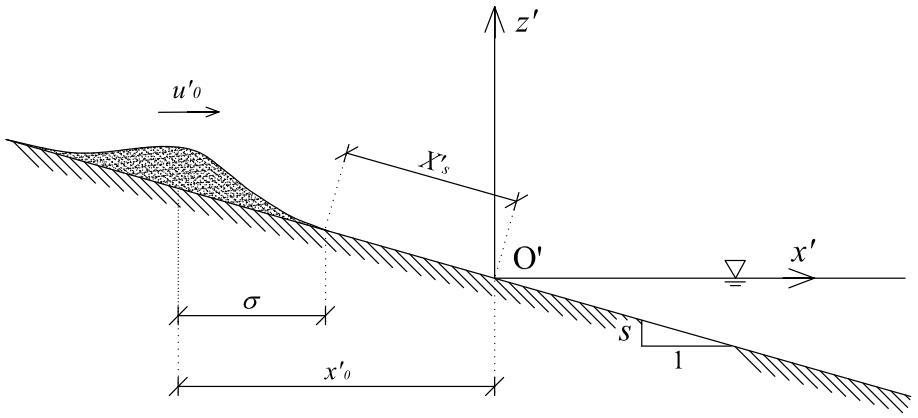

FIGURE 3.6: Double-Gaussian slide equivalent to the ellipsoidal slide of Di Risio et al. (2009a) (see table for dimensions) and notation employed. X'_s represents the landslide release distance, while x'_0 is the centroid initial position.

between the centroid initial position x'_0 and the release distance X'_s. Note that x'_0 and X'_s have opposite growth dicrections, i.e.

$$\frac{\partial x'_0}{\partial x'} > 0, \quad \frac{\partial X'_s}{\partial x'} < 0.$$

By substituting (3.2.15) and (3.2.16) into (3.2.14), the latter can be rewritten as

$$u'_0(x'_0) = 1.119 \cos\alpha - 1.139(\sigma + x'_0), \tag{3.2.17}$$

or in non-dimensional variables (3.1.10)

$$u_0(x_0) = \frac{1.119}{\sqrt{\sigma g s}} \cos\alpha - 1.139\sqrt{\frac{\sigma}{gs}}(1 + x_0). \tag{3.2.18}$$

This is a more complex relation between the landslide horizontal velocity u_0 and the centroid initial position x_0 (see figure 3.7), valid for the geometry of Di Risio et al. (2009a). It takes into account the shape, dimensions and weight of the slide, and the drag action exerted by the water on the body during its underwater motion.

3.2.2 Rectangular wedge

Referring to figure 3.8, let us consider a rectangular wedge of length σ and width λ sliding along an incline of slope s. Within the assumption of thin slide discussed above (i.e. $\lambda/\sigma \ll 1$), such a geometry can be modelled by the shape function

$$\begin{aligned} f'(x', y', t') &= s \cdot \left[x' - x'_c(t')\right] \mathrm{H}\left[x' - x'_c(t')\right] \mathrm{H}\left[x'_c(t') + \sigma - x'\right] \times \\ &\times \mathrm{H}\left(\frac{\lambda}{2} - y'\right) \mathrm{H}\left(\frac{\lambda}{2} + y'\right), \end{aligned} \tag{3.2.19}$$

where $x'_c(t')$ is the position of the upper edge at time t' (see again figure 3.8) and

$$\mathrm{H}(x) = \begin{cases} 1 & x > 0 \\ 0 & x < 0 \end{cases}$$

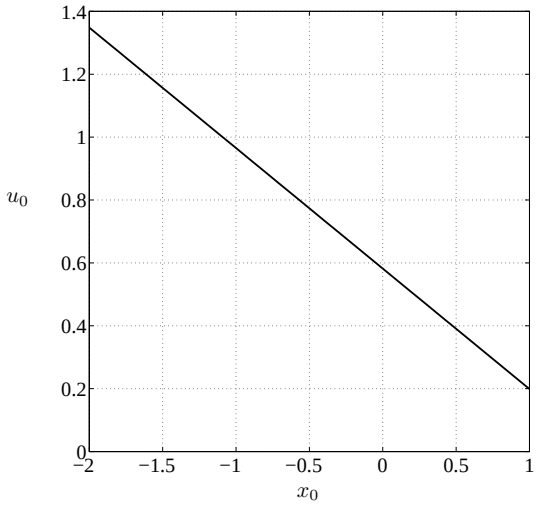

FIGURE 3.7: Behaviour of the non-dimensional horizontal slide velocity u_0 vs. the centroid initial position x_0 according to relation (3.2.18), based on the experimental results of Di Risio et al. (2009a).

is the Heaviside step function. Let us assume that the landslide moves with uniform velocity u_0' in the x-direction, then the position of the upper edge at time t' is

$$x_c'(t) = x_0' + u_0' t',$$

where x_0' is the upper edge initial position at time $t' = 0$. Substituting the latter expression into (3.2.19) and then transforming to non-dimensional variables (3.1.10), we obtain

$$\begin{aligned} f(x,y,t) &= \frac{s\sigma}{\eta}\left(x - x_0 - u_0 t\right) \mathrm{H}\left[\sigma\left(x - x_0 - u_0 t\right)\right] \mathrm{H}\left[\sigma\left(x_0 + u_0 t + 1 - x\right)\right] \times \\ &\times \mathrm{H}\left[\left(\sigma\frac{\lambda}{2\sigma} + y\right)\right] \mathrm{H}\left[\sigma\left(\frac{\lambda}{2\sigma} - y\right)\right]. \end{aligned} \tag{3.2.20}$$

In the latter expression u_0 is still the non-dimensional horizontal velocity of the slide. Now, the landlisde maximum thickness is $\eta = s\sigma$ and the Heaviside step function $\mathrm{H}(\alpha z) = \mathrm{H}(z)$ if $\alpha > 0$. By substituting these relations into (3.2.20), the expression for the forcing term relevant to the rectangular wedge becomes finally

$$\begin{aligned} f(x,y,t) &= \left(x - x_0 - u_0 t\right) \mathrm{H}\left(x - x_0 - u_0 t\right) \mathrm{H}\left(x_0 + u_0 t + 1 - x\right) \times \\ &\times \mathrm{H}\left(\frac{1}{2c} + y\right) \mathrm{H}\left(\frac{1}{2c} - y\right), \end{aligned} \tag{3.2.21}$$

where $c = \sigma/\lambda$ is again a shape coefficient. In the next sections we determine the proper form of the free-surface elevation (3.1.26) relevant to a double-gaussian shaped slide; research on the wave field generated by a sliding wedge is still ongoing.

3.3 Tsunami induced by a double-Gaussian shaped landslide

Expression (3.2.9) defines the forcing term $f(x,y,t)$ relevant to a double-Gaussian shaped slide and can be rewritten as

$$f(x,y,t) = \exp\left[-\left(x - x_0 - u_0 t\right)^2\right] s(y), \tag{3.3.1}$$

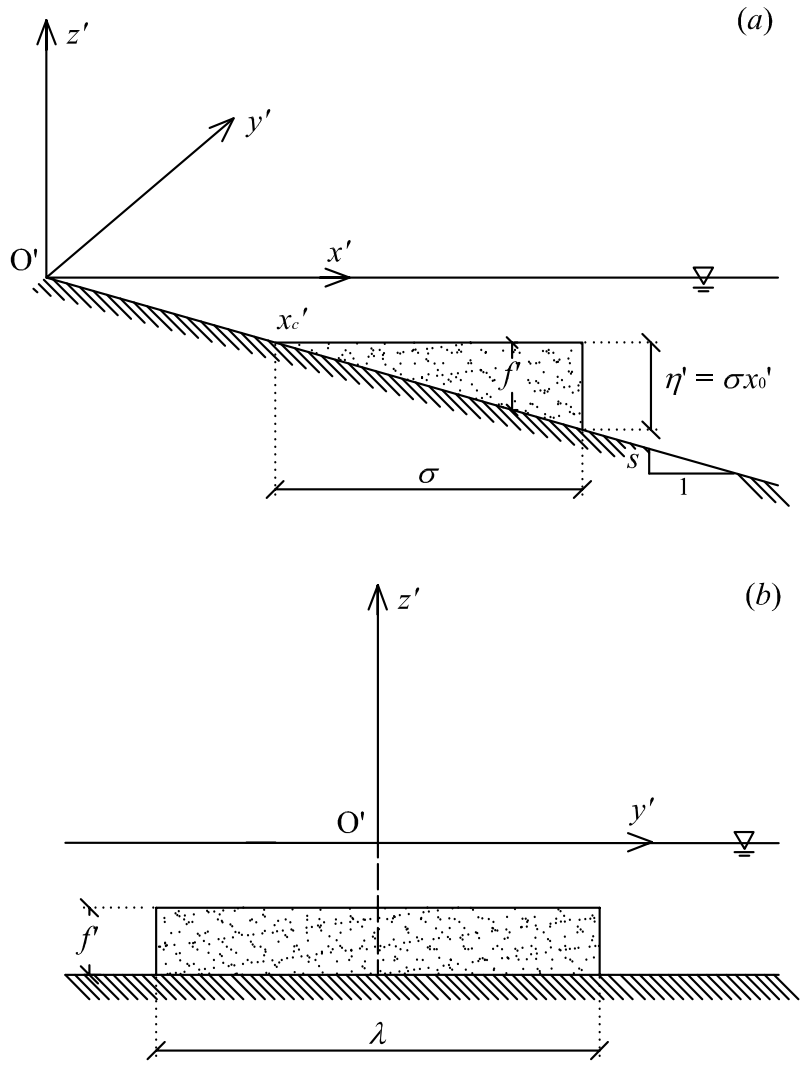

FIGURE 3.8: Phisical domain and geometry of the rectangular-wedge shaped landslide. (a) Side view, (b) vertical section.

where

$$s(y) = \exp\left[-(cy)^2\right] \tag{3.3.2}$$

is the lateral spreading function. Then, back to §3.1.2 the integral function (3.1.33) can be evaluated

$$\begin{aligned} I_n &= \omega_n \hat{s}(k) \left\{ \left[\omega_n a_n - \mathrm{e}^{-(\alpha-x_0)^2}\right] \cos\omega_n t + \right. \\ &- \left. \left[\frac{2u_0\ (\alpha - x_0)}{\omega_n}\, \mathrm{e}^{-(\alpha-x_0)^2} + \omega_n b_n\right] \sin\omega_n t + \mathrm{e}^{-(\alpha-x_0-u_0 t)^2} \right\}, \end{aligned} \tag{3.3.3}$$

where

$$\hat{s}(k) = \frac{\sqrt{\pi}}{2c}\, \mathrm{e}^{-k^2/4c^2}$$

is the cosine Fourier transform of the spreading function $s(y)$ (3.3.2) and

$$\begin{aligned} a_n &= a_n(\alpha, k, t) = \frac{\sqrt{\pi}}{2u_0}\, \mathrm{e}^{-\omega_n^2/4u_0^2}\, \mathrm{Im}\left\{ \mathrm{e}^{\mathrm{i}\omega_n(\alpha-x_0)/u_0} \right. \\ &\times \left. \left[\mathrm{erf}\left(\alpha - x_0 + \mathrm{i}\frac{\omega_n}{2u_0}\right) - \mathrm{erf}\left(\alpha - x_0 - u_0 t + \mathrm{i}\frac{\omega_n}{2u_0}\right) \right] \right\}, \end{aligned} \tag{3.3.4}$$

while

$$\begin{aligned} b_n &= b_n(\alpha, k, t) = \frac{\sqrt{\pi}}{2u_0}\, \mathrm{e}^{-\omega_n^2/4u_0^2}\, \mathrm{Re}\left\{ \mathrm{e}^{\mathrm{i}\omega_n(\alpha-x_0)/u_0} \right. \\ &\times \left. \left[\mathrm{erf}\left(\alpha - x_0 + \mathrm{i}\frac{\omega_n}{2u_0}\right) - \mathrm{erf}\left(\alpha - x_0 - u_0 t + \mathrm{i}\frac{\omega_n}{2u_0}\right) \right] \right\}. \end{aligned} \tag{3.3.5}$$

$\mathrm{Re}\{\}$ and $\mathrm{Im}\{\}$ indicate respectively the real and imaginary part of $\{\}$. Substituting (3.3.3) into expression (3.1.31) for T_n and then the latter into (3.1.34), we finally obtain the analytical form of the free-surface elevation.

$$\begin{aligned} \zeta(x, y, t) &= \frac{2}{\pi} \sum_{n=0}^{\infty} \int_0^{\infty} \mathrm{e}^{-kx} L_n(2kx) \frac{2k}{\omega_n} \times \\ &\times \int_0^{\infty} \mathrm{e}^{-k\alpha} L_n(2k\alpha) \omega_n \hat{s}(k) \left\{ \left[\omega_n a_n - \mathrm{e}^{-(\alpha-x_0)^2}\right] \cos\omega_n t + \right. \\ &- \left. \left[\frac{2u_0\ (\alpha - x_0)}{\omega_n}\, \mathrm{e}^{-(\alpha-x_0)^2} + \omega_n b_n\right] \sin\omega_n t + \mathrm{e}^{-(\alpha-x_0-u_0 t)^2} \right\} \mathrm{d}\alpha\, \cos ky\, \mathrm{d}k. \end{aligned} \tag{3.3.6}$$

For a simple physical interpretation, let us now define the integral transform $\mathcal{L}^n$ of a given function $u(\alpha, k, t)$ as

$$\mathcal{L}^n\left[u\right](k, t) = \frac{2k}{\omega_n} \int_0^{\infty} \mathrm{e}^{-k\alpha} L_n(2k\alpha) u(\alpha, k, t) \mathrm{d}\alpha, \tag{3.3.7}$$

so that expression (3.1.31) can be easily rewritten as $T_n = \mathcal{L}^n\left[I_n\right]$. Hence, by applying the transform $\mathcal{L}^n$ to (3.3.3) we can formally rewrite (3.3.6) as $\zeta = \zeta^o + \zeta^e$, where

$$\zeta^o = \frac{2}{\pi} \sum_{n=0}^{\infty} \int_0^{\infty} \mathrm{e}^{-kx} L_n(2kx) \left[A_n \cos\omega_n t + B_n \sin\omega_n t\right] \cos ky\, \mathrm{d}k, \tag{3.3.8}$$

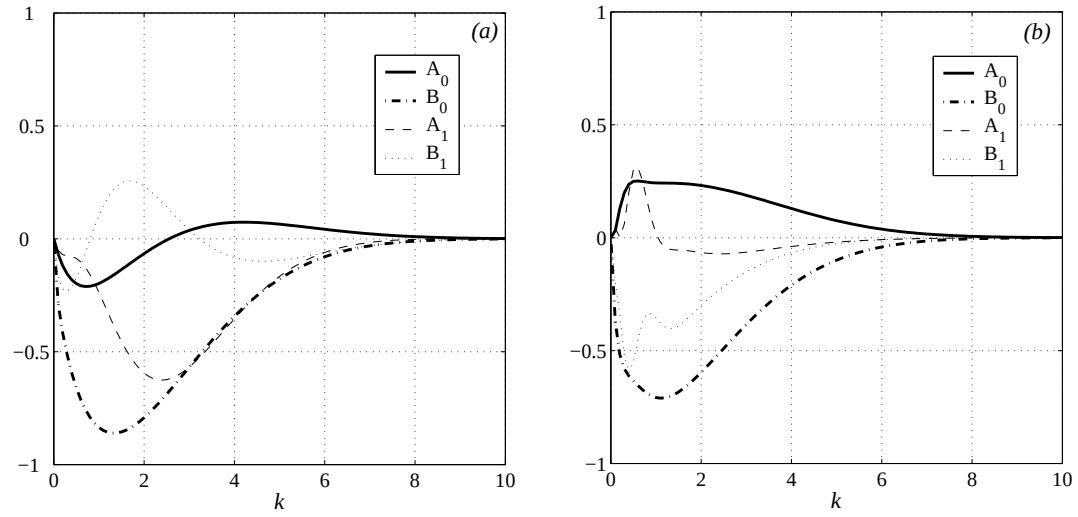

FIGURE 3.9: Numerical evaluation of A_n and B_n for the first two modes as functions of k. Parameters are $x_0 = 0$, $u_0 = 1$ and $c = 2$. *(a)* $t = 1$, *(b)* $t = 5$.

with

$$A_n = A_n(k,t) = \omega_n \hat{s}\mathcal{L}^n \left[\omega_n a_n(\alpha,k,t) - \mathrm{e}^{-(\alpha-x_0)^2}\right], \tag{3.3.9}$$

$$B_n = B_n(k,t) = -\hat{s}\mathcal{L}^n \left[2u_0\,(\alpha - x_0)\,\mathrm{e}^{-(\alpha-x_0)^2} + \omega_n^2 b_n(\alpha,k,t)\right], \tag{3.3.10}$$

and

$$\zeta^e = \frac{2}{\pi}\sum_{n=0}^{\infty}\int_0^{\infty} \mathrm{e}^{-kx} L_n(2kx)\,\omega_n \hat{s}\mathcal{L}^n\left[\mathrm{e}^{-(\alpha-x_0-u_0t)^2}\right]\cos ky\,\mathrm{d}k. \tag{3.3.11}$$

Now, ζ^o describes a transient oscillatory motion in time, depending on $\cos\omega_n t$ and $\sin\omega_n t$. Numerical evaluation of (3.3.9) and (3.3.10) shows that its coefficients A_n and B_n are fast-decaying functions of k for any given time t, hence the integral in (3.3.8) is fast convergent in k at all times. The magnitudes of A_n and B_n decrease for increasing n, as can be seen in figure 3.9. For large t, the second error function in expressions (3.3.4) and (3.3.5) tends to unity, and the a_n and b_n in (3.3.9) and (3.3.10) do not depend on time. Therefore A_n and B_n approach limiting values that depend only on k.

ζ^e decays with time, depending on $\mathrm{e}^{-(u_0t)^2}$. Hence, the landslide generates a twofold wave field made up by oscillatory and evanescent components, the latter rapidly vanishing with time. A more detailed description of the evanescent component is given in the following paragraph.

3.3.1 Time of decay

To estimate the time of decay of the evanescent term ζ^e, consider the $\mathcal{L}^n$ transform inside (3.3.11)

$$\begin{aligned}\mathcal{L}^n\left[\mathrm{e}^{-(\alpha-x_0-u_0t)^2}\right] &= \frac{2k}{\omega_n}\int_0^{\infty}\mathrm{e}^{-k\alpha}L_n(2k\alpha)\mathrm{e}^{-(\alpha-x_0-u_0t)^2}\,\mathrm{d}\alpha \\ &= \frac{2k}{\omega_n}\int_0^{\infty} g(\alpha)\mathrm{e}^{-(\alpha-x_0-u_0t)^2}\,\mathrm{d}\alpha,\end{aligned} \tag{3.3.12}$$

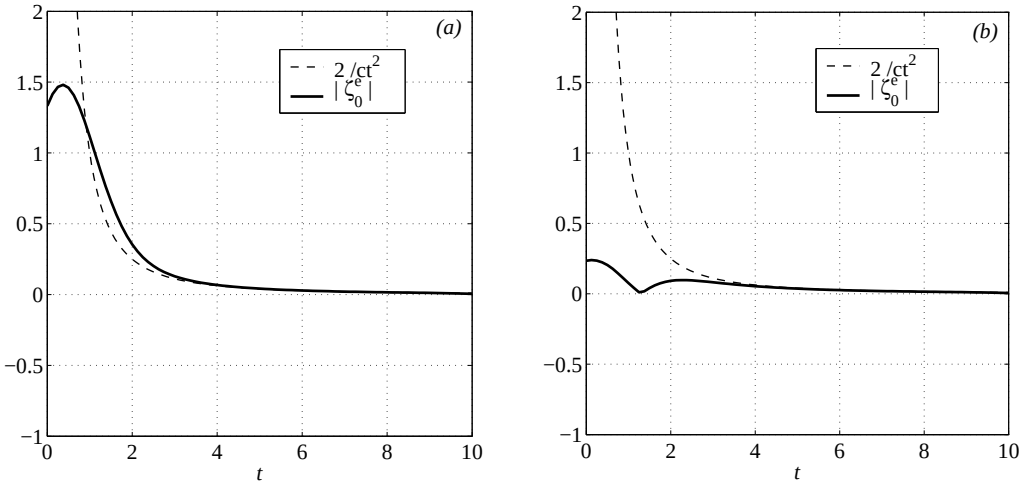

FIGURE 3.10: Decay of the evanescent term ζ^e for the fundamental mode $n = 0$ for an observer at the origin ($\xi = x/t = 0$) at *(a)* $(x, y) = (0, 0)$, *(b)* $(x, y) = (0, 1)$. Parameters are $x_0 = 0$, $u_0 = 1$, $c = 2$. Note that for large times $\zeta_0^e \simeq 2/ct^2$.

where

$$g(\alpha) = \mathrm{e}^{-k\alpha} L_n(2k\alpha). \tag{3.3.13}$$

When t is large, the leading behaviour of the integrand at the right-hand side of (3.3.12) is given by $\mathrm{e}^{-(\alpha - x_0 - u_0 t)^2}$, i.e. a fast-decaying function of α and t. Now, the contribution of $g(\alpha)$ (3.3.13) to the integral form (3.3.12) is significant only in a neighbourhood of the point where $\mathrm{e}^{-(\alpha - x_0 - u_0 t)^2}$ is maximum, i.e. $\alpha_0 = x_0 + u_0 t$ (see Cheng, 2007, for similar examples). Therefore, to obtain the asymptotic behaviour of the integral (3.3.12) we approximate $g(\alpha) \simeq g(\alpha_0)$, such that

$$\begin{aligned} \mathcal{L}^n \left[\mathrm{e}^{-(\alpha - x_0 - u_0 t)^2} \right] &\simeq \tfrac{2k}{\omega_n} \, \mathrm{e}^{-k\alpha_0} \, L_n(2k\alpha_0) \int_0^\infty \mathrm{e}^{-(\alpha - x_0 - u_0 t)^2} \mathrm{d}\alpha \\ &= \tfrac{\sqrt{\pi}\, k}{\omega_n} \left[\mathrm{erf}(x_0 + u_0 t) + 1 \right] \mathrm{e}^{-k(x_0 + u_0 t)} L_n(2k(x_0 + u_0 t)). \end{aligned} \tag{3.3.14}$$

Then, to the crudest approximation, for $t > 1$

$$|\zeta^e| \simeq |\zeta_0^e| \leq \frac{1}{c} \left[\mathrm{erf}(x_0 + u_0 t) + 1 \right] \int_0^\infty k \, \mathrm{e}^{-k(x_0 + u_0 t)} \, \mathrm{d}k. \tag{3.3.15}$$

Solving the last integral gives finally

$$|\zeta^e| \leq \frac{2}{c(\frac{x + x_0}{t} + u_0)^2 t^2}, \quad \forall y. \tag{3.3.16}$$

Hence an observer moving along the x direction at constant speed $x/t = \xi$ sees an elevation wave decaying as an $O(1/t^2)$ as shown in figure 3.10. Now, define a positive constant $\epsilon \ll 1$ and consider a fixed observer at the origin $x = 0$. Then

$$|\zeta^e| \leq \frac{2}{c(x_0 + u_0 t)^2} \leq \epsilon$$

when $t \geq t_{dec}$, where

$$t_{dec} = \frac{1}{u_0} \left(\sqrt{\frac{2}{\epsilon c}} - x_0 \right) \tag{3.3.17}$$

is the time of decay of the evanescent component. For $t > t_{dec}$, ζ^e can be neglected, and the free surface elevation is made only of the oscillatory component $\zeta \simeq \zeta^o$. As an example, for $\epsilon = 0.05$, $c = 2$, $x_0 = 0$ and $u_0 = 1$ the time of decay is $t_{dec} \simeq 4.5$. With the same order of approximation, (3.3.17) can be written in physical variables as

$$t'_{dec} \simeq \frac{\mathsf{f}\sqrt{\sigma\lambda}}{u'_0} - \frac{x'_0}{u'_0}, \quad \mathsf{f} = 6.32, \tag{3.3.18}$$

which is similar in form to the characteristic time of motion defined by Watts et al. (2003). The time of decay (3.3.18) is composed by two terms. The first is related to the characteristic dimensions of the slide (λ, σ) and its horizontal velocity u'_0. Relation (3.3.18) shows that the larger the landslide width λ and length σ, the slower the decay of the evanescent component; on the other hand, the faster the landslide speed, the faster the decay of ζ^e. The second term is the time needed by the centroid of a subaerial slide, starting from its initial position x'_0, to reach the origin $x' = 0$, moving at constant speed u'_0. Note that the higher the initial position of the slide on the incline (i.e. $x_0 \ll 0$), the larger the time of decay of the evanescent component. We next turn to the analysis of ζ^o.

3.3.2 Behaviour for large times

Numerical methods have shown that for $t \gg 0$ edge waves are propagating along the shoreline, while the perturbations rapidly diminish near the point of generation O (see Lynett and Liu, 2005). To demonstrate this analytically, consider the expression of the n-th modal free surface elevation at the shoreline, $\zeta_n(0, y, t)$. For t large enough to neglect the contribution of the evanescent term ζ^e, the free surface elevation becomes

$$\zeta_n(0, y, t) \simeq \zeta_n^o(0, y, t) = \frac{2}{\pi} \int_0^\infty [A_n(k, t) \cos \omega_n t + B_n(k, t) \sin \omega_n t] \cos ky \, \mathrm{d}k. \tag{3.3.19}$$

Let us now consider the integral in (3.3.19)

$$\frac{2}{\pi} \int_0^\infty A_n \cos \omega_n t \, \cos ky \, \mathrm{d}k = \frac{2}{\pi} \mathrm{Re} \left\{ \int_0^\infty A_n \frac{1}{2} \left[\mathrm{e}^{\mathrm{i}t(ky/t - \omega_n)} + \mathrm{e}^{\mathrm{i}t(ky/t + \omega_n)} \right] \mathrm{d}k \right\}, \tag{3.3.20}$$

where the exponential terms represent respectively a right-going wave and a left-going wave. The behaviour of these two waves at large times can be analysed with the method of *stationary phase* already employed in section 2.1.2. For $t \gg 1$, the exponential functions of phase

$$w_n(k) = ky/t \mp \omega_n = ky/t \mp \left[2k \left(n + \frac{1}{2} \right) \right]^{1/2} \tag{3.3.21}$$

oscillate quickly with varying k, sweeping a very small net area, and so determine the integrals in (3.3.20) to be approximately null. In a neighbourhood of the points $k_n = k_n^*$ where the phase is stationary, the exponential function stands over a larger net area, and the integral (3.3.20) becomes significant. If we denote

$$\frac{\mathrm{d}}{\mathrm{d}k} () = \dot{()},$$

for the right-going wave the stationary points occur at

$$\frac{y}{t} - \dot{\omega}_n = \frac{y}{t} - C_{g_n} = 0,$$

where

$$C_{g_n} = \dot{\omega}_n = \frac{\sqrt{2n+1}}{2\sqrt{k}}$$

is the n-th modal group celerity. Differentiating (3.3.21) and equating to zero yields

$$k_n^* = (2n+1)\left(\frac{t}{2y}\right)^2. \tag{3.3.22}$$

Note that for the left-going wave there are no stationary points. By Taylor-expanding the phase function w_n about the stationary point k_n^* ,

$$w_n(k) \simeq w_n(k_n^*) + \frac{1}{2}\ddot{\omega}_n(k_n^*)(k-k_n^*)^2,$$

the integral (3.3.20) can be approximated to

$$\frac{2}{\pi}\int_0^\infty A_n(k,t)\cos\omega_n t\,\cos ky\,\mathrm{d}k \simeq \frac{\sqrt{2}A_n(k_n^*,t)}{\left(\pi\, t|\ddot{\omega}_n(k_n^*)|\right)^{1/2}}\cos\left(k_n^* y - \omega_n t + \frac{\pi}{4}\right), \tag{3.3.23}$$

with

$$\ddot{\omega}_n(k) = -\frac{\sqrt{2n+1}}{4k^{3/2}}. \tag{3.3.24}$$

Analogous considerations can be made for

$$\frac{2}{\pi}\int_0^\infty B_n(k,t)\sin\omega_n t\,\cos ky\,\mathrm{d}k \simeq -\frac{\sqrt{2}B_n(k_n^*,t)}{\left(\pi\, t|\ddot{\omega}_n(k_n^*)|\right)^{1/2}}\sin\left(k_n^* y - \omega_n t + \frac{\pi}{4}\right). \tag{3.3.25}$$

By substituting (3.3.23) and (3.3.25) into (3.3.19) and summing up the single modes, we obtain

$$\begin{aligned}\zeta(0,y,t) \;&\simeq\; \sum_{n=0}^{\infty}\zeta_n^o(0,y,t) \simeq \sum_{n=0}^{\infty}\frac{\sqrt{2}}{\left(\pi\, t|\ddot{\omega}_n(k_n^*)|\right)^{1/2}}\times\\ &\times\; \left[A_n(k_n^*,t)\cos\left(k_n^* y - \omega_n t + \frac{\pi}{4}\right) + \right.\\ &-\; \left. B_n(k_n^*,t)\sin\left(k_n^* y - \omega_n t + \frac{\pi}{4}\right)\right].\end{aligned} \tag{3.3.26}$$

The latter equation is an approximated expression (error = $O(t^{-1})$, see Mei et al., 2005) of the free surface elevation at the shoreline for large times. In (3.3.26) each of the modal components is the sum of two waves, of amplitude

$$\frac{\sqrt{2}A_n(k_n^*,t)}{\sqrt{\pi t|\ddot{\omega}_n(k_n^*)|}} \tag{3.3.27}$$

and

$$\frac{\sqrt{2}B_n(k_n^*,t)}{\sqrt{\pi t|\ddot{\omega}_n(k_n^*)|}} \tag{3.3.28}$$

respectively, both vanishing with time as $t^{-1/2}$. Finally, by using the same method but for $x > 0$, we get the approximated expression of the free surface elevation for all (x, y) at large times:

$$\zeta(x,y,t) \simeq \sum_{n=0}^{\infty}\mathrm{e}^{-k_n^* x}L_n\left(2k_n^* x\right)\zeta_n^o(0,y,t). \tag{3.3.29}$$

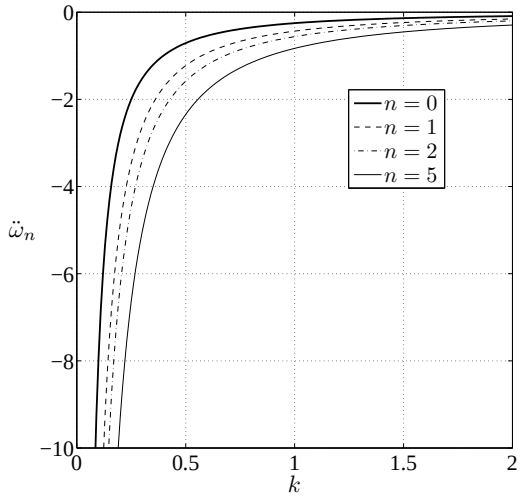

FIGURE 3.11: Behaviour of $\ddot{\omega}_n$ (3.3.24) vs. k. Note that $\ddot{\omega} \to -\infty$ as $k \to 0$.

Expression (3.3.29) shows the fast decay in x of the free surface oscillation, distinguishing feature of the edge waves. Therefore, at large times the motion consists of a system of edge waves propagating along the shoreline, with amplitudes proportional to $A_n \left|\ddot{\omega}_n\right|^{-1/2}$ and $B_n \left|\ddot{\omega}_n\right|^{-1/2}$. Now, figure 3.11 shows that $\ddot{\omega}_n \to -\infty$ for $k \to 0$; as a result the wave amplitudes (3.3.27) and (3.3.28) vanish for $k_n^* \to 0$, as shown in figure 3.12.

These crucial observations allow us to investigate the physics of expressions (3.3.26) and (3.3.29) more in detail. An observer moving along the shoreline at a fixed speed $\xi_1 = y/t$ sees the superposition of two wave trains decaying as $t^{-1/2}$. For larger speed $\xi_2 > \xi_1$, i.e. smaller wavenumber k_n^* (3.3.22), a faster-moving observer sees longer waves which are also of larger amplitude, since the amplitude functions (3.3.27) and (3.3.28) first increase as $k_n^* \to 0$ from larger values (see figure 3.12). Finally, an observer moving close to the front at a speed $\xi_3 = y/t \gg 1$ (i.e. $k_n^* \simeq 0$) sees a train of even longer waves, but with very small amplitudes, since both (3.3.27) and (3.3.28) vanish as k_n^* approaches zero (see figure 3.12). Hence at a given time t_1, longer waves, which travel faster, are not those of larger amplitude, as shown by the summarizing graph of figure 3.13. Let us now consider the spatial snapshot of figure 3.13 at a later time $t_2 > t_1$. All the observers have moved forward, thus increasing their mutual distance. As a consequence, the wave field appears to be stretched, and new wave crests are created during the propagation. This physical picture agrees with the results obtained with earlier numerical models and experimental tests (see, for example, Lynett and Liu, 2005). The lack of a properly defined leading wave for large times distinguishes landslide generated tsunamis on a plane beach from transient waves generated and propagating over a constant depth d (see Mei et al., 2005; Di Risio and Sammarco, 2008). In the latter case, in fact, the dispersion relation

$$\omega(k) = \sqrt{gk \tanh kd}$$

determines the wave amplitude, proportional to $|\ddot{\omega}|^{-1/2}$, to increase as k decreases (i.e. while moving toward the wave front), till it becomes unbounded at $k = 0$. Solution of this singularity (see Mei et al., 2005) yields the known expression of the leading wave in terms of the Airy function. In the present case, instead, there is no singularity at $k = 0$ as discussed above.

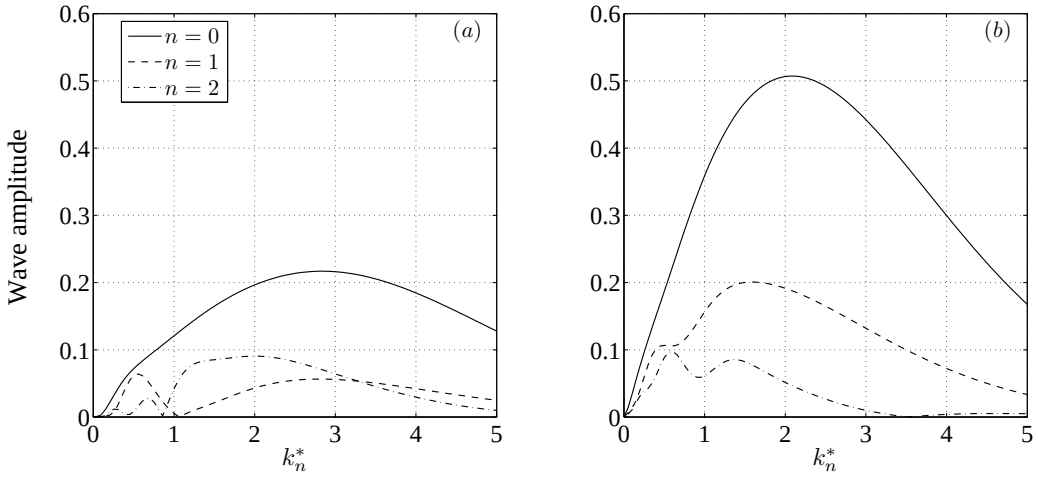

FIGURE 3.12: Behaviour of the wave amplitude functions (3.3.27) (a) and (3.3.28) (b) in absolute values versus k_n^*. Time is $t = 10$. Note that all amplitudes vanish as $k_n^* \to 0$.

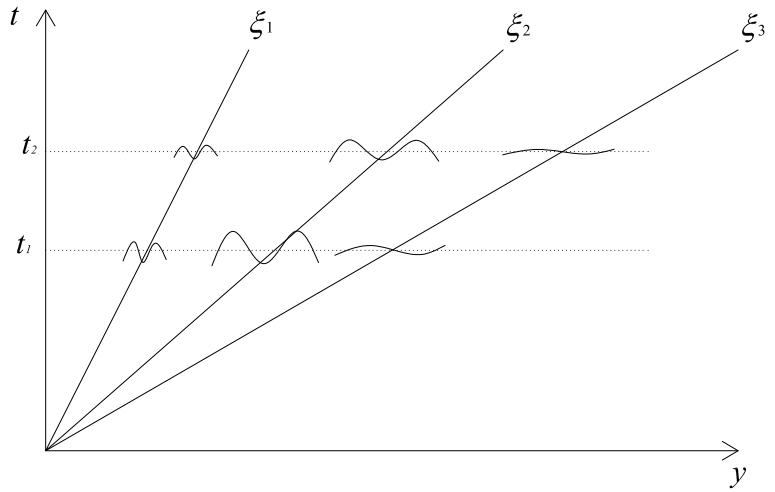

FIGURE 3.13: Qualitative shapshots of the propagating wave field for $t \gg 1$. Different views given by three moving obseervers at speed $\xi_1 < \xi_2 < \xi_3$ are depicted. Note the dispersive behaviour of the wave field. Longer waves travel faster and are followed by a tail of shorter waves. The maximum wave amplitude is reached in the middle of the wave train.

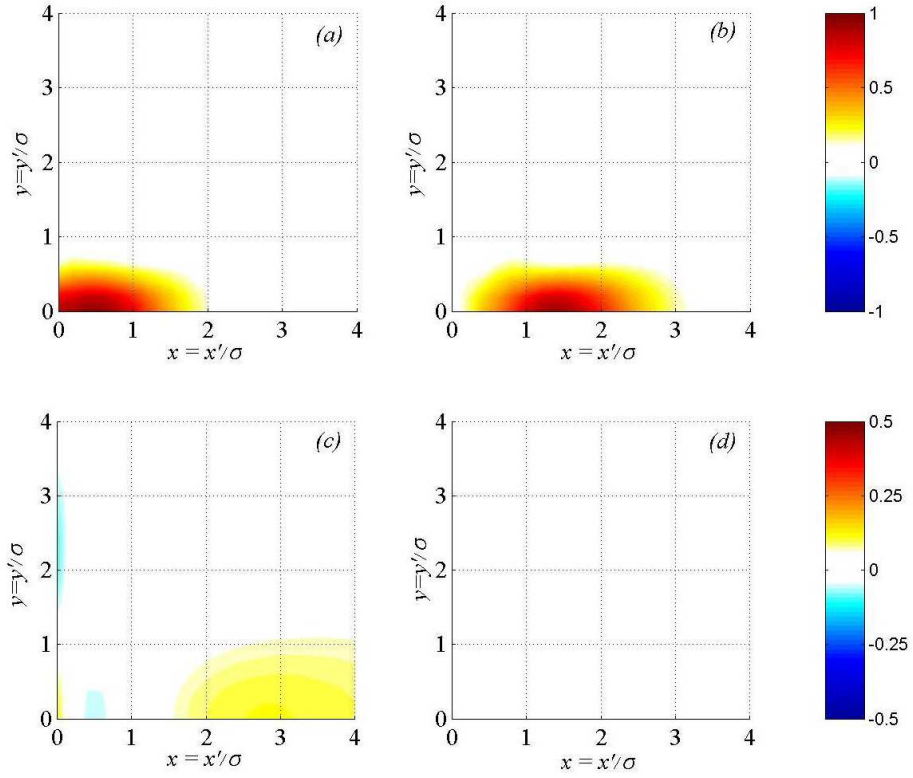

FIGURE 3.14: Contour levels of the evanescent component ζ^e in non-dimensional variables at times *(a)* $t = 0.5$, *(b)* $t = 1.5$, *(c)* $t = 4.5$, *(d)* $t = 7$. Parameters are $c = 2, x_0 = 0, u_0 = 1$. The first six modes have been considered.

3.3.3 The wave field

Let us analyse the wave motion generated by a characteristic landslide with parameters $c = \sigma/\lambda = 2, x_0 = 0$ and $u_0 = 1$. In figure 3.14(a–d) the contours of the evanescent component ζ^e, expression (3.3.11), at four different instants are shown. When t is small, ζ^e is non-zero only in a narrow area landward of the slide (see 3.14a). After some instants, the evanescent component is propagating mostly in the offshore direction (figure 3.14b), while its amplitude rapidly decreases as t approaches $t_{dec} \simeq 4.5$ (see 3.14c). Finally, for $t > t_{dec}$, ζ^e is zero everywhere in the fluid domain (figure 3.14d). Hence the evanescent term is a result of the early interaction between landslide and water, directly affecting the wave motion only during the phase of generation. In this phase, the occurrence of source-specific waves has also been shown via numerical investigation by Lynett and Liu (2005).

Now, let us focus on the actual free surface elevation $\zeta = \zeta^o + \zeta^e$, given by (3.3.8) and (3.3.11), and represented in figure 3.15(a–d). At the earliest times of motion, the landslide pushes water ahead and generates a leading elevation wave. The latter is propagating mostly in the offshore direction, due to the stretched shape of the slide, while along the shore is less noticeable. In the meantime, a depression wave occurs landwards (figure 3.15a). After few instants, the elevation wave is spreading also along the shoreline, while the depression wave dominates over a large area around the origin (figure 3.15b). At larger times the first elevation wave has already left the domain,

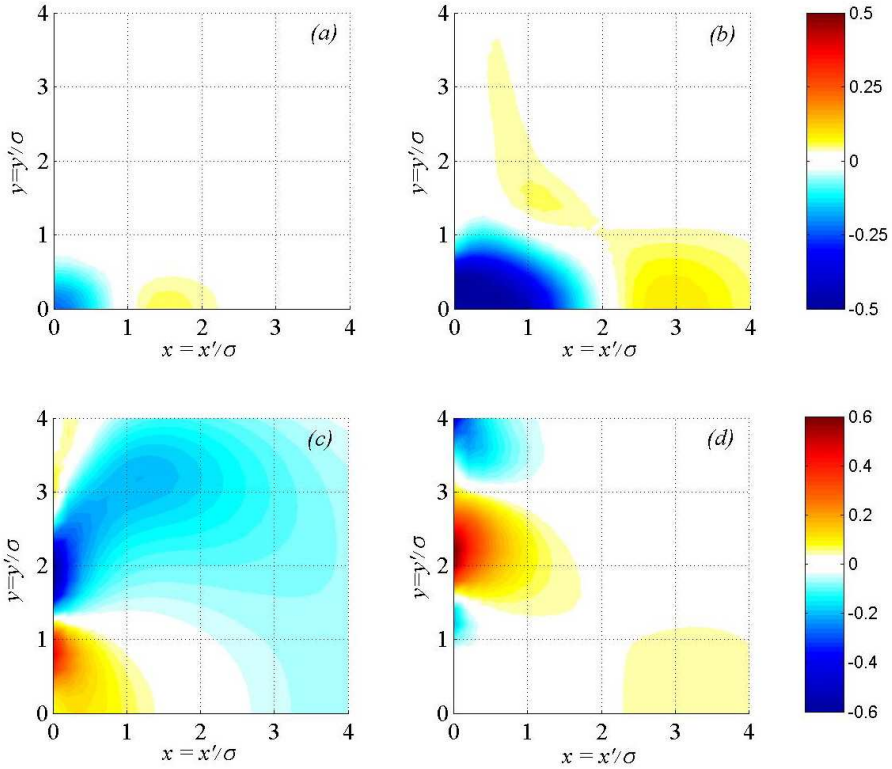

FIGURE 3.15: Contour levels of the free surface $\zeta = \zeta^e + \zeta^o$ in non-dimensional variables at times *(a)* $t = 0.5$, *(b)* $t = 1.5$, *(c)* $t = 4.5$, *(d)* $t = 7$. Parameters are $c = 2, x_0 = 0, u_0 = 1$. The first six modes have been considered.

followed by the propagating depression wave (figure 3.15*c*). In turn, the latter is wrapping a second elevation wave generated by the elastic rebound at the origin. Water motion along the shoreline becomes evident. Finally, for $t = 7$, the perturbation is travelling mostly in the longshore direction (figure 3.15*d*), while around the origin the water returns to the unperturbed position. The three-dimensional effects along the indefinite plane beach lying on the y axis can be further appreciated with the plots of figures 3.16 and 3.17. Here three-dimensional snapshots of the free-surface elevation are presented at fixed times, starting from the beginning of the motion ($t = 0.5$) with time increments $\delta t = 0.5$ till the perturbation is fully generated and propagating away from the source. Again, at the earliest times of motion the landslide pushes water ahead, while a deep depression generates just landwards of the slide (instants $t = 0.5$ to $t = 2$). Hence large free-surface gradients are created along the shoreline, driving strong fluxes to converge towards the centre ($t = 2.5, 3$). As a result, the convergent flows eventually collide at the origin to form a large elevation wave. Finally the rebound wave splits into two crests which symmetrically start to travel along the shoreline ($t = 3.5, 4$).

The plots of figure 3.18(a–d) show four snapshots of the free surface elevation at large times, and are obtained by using the stationary phase solution (3.3.29). Starting from the left, note the longshore wave motion becoming predominant already at $t = 10$ (see figure 3.18a–b). By $t = 20$, the wave motion is bounded at the shoreline (figure 3.18c), and progressing again in time only edge waves are present (see figure 3.18 d). The first occurring waves are not those of larger amplitude, as demonstrated above. Furthermore, new wave crests are created in the course of propagation, while the perturbation moves ahead from the origin. Longer waves travel faster and are followed by a tail of shorter waves, as obtained numerically by Lynett and Liu (2005).

The linear long wave theory, non-dispersive over bottoms of constant depth, *reproduces* the dispersive behaviour of the trapped waves over inclined bottoms!

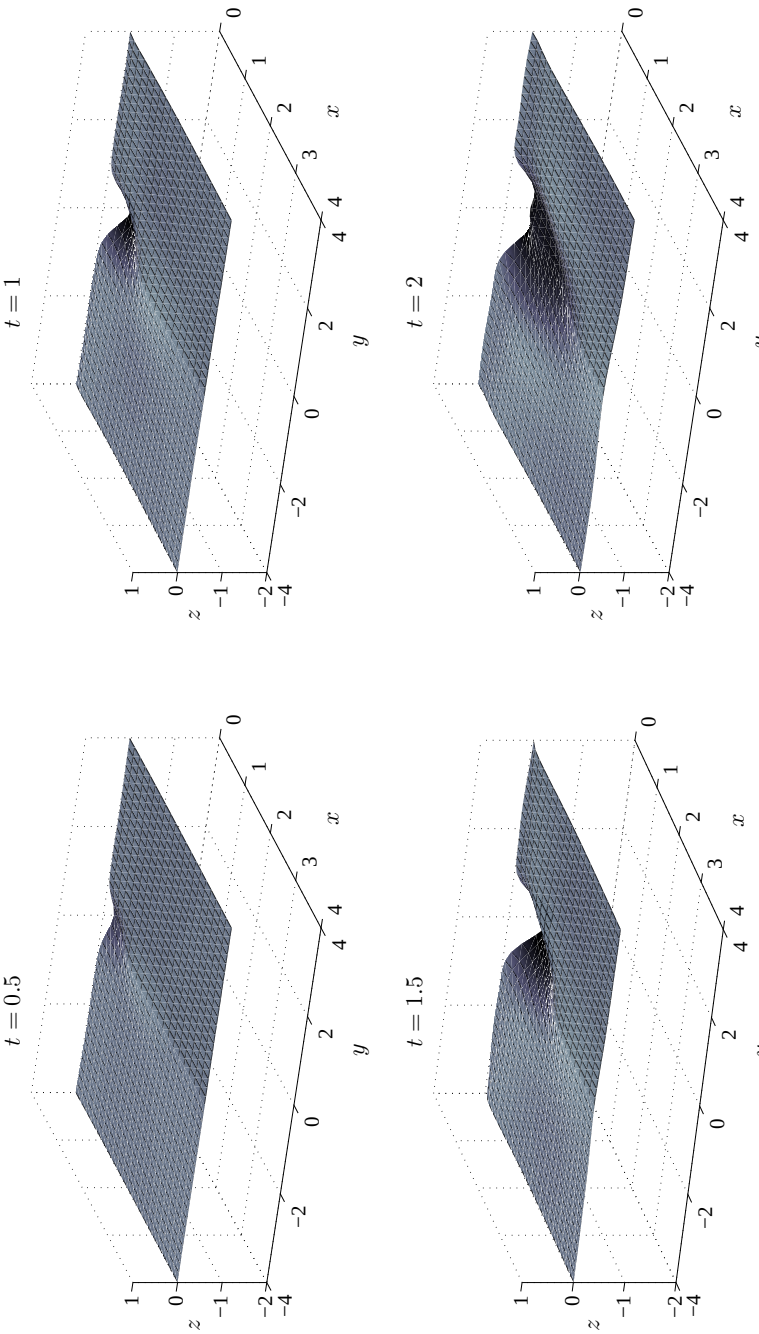

FIGURE 3.16: Snapshots of the free-surface profile in non-dimensional variables at the beginning of motion, for $t = 0.5$ to $t = 2$. Parameters are $c = 2, x_0 = 0, u_0 = 1$. The first six modes have been considered.

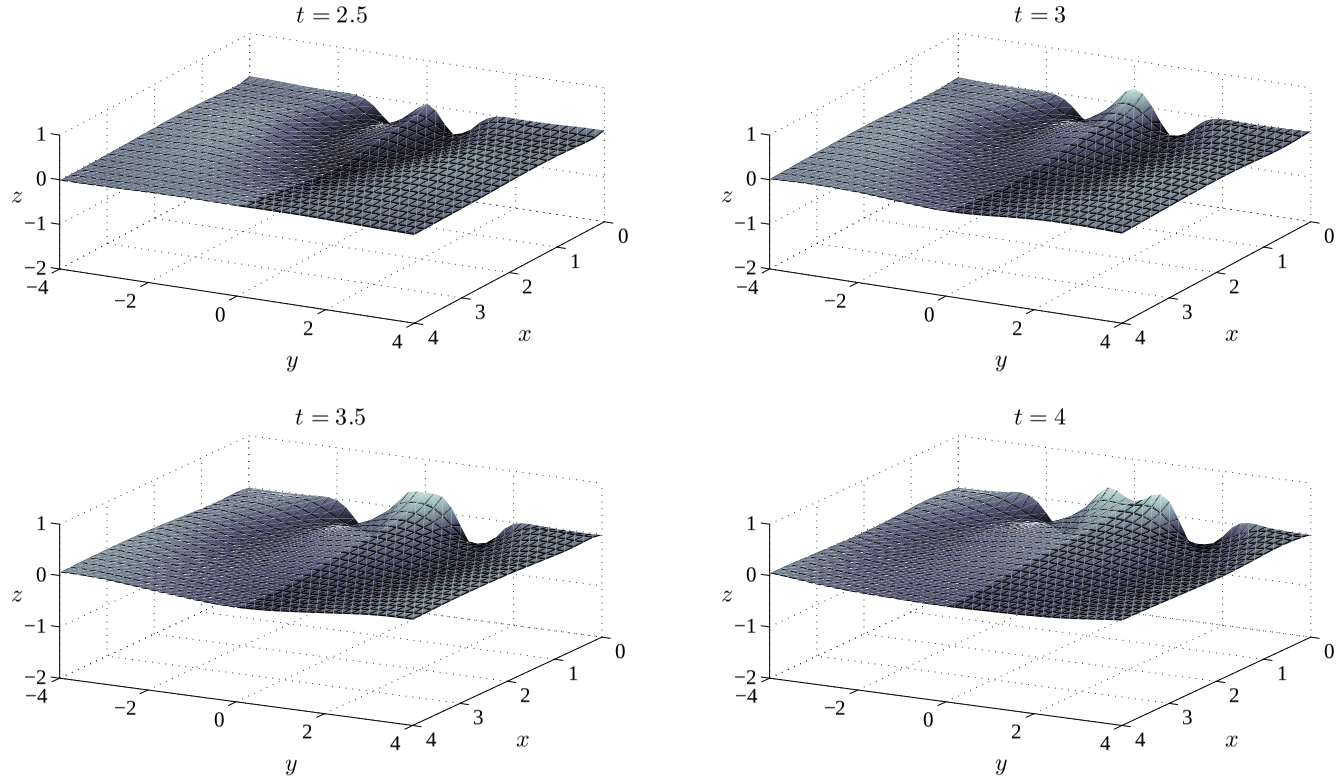

FIGURE 3.17: Snapshots of the free-surface profile in non-dimensional variables at the beginning of motion, for $t = 2.5$ to $t = 4$. Parameters are $c = 2, x_0 = 0, u_0 = 1$. The first six modes have been considered.

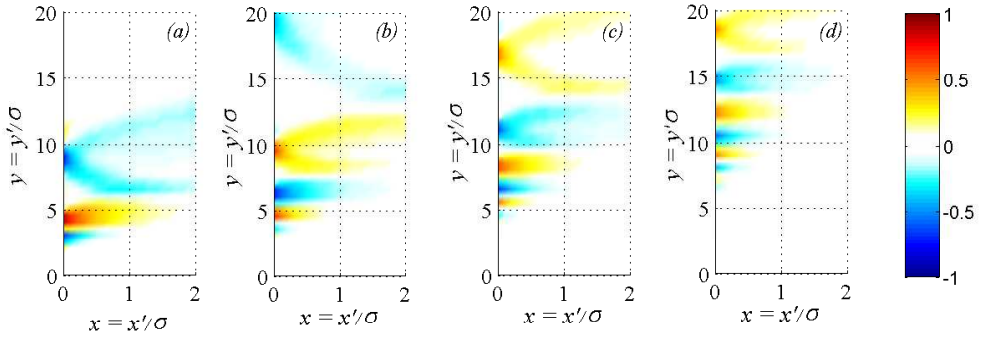

FIGURE 3.18: Contour levels of the free surface in non-dimensional variables at times *(a)* $t = 10$, *(b)* $t = 15$, *(c)* $t = 20$, *(d)* $t = 30$. The first five modes have been considered. All values have been multiplied by the magnifying factor $\sqrt{\pi}$.

3.4 Parametric analysis

In this section we investigate the influence of the landslide centroid initial position x_0 and velocity u_0 on the generated wave field for a double-Gaussian shaped landlslide (see section 3.2.1). As an application of the results obtained in the previous §3.3, let us first consider the limit case $x_0 = 0$ and $u_0 = 1$, which will be also useful for further comparison. This represents a landslide starting from a half-submerged position and moving along the incline with unit horizontal velocity. Take the oscillatory component ζ^o (3.3.8) of the free-surface elevation

$$\zeta^o = \frac{2}{\pi}\sum_{n=0}^{\infty}\int_0^{\infty} \mathrm{e}^{-kx} L_n(2kx)\,[A_n \cos\omega_n t + B_n \sin\omega_n t]\cos ky \,\mathrm{d}k.$$

The values of the amplitude coefficients A_n and B_n, expressions (3.3.9) and (3.3.10) respectively, for $x_0 = 0$ and $u_0 = 1$ are

$$A_n = A_n(k,t) = \omega_n \hat{s}\mathcal{L}^n\left[\omega_n a_n(\alpha,k,t) - \mathrm{e}^{-\alpha^2}\right]$$

and

$$B_n = B_n(k,t) = -\hat{s}\mathcal{L}^n\left[2\alpha\mathrm{e}^{-\alpha^2} + \omega_n^2 b_n(\alpha,k,t)\right]$$

respectively, where

$$a_n = a_n(\alpha,k,t) = \frac{\sqrt{\pi}}{2}\mathrm{e}^{-\omega_n^2/4}\mathrm{Im}\left\{\mathrm{e}^{\mathrm{i}\omega_n\alpha}\left[\mathrm{erf}\left(\alpha + \mathrm{i}\frac{\omega_n}{2}\right) - \mathrm{erf}\left(\alpha - t + \mathrm{i}\frac{\omega_n}{2}\right)\right]\right\},$$

while

$$b_n = b_n(\alpha,k,t) = \frac{\sqrt{\pi}}{2}\mathrm{e}^{-\omega_n^2/4}\mathrm{Re}\left\{\mathrm{e}^{\mathrm{i}\omega_n\alpha}\left[\mathrm{erf}\left(\alpha + \mathrm{i}\frac{\omega_n}{2}\right) - \mathrm{erf}\left(\alpha - t + \mathrm{i}\frac{\omega_n}{2}\right)\right]\right\}.$$

In the same limit, the evanescent component ζ^e (3.3.11) of the free-surface elevation becomes

$$\zeta^e = \frac{2}{\pi}\sum_{n=0}^{\infty}\int_0^{\infty} \mathrm{e}^{-kx} L_n(2kx)\,\omega_n \hat{s}\mathcal{L}^n\left[\mathrm{e}^{-(\alpha-t)^2}\right]\cos ky \,\mathrm{d}k.$$

In the following we shall first consider the influence of the two parameters x_0 and u_0 separately, in order to get a clear physical insight of the problem. The more complex issue of the combined influence between the two parameters x_0 and u_0 will be studied afterwards.

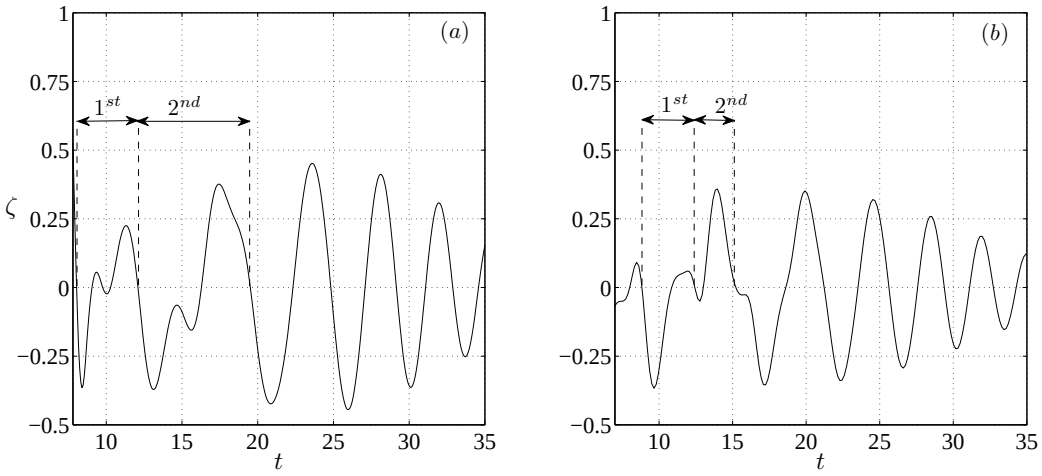

FIGURE 3.19: Time series of the free surface elevation (3.3.26) at $y = 8.38$. Landslide parameters are: $\sigma = 0.37\,\mathrm{m}$, $\eta = 0.045\,\mathrm{m}$, $u_0 = 1$; slope is $s = 1/3$. The initial position of the centroid is (a) $x_0 = -1$ and (b) $x_0 = 0$. The first five modes have been considered. The single waves are identified via the method of down zero-crossing. The first incoming perturbations at times $t \lesssim 10$ are not considered, being time too small to apply the stationary phase approximation with reliable accuracy.

3.4.1 Influence of the initial position x_0

In this section we analyse the influence of the centroid initial position x_0 on the generated wave field, for constant $u_0 = 1$. The analysis is made at large times, when the perturbation is already propagating along the shoreline far from the origin. Therefore the stationary-phase approximation (3.3.26) for $\zeta \simeq \zeta^o$ is employed.

A large number of simulations has been made considering a landslide of fixed characteristic length $\sigma = 0.37\,\mathrm{m}$ and height $\eta = 0.045\,\mathrm{m}$, sliding along an incline of slope $s = 1/3$ (i.e. that described in table 3.2, equivalent to the experimental slide of Di Risio et al. (2009a) described in table 3.1). The landslide centroid initial position x_0 increases from $x_0 = -2.1$, representing a subaerial slide (see §3.3), to $x_0 = 0.6$, relevant to a submerged slide. As an example, the time series of the free-surface elevation (3.3.26) at point $y = 8.38$ far from the origin are represented in figure 3.19 for $x_0 = -1$ (figure 3.19a) and $x_0 = 0$ (figure 3.19b) respectively. For each of the time series relevant to a fixed value of the parameter x_0, we first identify the single waves with the method of down zero-crossing, as shown in figure 3.19. Then we record the runup and drawdown values for each single wave. This procedure allows to investigate the influence of the centroid initail position x_0 on the runup and drawdown of the single waves, as shown in figure 3.20. Here the dash-dotted line $(-\cdot)$ shows the behaviour of the drawdown of the first incoming wave ($\mathrm{D1^{st}}$) at $y = 8.38$, versus x_0. In the same figure, the runup of the first and the second wave at the same point ($\mathrm{R1^{st}}$, $\mathrm{R2^{st}}$) are also plotted with a dashed $(--)$ and a solid $(-)$ line respectively, again versus x_0. First, note that at the chosen point, far from the origin, the runup reached by the second incoming wave is always larger than the runup reached by the first wave. This is a characteristic feature of edge waves propagating along a plane beach, as discussed in section 3.3.3. Figure 3.20 shows that this property is not affected by the initial position of the slide. On

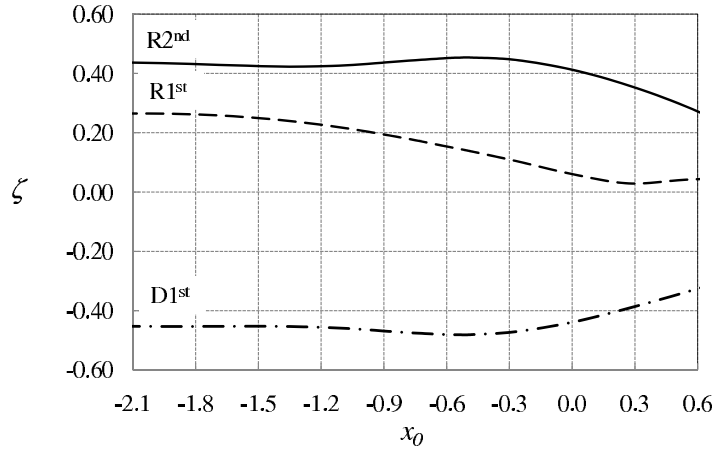

FIGURE 3.20: Runup of the first wave (dashed line, $--$), runup of the second wave (solid line, $-$) and drawdown of the first wave (dash-dotted line, $-\cdot$) vs. x_0. For $x_0 < 0$ the slide is defined as subaerial, otherwise submerged. Landslide parameters are: $\sigma = 0.37\,\mathrm{m}$, $\eta = 0.045\,\mathrm{m}$; slope is $s = 1/3$; $y = 8.38$ far from the origin. Values are obtained by numerically integrating expression (3.3.26).

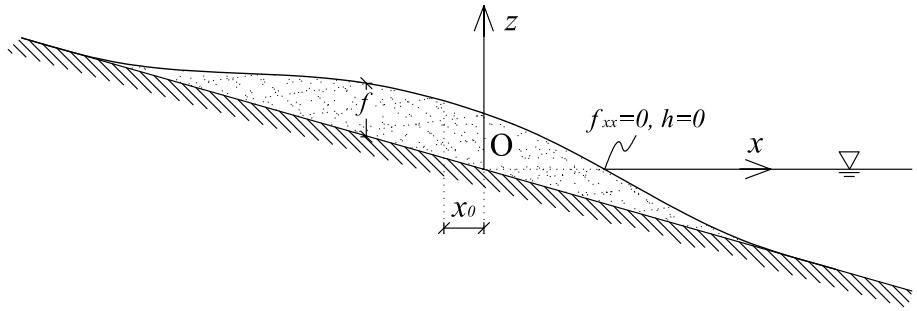

FIGURE 3.21: Initial position of the landslide which generates the maximum runup for the second incoming wave in figure 3.20, corresponding to (3.4.3). This is the condition under which the point of zero water depth coincides with the steepest point of the slide (for which $f_{xx} = 0$).

the other hand, the behaviour of the single runup and drawdown curves depends on x_0. Let us follow these curves from left (subaerial slide, $x_0 < 0$) to right (submerged slide, $x_0 > 0$). When $x_0 \ll 0$, i.e. the landslide is totally subaerial, the runup and drawdown are not much affected by the slide initial position. The generated wave field appears to be saturated. The largest possible amount of energy is transferred from the slide to the fluid, such that the maximum wave amplitude does not vary by further increasing the distance between the slide centroid and the origin (i.e. moving to the left of figure 3.20). Now let us gradually move to larger x_0 values, i.e. towards the right of figure 3.20; the behaviour of the three curves is now different. The runup of the first wave (dashed line $--$) decreases while increasing x_0, i.e. decreasing the initial distance of the slide from the water. On the other hand, the runup of the second wave (solid line $-$) first increases while diminishing x_0, reaching its maximum at $x_0 \simeq -0.5$, i.e. $x_0' \simeq 0.185$. For the specific geometry defined above, this configuration determines the landslide steepest point to touch the water at the starting position, as sketched in figure 3.21.

Let us demonstrate this statement analytically. Following §3.1.1, the bottom depth at a generic point $(x', 0)$ for $t' = 0$ is given by

$$h'(x') = -sx' + f'(x', 0, 0), \tag{3.4.1}$$

where f' is the landslide shape function (3.2.8). Also, the point of maximum steepness of f' along the offshore direction is

$$x'_s = \frac{\sqrt{2}}{2}\,\sigma + x'_0, \tag{3.4.2}$$

which is given by the positive solution of $f'_{x'x'} = 0$. Now, in order to have the point of zero water depth exactly at x'_s, we must require $h'(x'_s) = 0$. Therefore, combining (3.4.1), (3.2.8) and (3.4.2) we obtain in non-dimensional variables

$$-\sigma s \left(\frac{\sqrt{2}}{2} + x_0 \right) + \eta \mathrm{e}^{-1/2} = 0,$$

which is a function of x_0 only. Solution of this linear equation gives finally

$$x_0 = \frac{\eta}{\sigma s}\,\mathrm{e}^{-1/2} - \frac{\sqrt{2}}{2}. \tag{3.4.3}$$

The latter condition makes the point of zero water depth coincide with the steepest point of the slide, as sketched in figure 3.21. Substituting the current parameters $\sigma = 0.37\,\mathrm{m}$, $\eta = 0.045\,\mathrm{m}$ and $s = 1/3$ into (3.4.3), we finally obtain $x_0 \approx -0.5$ as anticipated above. From this discussion we infer that the behaviour of the runup and drawdown curves (figure 3.20) does not depend only on the initial position of the centroid x_0, but also on the shape of the landslide. Finally, note that for larger values of x_0, corresponding to a submerged slide, the runup and drawdown of each wave quickly decay to zero (see again figure 3.20). This is due to the reduced time of interaction between the landslide and the fluid at the beginning of motion, wich allows only a very small amount of energy to be transferred to the fluid.

3.4.2 Influence of the landslide velocity u_0

Let us analyse the influence of the landslide velocity u_0 on the generated wave field, for fixed $x_0 = 0$. Note that changing u_0 determines the slide kinetic energy (proportional to u_0^2) to change, while the slide potential energy (proportional to x_0) remains constant. The parameters of the landslide are still those of the previous section; the slide velocity along the x direction varies from $u_0 = 0.8$ to $u_0 = 1.5$. Figure 3.22 shows the behaviour of the drawdown of the first wave (dash-dotted line $-\cdot$), the runup of the first wave (dashed line $--$) and second wave (solid line $-$) versus u_0 at $y = 8.38$. Again, note that at a point far from the origin, the runup of the second wave is always larger than that induced by the first wave, as a typical feature of edge waves propagating along a plane beach. This property is not influenced by either changing the slide initial position or its velocity. Following the curves of figure 3.22 from left to right, the amplitude of the runup and drawdown increases almost linearly with increasing the slide velocity u_0. The influence of the initial velocity on the generated wave field is then straightforward: the larger u_0, the larger the amplitude of the propagating waves.

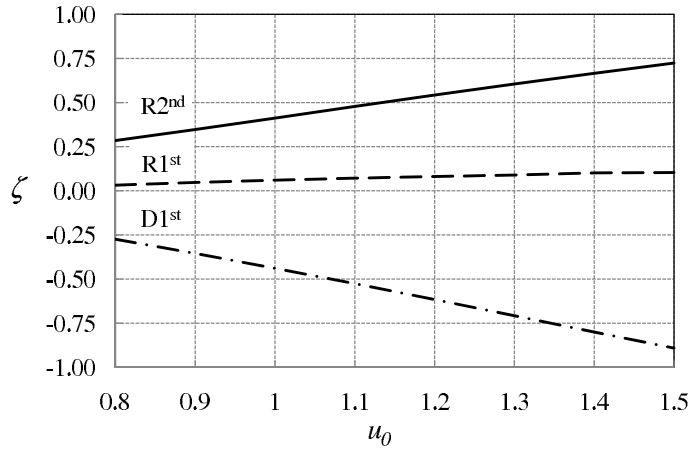

FIGURE 3.22: Runup of the first wave (dashed line, $--$), runup of the second wave (solid line, $-$) and drawdown of the first wave (dash-dotted line $-\cdot$) vs. u_0. Landslide parameters are: $\sigma = 0.37\,\mathrm{m}$, $\eta = 0.045\,\mathrm{m}$; slope is $s = 1/3$; $y = 8.38$ far from the origin. The runup values are obtained by numerically integrating expression (3.3.26).

3.4.3 Combined influence of initial position x_0 and velocity u_0

So far we have assumed the landlisde velocity along the x direction u_0 to be independent on the centroid initial position x_0. This assumption simplifies the algebra and allows to point out the influence of each parameter on the generated wave field separately. However, in reality the motion of the slide is induced by gravity, and the velocity depends on the centroid initial position: $u_0 = u_0(x_0)$. Several factors intervene in determining the relation between u_0 and x_0, like the slide shape, the characteristic parameters σ and η and the bottom friction. As already discussed in §3.3, we shall asssume

$$u_0(x_0) = \frac{1.119}{\sqrt{\sigma g s}} \cos\alpha - 1.139 \sqrt{\frac{\sigma}{gs}}\,(1 + x_0), \tag{3.4.4}$$

where the constants 1.119 and 1.139 have the dimensions of m/s and s^{-1} respectively and $\alpha = \arctan s$. This expression has been determined experimentally by employing a landslide of elliptic shape (see figure 3.4 for a sketch and table 3.1 for dimensions) sliding along an incline of slope $s = 1/3$. Recall that this landslide is equivalent in volume to the double-Gaussian shaped slide of parameters $\sigma = 0.37\,\mathrm{m}$ and $\eta = 0.045\,\mathrm{m}$ considered in this chapter (see figure 3.6 for a sketch and table 3.2 for dimensions). Relation (3.4.4) between x_0 and u_0 has been used here for various simulations. First, we set the value of x_0 and obtain u_0 from (3.4.4). With these values, we consider the time series of the free surface elevation (3.3.26) at a given point along the shoreline ($y = 8.38$ as above) and record the runup and drawdown reached by the single waves. Figure 3.23 shows the behaviour of the drawdown of the first wave (dash-dotted line $-\cdot$), together with the runup of the first wave (dashed line $--$) and the second wave (solid line $-$), versus x_0, at $y = 8.38$. When the variations of the initial centroid position x_0 and the slide velocity u_0 are combined, the effect of u_0 is dominant. The induced runup reaches its maximum values when the slide is fully subaerial and the corresponding velocity (3.4.4) is much larger than unity: $x_0 \ll 0$ and $u_0 \gg 1$. Hence the higher the slide initial position on the incline, the larger the amplitude of the induced wave field at a point on the shoreline far from the slide. Moving the landslide towards the origin both increases x_0 and reduces u_0. As a result, the runup and drawdown decay quickly, due

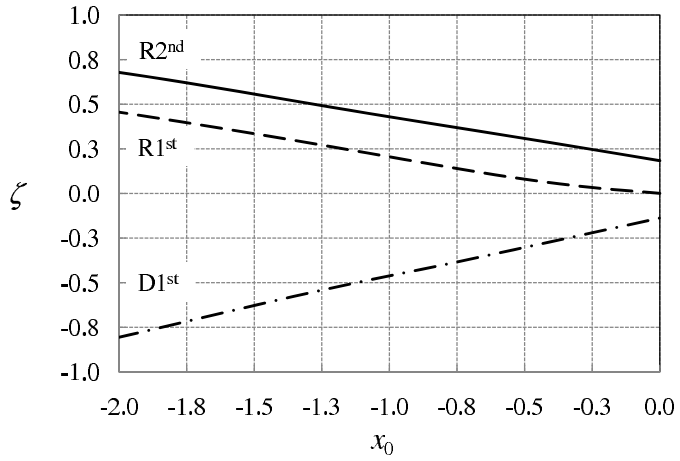

FIGURE 3.23: Combined influence of x_0 and u_0 on the wave field. Figure shows the runup of the first wave (dashed line), the runup of the second wave (solid line) and the drawdown of the first wave (dash-dotted line) vs. x_0. Expression (3.4.4) is used to relate the slide velocity u_0 with the centroid initial position x_0. Landslide parameters are: $\sigma = 0.37\,\mathrm{m}$, $\eta = 0.045\,\mathrm{m}$; slope is $s = 1/3$; $y = 8.38$ far from the origin. The runup values are obtained by numerically integrating expression (3.3.26).

to the small exchange of total energy between the slide and the fluid.

3.4.4 Maximum runup along the shoreline

We now investigate the influence of the slide initial position and velocity, x_0 and u_0 respectively, on the maximum runup $R_{\max}$ reached by the generated wave field along the shoreline. As an example, let us consider the plots of figure 3.24. Here the time series of the free-surface elevation (3.3.26) are represented at points $y = 6$ (figure 3.24*a*) and $y = 8.38$ (figure 3.24*b*) on the shore, for the sample slide of table 3.2. In both cases the slide centroid initial position is set at $x_0 = 0$, corresponding to an average velocity $u_0 = 0.582$, according to the empirical law (3.4.4). Note that at the first point $y = 6$ the maximum runup is reached by the second incoming wave (still identified via the down zero-crossing method), while at larger distance from the origin (point $y = 8.38$) the maximum runup is reached by the third wave, as a result of the dispersive effects described in section 3.3. If we perform a similar analysis for various points on the shoreline y and several values of the initial position x_0, we obtain the summarizing graph of figure 3.25. Here the behaviour of the maximum induced runup is plotted versus the shoreline coordinate y, for two different values of the centroid initial position x_0. Labels identify the wave reaching the maximum runup (i.e. second, third, etc). Note that, when the slide is fully subaerial ($x_0 = -1$, solid line of figure 3.25), the maximum runup is always reached by the second incoming wave at all distances from the origin. Since the first incoming waves are those more related to the strong elastic rebound occurring at the origin at earlier times, we infer that for a subaerial slide the early elastic effects dominate over dispersion, also at larger times. Now let us consider a partially submerged slide ($x_0 = 0$ dashed line of figure 3.25). Closer to the origin the maximum runup is still reached by the second wave (i.e. the wave field is still influenced by the early elastic rebound at $y = 0$), but at larger distances the maximum runup switches towards late-coming waves, due to the dispersive effects discussed in §3.3.3. Hence we infer that moving the initial position of the slide closer

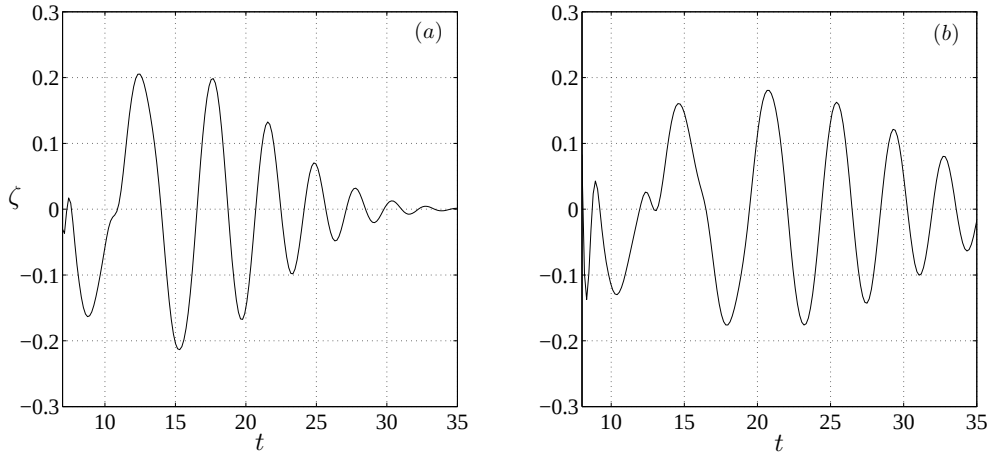

FIGURE 3.24: Time series of the free-surface elevation on the shoreline at points (a): $y = 6$, (b): $y = 8.38$. Landslide parameters are: $\sigma = 0.37\,\mathrm{m}$, $\eta = 0.045\,\mathrm{m}$; slope is $s = 1/3$; $x_0 = 0$ and $u_0 = 0.582$. The runup values are obtained by numerically integrating the stationary-phase approximation (3.3.26). The first five modes have been considered. Waves are individuated via the method of down zero-crossing. The first perturbations at smaller times are not considered, being time too small to apply the stationary phase approximation with reliable accuracy. Note that the maximum runup is reached by the second wave in (a) and by the third wave in (b).

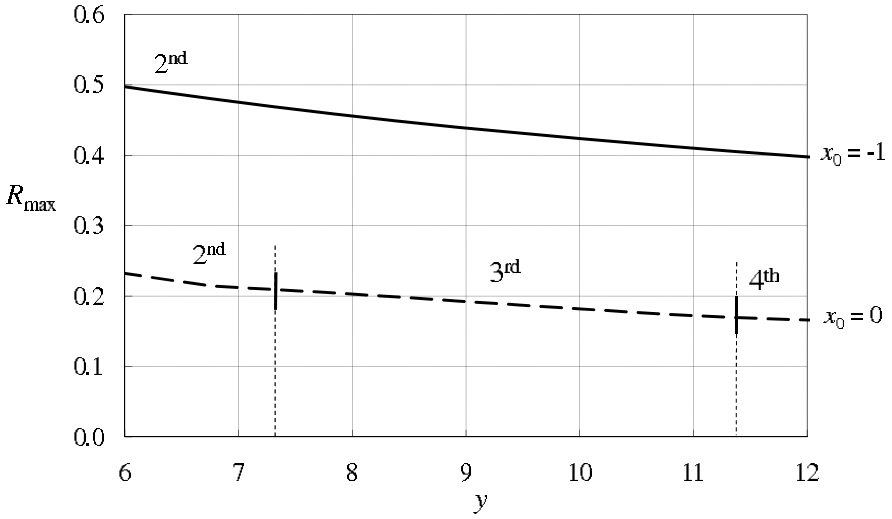

FIGURE 3.25: Maximum wave runup $R_{\max}$ vs. shoreline position y for a subaerial slide $x_0 = -1$ (solid line) and a partially submerged slide $x_0 = 0$ (dashed line). The vertical ticks separate the zones on the shoreline where the maximum runup is reached by the second, third and fourth waves. For $x_0 = -1$ (solid line) the maximum wave runup is always reached by the second wave. For $x_0 = 0$ the maximum wave runup switches towards the third and the fourth wave at large distances from the origin.

to water produces the combined effects of both decreasing the maximum runup and enhancing the dispersive behaviour of the fluid. In conclusion, the wave field generated by the fully subaerial slide $x_0 = -1$ is driven by the early elastic effects. On the other hand, the wave field generated by the partially submerged slide $x_0 = 0$ is driven by the elastic effects only close to the origin, dispersion becoming dominant at larger distances along the shoreline.

3.5 Experimental comparison

In this section the free-surface time series at the shoreline are evaluated and compared to experimental data of Di Risio et al. (2009a), which have been kindly given to the author. The latter have been obtained at LIAM (Laboratory of Maritime and Environmental Hydraulics of L'Aquila, Italy) by letting a ellipsoidal 0.8 m long by 0.4 m wide block slide down a steep slope, $s = 0.3$, as illustrated in figure 3.26. The landslide maximum thickness is 0.05 m, its maximum cross-sectional area is about 0.03 m^2. The basin of LIAM facility is 5.40 m long by 10.80 m wide, 0.8 m deep, as sketched in figure 3.27. Note that this experimental setup is the same of that discussed in §3.3 and here is summarised again in table 3.3. As anticipated before, by letting the model parameters be $\sigma = 0.37\,\mathrm{m}$, $\eta = 0.045\,\mathrm{m}$ and $c = 2$, the overall area beneath the double-Gaussian forcing function f' (3.2.8) approximates the landslide maximum cross-sectional area. Then the nonlinearity parameter ϵ and the dispersion parameter μ^2 (3.1.8) are respectively

$$\epsilon = \frac{\eta}{\sigma s} = 0.365\,, \quad \mu^2 = 4\pi^2 s^2 = 1.396,$$

while the Ursell number (3.1.6) is

$$\mathrm{U_r} = \frac{\epsilon}{\mu^2} \approx 0.26 < 1$$

i.e. dispersion cannot be completely neglected and is stronger than nonlinearity. As a consequence, the analytical model employed here might be inadequate in fully reproducing the dispersive behaviour of the fluid occurring in the experiments. The experimental release distance of the ellipsoidal slide is set to $X_s' = -0.2\,\mathrm{m}$. Let us consider the equivalent double-Gaussian shaped slide defined above. The centroid initial position relevant to the chosen experimental release distance X_s' is given by (3.2.16): $x_0' = -0.18\,\mathrm{m}$. Since $x_0' < 0$, the landslide centroid is outside the water at the starting position, while only the front part of the landslide is submerged. Finally, to estimate the horizontal velocity of the landslide relevant to the centroid initial position $x_0' = -0.18\,\mathrm{m}$, we shall employ the empirical relation (3.2.17) which gives $u_0' = 0.845\,\mathrm{m/s}$. The parameters indicated above are summarised in table 3.3 respectively for the experimental slide (left column) and the equivalent theoretical slide (right column). In figure 3.28 the time series of the free-surface elevation are plotted in physical variables at two different points along the shoreline $x' = 0$ and compared to the experimental data of Di Risio et al. (2009a). Figure 3.28(a) shows the time series at $y' = 3.10\,\mathrm{m}$ away from the point of generation; in figure 3.28(b) is instead depicted the free-surface time series at point $y' = 4.07\,\mathrm{m}$ from the origin. The main properties of the generated wave field, i.e. the shape of the waves, the time of arrival of crests and troughs and the maximum runup and drawdown, are predicted satisfactorily by the analytical model. The agreement

FIGURE 3.26: Experimental setup of Di Risio et al. (2009a), LIAM laboratory at the University of L'Aquila (Italy).

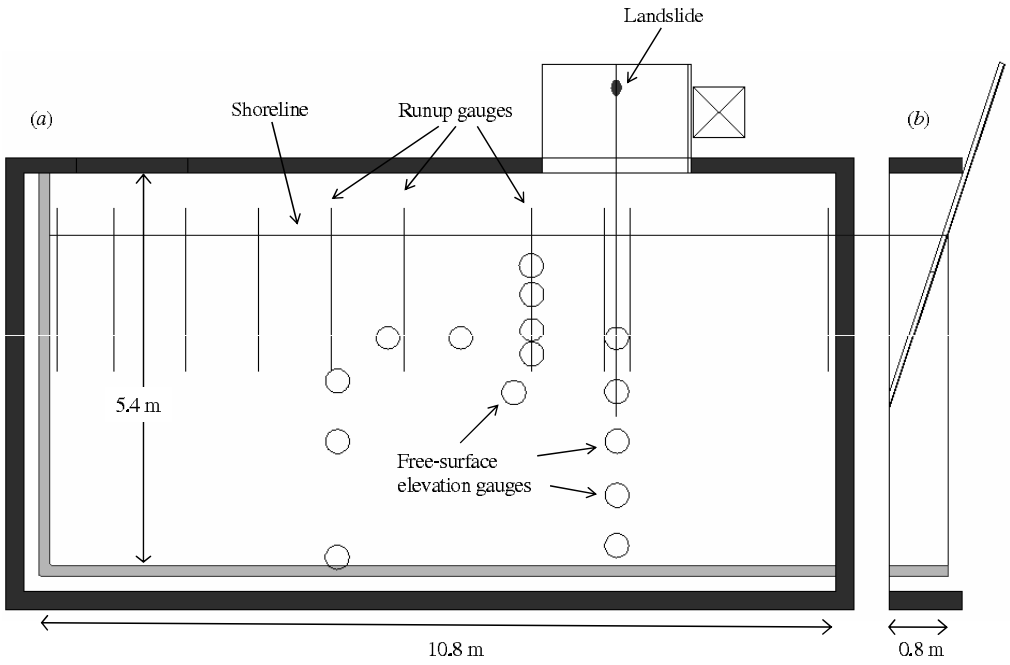

FIGURE 3.27: Sketch of the experimental setup of Di Risio et al. (2009a), LIAM laboratory at the University of L'Aquila (Italy). (a) plan view, (b) elevation.

Property	**Experiment**	**Property**	**Analytical model**
Shape	ellipsoidal	Shape	Double Gaussian
Length	0.8 m	Char. length	$\sigma = 0.37\,\mathrm{m}$
Width	0.4 m	Char. width	$\lambda = 0.185\,\mathrm{m}$
Max. vert. height	0.05 m	Max. vert. height	$\eta = 0.045\,\mathrm{m}$
Release distance	$X'_s = -0.2\,\mathrm{m}$	Cent. init. pos.	$x'_0 = -0.18\,\mathrm{m}$
Avg. vel. along slope	$U'_s = 0.87\,\mathrm{m/s}$	Velocity along x'	$u'_0 = 0.845\,\mathrm{m/s}$

TABLE 3.3: Properties of the experimental landslide of ellipsoidal shape (left column) used by Di Risio et al. (2009a) and the equivalent analytical double-Gaussian shaped landslide (right column).

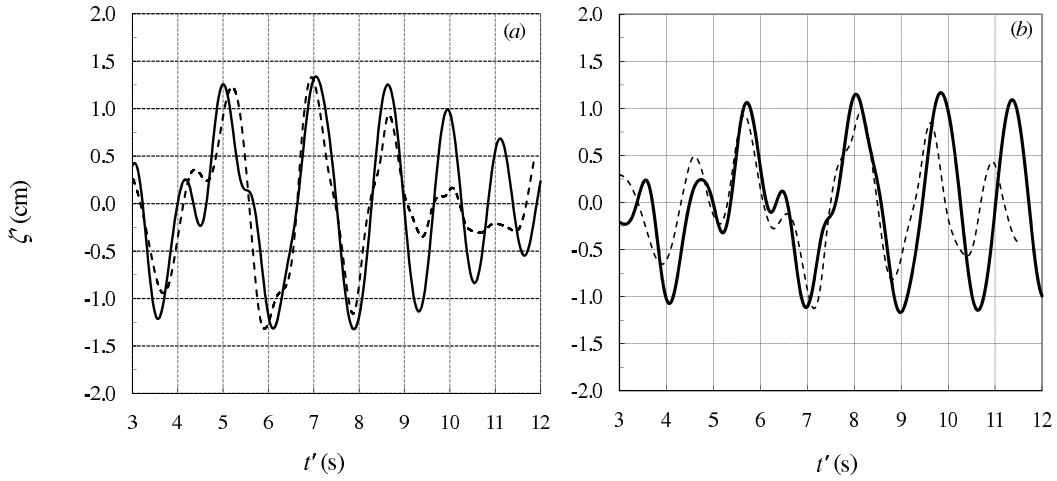

FIGURE 3.28: Free-surface time series in physical variables at (*a*) $(x', y') = (0, 3.10\,\mathrm{m})$ and (*b*) $(x', y') = (0, 4.07\,\mathrm{m})$. The bold dashed line shows the experimental data (visual imaging technique), the continuous line represents the theoretical values. ζ is evaluated with the stationary-phase approximation formula (3.3.26) and then transformed into dimensional form. The first five modes have been considered.

between analytical and experimental results is good up to $t = 8\,\mathrm{s}$. After that, waves reflected by the side walls in the experiment make the wave field not comparable with that given by the model.

Numerical values of the runup and drawdown reached by the first incoming waves at both points are reported in table 3.4 and table 3.5 respectively, and are compared again to the experimental data. The analytical model predicts the runup and drawdown with satisfactory accuracy, especially for the first sample point $y' = 3.10\,\mathrm{m}$. Also, the analytical values agree with the experimental ones when comparing the maximum values of runup and drawdown reached at both points, as shown in table 3.6. However, there are still some minor differences between the analytical and the experimental data, especially for the first incoming waves. Other than the role played by dispersion, several other factors can explain these differences. First, the analytical model does not take into account energy dissipation phenomena, such as shear actions or wave

Value at $y' = 3.10\,\mathrm{m}$	**Experimental**	**Analytical model**	**Rel. error** (%)
Max runup 1st wave (cm)	1.227	1.258	0.03
Min draw 1st wave (cm)	-0.942	-1.216	0.29
Max runup 2nd wave (cm)	1.328	1.341	0.01
Min draw 2nd wave (cm)	-1.318	-1.318	0.00

TABLE 3.4: Experimental and analytical values for the maximum runup and minimum drawdown of the first incoming waves at point $y' = 3.10\,\mathrm{m}$.

Value at $y' = 4.07\,\mathrm{m}$	**Experimental**	**Analytical model**	**Rel. error**(%)
Max runup 1st wave (cm)	0.490	0.244	0.50
Min draw 1st wave (cm)	-0.654	-1.071	0.64
Max runup 2nd wave (cm)	0.931	1.062	0.14
Min draw 2nd wave (cm)	-0.228	-0.321	0.40
Max runup 3rd wave (cm)	0.962	1.150	0.19
Min draw 3rd wave (cm)	-1.124	-1.115	0.01

TABLE 3.5: Experimental and analytical values for the maximum runup and minimum drawdown of the first incoming waves at point $y' = 4.07\,\mathrm{m}$.

Value	**Experimental**	**Analytical model**	**Rel. error**(%)
$y' = 3.10\,\mathrm{m}$			
Max runup (cm)	1.328	1.341	0.01
Min drawdown (cm)	-1.318	-1.318	0.00
$y' = 4.07\,\mathrm{m}$			
Max runup (cm)	0.962	1.150	0.19
Min drawdown	-1.124	-1.115	0.01

TABLE 3.6: Experimental and analytical values for the extreme runup and drawdown at points $y' = 3.10\,\mathrm{m}$ and $y' = 4.07\,\mathrm{m}$.

breaking, occurring in the experiment. Second, note also that the different shape of the landslide, whose front is much smoother in the analytical model than in the experiments, could have led to some differences in the propagating wave field, especially for the first incoming waves.

3.6 Validity of the hot-start condition

This discussion has been motivated by fruitful internal communication with Dr. P. Lynett, TAMU, U.S.A.

So far, the forced initial-value problem set by (3.1.11), with initial conditions $\zeta = 0$ and $\zeta_t = 0$ at $t = 0$, has been solved. The solution in terms of the free surface elevation ζ is given by (3.1.34). Recall that this model simulates the interaction between landslide and water at all stages of motion, rendered by the forcing term f in (3.1.11). However, several numerical codes are available which analyse a simplified system, based on the assumption of the so-called *hot-start* condition. Within this assumption, the early interaction between water and landslide is neglected. An equivalent unforced system is studied where the water motion is triggered by an initial free-surface bump, as it was generated previously by the landslide.

To discuss the validity of the hot-start condition, let us first rewrite the initial-value problem (3.1.11) as:

$$\Diamond\zeta = f_{tt}, \quad \zeta(x,y,0) = 0, \quad \zeta_t(x,y,0) = 0, \qquad (3.6.1a,b,c)$$

where $\Diamond(\cdot) = -\left[x(\cdot)_{xx} + x(\cdot)_{yy} + (\cdot)_x - (\cdot)_{tt}\right]$. The hot-start condition approach relies on the fact that at $t \simeq t_{dec}$, the landslide has already reached deeper water, so that wave forcing in shallow water is less effective. Also, the initial free surface perturbation generated by the slide starts to propagate from the shoreline in the horizontal plane. Therefore, when analysing the behaviour of the system near the shoreline, for $t \geq t_{dec}$, the forcing term in $(3.6.1a)$ can be neglected and a homogeneous initial-value problem starting at $t = t_{dec}$ can be considered instead. At this time the initial free surface elevation can be described by a known function of the spatial coordinates, $\zeta(x,y,0) = g(x,y)$. A double Gaussian function is often used to represent it:

$$g(x,y) = 2/\pi \left[\exp(-(x^2+y^2)) - a\,\exp(-(x^2+c^2y^2)/b^2)\right],$$

where a and b are shape parameters, depending on the characteristics of the landslide (see Carrier and Wu, 2003; Watts et al., 2005, for a compendium of possible wave forms). Hence to solve the problem, only the initial velocity $\zeta_t(x,y,0) = h(x,y)$ would need to be set. It has been widely assumed in the literature that after the landslide initiates, the total tsunami energy is almost all potential energy (see Watts et al., 2003, 2005). With this hypothesis, the initial velocity can be neglected: $h(x,y) \simeq 0$, and the problem becomes

$$\Diamond\zeta = 0, \quad \zeta(x,y,t_{dec}) = g(x,y), \quad \zeta_t(x,y,t_{dec}) = 0, \quad t \geq t_{dec} \qquad (3.6.2a,b,c)$$

i.e. a non-forced homogeneous initial-value system. This approach is currently employed in some landslide generated tsunamis forecasting models (see Watts et al., 2003). Here we further investigate on the analytical effectiveness of describing the fundamental behaviour of the fluid in this manner. In so doing, the following questions are posed: if it does really exist a homogeneous system equivalent to (3.6.1), and, for $t \geq t_{dec}$, if

this system is (3.6.2) indeed. In order to respond to the first question, define a function $\eta(x, y, t-\tau)$, with τ a positive real parameter, solution of

$$\Diamond\eta = 0, \quad \eta(x, y, 0) = 0, \quad \eta_t(x, y, 0) = f_{tt}(x, y, \tau), \quad t \geq \tau\,. \qquad (3.6.3a, b, c)$$

The latter is a homogeneous system, starting at $t = \tau$, with zero initial free surface elevation and initial velocity given by the forcing term $f_{tt}(x, y, \tau)$. Extension of the Duhamel's principle to the forced problem (3.6.1) reveals that

$$\zeta(x, y, t) = \int_0^t \eta(x, y, t-\tau)\,\mathrm{d}\tau \qquad (3.6.4)$$

is the solution of (3.6.1). Hence the first question has a positive answer: the homogeneous system (3.6.3), together with the Duhamel's integral formula (3.6.4), yield the solution of (3.6.1). No other equivalent homogeneous systems seem to exist. For a practical numerical simulation, solution (3.6.4) could be more suitable than solving directly the forced system (3.6.1). Now the second question: the equivalence between (3.6.1) and (3.6.2). Consider again the full problem (3.6.1), but with initial time $t = t_{dec}$:

$$\Diamond\zeta = f_{tt}(x, y, t), \quad \zeta(x, y, t_{dec}) = \bar{g}(x, y), \quad \zeta_t(x, y, t_{dec}) = \bar{h}(x, y), \qquad (3.6.5a, b, c)$$

where, taking only ζ^o,

$$\bar{g} = \frac{2}{\pi}\sum_{n=0}^{\infty}\int_0^{\infty} \mathrm{e}^{-kx} L_n(2kx)\,[A_n(k, t_{dec})\cos\omega_n t_{dec} + B_n(k, t_{dec})\sin\omega_n t_{dec}]\cos ky\,\mathrm{d}k, \qquad (3.6.6)$$

$$\begin{aligned}\bar{h} \;=\; & \frac{2}{\pi}\sum_{n=0}^{\infty}\int_0^{\infty} \mathrm{e}^{-kx} L_n(2kx)\omega_n \Big\{[A_{n,t} + \omega_n B_n]_{t=t_{dec}}\cos\omega_n t_{dec} + [B_{n,t} - \omega_n A_n]_{t=t_{dec}} \times \\ \times \;& \sin\omega_n t_{dec}\Big\}\cos ky\,\mathrm{d}k. \end{aligned} \qquad (3.6.7)$$

(3.6.6) and (3.6.7) are respectively the free surface elevation and velocity at $t = t_{dec}$ computed with (3.3.8). By definition, for $t \geq t_{dec}$ a rigorous analytical equivalence occurs only between systems (3.6.1) and (3.6.5). The latter is equal to (3.6.2) if and only if: (i) the forcing term f_{tt} is omitted, (ii) the initial free surface elevation (3.6.6) is substituted with the easier double Gaussian form $g(x, y)$, (iii) the initial velocity (3.6.7) is neglected. As discussed above, point (i) might not produce appreciable errors in shallow water. On the other hand, the approximations in points (ii) and (iii) might result in simulating a different physical behaviour of the system. Especially the total neglect of the initial velocity seems to have no analytical confirmation, since it can't be stated that (3.6.7) is zero in all the fluid domain for any shape of the landslide (i.e. for any t_{dec}). In conclusion, no analytical demonstration of the correctness of replacing the homogeneous problem (3.6.2) in lieu of (3.6.1) seems to exist: the hot-start condition cannot be validated analytically.

Chapter 4

Landslide tsunamis propagating along a semi-plane beach

In chapter 3 we have shown that, within the linear shallow-water theory, the landslide forced waves rapidly decay in the offshore direction, while a transient system of longshore travelling edge waves propagates away from the landslide. Indeed, given the geometry of an indefinite slope, the solution is expressed in terms of Laguerre polynomials and exponential decaying functions of the offshore coordinate x. However, an infinite slope does not fully represent a coastal area.

To obtain a more realistic model, in this chapter we investigate a different geometry, where the slope is extending to a finite length and further connects to a continental platform of constant depth.

4.1 Position of the problem

The physical domain of the model is shown in figure 4.1. Having set a $3D$ system of coordinates (x', y', z'), water is in the region $x' > 0$. At a distance b' from the coastline the slope ends and connects to a flat bottom of constant depth $h'_{b'}$. Due to the geometric discontinuity introduced by the flat-bottom zone, we shall define the *near field* as the domain $x' < b'$, where b' is the horizontal length of the incline. As a consequence, we shall also define the *far field* as the region $x' > b'$ where the bottom depth is constant $h' = h'_{b'} = sb'$, being s the slope of the incline. The system is assumed to be symmetric with respect to the y' axis; also assume that the landslide motion starts in a neighbourhood of the origin and that the landslide shape is symmetric with respect to x' and y'.

4.2 Governing equations

Within the assumption of linear shallow-water waves, the behaviour of the fluid is described by the forced long-wave equation

$$\frac{\partial^2 \zeta'}{\partial t'^2} - g\nabla \cdot \left(h' x' \nabla \zeta'\right) = \frac{\partial^2 f'}{\partial t'^2}, \tag{4.2.1}$$

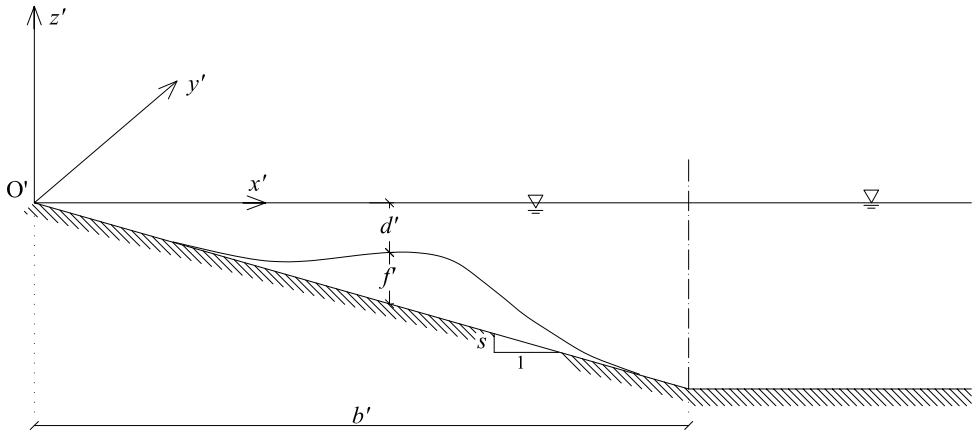

FIGURE 4.1: The fluid domain in physical coordinates. The dash-dotted line divides the near field $x' < b'$ from the far field $x' > b'$.

where the notation employed is the same of §3.1.1 and the bottom depth h' is now defined as

$$h'(x') = \begin{cases} sx' & \text{if } x' < b' \\ h'_{b'} = sb' & \text{if } x' \geq b' \end{cases}, \tag{4.2.2}$$

according to the geometry of figure 4.1. Let us introduce the same non-dimensional variables seen in chapter 3

$$(x, y) = (x', y')/\sigma, \quad t = \sqrt{gs/\sigma}t', \quad (\zeta, f) = \left(\zeta', f'\right)/\eta, \quad h = h'/\sigma s, \tag{4.2.3}$$

where σ denotes the characteristic length of the landslide and η its maximum vertical height. The equation of motion (4.2.1) becomes:

$$h\zeta_{xx} + h_x\zeta_x + h\zeta_{yy} = \zeta_{tt} - f_{tt}. \tag{4.2.4}$$

In (4.2.4) h is the non-dimensional bottom depth, obtained by substituting the latter of (4.2.3) into (4.2.2), i.e.

$$h(x) = \begin{cases} x & \text{if } x < b \\ h_b = b & \text{if } x \geq b \end{cases}, \tag{4.2.5}$$

where $b = b'/\sigma$ is the non-dimensional inclined beach length. As already done in chapter 3 for the plane beach, we require the free-surface elevation $\zeta(x, y, t)$ to be bounded at the shoreline

$$|\zeta(0, y, t)| < \infty \tag{4.2.6}$$

and to be an even function of the shoreline coordinate y. Finally, we require null initial free-surface elevation and velocity, i.e.

$$\zeta(x, y, 0) = 0, \quad \zeta_t(x, y, 0) = 0. \tag{4.2.7}$$

Now employ the cosine Fourier transform pair of ζ

$$\hat{\zeta}(x, k, t) = \int_0^\infty \zeta(x, y, t) \cos ky \, \mathrm{d}y, \quad \zeta(x, y, t) = \frac{2}{\pi} \int_0^\infty \hat{\zeta}(x, k, t) \cos ky \, \mathrm{d}k, \tag{4.2.8}$$

k being the non-dimensional transform parameter. The equation of motion (4.2.4) is then transformed into

$$h\hat{\zeta}_{xx} + h_x\hat{\zeta}_x - k^2 h\,\hat{\zeta} = \hat{\zeta}_{tt} - \hat{f}_{tt}(x,k,t), \tag{4.2.9}$$

while the boundary condition (4.2.6) can be rewritten as

$$\left|\hat{\zeta}(0,k,t)\right| < \infty \tag{4.2.10}$$

and the initial conditions (4.2.7) become

$$\hat{\zeta}(x,k,0) = 0, \quad \hat{\zeta}_t(x,k,0) = 0. \tag{4.2.11}$$

4.3 Eigenvalues

Recall that for the simple plane-beach geometry discussed in chapter 3, the solution of the homogeneous form of the governing equation (3.1.17), together with the boundary conditions (3.1.21), gives the system eigenfunctions in terms of Laguerre polynomials

$$\zeta_h(x,k,t) = L_n(2kx)\cos(\bar{\omega}_n t),$$

with relevant eigenvalues

$$\bar{\omega}_n = \sqrt{k\,(2n+1)}, \tag{4.3.1}$$

as shown in appendix A.2.

To determine the eigenfunctions and the eigenvalues of the semi-plane beach geometry we seek the solution ζ_h of the homogeneous equation associated to (4.2.9)

$$h\hat{\zeta}_{xx} + h_x\hat{\zeta}_x - k^2 h\,\hat{\zeta} - \hat{\zeta}_{tt} = 0. \tag{4.3.2}$$

By introducing the further transformations

$$\xi = 2kx, \quad \hat{\zeta} = \mathrm{e}^{-\xi/2} Z(\xi,k,t), \tag{4.3.3}$$

expression (4.3.2) becomes

$$4k^2\left[hZ_{\xi\xi} + (h_\xi - h)Z_\xi - \tfrac{1}{2}h_\xi Z\right] - Z_{tt} = 0, \tag{4.3.4}$$

while the boundedness condition at the shoreline (4.2.10) is

$$|Z(0,k,t)| < \infty. \tag{4.3.5}$$

To solve (4.3.4) with the boundary conditions (4.3.5) we shall assume the following separation of variables for $Z(\xi,k,t)$

$$Z = \mathrm{Re}\left\{X(\xi)\mathrm{e}^{-\mathrm{i}\omega t}\right\} \tag{4.3.6}$$

where $X(\xi)$ is the unknown spatial part of the homogeneous solution and ω a complex wave frequency. $\mathrm{Re}\{\}$ denotes the real part and will be omitted for brevity in the following. Note that the complex frequency $\omega = \omega_r + \mathrm{i}\omega_i$ must have a null or negative imaginary part $\omega_i \leq 0$ in order for (4.3.6) not to diverge for large t, i.e. $\omega \in \Omega$, where

$$\Omega = \{\omega \in \mathbb{C} : -\pi \leq \arg\omega \leq 0\} \tag{4.3.7}$$

is the lower complex half plane, real axis included. With the substitution dictated by (4.3.6), expression (4.3.4) can be finally rewritten as

$$hX_{\xi\xi} + (h_\xi - h)X_\xi - \left(\frac{h_\xi}{2} - \frac{\omega^2}{4k^2}\right) X = 0, \tag{4.3.8}$$

while the boundary condition (4.3.5) becomes simply

$$|X(0,k)| < \infty. \tag{4.3.9}$$

Equation (4.3.8) is to be solved separately in the two fields; the two solutions obtained will be matched afterwards at the common boundary to assure continuity of pressure and fluxes.

4.3.1 The near field

In the near field $h = x$ or, in terms of the transformed variables (4.3.3),

$$h = \frac{\xi}{2k}.$$

By using the latter expression, the homogeneous form of the governing equation (4.3.8) becomes

$$\xi X_{\xi\xi} + (1 - \xi)\, X_\xi - \alpha X = 0, \tag{4.3.10}$$

where

$$\alpha = \alpha(k,\omega) = \frac{1}{2} - \frac{\omega^2}{2k}, \tag{4.3.11}$$

and the boundedness condition at the shoreline is still $|X(0)| < \infty$. Expression (4.3.10) is the Kummer equation of parameter α, whose general solution is a linear combination of the Kummer functions of first and second kind, respectively M and U (see appendix A), i.e.

$$X(\xi,k) = AM(\xi,\alpha) + BU(\xi,\alpha),$$

where A and B are integration constants. Since the Kummer function of second kind has a logarithmic singularity at the origin, application of the boundedness condition at the shoreline (4.3.9) requires $B = 0$, i.e.

$$X(\xi,k) = AM(\xi,\alpha), \quad \xi < 2kb. \tag{4.3.12}$$

Hence the homogeneous solution of (4.3.4) is simply

$$Z(\xi,k,t) = X(\xi,k)\mathrm{e}^{-\mathrm{i}\omega t} = AM(\xi,\alpha)\mathrm{e}^{-\mathrm{i}\omega t}, \quad \xi < 2kb,$$

and, in terms of the original variables (4.3.3),

$$\hat{\zeta}_h(x,k,t) = A\mathrm{e}^{-kx}M(2kx,\alpha)\mathrm{e}^{-\mathrm{i}\omega t}, \quad x < b. \tag{4.3.13}$$

4.3.2 The far field

In the far field $h = b$. By using the latter expression, the homogeneous form of the governing equation (4.3.8) becomes

$$X_{\xi\xi} - X_\xi + \frac{\omega^2}{4bk^2} X = 0. \tag{4.3.14}$$

This is also a linear ordinary differential equation of the second order, whose general solution is

$$X(\xi, k) = C\mathrm{e}^{(1-\beta)\xi/2} + D\mathrm{e}^{(1+\beta)\xi/2} \tag{4.3.15}$$

with C and D integration constants and

$$\beta = \beta(k, \omega) = \sqrt{1 - \frac{\omega^2}{bk^2}} = \frac{1}{k\sqrt{b}} \left(k\sqrt{b} - \omega\right)^{1/2} \left(k\sqrt{b} + \omega\right)^{1/2} \tag{4.3.16}$$

a complex parameter. The solution of the homogeneous equation (4.3.4) is then obtained by substituting the spatial component X (4.3.15) into the general form (4.3.6), i.e.

$$Z(\xi, k, t) = X(\xi, k)\mathrm{e}^{-\mathrm{i}\omega t} = C\mathrm{e}^{(1-\beta)\xi/2}\mathrm{e}^{-\mathrm{i}\omega t} + D\mathrm{e}^{(1+\beta)\xi/2}\mathrm{e}^{-\mathrm{i}\omega t}, \quad \xi > 2kb,$$

and, back to the original variables via (4.3.3)

$$\hat{\zeta}_h(x, k, t) = C\mathrm{e}^{-\beta kx - \mathrm{i}\omega t} + D\mathrm{e}^{\beta kx - \mathrm{i}\omega t}, \quad x > b, \tag{4.3.17}$$

Note that the complex parameter β (4.3.16) is given by the product of two square roots of complex variable. Now, it is a trivial fact that the square root of a positive real number t has two values, $\pm\sqrt{t}$. We wonder if this property still holds for complex numbers and, in case, how multivaluedness can be avoided.

Let us first consider the complex function

$$f(z) = \sqrt{z}, \quad z \in \mathbb{C}.$$

The complex number z can be rewritten in its polar form as

$$z = r\mathrm{e}^{\mathrm{i}(2n\pi + \theta)}$$

where r is the magnitude, θ the phase angle and $n = 0, 1, 2, \ldots$ a positive integer. Substituting the latter expression into $f(z)$ we get then

$$f = \begin{cases} r^{1/2}\mathrm{e}^{\mathrm{i}\theta/2} & \text{if } n \text{ is even} \\ -r^{1/2}\mathrm{e}^{\mathrm{i}\theta/2} & \text{if } n \text{ is odd} \end{cases}. \tag{4.3.18}$$

To investigate this fundamental property, consider a point on the complex plane $z = r\mathrm{e}^{\mathrm{i}\theta}$, where $f = \sqrt{r}\mathrm{e}^{\mathrm{i}\theta/2}$. Then make a complete loop around $z_0 = 0$ and stop again at z. In so doing, z returns to the initial value but θ has increased by 2π. As a result $f(z) = \sqrt{r}\mathrm{e}^{\mathrm{i}(\pi+\theta/2)} = -\sqrt{r}\mathrm{e}^{\mathrm{i}\theta/2}$, i.e. f is double-valued. The same happens if we trace several loops around the point $z_0 = 0$ and return to z: the complex function f (4.3.18) changes its sign from positive to negative and vice-versa at each loop. Generally, if a function $f(z)$ does not return to its initial value when tracing a complete loop around a given point z_0 in the complex plane z, then z_0 is called a *branch point* for $f(z)$. In

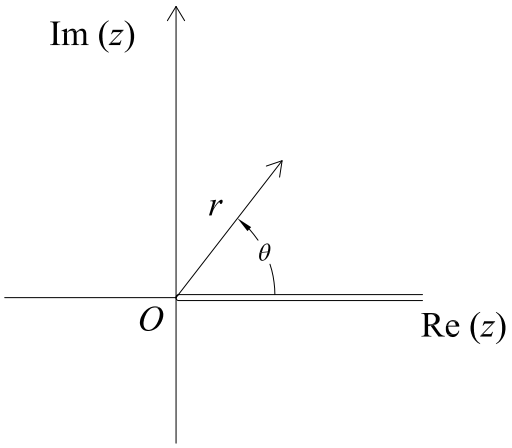

FIGURE 4.2: Branch point at the origin and branch cut along the positive real axis for $f(z) = \sqrt{z}$, where $z = re^{i\theta}$. To avoid multi-valuedness of f, crossing of the cut is not allowed.

our case the origin $z_0 = 0$ is a branch point for the function $f(z) = \sqrt{z}$. Analogously, let now $\zeta = 1/z$, so that $f(z) = \zeta^{-1/2}$; it is straightforward to show that f has another branch point at $\zeta = 0$, i.e. $z = \infty$. To avoid multivaluedness, first cut the z plane along any line connecting the branch points, then do not permit crossing of this line. This geometric construction on the complex plane is called a *branch cut*. As an example, for

$$f(z) = \sqrt{z} = r^{1/2} e^{i(n\pi + \theta/2)}$$

we can set the branch cut along the positive real axis joining 0 to ∞, as shown in figure 4.2, thus getting two separate regions. On the first region $\theta \in (0, 2\pi]$ and $f = \sqrt{r} e^{i\theta/2}$, while on the second region $\theta \in (2\pi, 4\pi]$ and $f = -\sqrt{r} e^{i\theta/2}$. Each region where z is single-valued is called a *branch*; each of the branches can be figured as a sheet of paper joined to the others along the branch cut, thus forming a 3D structure called *Riemann surface* (see Mei, 1997, for examples). For the complex square root $f(z) = \sqrt{z}$, the Riemann surface defined by the branch cut of figure 4.2 is a twin-sheet structure and f (4.3.18) is single-valued on each of the two sheets (branches) introduced above.

Let us now go back to the complex parameter β, expression (4.3.16). Note that β has two branch points in the complex domain Ω (4.3.7), respectively at $\omega = \mp k\sqrt{b}$, i.e. the zeros of the square roots. With the same procedure as above, we introduce two semi-infinite branch cuts along the real axis of Ω, as shown in figure 4.3 (see Mei, 1997, for a similar example). To evaluate β correctly on the different edges of the cuts of figure 4.3, let us define

$$\omega + k\sqrt{b} = r_1 e^{i\theta_1} , \quad k\sqrt{b} - \omega = r_2 e^{i(\theta_2 - \pi)}, \tag{4.3.19}$$

where the phase angles $\theta_{1,2}$ are measured counterclockwise from the positive real axis. To avoid multivaluedness of the square roots in (4.3.16), let us first consider the Riemann sheet defined by

$$\theta_1 \in [-\pi, \pi] , \quad \theta_2 \in [0, 2\pi] . \tag{4.3.20}$$

Then restrict the range of variation of $\theta_{1,2}$ (4.3.20) by requiring $\omega \in \Omega$ (unshaded region of figure 4.3, including the real axis), so that

$$\theta_1 \in \{\pi\} \cap [-\pi, 0] , \quad \theta_2 \in \{0\} \cap [\pi, 2\pi] . \tag{4.3.21}$$

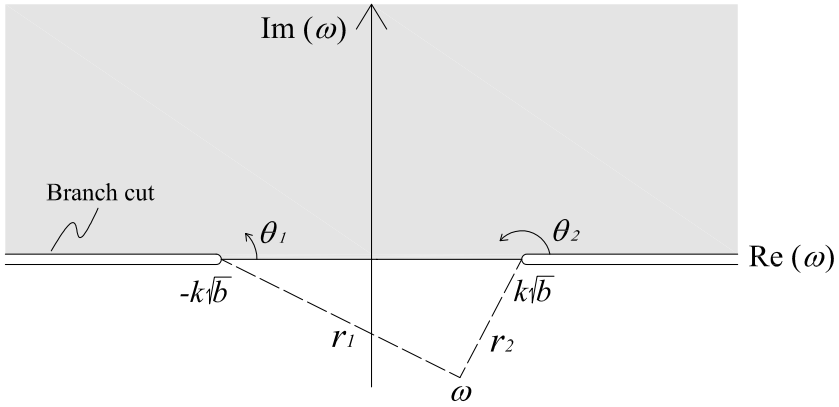

FIGURE 4.3: Branch cuts in the complex plane for $\beta(k,\omega)$ (4.3.16). The complex frequency $\omega \in \Omega$ (4.3.7), which is the unshaded area corresponding to the lower half-plane, real axis included. Angles θ_1 and θ_2 are measured counterclockwise from the real axis on the chosen Riemann sheet (4.3.21).

Note that, according to (4.3.21), $\theta_1 = \pi$ $(-\pi)$ describes the upper (lower) edge of the left-hand cut on the negative real axis, while $\theta_2 = 0$ (2π) describes the upper (lower) edge of the right-hand cut on the positive real axis. Substituting (4.3.19) into (4.3.16), we obtain for the complex parameter β

$$\beta = \sqrt{\frac{r_1 r_2}{bk^2}}\, \mathrm{e}^{\mathrm{i}(\theta_1+\theta_2-\pi)/2}. \tag{4.3.22}$$

Now, if the frequency ω is anywhere along the upper edge of the right-hand cut, $\theta_1 = 0$ and $\theta_2 = 0$, so that

$$\beta = \sqrt{\frac{r_1 r_2}{bk^2}}\, (-\mathrm{i}) = -\mathrm{i}\,|\beta|$$

is imaginary with negative sign. On the other hand, if ω is on the lower edge of the right-hand cut, $\theta_1 = 0$ and $\theta_2 = 2\pi$, so that

$$\beta = \sqrt{\frac{r_1 r_2}{bk^2}}\mathrm{i} = \mathrm{i}\,|\beta|$$

is imaginary with positive sign. Therefore $\mathrm{Im}\{\beta\}$ (4.3.16) has the same absolute value, but opposite signs along the two edges of the right-hand cut. A similar analysis can be done also for the left-hand cut, where $\beta = \pm\mathrm{i}\,|\beta|$ respectively on the upper and lower edge of the cut. In all these cases the corresponding free-surface elevation in the far field (4.3.17) is an oscillating function of the offshore coordinate x. Finally, if ω is on the real axis between $-k\sqrt{b} < \omega < k\sqrt{b}$, then $\theta_1 = 0$ and $\theta_2 = \pi$ so that (4.3.22) gives

$$\beta = \frac{\sqrt{r_1 r_2}}{k\sqrt{b}},$$

i.e. a positive real number. As a consequence, the second term of the far-field solution (4.3.17) would grow without boundaries as $x \to \infty$ unless $D = 0$. With this position the homogeneous solution in the far field (4.3.17) becomes

$$\hat{\zeta}_h(x,k,t) = C\mathrm{e}^{-\beta k x - \mathrm{i}\omega t}, \quad x > b, \tag{4.3.23}$$

while the relevant spatial component (4.3.15) reduces to

$$X(\xi) = C\mathrm{e}^{(1-\beta)\xi/2}, \quad \xi > 2kb. \tag{4.3.24}$$

4.3.3 Matching

The solutions of the homogeneous equation (4.3.2) in the near field and in the far field, (4.3.13) and (4.3.23) respectively, must now be matched at the common boundary $x = b$. Continuity of the free-surface elevation ζ and the fluxes $\partial\zeta/\partial x$ yields respectively

$$\begin{aligned} Ae^{-kb}M(2kb,\alpha) &= Ce^{-\beta kb} \\ A\mathrm{e}^{-kb}\left[-kM(2kb,\alpha) + M_x(2kb,\alpha)\right] &= -C\beta k\mathrm{e}^{-\beta kb}, \end{aligned} \tag{4.3.25}$$

This homogeneous system with unknowns A and C admits a non-trivial solution $(A, C) \neq (0, 0)$ if and only if

$$\Delta(k,\omega) = M_x(2kb,\alpha) + k\,(\beta - 1)\,M(2kb,\alpha) = 0, \tag{4.3.26}$$

where $\Delta \in \mathbb{C}$, $k > 0$ is a real parameter and $\alpha(\omega)$ and $\beta(\omega)$ are given by (4.3.11) and (4.3.16) respectively.

Expression (4.3.26) represents the eigenvalue condition of the matching system (4.3.25); the complex values ω_n for which (4.3.26) is satisfied are the sought eigenvalues. Before solving (4.3.26) numerically, we shall investigate some properties of $\Delta(k, \omega)$. Note that Δ depends linearly on β; hence the branch cuts of figure 4.3 introduced for β also apply to Δ. Now, when ω is anywhere along the real axis, the parameter α (4.3.11) is always real; then the Kummer function $M(2kb, \alpha)$ and its derivative $M_x(2kb, \alpha)$ in (4.3.26) are also real, since they are power series of real arguments (see §A). However β (4.3.16) can be either positive real or positive (or negative) imaginary, according to which segment of the real axis ω is on, as already discussed. If ω is along the real axis on the upper edge of the right-hand cut (see figure 4.3), $\beta = -\mathrm{i}\,|\beta|$ so that from (4.3.26) we obtain

$$\mathrm{Re}\,\{\Delta(k,\omega)\} = M_x(2kb,\alpha) - kM(2kb,\alpha)$$

and

$$\mathrm{Im}\,\{\Delta(k,\omega)\} = -k\,|\beta|\,M(2kb,\alpha).$$

On the other hand, if ω is on the lower edge of the right-hand cut, $\beta = \mathrm{i}\,|\beta|$, so that $\mathrm{Re}\,\{\Delta\}$ does not change, but

$$\mathrm{Im}\,\{\Delta(k,\omega)\} = k\,|\beta|\,M(2kb,\alpha).$$

Therefore $\mathrm{Im}\,\{\Delta\}$ has the same absolute value, but opposite signs along the two edges of the right-hand cut. A similar analysis can be done also for the left-hand cut. Finally, if ω lies on the real axis $-k\sqrt{b} < \omega < k\sqrt{b}$, then $\beta = |\beta|$, so that Δ (4.3.26) is real with a null imaginary part. As a consequence, the segment $-k\sqrt{b} < \omega < k\sqrt{b}$ is a zero-level contour for $\mathrm{Im}\,\{\Delta(k, \omega)\}$.

Numerical solution of (4.3.26) shows that for a given value of k, there is an enumerable set of $2 \cdot [N(k, b) + 1]$ real eigenvalues $\pm\omega_0, \pm\omega_1 \cdots \pm\omega_n \cdots \pm\omega_N$ on the chosen Riemann sheet, such that

$$-k\sqrt{b} < -\omega_N < \cdots < -\omega_1 < \omega_0 < 0 < \omega_0 < \omega_1 < \cdots < \omega_N < k\sqrt{b},$$

i.e.

$$\pm\omega_n \in \left(-k\sqrt{b}, k\sqrt{b}\right), \quad n = 0, 1, \ldots, N(k, b)$$

as shown in figure 4.4. When $\omega = \pm\omega_n$, the solution of the system (4.3.25) is straight-

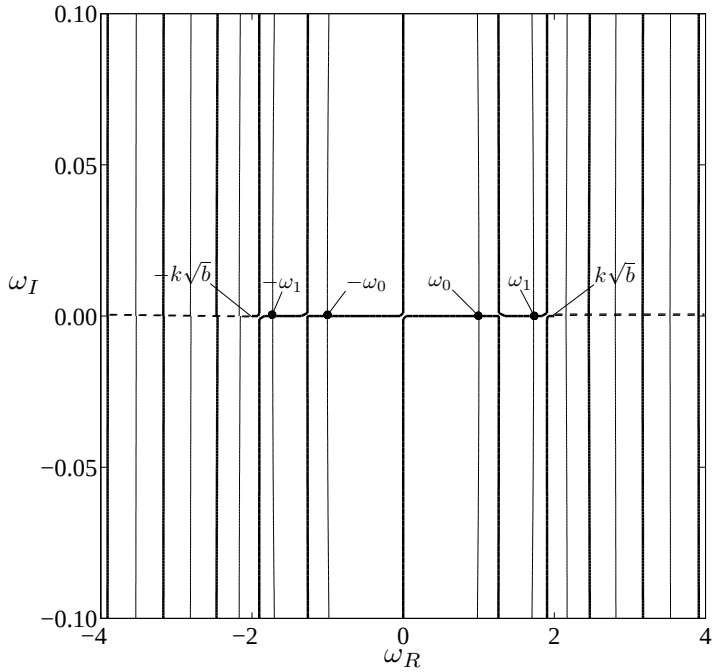

FIGURE 4.4: Contour plots of $\mathrm{Re}\{\Delta\} = 0$ (solid line) and $\mathrm{Im}\{\Delta\} = 0$ (bold line). The bold dashed lines represent the two branch cuts on the real axis for $|\omega| \geq k\sqrt{b}$. The zeros of Δ are the complex roots of (4.3.26) occurring at the intersections of the two contour levels (bold points). Parameters are $k = 1$, $b = 4$, for which a set of four eigenvalues, $\pm\omega_0 = \pm 0.999$ and $\pm\omega_1 = \pm 1.722$ is found.

forward:

$$C = M(2kb, \alpha_n)\mathrm{e}^{(\beta_n - 1)kb},$$

having set the arbitrary parameter $A = 1$.

Now consider the spatial eigenfunctions in the near and far field given respectively by (4.3.12) and (4.3.24), with $\omega = \omega_n$:

$$X_n(\xi) = \begin{cases} M(\xi, \alpha_n) & \text{if } \xi < 2kb \\ M(2kb, \alpha_n)\mathrm{e}^{(1-\beta_n)(\xi/2 - kb)} & \text{if } \xi \geq 2kb \end{cases}, \tag{4.3.27}$$

with $n = 0, 1, \ldots, N(k, b)$, where

$$M(\xi, \alpha_n) = \sum_{m=0}^{\infty} a_{nm}(\omega)\xi^m, \tag{4.3.28}$$

and

$$a_{nm} = \frac{(\alpha_n)_m}{(m!)^2},$$

being $(\alpha_n)_m = \alpha_n(\alpha_n + 1)(\alpha_n + 2)\ldots(\alpha_n + m - 1)$ (see appendix A). Finally, in (4.3.27)

$$\alpha_n = \alpha(\omega_n) = \frac{1}{2} - \frac{\omega_n^2}{2k}, \tag{4.3.29}$$

$$\beta_n = \beta(\omega_n) = \sqrt{1 - \frac{\omega_n^2}{bk^2}}\,. \tag{4.3.30}$$

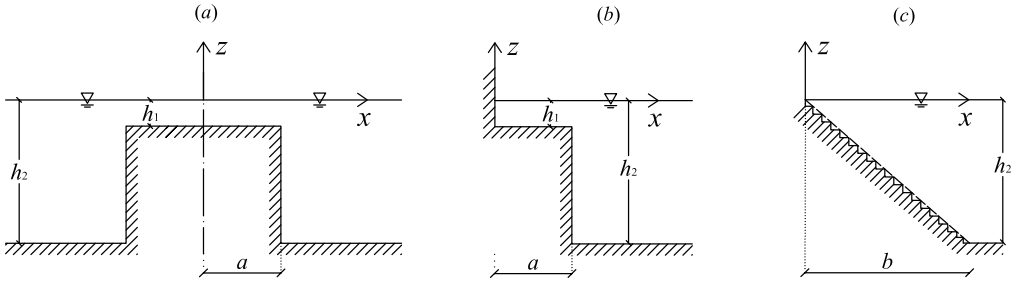

FIGURE 4.5: Geometries for different problems of wave propagation from shallow to deep water. (a) Stepped ridge and (b) shelf lying on a continental platform studied by Mei et al. (2005); (c) construction of a semi-plane beach by the superposition of small shelves.

and again $\xi = 2kx$. Note that for a given modal order n, both the real eigenvalues $\pm\omega_n$ correspond to the same real parameters α_n (4.3.29) and β_n (4.3.30), i.e. both $\pm\omega_n$ are relevant to the same spatial eigenfunction (4.3.27). Therefore, to ensure uniqueness of the solution we retain only the eigenmodes (4.3.27) associated to the positive eigenvalues $\omega_n \in \left(0, k\sqrt{b}\right)$. Recurring back to (4.3.3) and (4.3.6), the solution of the homogeneous equation (4.3.8) can be written as the linear superposition of all the $(N+1)$ modes for a given parameter k

$$\hat{\zeta}_h(x,k,t) = \sum_{n=0}^{N(k)} \mathrm{e}^{-kx} X_n(2kx) \mathrm{e}^{-\mathrm{i}\omega_n t}, \tag{4.3.31}$$

where the X_ns are given by (4.3.27).

To investigate the physical nature of the perturbation described by (4.3.31), let us consider the spatial part

$$\hat{\eta}_n(x,k,t) = \mathrm{e}^{-kx} X_n(2kx) \tag{4.3.32}$$

of the n-th modal component of the free-surface elevation $\hat{\zeta}_h(x,k,t)$. Using (4.3.27) to express the eigenfunctions X_n, (4.3.32) becomes

$$\hat{\eta}_n(x,k,t) = M(2kx,\alpha_n)\mathrm{e}^{-kx} \tag{4.3.33}$$

in the near field $x < b$ and

$$\hat{\eta}_n(x,k,t) = M(2kb,\alpha_n)\mathrm{e}^{-kb(1-\beta_n)}\mathrm{e}^{-\beta_n kx}, \tag{4.3.34}$$

in the far field $x \geq b$. Since the eigenvalues ω_n are all real and positive, with $\omega_n < k\sqrt{b}$, the parameter β_n (4.3.30) is a positive real number too. As a consequence, all the spatial components $\hat{\eta}_n$ of the free-surface elevation, proportional to $\mathrm{e}^{-\beta_n kx}$ in the far field (see 4.3.34), decay exponentially while moving in the offshore direction at large distance from the shore. Hence all the natural eigenmodes of the semi-plane beach are trapped along the shoreline and no wave propagates to infinity, even if the presence of the flat-bottom region would suggest a propagating nature of the perturbation.

This somehow unexpected fact, i.e. that waves existing at a slope discontinuity are unable to propagate to deep water, has been pointed out first by Longuet-Higgins (1967) and then further investigated by Mei et al. (2005). As an example, Mei et al. (2005) studied the trapping of waves by a stepped ridge with two edges at a distance $2a$ apart, as shown in figure 4.5(a). The water depth is h_2 above the ridge and $h_1 > h_2$ over the continental platform away from it. By solving the long-wave equation in each field separately and matching pressures and fluxes at the common boundaries $x = \pm a$,

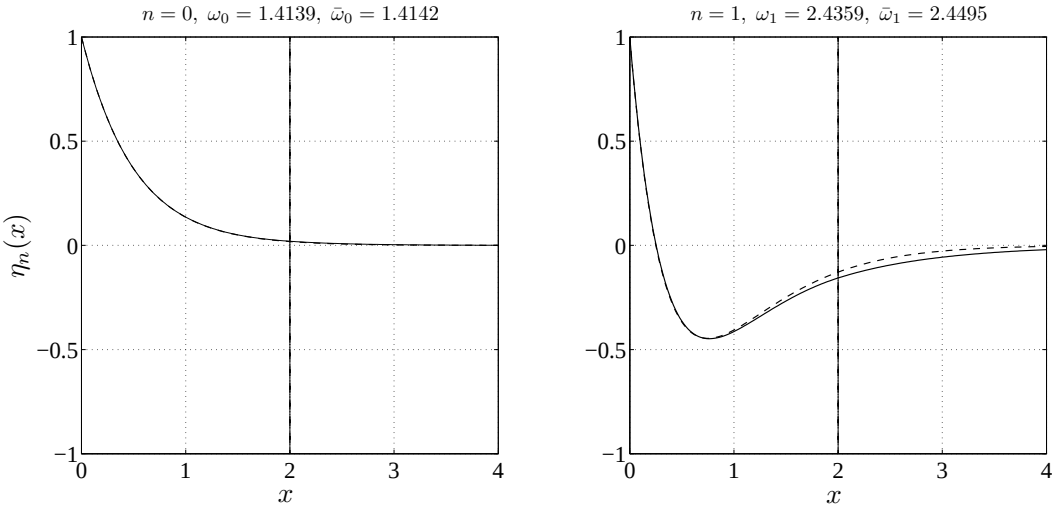

FIGURE 4.6: Profiles of the first two modes of the trapped waves on a semi-plane beach (solid line –) and on a plane beach (dashed line - -) in non-dimensional variables. Parameters are $k = 2$, $b = 2$. The vertical dash-dotted line (-·) indicates the beginning of the continental platform at $x = b$. In each of the subplots the modal order n, the relevant eigenfrequency ω_n and the corresponding eigenfrequency of the plane-beach model $\bar{\omega}_n$ are shown. Note that the eigenmodes of the semi-plane beach decay slower than those of the plane beach in the offshore direction.

Mei et al. (2005) showed the eigenmodes of the system to be proportional to $\mathrm{e}^{\pm\lambda_n(x\pm a)}$ respectively for $x < -a$ (left of the shelf) and $x > a$ (right of the shelf); the parameters λ_n are the roots of the matching system described above. Analytical investigation showed that there is no solution corresponding to imaginary λ_n: no propagation along x is possible and all the eigenmodes are trapped on the ridge. As pointed out by Mei et al. (2005), the even modes over the ridge can be also regarded as the trapped modes on a shelf lying upon a continental platform, with $x = 0$ being the coastline, as depicted in figure 4.5(b). Again, for this system no propagation to infinity can occur. Therefore, one can imagine the semi-plane beach as made by a superposition of a large number of infinitesimal shelves, as shown in figure 4.5(c), all of them trapping a small amount of energy and preventing the perturbation from propagating away in the far field.

The profiles of the first modes $\hat{\eta}_n$ (4.3.32) of the semi-plane beach are plotted along the offshore direction x with solid lines in figure 4.6, for given wavenumber k and beach non-dimensional horizontal depth b. Furthermore, in the same figure 4.6 the dashed lines show the edge-wave modes corresponding to the same modal orders, but relevant to an indefinite plane beach , i.e. $b = \infty$. First, note that when ω_n is small, the eigenmodes of the plane-beach resemble very closely those of the indefinite plane beach with same order n. On the other hand, differences occur for higher eigenfrequencies. In the semi-plane beach, waves of larger ω_n travel larger distances along the x direction than their plane-beach counterparts, before attenuating exponentially far from the shoreline. Physically, all the eigenmodes are trapped by the beach-continental shelf system, and no propagation to infinity occurs. However, wave trapping is more effective for longer waves than for shorter waves. In conclusion, the semi-plane beach acts as a perfect barrier whose trapping power is maximised for low eigenfrequencies.

4.4 Orthogonality of natural modes

It is a well-known result that the spatial eigenfunctions of the plane beach problem, namely the Laguerre polynomials L_n, are orthogonal with respect to the weighting function $\mathrm{e}^{-\xi}$ (see Abramowitz and Stegun, 1972), i.e.

$$\int_0^\infty \mathrm{e}^{-\xi} L_n(\xi)\, L_m(\xi)\, \mathrm{d}\xi = \delta_{nm}.$$

In this subsection we wonder if a similar property still holds for the spatial eigenfunctions X_n (4.3.27) of the semi-plane beach problem. To perform this investigation, recall that the X_ns are the independent solutions of (4.3.8), in other words they satisfy

$$hX_{n,\xi\xi} + (h_\xi - h)X_{n,\xi} + \left(\frac{\omega_n^2}{4k^2} - \tfrac{1}{2}h_\xi\right) X_n = 0, \tag{4.4.1}$$

with ω_n the system eigenvalues solving (4.3.26). Now, every 2^{nd}-order differential equation of the general form

$$a(\xi)X_{\xi\xi} + b(\xi)X_\xi + [\lambda\, c(\xi) - d(\xi)]\, X = 0 \tag{4.4.2}$$

can be reduced to its corresponding Sturm-Liouville form

$$[s(\xi)X_\xi]_\xi + [\lambda\rho(\xi) - q(\xi)]\, X = 0, \tag{4.4.3}$$

provided

$$s(\xi) = \mathrm{e}^{\int^\xi \frac{b(u)}{a(u)}\,\mathrm{d}u}, \quad \rho(\xi) = s(\xi)\frac{c(\xi)}{a(\xi)}, \quad q(\xi) = s(\xi)\frac{d(\xi)}{a(\xi)}.$$

In the present case the variable coefficients of (4.4.1) are respectively

$$a = h(\xi), \quad b = h_\xi - h, , \quad c = 1, \quad d = \tfrac{1}{2}h_\xi, \quad \lambda = \frac{\omega_n^2}{4k^2},$$

such that

$$s(\xi) = h\mathrm{e}^{-\xi}, \quad \rho(\xi) = \mathrm{e}^{-\xi}, \quad q(\xi) = \tfrac{1}{2}h_\xi \mathrm{e}^{-\xi}$$

and (4.4.1) can be rewritten in the Sturm-Liouville form (4.4.3) as

$$\left[h(\xi)\mathrm{e}^{-\xi}X_{n,\xi}\right]_\xi - \left(\tfrac{1}{2}h_\xi(\xi) - \frac{\omega_n^2}{4k^2}\right)\mathrm{e}^{-\xi}X_n = 0. \tag{4.4.4}$$

Now, let us consider two independent solutions of (4.4.4), X_p and X_q, of eigenvalues ω_p and ω_q respectively, with $p, q \in \mathbb{N}$ and $p \neq q$. If we first write (4.4.4) for X_p and for X_q separately, multiply the first equation by X_q, the second by X_p and then subtract the two of them, we get

$$\left[h\mathrm{e}^{-\xi}X_{p,\xi}\right]_\xi X_q - \left[h\mathrm{e}^{-\xi}X_{q,\xi}\right]_\xi X_p = \left(\frac{\omega_p^2 - \omega_q^2}{4k^2}\right)\mathrm{e}^{-\xi}X_pX_q.$$

The latter expression can be further simplified by using the differential form

$$\frac{\mathrm{d}}{\mathrm{d}\xi}\left[h\mathrm{e}^{-\xi}\left(X_qX_{p,\xi} - X_pX_{q,\xi}\right)\right] = \left(\frac{\omega_p^2 - \omega_q^2}{4k^2}\right)\mathrm{e}^{-\xi}X_pX_q. \tag{4.4.5}$$

Integrating (4.4.5) in all the fluid domain $\xi \in (0, \infty)$ yields

$$\frac{\omega_p^2 - \omega_q^2}{4k^2} \int_0^\infty \mathrm{e}^{-\xi} X_p X_q \, \mathrm{d}\xi = \int_0^\infty \frac{\mathrm{d}}{\mathrm{d}\xi} \left[h \mathrm{e}^{-\xi} \left(X_q X_{p,\xi} - X_p X_{q,\xi} \right) \right]. \tag{4.4.6}$$

To solve the latter integral, express the bottom depth h (4.2.5) at the right-hand side in terms of the transformed variable ξ (4.3.3):

$$h(\xi) = \begin{cases} \frac{\xi}{2k} & \text{if } \xi < 2kb \\ b & \text{if } \xi \geq 2kb \end{cases}.$$

Note that h is a continuous function of ξ; also, continuity of the free-surface elevation and of the fluxes (4.3.26) determines $X(\xi)$ and $X_\xi(\xi)$ to be continuous over the entire domain $\xi \in (0, \infty)$. As a result, the integrands at both sides of (4.4.6) are continuous functions of ξ. Solving the integral at the right-hand side of (4.4.6) gives then

$$\frac{\omega_p^2 - \omega_q^2}{4k^2} \int_0^\infty \mathrm{e}^{-\xi} X_p X_q \, \mathrm{d}\xi = \left| h(\xi) \mathrm{e}^{-\xi} \left(X_q X_{p,\xi} - X_p X_{q,\xi} \right) \right|_0^\infty = 0, \tag{4.4.7}$$

since $h(0) = 0$ and by virtue of (4.3.27)

$$\lim_{\xi \to +\infty} h(\xi) \mathrm{e}^{-\xi} \left(X_q X_{p,\xi} - X_p X_{q,\xi} \right) = const \cdot \lim_{\xi \to \infty} \mathrm{e}^{-(\beta_p + \beta_q)\xi/2} = 0.$$

As a consequence, (4.4.7) simply becomes

$$\int_0^\infty \mathrm{e}^{-\xi} X_n(\xi) X_m(\xi) \, \mathrm{d}\xi = 0 \quad \text{if } n \neq m. \tag{4.4.8}$$

Let us now define the square norm of the eigensolutions X_n (4.3.27) as

$$\chi_n^2(k) = \int_0^\infty \mathrm{e}^{-\xi} X_n^2(\xi) \, \mathrm{d}\xi = \int_0^{2kb} \mathrm{e}^{-\xi} M^2(\xi, \alpha_n) \, \mathrm{d}\xi + \frac{\mathrm{e}^{-2kb} M^2(2kb, \alpha_n)}{\beta_n}; \tag{4.4.9}$$

hence coupling (4.4.8) and (4.4.9) yields the orthogonality relation satisfied by the spatial eigenfunctions X_n of the governing equation (4.3.8)

$$\int_0^\infty \mathrm{e}^{-\xi} X_n(\xi) X_m(\xi) \, \mathrm{d}\xi = \chi_n^2 \delta_{nm}. \tag{4.4.10}$$

4.5 Wave field

After having investigated the homogeneous problem (4.3.2), we now seek the solution of the forced equation of motion (4.2.9), subject to the boundary condition (4.2.10) and the initial conditions (4.2.11). By using the transformations dictated by (4.3.3), (4.2.9) becomes

$$4k^2 \left[h Z_{\xi\xi} + (h_\xi - h) Z_\xi - \tfrac{1}{2} h_\xi Z \right] - Z_{tt} = -\mathrm{e}^{-\xi/2} \hat{f}_{tt}(\xi/2, k, t). \tag{4.5.1}$$

To solve the latter equation, we shall employ the method of variation of parameters, assuming for $Z(\xi, k, t)$ the following expression

$$Z(\xi, k, t) = \sum_{n=0}^{N(k)} X_n(\xi) T_n(k, t), \tag{4.5.2}$$

where X_n (4.3.27) are the spatial eigenfunctions of the associated homogeneous problem (4.3.8) and T_n are unknown functions to be determined. Following the same procedure as in §3.3, substitute the series expansion (4.5.2) into the governing equation (4.5.1) and exploit the orthogonality property (4.4.10) of the homogeneous eigensolutions X_n, thus getting

$$T_{n,tt} + \omega_n^2 T_n = \frac{1}{\chi_n^2} \int_0^\infty \mathrm{e}^{-\xi} X_n(\xi) \hat{f}_{tt}(\xi/2, k, t) \mathrm{e}^{-\xi/2} \, \mathrm{d}\xi \tag{4.5.3}$$

for the unknown functions T_n. Similarly, the initial conditions (4.2.11) in terms of T_n now become

$$T_n(k, 0) = 0, \quad T_{n,t}(k, 0) = 0. \tag{4.5.4}$$

In (4.5.3) ω_n are still the eigenvalues of the associated homogeneous problem, as discussed in §4.3 , and χ_n (4.4.9) is the square norm of the relevant eigenfunctions (4.3.27); finally $\hat{f}$ is the cosine Fourier transform of the landslide shape function. By making the same algebraic operations as §3.1.1, solution of the Cauchy problem (4.5.3)–(4.5.4) is straightforward:

$$T_n(k, t) = \frac{2k}{\omega_n \chi_n^2} \int_0^\infty \mathrm{e}^{-k\rho} X_n(2k\rho) I_n(\rho, k, t) \, \mathrm{d}\rho, \tag{4.5.5}$$

with $\rho = \xi/2k$ and

$$I_n(\rho, k, t) = \int_0^t \hat{f}_{\tau\tau}(\rho, k, \tau) \sin \omega_n (t - \tau) \, \mathrm{d}\tau \,, \tag{4.5.6}$$

which is the same expression as (3.1.32) for the indefinite plane beach. Again, (4.5.6) can be solved twice by parts to obtain

$$\begin{aligned} I_n(\rho, k, t) &= -\hat{f}_\tau(\rho, k, 0) \sin \omega_n t + \omega_n \hat{f}(\rho, k, t) - \omega_n \hat{f}(\rho, k, 0) \cos \omega_n t + \\ &- \omega_n^2 \int_0^t \hat{f}(\rho, k, \tau) \sin \omega_n (t - \tau) \, \mathrm{d}\tau, \end{aligned} \tag{4.5.7}$$

which can be fully determined only once the landslide shape function f is defined. Finally, inverse transform of (4.5.2) together with the substitutions dictated by (4.3.3) yelds the free-surface elevation

$$\zeta(x, y, t) = \frac{2}{\pi} \int_0^\infty \sum_{n=0}^{N(k)} X_n(2kx) T_n(k, t) \cos ky \, \mathrm{d}k, \tag{4.5.8}$$

where the T_n are given by (4.5.5) and X_n (4.3.27) are the eigenfunctions of the associated homogeneous problem (4.3.4). Further analysis can be done only after the forcing function $f(x, y, t)$ is specified.

4.6 Tsunami generated by a double-Gaussian shaped landslide

In this section we determine the analytical form of the free-surface elevation (4.5.8) generated by a landslide whose shape function is

$$f(x, y, t) = \begin{cases} \exp\left[-(x - x_0 - u_0 t)^2\right] \, s(y) & \text{if } x < b \\ 0 & \text{if } x \geq b \end{cases}, \tag{4.6.1}$$

where

$$s(y) = \mathrm{e}^{-(cy)^2} \tag{4.6.2}$$

is still the lateral spreading function and $c = \sigma/\lambda$ the landslide shape coefficient. Expression (4.6.1) represents a double-Gaussian shaped landslide sliding along the incline with uniform velocity u_0 from the initial position x_0. With the position (4.6.1) f is non-zero only in the near field $x < b$, while in the far field $x \geq b$ the direct influence of the forcing term on the generated perturbation is assumed to be negligible, i.e. $f \simeq 0$. Since the effects of the parameters x_0 and u_0 on the generated wave field have been already investigated in §3.4, in this subsection we shall limit our analysis to the case $x_0 = 0$ and $u_0 = 1$, describing a half-submerged landslide moving with unit horizontal velocity. This assumption simplifies the algebra, yet allowing us to investigate the influence of the beach horizontal length b upon the generated wave field. Substituting (4.6.1) with $x_0 = 0$ and $u_0 = 1$ into (4.5.7), the I_n become

$$I_n = \omega_n \hat{s}(k) \left\{ \left[\omega_n a_n - \mathrm{e}^{-\rho^2} \right] \cos \omega_n t - \left[\frac{2\rho}{\omega_n} \mathrm{e}^{-\rho^2} + \omega_n b_n \right] \sin \omega_n t + \mathrm{e}^{-\rho^2} \right\}, \tag{4.6.3}$$

with $\rho < b$, where

$$\hat{s}(k) = \frac{\sqrt{\pi}}{2c} \mathrm{e}^{-k^2/4c^2}$$

is the cosine Fourier transform of the spreading function $s(y)$ (4.6.2) and

$$a_n = a_n(\rho, k, t) = \frac{\sqrt{\pi}}{2} \mathrm{e}^{-\omega_n^2/4} \operatorname{Im} \left\{ \mathrm{e}^{\mathrm{i}\omega_n \rho} \left[\operatorname{erf}\left(\rho + \mathrm{i}\frac{\omega_n}{2} \right) - \operatorname{erf}\left(\rho - t + \mathrm{i}\frac{\omega_n}{2} \right) \right] \right\}, \tag{4.6.4}$$

while

$$b_n = b_n(\rho, k, t) = \frac{\sqrt{\pi}}{2} \mathrm{e}^{-\omega_n^2/4} \operatorname{Re} \left\{ \mathrm{e}^{\mathrm{i}\omega_n \rho} \left[\operatorname{erf}\left(\rho + \mathrm{i}\frac{\omega_n}{2} \right) - \operatorname{erf}\left(\rho - t + \mathrm{i}\frac{\omega_n}{2} \right) \right] \right\}. \tag{4.6.5}$$

$\operatorname{Re}\{\}$ and $\operatorname{Im}\{\}$ are respectively the real and imaginary part of $\{\}$. Substituting (4.6.3) into T_n (4.5.5) and then the latter into (4.5.8), we finally obtain the analytical form of the free-surface elevation $\zeta(x, y, t)$.

Let us now follow the same steps of §3.3 to investigate the physical meaning of (4.5.8). First, define the integral transform $\mathcal{M}^n$ of a given function $u(\rho, k, t)$

$$\mathcal{M}^n[u](k, t) = \frac{2k}{\omega_n \chi_n^2} \int_0^b \mathrm{e}^{-k\rho} M(2k\rho, \alpha_n)\, u(\rho, k, t)\, \mathrm{d}\rho, \tag{4.6.6}$$

where M is still the Kummer function of first kind and α_n is given by (4.3.29). Then, by making use of (4.6.6), rewrite expression (4.5.5) as

$$T_n = \mathcal{M}^n \left[I_n \right].$$

Hence, by simply applying the transform $\mathcal{M}^n$ to (4.5.8), we can formally write again $\zeta = \zeta^o + \zeta^e$, where

$$\zeta^o = \frac{2}{\pi} \int_0^\infty \sum_{n=0}^{N(k)} \mathrm{e}^{-kx} X_n(2kx) \left[A_n \cos \omega_n t + B_n \sin \omega_n t \right] \cos ky \, \mathrm{d}k, \tag{4.6.7}$$

with

$$A_n = A_n(k, t) = \omega_n \hat{s} \mathcal{M}^n \left[\omega_n a_n(\rho, k, t) - \mathrm{e}^{-\rho^2} \right], \tag{4.6.8}$$

$$B_n = B_n(k,t) = -\hat{s}\mathcal{M}^n\left[2\rho \mathrm{e}^{-\rho^2} + \omega_n^2 b_n(\rho,k,t)\right], \tag{4.6.9}$$

and

$$\zeta^e = \frac{2}{\pi}\int_0^\infty \sum_{n=0}^{N(k)} \mathrm{e}^{-kx} X_n(2kx)\,\omega_n \hat{s}\mathcal{M}^n\left[\mathrm{e}^{-(\rho-t)^2}\right]\cos ky\,\mathrm{d}k, \tag{4.6.10}$$

X_n being the eigenfunctions (4.3.27). Now, ζ^o (4.6.7) describes a transient oscillatory motion in time. The coefficients A_n and B_n are formally similar to those already found in §3.3 for the indefinite plane beach, respectively (3.3.9) and (3.3.10). The differences lie in three aspects: (1) the usage of the Kummer transform $\mathcal{M}^n$ instead of the Laguerre one, $\mathcal{L}^n$, (2) the presence of the eigenfunctions X_n instead of the Laguerre polynomials L_n and finally (3) the truncation of the sum to the order $N(k)$.

ζ^e is an evanescent component decaying with time, its expression being similar to the evanescent term (3.3.11) of the indefinite plane beach of section 3. Again, the landslide generates a twofold wave field made up by oscillatory and evanescent components, the latter rapidly vanishing with time. Due to the analytical similarity between the wave field of the semi-plane beach and that of the indefinite plane beach, all the observations already made in §3.3 about the behaviour of the coefficients A_n and B_n and the time of decay of ζ^e can be repeated also for the current system. On the other hand, note that the stationary phase approximation of the free-surface elevation (4.5.8) for large t (see §3.3.2) cannot be performed here. Recall that to apply the method of the stationary phase the analytical expressions of ω_n and their derivatives are needed, while the eigenfrequencies ω_n of the semi-plane beach can be determined only numerically from (4.3.26) and not analytically. In the following we shall focus our attention on the influence of the main system parameter, i.e. the non-dimensional horizontal length of the incline b, on the behaviour of the generated wave field.

4.7 Influence of b

As a first step to investigate the influence of the beach non-dimensional horizontal length $b = b'/\sigma$ on the generated wave field, let us consider the variation of the system eigenvalues ω_n with b. Recall that the ω_n are the positive solutions of the eigenvalue condition (4.3.26), with

$$\omega_n \in \left(0, k\sqrt{b}\right), \quad n = 0,\ldots,N(k,b). \tag{4.7.1}$$

Figure 4.7 shows the behaviour of the first four eigenvalues ω_n, $n = 0,\ldots,3$, versus b for the fixed parameter $k = 1$; the bold line represents the upper limit $k\sqrt{b}$. When b is very small, i.e. the domain (4.7.1) is very narrow, only the first eigenvalue ω_0 exists. Increasing b, ω_0 increases and quickly reaches a limiting value, corresponding numerically to the first eigenvalue of the indefinite plane beach $\bar{\omega}_0(k=1) = 1$ (see 4.3.1), as shown in table 4.1. For larger values of b, the upper limit of the domain (4.7.1) increases as $\sqrt{b}$, thus leaving room for higher-order eigenvalues to appear. As a consequence, the sequence of eigenvalues $\omega_0,\ldots,\omega_N$, $N = 1,2,\ldots$ forms progressively, all the ω_n quickly converging to their relevant indefinite plane-beach values $\bar{\omega}_n$, as shown again in table 4.1. For very large b all the eigenvalues of the semi-plane beach ω_n eventually equate those of the indefinite plane beach $\bar{\omega}_n$ (4.3.1) and $N(k,b)$ grows to infinity, i.e.

$$\omega_n \to \bar{\omega}_n = \sqrt{k(2n+1)} \quad \text{and} \quad N(k,b) \to \infty. \tag{4.7.2}$$

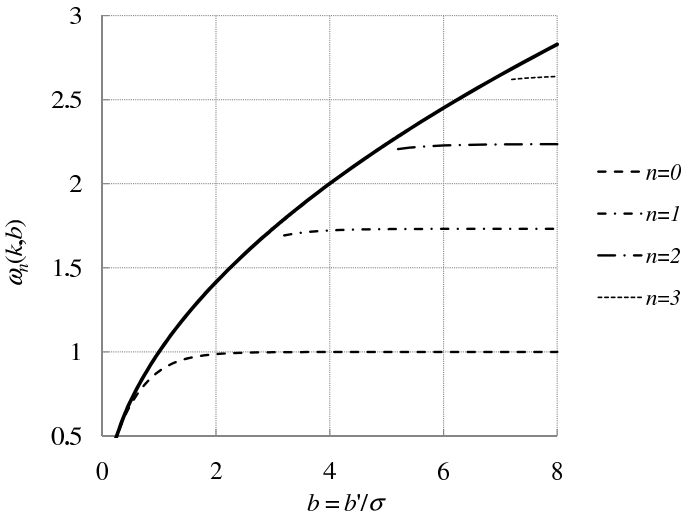

FIGURE 4.7: Behaviour of the first eigenvalues ω_n, $n = 0, 1, 2, 3$, versus b for $k = 1$. The bold line represents the upper limit $\omega = k\sqrt{b}$ of the domain (4.7.1). Note that $\omega_n \to \bar{\omega}_n$, expression (4.3.1), as $b \to \infty$.

b	ω_0	ω_1	ω_2	ω_3
1	0.885627780			
2	0.987173095			
3	0.998465306			
4	0.999804966	**1.7**22438019		
5	0.999974516	**1.73**0317688		
6	0.999996626	**1.73**1740172	**2.2**27485105	
7	0.999999550	**1.73**1996273	**2.23**4185862	
8	0.999999939	**1.7320**41454	**2.23**5660036	**2.6**37757193
...	...	...	...	...
∞	1.000000000	1.732050808	2.236067977	2.645751311

TABLE 4.1: Values of the first four eigenvalues ω_n, $n = 0, 1, 2, 3$, obtained by solving numerically (4.3.26) via the Newton-Raphson method (see Dahlquist and Björck, 2008, for further reference); $k = 1$. In the last row the theoretical eigenvalues $\bar{\omega}_n = \sqrt{2n+1}$ obtained in the limit $b \to \infty$ are reported for comparison. Digits common in ω_n and $\bar{\omega}_n$ are shown with bold characters.

Now, in the limit $b \to \infty$ the parameter α_n becomes

$$\alpha_n = \frac{1}{2} - \frac{\omega_n^2}{2k} \to -n, \quad n = 0, 1, \dots$$

and the relevant Kummer function $M(\xi, \alpha_n)$ (4.3.28) of the first kind and order n transforms into the Laguerre polynomial $L_n(\xi)$, i.e.

$$M(\xi, \alpha_n) \to M(\xi, -n) = L_n(\xi)$$

as shown in appendix A.2. As a consequence, for $b \to \infty$, the eigenfunctions (4.3.27) are given by

$$X_n(\xi) \to M(\xi, -n) = L_n(\xi), \quad \xi \in (0, \infty)$$

while the distinction between the near field and the far field becomes meaningless, since the geometry is that of an indefinite plane beach. Finally, note that the square norm of the eigenfunctions (4.4.9) becomes

$$\chi_n^2(k) \to \int_0^\infty \mathrm{e}^{-\xi} L_n^2(\xi)\, \mathrm{d}\xi = 1$$

as $b \to \infty$, so that (4.6.6) can be rewritten as

$$\mathcal{M}^n\left[u\right](k,t) \to \frac{2k}{\bar{\omega}_n} \int_0^\infty \mathrm{e}^{-k\rho} L_n(2k\rho)\, u(\rho, k, t)\, \mathrm{d}\rho = \mathcal{L}^n\left[u\right](k,t),$$

where $\mathcal{L}^n$ is the Laguerre integral transform (3.3.7). As a consequence, the asymptotic forms of the oscillatory and the evanescent components of the free-surface elevation, expressions (4.6.7) and (4.6.10), are respectively

$$\zeta^o(x,y,t) \to \frac{2}{\pi} \sum_{n=0}^{\infty} \int_0^\infty \mathrm{e}^{-kx} L_n(2kx) \left[A_n \cos\omega_n t + B_n \sin\omega_n t\right] \cos ky\, \mathrm{d}k \tag{4.7.3}$$

and

$$\zeta^e(x,y,t) \to \frac{2}{\pi} \sum_{n=0}^{\infty} \int_0^\infty \mathrm{e}^{-kx} L_n(2kx)\, \omega_n \hat{s} \mathcal{L}^n \left[\mathrm{e}^{-(\rho-t)^2}\right] \cos ky\, \mathrm{d}k, \tag{4.7.4}$$

as $b \to \infty$, where the A_ns and B_ns are still given by (4.6.8) and (4.6.9) respectively, replacing ω_n with $\bar{\omega}_n$ and $\mathcal{M}^n$ with $\mathcal{L}^n$. Now note that the asymptotic forms of the free-surface components ζ^o (4.7.3) and ζ^e (4.7.4) coincide with the analogous expressions of the indefinite plane beach, (3.3.8) and (3.3.11) respectively, provided $x_0 = 0$ and $u_0 = 1$. Therefore, in the limit $b \to \infty$, the semi-plane beach model perfectly agrees with the indefinite plane beach model.

In the following we investigate the influence of $b = b'/\sigma$ on the generated wave field by analysing the tsunami propagating along a semi-plane beach, either for small $b = O(1)$ and large $b > O(1)$ and comparing the results to those obtained for the indefinite plane beach of §3.

4.7.1 Behaviour for small b

If $b = O(1)$, then $b' \simeq \sigma$, i.e. the characteristic length of the landslide is comparable to the horizontal length of the incline. As an example, this situation can occur for unstable rock faces falling into the ocean. To analyse the wave field propagating in such

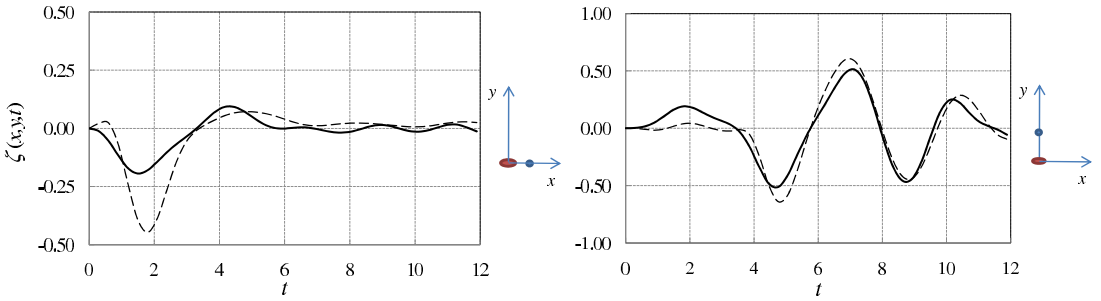

FIGURE 4.8: Time series of the free-surface elevation at points: (a): $(x, y) = (0.148, 0)$, corresponding to $(x', y') = (0.4, 0)$ m, and (b): $(x, y) = (0, 0.296)$, corresponding to $(x', y') = (0, 0.8)$ m. Landslide parameters are those of §3.3.3. Solid lines (–) represent the time series for the semi-plane beach of horizontal length $b = 1$, while dashed lines (- -) are relevant to the indefinite plane beach model.

a geometry, let us consider the same landslide of §3.3.3, with parameters $\sigma = 0.37\,\mathrm{m}$, $c = \sigma/\lambda = 2$, $x_0 = 0$, $u_0 = 1$, sliding along an incline of slope $s = 1/3$ and take $b' = \sigma$, i.e. $b = b'/\sigma = 1$ as a limit case. The solid lines (–) of figure 4.8(a, b) show the time series of the free-surface elevation $\zeta(x, y, t)$, expression (4.5.8), at points respectively $(x, y) = (0.148, 0)$, corresponding to $(x', y') = (0.4, 0)$ m offshore, and $(x, y) = (0, 0.296)$, corresponding to $(x', y') = (0, 0.8)$ m on the shoreline, evaluated via the Gauss-Laguerre numerical method described in §B. In the same figure 4.8(a, b), the time series of the-free surface elevation obtained at the same points, but for an indefinite plane beach, are reported with dashed lines (- -) for comparison. First, note that the maximum runup and drawdown of the generated wave field are larger for the indefinite plane beach than the semiplane beach, i.e. the wave field generated in the semi-plane beach is less energetic. This happens since for small b only the very first eigenmodes are excited and concur to generate the propagating wave field. Physically, having required the forcing function f, expression (4.6.1), to annihilate in the far field, determines the landslide mass to disappear suddenly as it reaches the boundary $x = b$. The reduced time of interaction between landslide and water for small b is therefore responsible of a strong decrease in the amount of the total energy yielded by the landslide to the water, especially in the offshore direction (see figure 4.8a). This determines the amplitude reduction of the generated waves in the semi-plane beach. However this does not imply loss of physical meaning for this case: the landslide accumulates and stops at the toe of the slope.

4.7.2 Behaviour for large b

Now let $b >> 1$, or in physical variables $b' >> \sigma$, i.e. the characteristic length of the slide is small if compared to the horizontal length of the incline. Physically, this situation represents a landslide involving only a small part of the beach. As an example, here we consider the same slide of the previous subsection, but increase the non-dimensional horizontal length of the incline to the value $b = 10$. In figure 4.9(a, b) are represented the time series of the free-surface elevation in non-dimensional variables both for the semi-plane beach (solid line, –) and the indefinite beach (dashed line, - -) at points $(x, y) = (0.148, 0)$, corresponding to $(x', y') = (0.4, 0)$ m, and $(x, y) = (0, 0.296)$, corresponding to $(x', y') = (0, 0.8)$ m respectively. Note that for $b = 10$ the semi-plane beach and the indefinite beach models agree almost completely, i.e. the influence of the flat

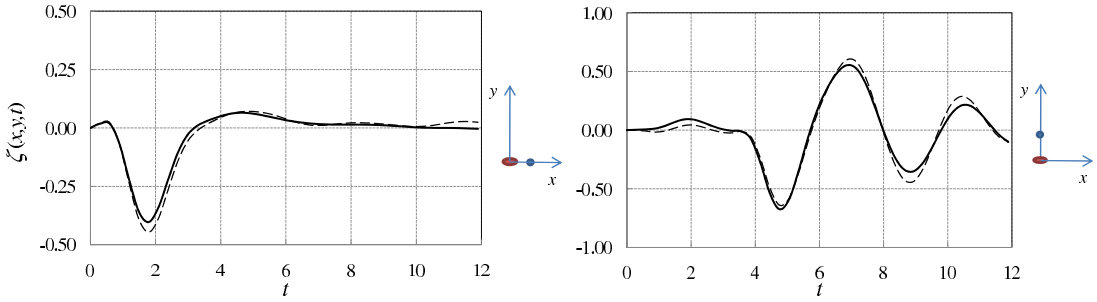

FIGURE 4.9: Time series of the free-surface elevation at points: (a): $(x, y) = (0.148, 0)$, corresponding to $(x', y') = (0.4, 0)$ m, and (b): $(x, y) = (0, 0.296)$, corresponding to $(x', y') = (0, 0.8)$ m. Landslide parameters are those of §3.3.3. Solid lines (–) represent the time series for the semi-plane beach of horizontal length $b = 10$, while solid lines (–) are relevant to the indefinite plane-beach model. Note that for $b \gg 1$ the two models converge to the same results.

bottom on the generated wave field is negligible. In such cases, application of the plane beach model is preferable, due to its easiness in calculations and to the availability of a closed form for the free-surface elevation at large times, obtained via the method of the stationary phase (see §3.3.2).

4.8 Experimental comparison

Experimental data available for comparison are still those of Di Risio et al. (2009a), already discussed in §3.5. In the wave tank employed by Di Risio et al. (2009a), 5.40 m long by 10.80 m wide, the horizontal length of the incline, slope 1/3, is $b' = 3.25$ m. Since the characteristic length of the slide is still $\sigma = 0.37$ m, the non-dimensional horizontal length of the beach is $b = b'/\sigma \simeq 9$, i.e. $b \gg 1$. As pointed out in the previous subsection, when b is large the influence of the flat bottom on the generated wave field is negligible, and the indefinite plane beach model can be applied with excellent accuracy and less computational effort. This justifies the employment of the plane beach model of §3.5 for the experimental comparison with the available data of Di Risio et al. (2009a).

Chapter 5

Landslide tsunamis propagating around a conical island

The occurrence of some destructive events, such as the landslide tsunami of the Stromboli island (2002, Italy, South Mediterranean Sea) has recently renewed the interest in studying tsunamis propagating around islands (see Tinti et al., 2005). In the literature, the first known event of coastal inundation by tsunamis is dated back to 1620BC, referring to the eruption of the Thera volcano in the eastern Mediterranean (see Bruins et al., 2008). Several similar tsunamis occurred through the centuries, like the devastating Krakatau island tsunami of 1883 (see Bruins et al., 2008) or the more recent Hokkaido island tsunami of 1993 (see Liu et al., 1995). Among these, the 1992 Flores island tsunami is of great interest, mostly because of the unexpectedly large runup reached in the lee side of the Babi island (Yeh et al., 1994; Bardet et al., 2003). Such recurring events led several authors to investigate on the scattering of incident long waves by circular islands (see Lautenbacher, 1970; Smith and Sprinks, 1975; Zhang and Zhu, 1994; Fujima et al., 1995; Kanoglu and Synolakis, 1998; Mei et al., 2005; Synolakis et al., 2008). Lautenbacher (1970) analysed the refractive influence of the bottom topography on tsunami runup around a conical island. He did not solve analytically the the long-wave equation of motion, but transformed it into an integral form, which he eventually solved numerically. With this methodology, Lautenbacher (1970) showed that island runup can exceed runup of mono-dimensional plane beaches if the tsunami wavelength λ is comparable to the island diameter L, i.e. $\lambda/L \simeq 1$. Later on, Zhang and Zhu (1994) studied the propagation of water waves over variable depths in a circular geometry and found a so-called "new" solution to the problem. They presented a transformation of the original equation and then provided a power series solution. Nevertheless, the governing equation of motion studied by Zhang and Zhu (1994) is known as a confluent form of the Heun's equation and had already been investigated long time ago (see Heun, 1899). Then Fujima et al. (1995) described the characteristics of long-wave trapping around a conical island. They also solved the governing equation via the Frobenius power series expansion, but using a different and more complex transformation than that employed by Zhang and Zhu (1994). Finally Kanoglu and Synolakis (1998) developed an original analytical solution for long-wave runup around a conical island. Knowing the existing solution of the linear shallow-water wave equation for a cylinder over a flat bottom, Kanoglu and Synolakis (1998) were able to construct a conical island from sills. Then solved the long-wave equation for each of the sills separately, in terms of Bessel functions. Finally they obtained the complete solution

by matching the free-surface elevation and the fluxes at the geometrical discontinuities of the piecewise island. The methodology produced good comparison with laboratory data of Liu et al. (1995) in terms of time histories of free-surface elevation and maximum runup distribution around the island. Again, neither Fujima et al. (1995) nor Kanoglu and Synolakis (1998) recognised the governing equation to be a confluent form of the Heun equation (Heun, 1899). However, note that either Zhang and Zhu (1994), Fujima et al. (1995) and Kanoglu and Synolakis (1998) started their investigations before Slavyanov (1995) had formally developed and tuned the theory of confluent Heun equations. Several analytical studies of landslide generated tsunamis along a plane beach are also available in the literature, from the seminal work of Tuck and Hwang (1972), who first analysed and solved the one-dimensional forced long-wave equation, to the new one-dimensional model introduced by Liu et al. (2003).

On the other hand, the analysis of tsunamis directly generated on the coast of a round island and propagating around and from it has not been fully developed. Tinti and Vannini (1995) worked out an analytical model of long waves propagating around a circular island lying over a flat bottom and enclosed in a large but finite ocean basin. The perturbation was induced by a bottom displacement occurring in the proximities of the island itself. A null free-surface elevation condition was imposed at the basin boundary, i.e. they assumed that the perturbation should decay at a finite distance from the island. As a consequence of this somewhat arbitrary assumption, Tinti and Vannini (1995) observed the occurrence of a local system of rotating edge waves, persisting long time after their generation. Indeed their results differ from those found earlier by Longuet-Higgins (1967), Meyer (1971) and Summerfield (1971): long waves propagating about a round island can't be perfectly trapped. In the following we will show this fundamental result via the asymptotic analysis of the governing equation of motion.

5.1 Trapping power of a conical island

Let us consider the long-wave equation

$$g\nabla \cdot (h\nabla\zeta) = \frac{\partial^2\zeta}{\partial t^2}\,, \tag{5.1.1}$$

where g is the acceleration due to gravity, ∇ is the nabla operator in polar coordinates (r,θ), t time, ζ the free-surface elevation and $h = h(r)$ the water depth, to be specified further on. Now assume the free-surface elevation to be of the form $\zeta(r,\theta,t) = \eta(r)\mathrm{e}^{\mathrm{i}(n\theta-\omega t)}$, being i the imaginary unit and $n \in \mathbb{N}$; $\omega > 0$ is a given wave frequency. Physically, this form represents a wave propagating around the island, with a generic shape $\eta(r)$ in the radial direction to be determined. Under these assumptions the long-wave equation (5.1.1) can be written in the Sturm-Liouville form (see Mei et al., 2005)

$$\frac{\partial}{\partial r}\left(hr\frac{\partial\eta}{\partial r}\right) + \left(\frac{\omega^2}{g} - \frac{n^2 h}{r^2}\right) r\eta = 0. \tag{5.1.2}$$

After differentiating and grouping terms of the same order, (5.1.2) simplifies to

$$\frac{\mathrm{d}^2\eta}{\mathrm{d}r^2} + p(r)\frac{\mathrm{d}\eta}{\mathrm{d}r} + q(r)\eta = 0, \tag{5.1.3}$$

where

$$p(r) = \frac{1}{r} + \frac{1}{h}\frac{\mathrm{d}h}{\mathrm{d}r} \tag{5.1.4}$$

and

$$q(r) = \frac{\omega^2}{gh} - \frac{n^2}{r^2}. \tag{5.1.5}$$

Expression (5.1.3) is an ordinary differential equation of the second order with variable coefficients. Now, if the coefficients $p(r)$ (5.1.4) and $q(r)$ (5.1.5) were constant instead, the most general solution of (5.1.3) would be an exponential of complex argument. Therefore it is reasonable to assume

$$\eta(r) = \mathrm{e}^{S(r)} \tag{5.1.6}$$

as a solution of (5.1.3), with $S(r)$ an unknown phase function to be found. Substituting the latter into (5.1.3), we obtain

$$\frac{d^2S}{dr^2} + \left(\frac{dS}{dr}\right)^2 + p(r)\frac{dS}{dr} + q(r) = 0, \tag{5.1.7}$$

whose solution is not straightforward yet. However, (5.1.7) undergoes a strong simplification if we assume

$$\left|\frac{\mathrm{d}^2S}{\mathrm{d}r^2}\right| < \left|\frac{\mathrm{d}S}{\mathrm{d}r}\right|^2, \tag{5.1.8}$$

which needs to be confirmed at the end of our calculations. Under this simplifying assumption, (5.1.7) becomes a quadratic equation for $\mathrm{d}S/\mathrm{d}r$, whose solution is simply

$$\frac{\mathrm{d}S}{\mathrm{d}r} = \frac{-p(r) \pm \sqrt{p^2(r) - 4q(r)}}{2}. \tag{5.1.9}$$

Now, assuming the water depth to vary smoothly with r and to be finite at infinity, i.e. $h \to h_\infty < \infty$, yields $\mathrm{d}h/\mathrm{d}r \to 0$ as $r \to \infty$, so that $p(r) \to 0$ and (5.1.9) becomes

$$\frac{\mathrm{d}S}{\mathrm{d}r} \simeq \pm\sqrt{-q(r)} \tag{5.1.10}$$

for large r. Integrating the latter equation and substituting the result into (5.1.6), we finally obtain the leading behaviour of the radial component of the free-surface elevation at large distance from the shoreline

$$\eta(r) \simeq \mathrm{e}^{\pm\int^r \sqrt{-q(\rho)}\,\mathrm{d}\rho}, \tag{5.1.11}$$

where the signs $\pm$ take into account both the two independent solutions of the second-order equation (5.1.3). Now, the square root inside the integral of (5.1.11) is a purely imaginary number if $q(r) > 0$ or a positive real number if $q(r) < 0$. Hence, recalling expression (5.1.5), $\eta(r)$ will be oscillatory ($q > 0$) or exponential ($q < 0$) following

$$\frac{\omega^2}{gn^2} \gtrless \frac{h}{r^2}, \quad \begin{matrix}\text{oscillatory} \\ \text{exponential}\end{matrix}, \tag{5.1.12}$$

which are the same conditions obtained by Mei et al. (2005). Now, assuming the water depth at infinity to be finite yields

$$q(r) \simeq \frac{\omega^2}{gh_\infty} > 0$$

for large r, so that (5.1.11) becomes

$$\eta(r) \simeq \mathrm{e}^{\pm \mathrm{i} k_\infty r},$$

where

$$k_\infty = \frac{\omega}{\sqrt{g h_\infty}}$$

is the wavenumber in the far field at large distances from the island. All the radial solutions $\eta(r)$ of the governing equation (5.1.2) exhibit an oscillatory leading behaviour at large distances from the origin, even for small ω (see Longuet-Higgins, 1967; Meyer, 1971; Mei et al., 2005). Incidentally, note also that the initial assumption (5.1.8) is verified, being

$$\left| \frac{\mathrm{d}S}{\mathrm{d}r} \right|^2 \simeq k_\infty^2$$

and

$$\left| \frac{\mathrm{d}^2 S}{\mathrm{d}r^2} \right| \simeq \left| \frac{1}{2\sqrt{-q(r)}} \frac{\mathrm{d}q(r)}{\mathrm{d}r} \right| \simeq 0$$

for large r.

We have shown that perfect trapping is not possible in a polar-symmetric topography where $h/r^2 \to 0$ as $r \to \infty$. As an application of the general theory exposed above, Summerfield (1971) studied the free-surface oscillations around a circular vertical island of radius $r = a_1$ with a vertical edge at $r = a_2 > a_1$, lying on a continental shelf. Assuming again the free-surface elevation to be of the form $\zeta(r, \theta, t) = \eta(r)\mathrm{e}^{\mathrm{i}(n\theta - \omega t)}$, he solved the long-wave equation (5.1.1) separately for the two domains $r < a_2$ and $r > a_2$ respectively, in terms of Hankel functions. Then, by matching the two solutions at the common boundary $r = a_2$, he found the existence of a discrete set of complex eigenfrequencies $\omega_{nm} = \xi_{nm} - \mathrm{i}\epsilon_{nm}\,, m \in \mathbb{N}$, for each of the n-th angular modes. These eigenfrequencies are characterized by a negative imaginary part, whose absolute value ϵ_{nm} physically represents the rate of energy loss in time (damping factor). Modes with very small damping factor ϵ_{nm} (for which energy leakage in time is small) were classified qualitatively as "almost trapped" on the shelf; their amplitude was shown to attenuate exponentially while moving towards the ocean. On the other hand, modes with large ϵ_{nm} were defined "leaky", with a profile of a propagating wave to infinity. Regardless of the amount of damping, all the free modes propagate some amount of energy towards infinity. Hence, we infer that the free modes cannot be directly excited by local transient sources such as a landslide, which generates local perturbations, not in the form of radiating waves to infinity. Indeed, the free-modes of an island-shelf system could resonate only if excited by incoming wave trains (or travelling plane impulses, see Summerfield, 1971). This observation has a counterpart with that of Meyer (1971), who noted that edge-wave modes on a sloping beach, due to their exponential decay in the offshore direction, can be excited only by local disturbances and not by waves incident from infinity (unless a nonlinear mechanism of subharmonic resonance is invoked, Guza and Davis, 1974). In conclusion, for landslide-generated tsunamis propagating around a conical island, the free-surface elevation cannot be expressed either as a system of rotating edge waves or in terms of the free modes of oscillation of the island-shelf system.

In §5.2, an analytical two-horizontal-dimension model of landslide tsunamis propagating around a conical island-shelf system is presented, based on the forced linear

long-wave equation. The fluid domain is divided into a near field and a far field according to the discontinuities of the bottom slope. Separation of variables and the Laplace transform methods are employed to obtain the solutions of the governing equations in terms of the free-surface elevation in each field. The two solutions are then matched at the common boundary. An analytical representation of the free-surface elevation is derived in each field, consisting in an integral form of an analytic function (Confluent Heun for the near field and Hankel for the far field), multiplied by amplitude factors depending on the characteristics of the slide. In §5.3, results obtained are shown to agree with the theoretical observations made by Meyer (1971) and summarised in Mei et al. (2005). The existence of a transient leading wave propagating outwards in the far field and decaying as $O(t^{-1/2})$ is also shown. In §5.4 the time series of the free-surface runup generated by a subaerial slide are satisfactorily compared with the available experimental results of Di Risio et al. (2009b). At the sampled points on the shoreline, the first incoming wave generated by the subaerial landslide is an elevation wave, followed by a deep trough, while the highest runup is reached by the second or third wave. This is due to the excitation of imperfect edge-wave like components of the wave motion generated by the landslide. Finally, further investigation demonstrates that tsunamis propagating along a conical island generate smaller runup than those propagating along a plane beach with similar landslide characteristics. This is due to the energy leakage phenomenon always occurring with waves propagating in a round geometry.

5.2 Wave field

Consider a conical island of bottom radius b' lying on an indefinite horizontal continental platform; the island flanks have a uniform slope s (see figure 5.1). Let the primes denote physical dimensional quantities. In the cylindrical reference system (r', θ, z') the r' axis is directed radially, the z' axis rises up from the undisturbed water level and $\theta \in (-\pi, \pi)$ is the angular coordinate, positive counter-clockwise. The origin O' is at the intersection of the undisturbed water level and the island vertical axis. Water is in the region $r' > r'_0$, being r'_0 the radius of the wet contour located in the upper part of the island. Assume that the landslide originates in a neighbourhood of the origin O' and is symmetric with respect to θ.

5.2.1 The governing equations

In the whole fluid domain, consider the forced linear long-wave equation of motion in polar coordinates (r', θ)

$$\zeta'_{t't'} - gh' \left(\frac{1}{r'} \zeta'_{r'} + \zeta'_{r'r'} + \frac{1}{r'^2} \zeta'_{\theta\theta} \right) - gh'_{r'} \zeta'_{r'} = f'_{t't'} \,, \tag{5.2.1}$$

where $\zeta'(r', \theta, t')$ is the free-surface elevation, t' time. Subscripts denote derivation with respect to the relevant variable. In (5.2.1), $h'(r')$ is the overall bottom depth, in the absence of the landslide, measured with respect to the undisturbed water surface $z' = 0$. Hence $h' = s(r' - r'_0)$ if $r'_0 < r' < b'$; $h' = s(b' - r'_0) \equiv h'_b$ if $r' > b'$, with h'_b the water head over the continental shelf. Finally, $f'(r', \theta, t')$ is a time-dependent perturbation of the sea-floor, representing the landslide moving along the flanks of the island (see again figure 5.1). Now let σ and η be respectively the characteristic length and maximum

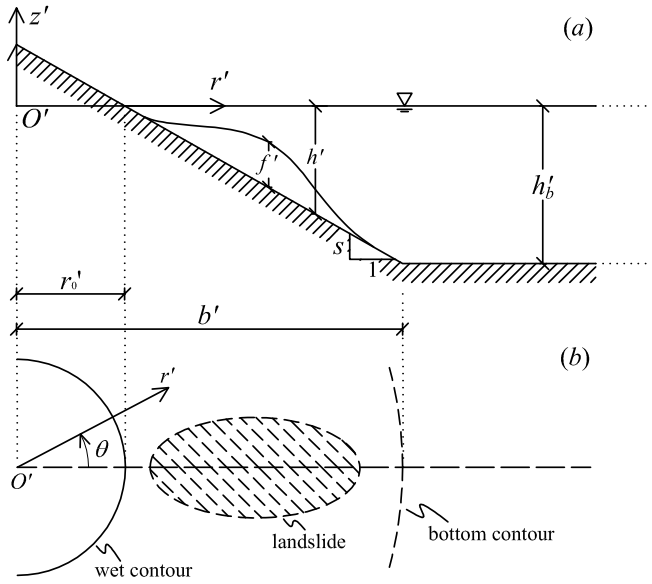

FIGURE 5.1: The fluid domain in physical coordinates. Radial section (a) and plan view (b) of the conical island, the continental platform and the landslide.

vertical thickness of the landslide; then the following non-dimensional variables can be defined:

$$\left\{ \begin{array}{c} r \\ r_0 \\ b \end{array} \right\} = \left\{ \begin{array}{c} r' \\ r_0' \\ b' \end{array} \right\} /\sigma\,, \quad t = \sqrt{\frac{gs}{\sigma}}\, t'\,, \quad \left\{ \begin{array}{c} \zeta \\ f \end{array} \right\} = \left\{ \begin{array}{c} \zeta' \\ f' \end{array} \right\} /\eta\,, \quad h = \frac{h'}{\sigma s}. \tag{5.2.2}$$

The long-wave equation (5.2.1) becomes

$$\zeta_{tt} - h\left(\frac{1}{r}\,\zeta_r + \zeta_{rr} + \frac{1}{r^2}\,\zeta_{\theta\theta}\right) - h_r\,\zeta_r = f_{tt}\,. \tag{5.2.3}$$

Boundedness of the free-surface is required at every time in all the fluid domain: $|\zeta(r,\theta,t)| < \infty$. Zero initial free-surface elevation ζ and velocity ζ_t are also prescribed:

$$\zeta(r,\theta,0) = 0, \quad \zeta_t(r,\theta,0) = 0.$$

To solve the equation of motion (5.2.3) we employ the Laplace transform pair

$$\hat{\zeta}(r,\theta;\omega) = \int_0^\infty \zeta(r,\theta,t)\,\mathrm{e}^{-\omega t}\mathrm{d}t, \quad \zeta(r,\theta,t) = \frac{1}{2\pi\mathrm{i}}\int_{c-\mathrm{i}\infty}^{c+\mathrm{i}\infty} \hat{\zeta}(r,\theta;\omega)\,\mathrm{e}^{\omega t}\mathrm{d}\omega \tag{5.2.4}$$

$\omega = c + \mathrm{i}d$ being the complex non-dimensional transform parameter; $c > 0$ is a real constant, large enough so that the integrals in (5.2.4) exist. Transform of (5.2.3) gives

$$r^2\hat{\zeta}_{rr} + r\left(1 + r\,\frac{h_r}{h}\right)\hat{\zeta}_r - \frac{\omega^2 r^2}{h}\,\hat{\zeta} + \hat{\zeta}_{\theta\theta} = -\frac{r^2}{h}\hat{f}_{tt}\,, \tag{5.2.5}$$

where

$$\hat{f}_{tt} = \int_0^\infty f_{tt}(r,\theta,t)\mathrm{e}^{-\omega t}\mathrm{d}t$$

is the Laplace transform of the forcing term f_{tt} of the governing equation (5.2.3). Referring to the whole fluid domain as sketched in figure 5.1, we shall define the *near field* as the domain where $r_0 < r < b$, and the *far field* the remaining indefinite region $r > b$. The equation of motion (5.2.5) will be solved in each field separately, starting from the near field and then moving to the far field. The two solutions will be matched afterwards at the boundary $r = b$.

5.2.2 Solution of transformed equation

The near field $r_0 < r < b$

In the near field $h = r - r_0$, then (5.2.5) becomes

$$r^2\hat{\zeta}_{rr} + r\left(1 + \frac{r}{r - r_0}\right)\hat{\zeta}_r - \frac{\omega^2 r^2}{r - r_0}\,\hat{\zeta} + \hat{\zeta}_{\theta\theta} = -\frac{r^2}{r - r_0}\hat{f}_{tt}\,, \tag{5.2.6}$$

which is an inhomogeneous second order partial differential equation. To obtain its solution, let us consider the associated homogeneous equation

$$r^2\hat{\zeta}_{rr} + r\left(1 + \frac{r}{r - r_0}\right)\hat{\zeta}_r - \frac{\omega^2 r^2}{r - r_0}\,\hat{\zeta} + \hat{\zeta}_{\theta\theta} = 0. \tag{5.2.7}$$

Separation of variables $\hat{\zeta}(r, \theta; \omega) = R(r; \omega)\Theta(\theta)$ yields $\Theta_n(\theta) = \cos n\theta,\ n = 0, 1, 2, \ldots$ for the angular part Θ, having required Θ to be a periodic function of period 2π and to be symmetric with respect to $\theta = 0$. Back to the homogeneous equation, separation of variables yields the following ordinary differential equation for the radial function $R = R_n(r; \omega)$:

$$R_{n,rr} + \left(\frac{1}{r} + \frac{1}{r - r_0}\right)R_{n,r} + \left[\frac{(\mathrm{i}\omega)^2}{r - r_0} - \frac{n^2}{r^2}\right]R_n = 0, \tag{5.2.8}$$

which is a confluent Heun equation in its natural general form (CHE in the following, see Slavyanov, 1995), r being the independent variable and $(\mathrm{i}\omega)$ a complex parameter. Solution of (5.2.8) can be found by applying the Frobenius method of power series, as shown in section C.1, thus obtaining

$$R_n(r; \mathrm{i}\omega) = \alpha_n Hc_n^{(1)}(r; \mathrm{i}\omega) + \beta_n Hc_n^{(2)}(r; \mathrm{i}\omega)\,,$$

α_n and β_n being the integration constants. $\mathrm{Hc}_n^{(1,2)}$ are the confluent Heun functions of order n of $(1^{\mathrm{st}}, 2^{\mathrm{nd}})$ kind (see section C.1) respectively

$$Hc_n^{(1)}(r; \mathrm{i}\omega) = \sum_{m=0}^{\infty} a_{nm}(\mathrm{i}\omega)\left(1 - \frac{r_0}{r}\right)^m, \tag{5.2.9}$$

and

$$Hc_n^{(2)}(r; \mathrm{i}\omega) = \ln\left(1 - \frac{r_0}{r}\right) Hc_n^{(1)}(r; \mathrm{i}\omega) + \sum_{m=0}^{\infty} b_{nm}(\mathrm{i}\omega)\left(1 - \frac{r_0}{r}\right)^m, \tag{5.2.10}$$

where parametric dependence on the radius r_0 is omitted for brevity. The series coefficients a_{nm} in (5.2.9) and b_{nm} in (5.2.10) are given respectively by

$$a_{nm}(\mathrm{i}\omega) = \frac{1}{m^2}\sum_{k=1}^{m} a_{n,m-k}\left[n^2(k-1) + \frac{\omega^2 r_0}{2}\left(k + k^2\right)\right],$$

and

$$b_{nm}(\mathrm{i}\omega) = \frac{1}{m^2}\sum_{k=1}^{m} b_{n,m-k}\left[n^2(k-1) + \frac{\omega^2 r_0}{2}(k+k^2)\right] - \frac{2}{m}\,a_{nm}\,,$$

with $m = 1, 2, \ldots$, $a_{n0} = 1$ and $b_{n0} = 0$. Since the confluent Heun function of the second kind $Hc_n^{(2)}$ has a logarithmic singularity for $r \to r_0$ (see 5.2.10), boundedness of the free-surface elevation at $r = r_0$ is satisfied only if $\beta_n = 0$. Hence

$$R_n(r;\omega) = \alpha_n Hc_n^{(1)}\,(r;\mathrm{i}\omega)\,. \tag{5.2.11}$$

The solution $\hat{\zeta}_h$ of the homogeneous equation (5.2.7) associated to (5.2.6) is then:

$$\hat{\zeta}_h(r,\theta,t) = \sum_{n=0}^{\infty} \alpha_n R_n(r;\omega)\Theta_n(\theta) = \sum_{n=0}^{\infty} \alpha_n Hc_n^{(1)}\,(r;\mathrm{i}\omega)\cos n\theta. \tag{5.2.12}$$

The method of variation of parameters can now be employed to find the solution $\hat{\zeta}(r,\theta;\omega)$ of the inhomogeneous equation of motion (5.2.6). We assume for $\hat{\zeta}$ the same algebraic expression as $\hat{\zeta}_h$, i.e.

$$\hat{\zeta}(r,\theta;\omega) = \sum_{n=0}^{\infty} G_n(r;\omega)\cos n\theta\,, \tag{5.2.13}$$

with G_n unknown functions. By using the expansion (5.2.13) into the inhomogeneous equation (5.2.6) and employing the orthogonality property

$$\int_{-\pi}^{\pi} \cos m\theta \cos n\theta \mathrm{d}\theta = \frac{2\pi}{\epsilon_n}\,\delta_{nm}\,,$$

ϵ_n being the Jacobi function and δ_{nm} the Kronecker operator, an inhomogeneous ordinary differential equation for $G_n(r;\omega)$ is obtained:

$$G_{n,rr} + \left(\frac{1}{r} + \frac{1}{r-r_0}\right) G_{n,r} + \left[\frac{(\mathrm{i}\omega)^2}{r-r_0} - \frac{n^2}{r^2}\right] G_n = -\frac{1}{r-r_0}\,F_n(r;\omega), \tag{5.2.14}$$

which is the CHE of complex parameter $\mathrm{i}\omega$ (5.2.8), forced by the function

$$F_n(r;\omega) = \frac{\epsilon_n}{2\pi}\int_{-\pi}^{\pi} \hat{f}_{tt}(r,\theta;\omega)\cos n\theta\,\mathrm{d}\theta. \tag{5.2.15}$$

For a translating Gaussian sea-floor movement with initial position of the landslide centroid $r_s = r_s'/\sigma$, the time-dependent perturbation of the sea-floor is

$$f(r,\theta,t) = \exp\left\{-\left[r - r_c(t)\right]^2 - (\gamma\theta)^2\right\}, \tag{5.2.16}$$

where $\gamma = 1/\theta_0$, θ_0 is the characteristic angle subtended by the landslide and $r_c(t) = r_s + t$ the radial coordinate of the centroid, moving at the uniform speed $u = 1$. With reference to figure 5.2, if λ is the characteristic width of the landslide, then

$$\gamma = \frac{1}{\theta_0} = \frac{r_s'}{2\lambda}.$$

The forcing term F_n, expression (5.2.15), can be integrated twice by parts, yielding

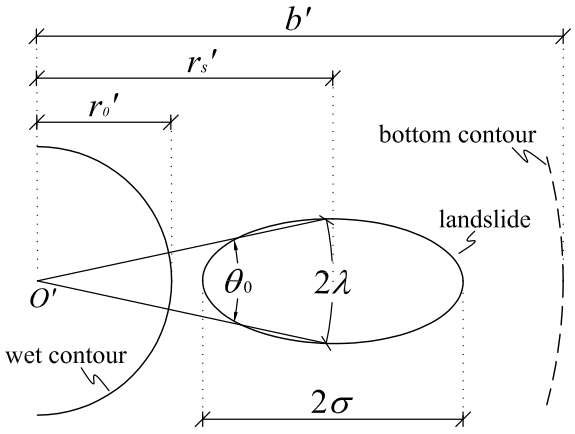

FIGURE 5.2: Landslide specifications. σ and λ are the characteristic dimensions of the slide, while $\theta_0 = 1/\gamma$ is the characteristic angle subtended by the slide with respect to the origin of the reference system.

$$\begin{aligned} F_n(r;\omega) &= \Pi_n \left\{ -\left[2(r-r_s)+\omega\right] \mathrm{e}^{-(r-r_s)^2} + \right. \\ &+ \left. \omega^2 \frac{\sqrt{\pi}}{2} \mathrm{e}^{-\omega(r-r_s)+\omega^2/4} \left[1 + \mathrm{erf}\left(r - r_s - \frac{\omega}{2}\right)\right] \right\}, \end{aligned} \tag{5.2.17}$$

where

$$\Pi_n = \frac{\epsilon_n \mathrm{e}^{-n^2/4\gamma^2}}{4\gamma\sqrt{\pi}} \left[\mathrm{erf}\left(\gamma\pi + \frac{\mathrm{i}n}{2\gamma}\right) + \mathrm{c.c.} \right], \tag{5.2.18}$$

c.c. being the complex conjugate. Π_n is a real amplitude factor dependent on the landslide characteristic angle $1/\gamma$; figure 5.3 shows the fast decay of Π_n for increasing modal order n. The solution of the forced ordinary differential equation (5.2.14), subject to the boundary condition $|G_n(r_0;\omega)| < \infty$, is then

$$G_n(r;\omega) = \alpha_n H c_n^{(1)}(r;\mathrm{i}\omega) - P_n(r;\omega). \tag{5.2.19}$$

In (5.2.19) P_n is the particular solution

$$P_n(r;\omega) = \int_{r_0}^{r} \frac{F_n(\rho;\omega)}{(\rho - r_0)\, W(\rho)} \left[H c_n^{(1)}(\rho;\mathrm{i}\omega) H c_n^{(2)}(r;\mathrm{i}\omega) - H c_n^{(2)}(\rho;\mathrm{i}\omega) H c_n^{(1)}(r;\mathrm{i}\omega) \right] \mathrm{d}\rho. \tag{5.2.20}$$

$$W(r) = \frac{r_0}{r(r-r_0)}$$

is the Wronskian of the two homogeneous solutions $Hc_n^{(1)}(r;\mathrm{i}\omega)$ and $Hc_n^{(2)}(r;\mathrm{i}\omega)$ of the CHE (5.2.8), as shown in section C.2. By substituting (5.2.19) into the series expansion (5.2.13), the complete expression of the free-surface elevation transform in the near field is obtained

$$\hat{\zeta}(r,\theta;\omega) = \sum_{n=0}^{\infty} \left[\alpha_n H c_n^{(1)}(r;\mathrm{i}\omega) - P_n(r;\omega) \right] \cos n\theta. \tag{5.2.21}$$

The integration constants α_n in the above expression are to be determined by applying the matching conditions at the boundary $r = b$.

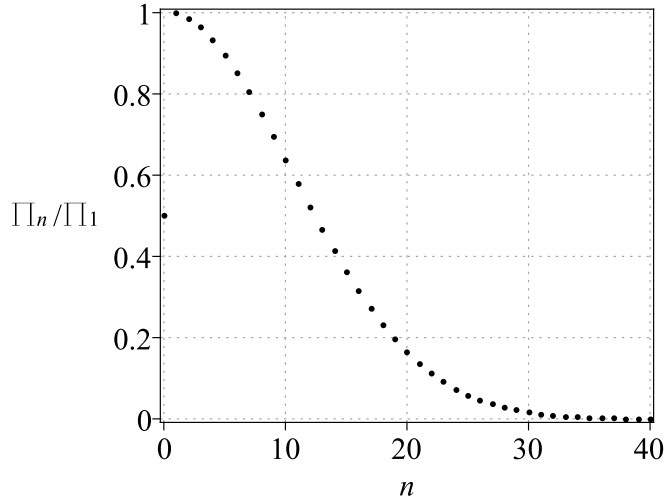

FIGURE 5.3: Behaviour of the ratio Π_n/Π_1 with increasing modal order n. Parameters are: $\sigma = 0.175\,\mathrm{m}$, $\lambda = \sigma/2$, $r_s = 7.43$, $\gamma = 7.43$, modelling the geometry of the conical island of §5.4.

The far field $r > b$

In the far field, the bottom depth is constant everywhere: $h = h_b = b - r_0$, and the direct influence of the forcing term on the behaviour of the fluid is negligible: $f(r, \theta, t) \simeq 0$. Then the governing equation (5.2.5) simplifies into

$$r^2\hat{\zeta}_{rr} + r\hat{\zeta}_r - \frac{\omega^2 r^2}{h_b}\hat{\zeta} + \hat{\zeta}_{\theta\theta} = 0.$$

Separation of variables $\hat{\zeta}(r, \theta; \omega) = R(r; \omega)\Theta(\theta)$ yields the same angular solution as in the near field, $\Theta_n = \cos n\theta$, $n = 0, 1, 2\ldots$ while for the radial part R_n

$$r^2 R_{n,rr} + rR_{n,r} - \left(\frac{\omega^2 r^2}{h_b} + n^2\right) R_n = 0. \tag{5.2.22}$$

With the change of variables $x = kr$, with

$$k = \frac{\omega}{\sqrt{h_b}},$$

(5.2.22) becomes a standard modified Bessel equation,

$$x^2 R_{n,xx} + xR_{n,x} - \left(x^2 + n^2\right) R_n = 0. \tag{5.2.23}$$

The independent solutions of (5.2.23) are the two modified Bessel functions $I_n(x)$ and $K_n(x)$. Then the general solution of the governing equation (5.2.22) is

$$R_n(r; \omega) = \alpha_n I_n\left(\frac{\omega r}{\sqrt{h_b}}\right) + \beta_n K_n\left(\frac{\omega r}{\sqrt{h_b}}\right),$$

which has a branch-cut on the negative real axis of the complex plane ω introduced by K_n. Note that, since $\omega = c + \mathrm{i}d$ has a positive real part c,

$$\arg\left(\frac{\omega r}{\sqrt{h_b}}\right) \in \left(-\frac{\pi}{2}, \frac{\pi}{2}\right).$$

Now, for $|\arg(x)| < \pi/2$ the modified Bessel function of first kind

$$I_n(x) \simeq \frac{\mathrm{e}^x}{\sqrt{2\pi x}}$$

as $|x| \to \infty$. Hence, boundedness of the free-surface elevation as $r \to \infty$ requires $\alpha_n = 0$ and

$$R_n(r;\omega) = \beta_n K_n\left(\frac{\omega r}{\sqrt{h_b}}\right).$$

Finally, the free-surface elevation $\hat{\zeta}$ in the far field is

$$\hat{\zeta}(r,\theta;\omega) = \sum_{n=0}^{\infty} R_n(r,\omega)\,\Theta_n(\theta) = \sum_{n=0}^{\infty} \beta_n\, K_n\left(\frac{\omega r}{\sqrt{h_b}}\right)\cos n\theta, \quad r > b. \tag{5.2.24}$$

The coefficients β_n in the above expression can be obtained by matching (5.2.24) with (5.2.21).

Matching

The near field solution (5.2.21) and the far field solution (5.2.24) are now matched at the common boundary $r = b$. Continuity of the free-surface elevation $\hat{\zeta}$ and the radial fluxes $\hat{\zeta}_r$ yields respectively for each $n = 0, 1, 2, \ldots$

$$\alpha_n H c_n^{(1)}(b;\mathrm{i}\omega) - P_n(b;\omega) = \beta_n K_n\left(\frac{\omega b}{\sqrt{h_b}}\right)$$
$$\alpha_n H c_{n,r}^{(1)}(b;\mathrm{i}\omega) - P_{n,r}(b;\omega) = \beta_n K_{n,r}\left(\frac{\omega b}{\sqrt{h_b}}\right).$$

The solution of the above inhomogeneous linear system is

$$\alpha_n(\omega) = \frac{1}{r_0}\int_{r_0}^{b} F_n(\rho;\omega)\rho\left[H c_n^{(1)}(\rho;\mathrm{i}\omega)\frac{\Delta_n^{(2)}(\omega)}{\Delta_n^{(1)}(\omega)} - H c_n^{(2)}(\rho;\mathrm{i}\omega)\right]\mathrm{d}\rho \tag{5.2.25}$$

$$\beta_n(\omega) = \frac{1}{b\,h_b\Delta_n^{(1)}(\omega)}\int_{r_0}^{b} F_n(\rho;\omega)\rho\, H c_n^{(1)}(\rho;\mathrm{i}\omega)\,\mathrm{d}\rho \tag{5.2.26}$$

where

$$\Delta_n^{(1,2)}(\omega) = -\mathrm{Hc}_n^{(1,2)}(b;\mathrm{i}\omega)\,K_{n,r}\left(\frac{\omega b}{\sqrt{h_b}}\right) + K_n\left(\frac{\omega b}{\sqrt{h_b}}\right)\mathrm{Hc}_{n,r}^{(1,2)}(b;\mathrm{i}\omega). \tag{5.2.27}$$

The free-surface elevation transform in the complex half-plane $|\arg(\omega)| < \pi/2$ is then

$$\hat{\zeta}(r,\theta;\omega) = \sum_{n=0}^{\infty}\left\{\begin{array}{c} \alpha_n H c_n^{(1)}(r;\mathrm{i}\omega) - P_n(r;\omega) \\ \beta_n K_n\left(\frac{\omega r}{\sqrt{h_b}}\right)\end{array}\right\}\cos n\theta \quad \text{if} \left\{\begin{array}{c} r_0 < r < b \\ r > b\end{array}\right\} \tag{5.2.28}$$

for the near field and the far field respectively, with α_n and β_n given by (5.2.25) and (5.2.26) respectively.

5.3 Physical description

Inverse transform of (5.2.28) can be obtained by means of complex analysis. For the sake of clarity we shall first consider the free-surface elevation in the far field $r > b$.

5.3.1 The far field

Inverse transform of (5.2.28) yields

$$\zeta(r,\theta,t) = \frac{1}{2\pi \mathrm{i}} \sum_{n=0}^{\infty} \int_{c-\mathrm{i}\infty}^{c+\mathrm{i}\infty} \beta_n(\omega) K_n\left(\frac{\omega r}{\sqrt{h_b}}\right) \mathrm{e}^{\omega t} \mathrm{d}\omega \, \cos n\theta.$$

Upon substitution of (5.2.26) for β_n, the latter expression becomes

$$\zeta(r,\theta,t) = \sum_{n=0}^{\infty} \frac{1}{2\pi \mathrm{i} b h_b} \int_{r_0}^{b} \rho \int_{c-\mathrm{i}\infty}^{c+\mathrm{i}\infty} f_n(\omega) \mathrm{e}^{\omega t} \mathrm{d}\omega \, \mathrm{d}\rho \, \cos n\theta, \tag{5.3.1}$$

having defined

$$f_n(\omega) = \frac{F_n(\rho;\omega) H c_n^{(1)}(\rho;\mathrm{i}\omega) K_n(\omega r/\sqrt{h_b})}{\Delta_n^{(1)}(\omega)}, \tag{5.3.2}$$

where $\rho \in (r_0, b)$ and $r \in (b, \infty)$ are regarded as parameters, the forcing function F_n is given by (5.2.17) and the denominator $\Delta_n^{(1)}$ by (5.2.27). Now, let us evaluate the inner integral of expression (5.3.1).

For $t < 0$, contour integration in the complex plane and usage of the asymptotic expressions of the confluent Heun functions (5.2.9) and (5.2.10) (see appendix C.3) yield simply

$$\int_{c-\mathrm{i}\infty}^{c+\mathrm{i}\infty} f_n(\omega) \mathrm{e}^{\omega t} \mathrm{d}\omega = 0,$$

as shown in appendix D.1. As a consequence, $\zeta(r,\theta,t) = 0$ for $t < 0$.

For $t > 0$, contour integration in the complex plane gives

$$\int_{c-\mathrm{i}\infty}^{c+\mathrm{i}\infty} f_n(\omega) \mathrm{e}^{\omega t} \mathrm{d}\omega = \mathrm{i} \int_{-\infty}^{+\infty} f_n(\mathrm{i}s) \mathrm{e}^{\mathrm{i}st} \mathrm{d}s \tag{5.3.3}$$

as shown by some lengthy algebra in appendix D.1. Now, substituting the latter result into (5.3.1), writing back the integrand in terms of β_n by using (5.3.2) and (5.2.26), and further transforming $s = -\omega$, yield

$$\zeta(r,\theta,t) = \sum_{n=0}^{\infty} \cos n\theta \frac{1}{2\pi} \int_{-\infty}^{\infty} \beta_n(-\mathrm{i}\omega) K_n\left(\frac{-\mathrm{i}\omega r}{\sqrt{h_b}}\right) \mathrm{e}^{-\mathrm{i}\omega t} \mathrm{d}\omega \tag{5.3.4}$$

for the free-surface elevation in the far field. If now we define

$$z = -\frac{\mathrm{i}\omega r}{\sqrt{h_b}} = \frac{r}{\sqrt{h_b}} (d - \mathrm{i}c),$$

then

$$-\pi < \arg(z) < 0,$$

since $\omega = c + \mathrm{i}d$ and $c > 0$ as defined above. Recalling that

$$K_n(z) = \frac{\pi}{2} \mathrm{i}^{n+1} \mathrm{H}_n(\mathrm{i}z), \quad -\pi < \arg(z) \leq \pi/2$$

where H_n is the Hankel function of first kind and order n, the free-surface elevation (5.3.4) in the far field $r > b$ assumes the form

$$\zeta(r,\theta,t) = \sum_{n=0}^{\infty} \cos n\theta \int_{-\infty}^{\infty} C_n(\omega) \mathrm{H}_n\left(\frac{\omega r}{\sqrt{h_b}}\right) \mathrm{e}^{-\mathrm{i}\omega t} \mathrm{d}\omega, \tag{5.3.5}$$

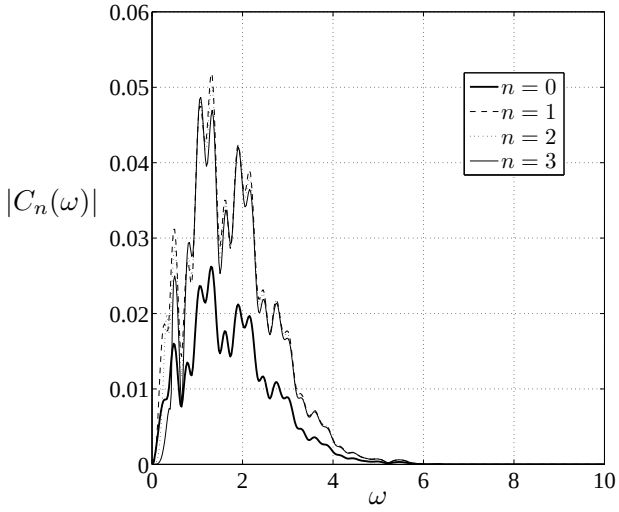

FIGURE 5.4: Plots of $|C_n|$ vs. ω; 25 Gauss points are needed for (5.3.6) to converge. Non-dimensional parameters are: $r_0 = 11.83$, $r_s = \gamma = 7.43$ modelling the conical island of §5.4.

having defined

$$C_n(\omega) = \frac{\mathrm{i}^{n+1}}{4}\beta_n(-\mathrm{i}\omega) = \frac{1}{4bh_b}\frac{i^{\,n+1}}{\Delta_n^{(1)}(-\mathrm{i}\omega)}\int_{r_0}^{b}\rho\, F_n(\rho;-\mathrm{i}\omega)Hc_n^{(1)}(\rho;\omega)\,\mathrm{d}\rho. \qquad (5.3.6)$$

Let us further introduce the symbol $()^*$ to denote the complex conjugate of (). Then from (5.3.6) it is straightforward to show that the integrand of (5.3.5) satisfies the property

$$C_n(-\omega)\mathrm{H}_n\left(\frac{-\omega r}{\sqrt{h_b}}\right)\mathrm{e}^{\mathrm{i}\omega t} = C_n^*(\omega)\mathrm{H}_n^*\left(\frac{\omega r}{\sqrt{h_b}}\right)\left(\mathrm{e}^{-\mathrm{i}\omega t}\right)^*.$$

As a consequence, the free-surface elevation (5.3.5) becomes

$$\zeta(r,\theta,t) = \sum_{n=0}^{\infty}\cos n\theta\int_0^{\infty}C_n(\omega)\mathrm{H}_n\left(\frac{\omega r}{\sqrt{h_b}}\right)\mathrm{e}^{-\mathrm{i}\omega t}\mathrm{d}\omega + \text{c.c.}\,, \qquad (5.3.7)$$

i.e. a real number. Integrals like (5.3.6) on the finite domain (r_0, b) can be conveniently evaluated via the Gauss-Legendre quadrature method (see Press et al., 1986, for details). Numerical evaluation of (5.3.6) shows that the $|C_n(\omega)|$ fast decay with increasing ω, as depicted in figure 5.4; as a result the convergence of the integral (5.3.7) is assured. Now define

$$k = \frac{\omega}{\sqrt{h_b}}$$

the wavenumber in the far field. Then note that each spectral component of the free-surface elevation (5.3.7) is proportional to

$$\mathrm{H}_n(kr)\mathrm{e}^{-\mathrm{i}\omega t},$$

i.e. outgoing in the far field. This result agrees with the general theory of Longuet-Higgins (1967), Meyer (1971) and Summerfield (1971) already discussed in §5.1. Note also that $\zeta(r,\theta,t)$ (5.3.7) is obtained by integrating the frequency response $\mathrm{H}_n(kr)$ to

an incident wavetrain of unit amplitude, multiplied by the forcing factor $C_n(\omega)$. This solution is similar to many other linear-system responses to transient excitations, like for example the harbour response to a transient incident wave (see Mei et al., 2005).

5.3.2 The leading wave

As anticipated in §5.1, the transient landslide-generated disturbance propagating around the island is not perfectly trapped. In this section we investigate on the existence of a leading wave propagating radially at large distances from the coastline, $r \gg 1$. Let us consider the free-surface elevation (5.3.7); to obtain an approximate expression of ζ at large distances from the island, use the asymptotic expansion of the Hankel function for large argument

$$\mathrm{H}_n(x) \simeq \sqrt{\frac{2}{\pi x}}\, \mathrm{e}^{\mathrm{i}(x-\pi n/2-\pi/4)},$$

so that

$$\zeta(r,\theta,t) \simeq \sum_{n=0}^{\infty} \cos n\theta\, \mathrm{e}^{-\mathrm{i}\left(\frac{\pi n}{2}+\frac{\pi}{4}\right)} \int_0^{\infty} C_n(\omega) \sqrt{\frac{2\sqrt{h_b}}{\pi\omega r}} \mathrm{e}^{\mathrm{i}\omega\left(r/\sqrt{h_b}-t\right)}\, \mathrm{d}\omega + \text{c.c.}. \tag{5.3.8}$$

Since the wave front moves at the group celerity

$$C_g = \frac{\mathrm{d}\omega}{\mathrm{d}k} = \sqrt{h_b},$$

its position at a given time is described by $r = \sqrt{h_b}t$. Substitution of the latter relation inside (5.3.8), yields the expression of the leading wave $\zeta_l(\theta,t)$

$$\zeta_l\,(\theta,t) \simeq \sqrt{\frac{2}{\pi t}} \sum_{n=0}^{\infty} \mathcal{A}_n \cos n\theta, \tag{5.3.9}$$

where the real values

$$\mathcal{A}_n = \mathrm{e}^{-\mathrm{i}\left(\frac{\pi n}{2}+\frac{\pi}{4}\right)} \int_0^{\infty} \frac{C_n(\omega)}{\sqrt{\omega}} \mathrm{d}\omega + \text{c.c.} \tag{5.3.10}$$

are modal amplitudes. The latter integral on the infinite domain $(0,\infty)$ can be evaluated by employing the more advanced Gauss-Kronrod iterative method.

Note that the leading wave (5.3.9) decays as $O(t^{-1/2})$ in the three-dimensional geometry of the shelf. Therefore it has the same asymptotic behaviour of the non-dispersive transient waves propagating on a flat bottom, already studied in §2, but it vanishes slower than the evanescent component, $O(t^{-2})$, of the landslide-generated wave field propagating offshore in a plane-beach geometry (see §3.3).

Let us now investigate on the influence of the distinctive parameters of the system, b' (bottom radius) and σ (characteristic length of the slide), upon the characteristics of the leading wave travelling offshore. The amplitude $\mathcal{A}_n$ of the n-th leading wave component (5.3.10) depends on C_n (5.3.6), which in turn is a function of the ratio $b = b'/\sigma$. As shown in figure 5.5, the $\mathcal{A}_n$ fast decay as b increases. Physically, the submerged beach surrounding the island acts as a barrier to trap wave energy: the longer the beach with respect to the slide, the less the energy propagated offshore. We now turn to the analysis of the near field and the free-surface runup.

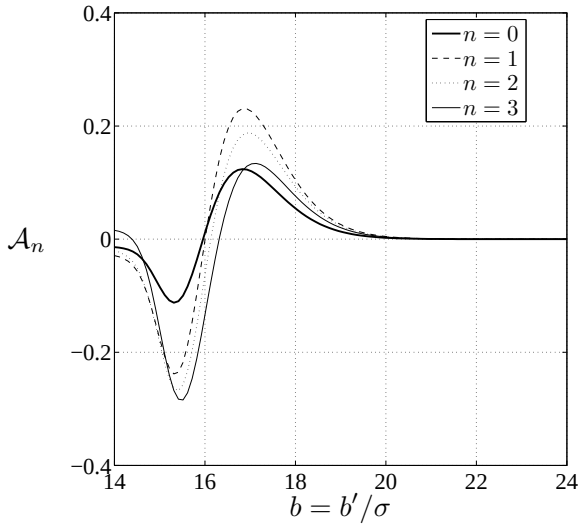

FIGURE 5.5: Plots of $\mathcal{A}_n$ vs. $b = b'/\sigma$, evaluated with the Gauss-Kronrod quadrature method. Non-dimensional parameters are: $r_0 = 11.83$, $r_s = \gamma = 7.43$, modelling the conical island of §5.4. Note that the $\mathcal{A}_n$ fast decay by increasing b.

5.3.3 The near field

In the near field $r < b$ inverse transform of (5.2.28) yields

$$\zeta(r,\theta,t) = \frac{1}{2\pi \mathrm{i}} \sum_{n=0}^{\infty} \int_{c-\mathrm{i}\infty}^{c+\mathrm{i}\infty} \left[\alpha_n(\omega) H c_n^{(1)}(r/r_0; \mathrm{i}\omega) - P_n(r;\omega)\right] \mathrm{e}^{\omega t} \mathrm{d}\omega \, \cos n\theta.$$

By using (5.2.25) for α_n and (5.2.20) for the particular solution P_n, the free-surface elevation can be expressed as

$$\begin{aligned} \zeta(r,\theta,t) &= \frac{1}{2\pi \mathrm{i} r_0} \sum_{n=0}^{\infty} \cos n\theta \left[\int_{r_0}^{b} \rho \int_{c-\mathrm{i}\infty}^{c+\mathrm{i}\infty} f_{1n}(\rho,\omega) \mathrm{e}^{\omega t} \mathrm{d}\omega \, \mathrm{d}\rho + \right. \\ &- \left. \int_{r_0}^{r} \rho \int_{c-\mathrm{i}\infty}^{c+\mathrm{i}\infty} f_{2n}(\rho,\omega) \mathrm{e}^{\omega t} \mathrm{d}\omega \, \mathrm{d}\rho \right]. \end{aligned} \tag{5.3.11}$$

In (5.3.11) the two integrand functions are

$$f_{1n}(\rho,\omega) = F_n(\rho;\omega) \left[H c_n^{(1)}(\rho;\mathrm{i}\omega) \frac{\Delta_n^{(2)}(\omega)}{\Delta_n^{(1)}(\omega)} - H c_n^{(2)}(\rho;\mathrm{i}\omega) \right] H c_n^{(1)}(r;\mathrm{i}\omega) \tag{5.3.12}$$

and

$$\begin{aligned} f_{2n}(\rho,\omega) = F_n(\rho;\omega) \quad & \left[H c_n^{(1)}(\rho;\mathrm{i}\omega) H c_n^{(2)}(r;\mathrm{i}\omega) + \right. \\ & \left. - H c_n^{(2)}(\rho;\mathrm{i}\omega) H c_n^{(1)}(r;\mathrm{i}\omega) \right] \end{aligned} \tag{5.3.13}$$

respectively. In the latter expressions, F_n is the forcing function (5.2.17), while $\Delta_n^{(1,2)}$ are given by (5.2.27). In order to solve (5.3.11), consider the contour integrals

$$\int_{c-\mathrm{i}\infty}^{c+\mathrm{i}\infty} f_{jn}(\rho,\omega) \mathrm{d}\omega, \quad j = 1,2 \tag{5.3.14}$$

and employ again the technique used to get the inverse-transform of ζ in the far field.

For $t < 0$, as shown in appendix D.2, it is straightforward to show

$$\int_{c-\mathrm{i}\infty}^{c+\mathrm{i}\infty} f_{jn}(\rho,\omega)\mathrm{d}\omega = 0, \quad j = 1,2$$

implying $\zeta(r,\theta,t) = 0$.

For $t > 0$ contour integration in the complex plane yields

$$\int_{c-\mathrm{i}\infty}^{c+\mathrm{i}\infty} f_{jn}\mathrm{e}^{\omega t}\mathrm{d}\omega = \mathrm{i}\int_{-\infty}^{+\infty} f_{jn}(\mathrm{i}s)\mathrm{e}^{\mathrm{i}st}\mathrm{d}s, \quad j = 1,2 \tag{5.3.15}$$

as shown in appendix D.2. Substituting (5.3.15) back into (5.3.11) and further transforming $s = -\omega$, we obtain

$$\begin{aligned}\zeta(r,\theta,t) &= \frac{1}{2\pi r_0}\sum_{n=0}^{\infty}\cos n\theta\left[\int_{r_0}^{b}\rho\int_{-\infty}^{\infty} f_{1n}(\rho,-\mathrm{i}\omega)\mathrm{e}^{-\mathrm{i}\omega t}\mathrm{d}\omega\,\mathrm{d}\rho + \right.\\ &- \left.\int_{r_0}^{r}\rho\int_{-\infty}^{\infty} f_{2n}(\rho,-\mathrm{i}\omega)\mathrm{e}^{-\mathrm{i}\omega t}\mathrm{d}\omega\,\mathrm{d}\rho\right].\end{aligned} \tag{5.3.16}$$

By making use of both definitions (5.3.12) and (5.3.13) for the f_{jn}, the free-surface elevation in the near field (5.3.11) can be finally expressed as

$$\zeta(r,\theta,t) = \sum_{n=0}^{\infty}\cos n\theta\int_{0}^{+\infty}\left[A_n(r;\omega)Hc_n^{(1)}(r;\omega) + B_n(r;\omega)Hc_n^{(2)}(r;\omega)\right]\mathrm{e}^{-\mathrm{i}\omega t}\mathrm{d}\omega + \text{c.c.}, \tag{5.3.17}$$

where

$$\begin{aligned}A_n(r;\omega) &= \frac{1}{2\pi r_0}\int_{r_0}^{b}\rho\,F_n(\rho;-\mathrm{i}\omega)\left[Hc_n^{(1)}(\rho;\omega)\frac{\Delta_n^{(2)}(-\mathrm{i}\omega)}{\Delta_n^{(1)}(-\mathrm{i}\omega)} - Hc_n^{(2)}(\rho;\omega)\right] + \\ &+ \frac{1}{2\pi r_0}\int_{r_0}^{r}\rho\,F_n(\rho;-\mathrm{i}\omega)Hc_n^{(2)}(\rho;\omega)\mathrm{d}\rho\end{aligned} \tag{5.3.18}$$

and

$$B_n(r;\omega) = -\frac{1}{2\pi r_0}\int_{r_0}^{r}\rho\,F_n(\rho;-\mathrm{i}\omega)Hc_n^{(1)}(\rho;\omega)\mathrm{d}\rho\,, \tag{5.3.19}$$

being $A_n(r;-\omega) = A_n^*(r;\omega)$ and $B_n(r;-\omega) = B_n^*(r;\omega)$. As shown in figure 5.6, the terms $|A_n|$ and $|B_n|$ are fast-decaying oscillating functions of ω, so that the integral in (5.3.17) is convergent. Finally we need to show that in the limit $r \to b$, the expressions of the free-surface respectively in the near field (5.3.17) and in the far field (5.3.7) coincide. Evaluating the term in the square brackets of (5.3.17) at $r = b$ we obtain

$$\begin{aligned}[\cdot] &= A_n(b;\omega)Hc_n^{(1)}(b;\omega) + B_n(b;\omega)Hc_n^{(2)}(b;\omega)\\ &= \frac{1}{2\pi r_0}\int_{r_0}^{b}\frac{\rho F_n(\rho;-\mathrm{i}\omega)}{\Delta_n^{(1)}(-\mathrm{i}\omega)}Hc_n^{(1)}(\rho;\omega)\,\mathrm{d}\rho\,W(b)K_n\left(\frac{-\mathrm{i}\omega b}{\sqrt{h_b}}\right),\end{aligned} \tag{5.3.20}$$

where

$$W(b) = \frac{r_0}{b - r_0}$$

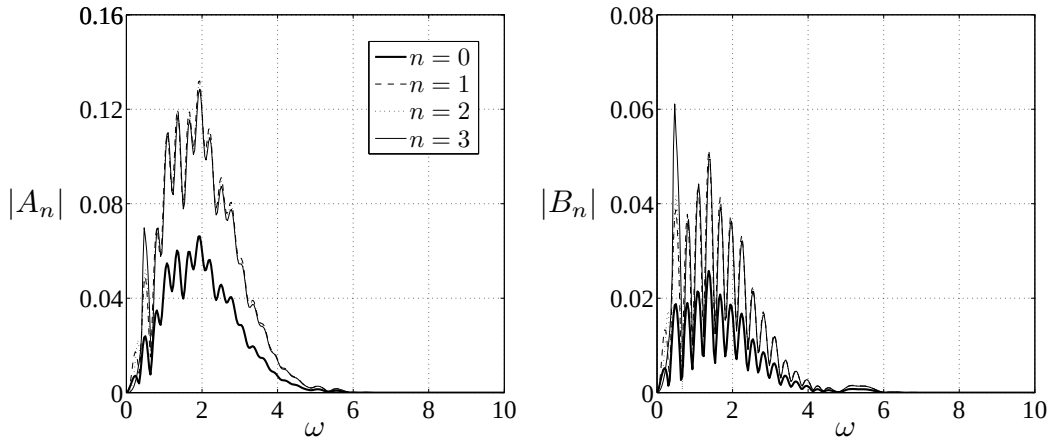

FIGURE 5.6: Plots of (a): $|A_n|$ and $|B_n|$ vs. ω at $r = 15$. Non-dimensional parameters are: $r_0 = 11.83$, $r_s = \gamma = 7.43$, modelling the conical island of §5.4.

is the Wronskian evaluated at $r = b$ and use of (5.3.18) and (5.3.19) respectively for A_n and B_n has been made. Now, recalling that

$$K_n\left(\frac{-\mathrm{i}\omega b}{\sqrt{h_b}}\right) = \frac{\pi}{2}\mathrm{i}^{n+1}H_n\left(\frac{\omega b}{\sqrt{h_b}}\right),$$

(5.3.20) becomes

$$[\cdot] = \frac{1}{4bh_b}\frac{i^{\,n+1}}{\Delta_n^{(1)}(-\mathrm{i}\omega)}\int_{r_0}^{b}\rho\, F_n(\rho;-\mathrm{i}\omega)Hc_n^{(1)}(\rho;\omega)\,\mathrm{d}\rho\; H_n\left(\frac{\omega b}{\sqrt{h_b}}\right) = C_n(\omega)H_n\left(\frac{\omega b}{\sqrt{h_b}}\right), \tag{5.3.21}$$

which is exactly the integrand of the free-surface elevation in the far field (5.3.7) evaluated at $r = b$. Therefore the near-field expression (5.3.17) coincides with the far-field one (5.3.7) if both are evaluated at $r = b$, so that the matching is verified.

The solution (5.3.17) in the near field is a transient propagating wave. It is obtained by summing over the positive real frequency spectrum the two independent solutions $Hc_n^{(1)}$ and $Hc_n^{(2)}$ of the governing equation (5.2.8), multiplied by the forcing factors A_n and B_n respectively. The free-surface elevation in the far field (5.3.7) and in the near field (5.3.17) can be evaluated by solving numerically the relevant integral expressions over the infinite domain $\omega \in (0, \infty)$; fast-converging method such as the Gauss-Kronrod quadrature can be employed with reliable accuracy.

5.3.4 The free-surface runup

The runup at the shoreline is a variable of interest for risk assessment purposes. Substitution of $r = r_0$ into the free-surface elevation ζ, expression (5.3.17), determines the second integral in (5.3.18) and the B_n's to be null. The corresponding value of the free-surface runup is therefore

$$\zeta(r_0,\theta,t) = \sum_{n=0}^{\infty}\cos n\theta\int_0^{+\infty}A_n\,(r_0,\omega)\,\mathrm{e}^{-\mathrm{i}\omega t}\mathrm{d}\omega + \text{c.c.}\,, \tag{5.3.22}$$

Basin			
Length (m)	Width (m)	Depth (m)	
50.00	30.00	3.00	
Island			
Wet contour r_0' (m)	Bottom radius b' (m)	Flank slope s	
2.07	4.45	1/3	
Landslide			
Length (m)	Width (m)	Max vert. height H (m)	Initial position r_s' (m)
0.80	0.40	0.045	1.3

TABLE 5.1: Basin, island and landslide dimensions of the laboratory experiment made by Di Risio et al. (2009b)

where

$$A_n\left(r_0,\omega\right)=\frac{1}{2\pi r_0}\int_{r_0}^{b}\rho F_n(\rho,-\mathrm{i}\omega)\left[Hc_n^{(1)}(\rho;\omega)\frac{\Delta_n^{(2)}(-\mathrm{i}\omega)}{\Delta_n^{(1)}(-\mathrm{i}\omega)}-Hc_n^{(2)}(\rho;\omega)\right]\mathrm{d}\rho. \quad (5.3.23)$$

In (5.3.23) $\Delta_n^{(1,2)}$ are still given by (5.2.27), while F_n is again the forcing function defined by (5.2.17). In the following, parametric discussion of the free-surface runup is made; the physical observations on the free-surface runup, heights and periods made by Di Risio et al. (2009b) are compared with numerical integration of expression (5.3.22). Finally, discussion is made on the mean features of the solution, pointing out the differences between tsunamis propagating around a conical island and tsunamis propagating along a plane beach.

5.4 Experimental comparison

In order to validate the theory, comparison is made with the experimental results of Di Risio et al. (2009b). The dimensions of the basin, the island and the landslide used in the experiments, are indicated in table 5.1. The initial position of the landslide centroid, $r_s'=1.3\,\mathrm{m}$, is such that the mass at the starting position rests completely out of the water, thus representing a subaerial slide. The mass, reproducing half of an ellipsoid, is a rigid block with flat bottom, sliding along a plane slope 0.5 m wide, as shown in figure 5.7. The resulting geometry is that of a plane slope connected to the curved flanks of a conical island, i.e. slightly different from the conical island of the analytical model. Note also that the landslide used in the experiments preserves its shape during all the phases of motion. On the other hand, the landslide described analytically by (5.2.16) modifies its shape adapting to the curvature of the island while sliding along its flanks. As a result, the theoretical volume of the slide

$$\begin{aligned}V'(t) &= \sigma^2 H\int_{-\pi}^{\pi}\int_{0}^{\infty} f(r,\theta,t)\,r\,\mathrm{d}r\,\mathrm{d}\theta\\ &= \frac{\sqrt{\pi}}{2}\frac{\sigma^2 H\mathrm{erf}(\gamma\pi)}{\gamma}\left\{\mathrm{e}^{-(r_s-t)^2}+\sqrt{\pi}\left[\mathrm{erf}\left(r_s+t\right)+1\right]\left(r_s+t\right)\right\} \quad (5.4.1)\end{aligned}$$

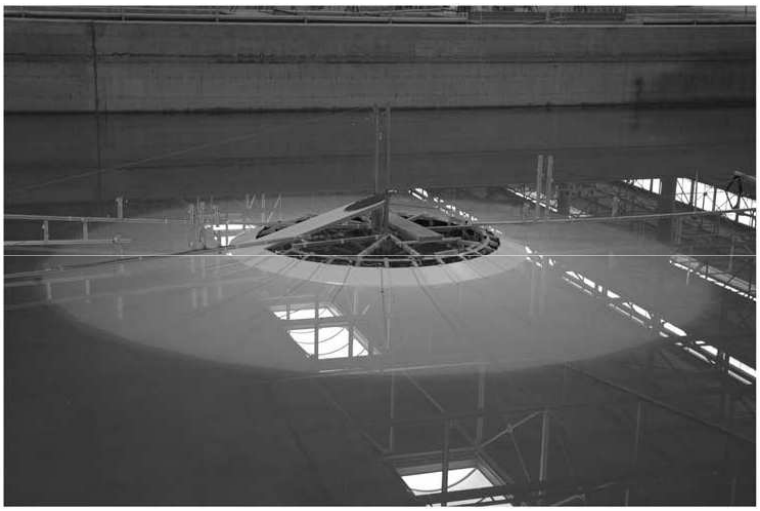

FIGURE 5.7: View of the experimental device used by Di Risio et al. (2009b). The landslide is forced to move along a plane incline 0.5 m wide; as a result the geometry of the experimental model is that of a very thin plane-beach strip connected to the curved flanks of a conical island.

depends on time, increasing linearly for large t. This curvature-induced increase of volume, even if physically reasonable, is absent in the experimental model, therefore the equivalence in volume of the analytical and the experimental slides cannot be strictly applied. However mean quantities can still be represented. We choose the characteristic parameters $\sigma = 0.175\,\mathrm{m}$ and $\lambda = \sigma/2$ to match respectively the wave period time scale in the experiments $T'\left(\propto \sqrt{\sigma/gs}\right) \simeq 2\,\mathrm{s}$ and the shape of the landslide, whose characteristic width to length ratio is $\lambda : \sigma = 1 : 2$. With this choice, the volume of the theoretical landslide at the beginning of motion is $V'(0) = 0.0045\,\mathrm{m}^3$ and then increases linearly, equating the volume of the experimental slide $V'_{exp} = 0.0084\mathrm{m}^3$ at about $t' \simeq 1.6\,\mathrm{s}$, as shown in figure 5.8. At larger times $V' > V'_{exp}$ and still increasing, but the slide approaches deeper water and its influence on the generated wave field can be neglected.

The sample points along the shoreline 2R(20.6°), 4R(47.6°), 5R(60.2°) and 7R(86.3°) of Di Risio et al. (2009b), sketched in figure 5.9, have been chosen for comparison ("R" stands for "runup"). In figure 5.10(a–d), the time series of the free-surface runup, expression (5.3.22), are plotted in physical variables at the chosen sample points (see figure 5.9) and compared to the experimental time series of Di Risio et al. (2009b). Figure 5.10(a) shows the time series of the free-surface runup at $\theta = 20.6°$ (gauge 2R), i.e. about 0.72 m ($\simeq 4\sigma$) from the point of tsunami generation. In figure 5.10(b) is instead depicted the time series of the free-surface runup at $\theta = 47.6°$ (gauge 4R), i.e. about 1.24 m ($\simeq 7\sigma$) far from the origin. Figure 5.10(c) shows the runup time series at $\theta = 60.2°$ (gauge 5R), i.e. about 2.17 m ($\simeq 12\sigma$) far from the origin and finally in figure 5.10(d) is depicted the runup time series at $\theta = 86.3°$ (gauge 7R), i.e. about 3.12 m ($\simeq 18\sigma$) from the point of tsunami generation. Overall, the graphs show good correspondence between the analytical results and the experimental ones. The main

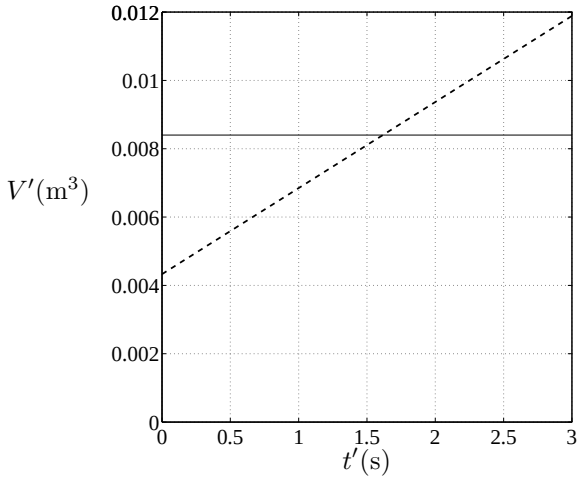

FIGURE 5.8: Volume of the analytical landslide (bold dashed line) evaluated with (5.4.1) and of the experimental landslide (continuous line) vs. time. The first one increases almost linearly with time while the landslide moves along the flanks of the island; the second one is constant during all the phases of motion.

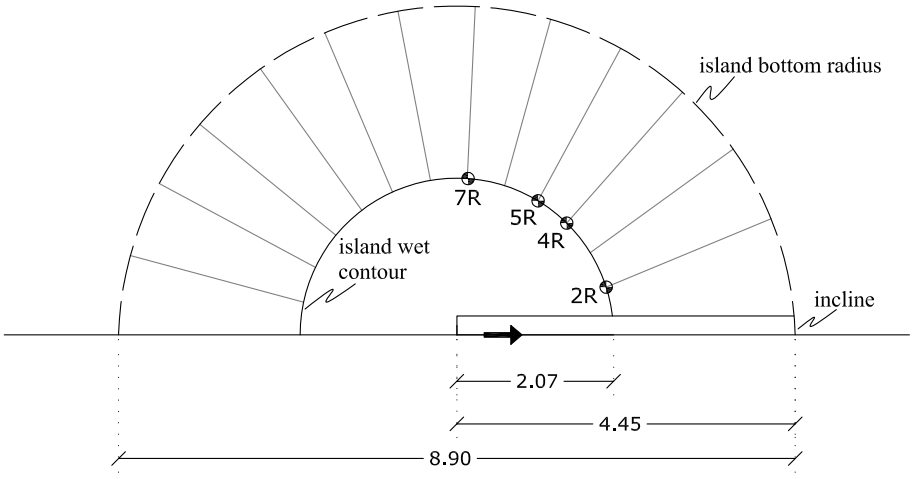

FIGURE 5.9: Skecth of half of the conical island with the positions of the sample points considered for experimental comparison and indication of the island dimensions (in metres). The solid line (–) represents the island wet contour r'_0, while the island bottom radius b' is indicated by the dashed line (– –). The bold arrow indicates the direction of motion of the sliding mass. Segments on the island flanks indicate the position of the gauges employed in the experiments of Di Risio et al. (2009b)

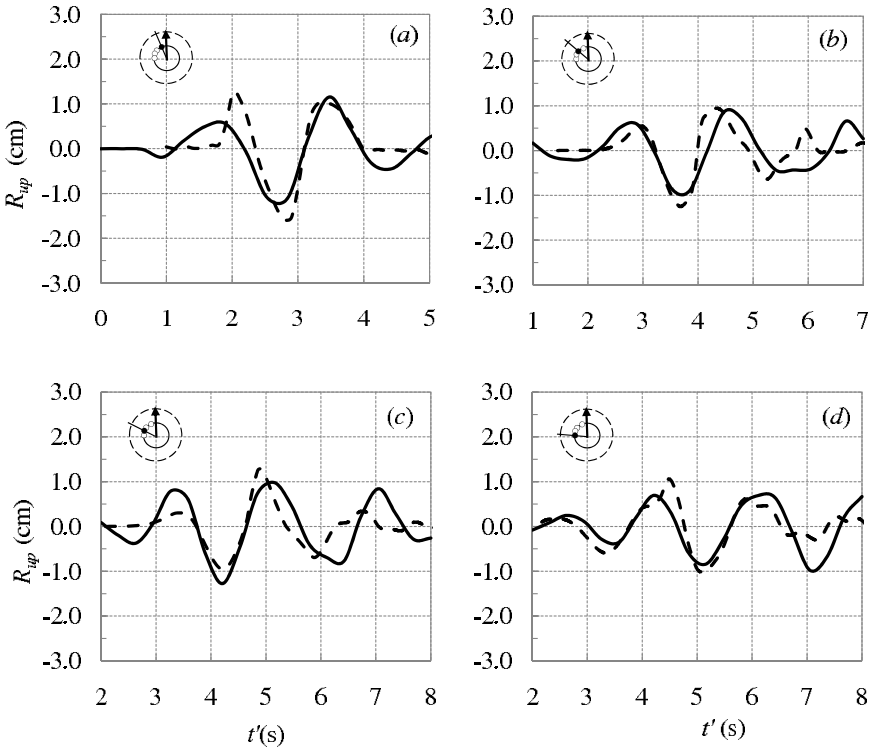

FIGURE 5.10: Analytical (bold line) and experimental (bold dashed line) time series of the free-surface runup $R_{up} = \zeta'(r'_0, \theta, t')$ at the shoreline in physical variables. The geometry of the island and the landslide is reported in table 5.1. The Gauss-Kronrod quadrature method has been used for numerical integration of (5.3.22), modes $n = 0 \dots 10$ have been taken into account. Subplot (a) refers to the shoreline point 2R located at $\theta = 20.6°$, subplot (b) refers to 4R located at $\theta = 47.6°$, subplot (c) to 5R located at $\theta = 60.2°$ and subplot (d) to 7R located at $\theta = 86.3°$. In each of the subplots, a plant view of the island is sketched on the top left corner. Here, the solid line (–) represents the island wet contour, while the dashed line (– –) represents the island bottom radius. The arrow indicates where the slide enters the water and the filled circle specifies the position of the relevant runup gauge.

properties of the generated wave field, i.e. the shape of the waves, the time of arrival of crests and troughs and the maximum runup and drawdown, are predicted satisfactorily by the analytical model. Other than the difference in landslide volumes pointed up above, several minor factors can also explain the slight differences between the analytical and the experimental data. First, recall that the geometry of the experimental model is a narrow plane beach surrounded by a conical island. The presence of this thin-strip plane beach influences the overall behaviour of the fluid in the neighbourhood of the generation zone. Due to the energy-trapping property of the straight coast, the maximum runup obtained in the experiment is larger than the one obtained with the analytical model for a purely conical island (which is unable to trap energy completely) especially near the generation zone (see point 2R in figure 5.10a). Second, note that the long-wave governing equation (5.1.1) used in the model is non-dispersive, hence the dispersive behaviour of water waves on a bottom with varying depth cannot be properly rendered with the analytical model used here. As a result, while in the experimental time series the period of the first incoming waves is longer than that of the following group, in the analytical model the wave period is almost constant for all the waves in the group (see figure 5.10b,c). Finally note that the landslide used in the experiments is not of a double Gaussian shape, but is an half an ellipsoid. The difference in the front shape, which in the model is much smoother than in the experiments, could have led to some diversities in the shape of the first propagating waves.

5.5 Tsunami generation and propagation around the island

After having shown a good agreement between the theoretical and the experimental data, we analyse the tsunami generation and propagation mechanisms more in detail. In figure 5.11$(a-d)$ snapshots of the non-dimensional free-surface runup $\zeta(r_0,\theta,t)$ at four different times are shown, together with the contour of the slide $f(r_0,\theta,t)$. The geometry of the island is still that of table 5.1. The landslide is kept subaerial ($r_s' = 1.3\,\mathrm{m}$), but its characteristic length is increased to $\sigma = 0.37\,\mathrm{m}$ ($r_s = r_s'/\sigma = 3.51$), still being $\lambda = \sigma/2$. The larger ratio σ/b' allows to gain a clearer insight on the early interaction between the slide and the water occurring during the generation process. At the first instants of motion (figure 5.11a,b) the shoreline recedes as the landslide pushes water away. The early depression wave formed landwards of the slide is clearly a source-related perturbation, having the same width as that of the slide (Lynett and Liu, 2005, found numerically a similar result for landslide tsunamis along a plane beach). Moving ahead in time, the slide disappears in deeper water (figure 5.11c,d). At the origin the shoreline inverts its motion and goes back up the incline (figure 5.11c), due to the elastic rebound. The perturbation leaves the origin with the profile of a positive N-wave along the coastline, as shown in figure 5.11(c). Finally water inundates the the dry land at the origin (figure 5.11d), meanwhile the leading elevation wave is travelling around the island, followed by a deeper trough. Note that the generation mechanisms of landslide tsunamis around a conical island do not differ from those of landslide tsunamis along a plane beach (see Lynett and Liu, 2005). In fact, the shoreline snapshots of figure 5.11$(a-d)$ resemble very closely the digital pictures of the shoreline position taken by Di Risio et al. (2009a) during the experimental modelling of landslide tsunamis along a plane beach. At larger times, however, the smaller refractive power of the island enhances the amount of energy radiated to infinity. As a result, the wave field

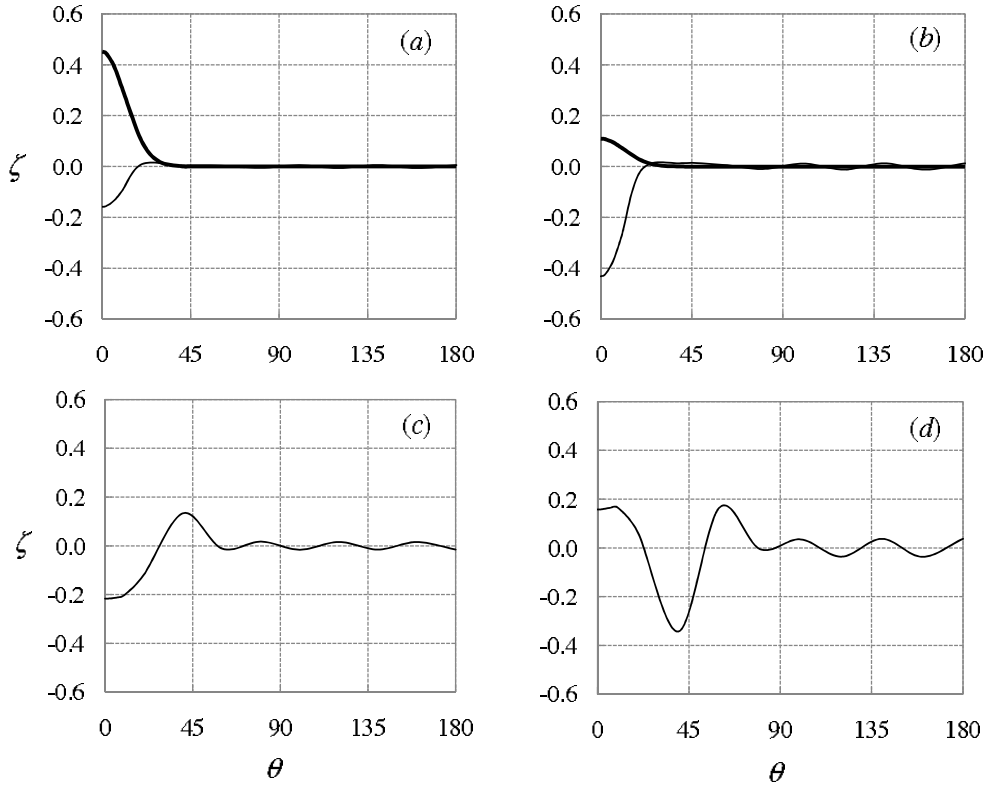

FIGURE 5.11: Spatial snapshots of the free-surface elevation in non-dimensional variables for a subaerial landslide at the shoreline. θ in degrees. The dimensions of the island are those of table 5.1, the slide characteristic length is $\sigma = 0.37\,\mathrm{m}$, $\lambda = \sigma/2$. The centroid initial position is $r_s = 3.51$ ($r'_s = 1.3\,\mathrm{m}$). Bold lines depict the landslide surface contour $f(r_0, \theta, t)$ at the given times, solid lines represent the free-surface elevation $\zeta(r_0, \theta, t)$. Subplot (a) refers to $t = 2.97$ ($t' = 1\,\mathrm{s}$), subplot (b) refers to $t = 3.57$ ($t' = 1.2\,\mathrm{s}$), subplot (c) to $t = 5.94$ ($t' = 2\,\mathrm{s}$) and finally subplot (d) refers to $t = 8.92$ ($t' = 3\,\mathrm{s}$). Modes $n = 0$–9 have been considered. Note that the symmetry condition $\partial\zeta/\partial\theta = 0$ at $\theta = 0$ is fully reproduced by the model.

propagating around the island differs from the one propagating along the plane beach, as shown in the following section.

5.5.1 The conical island vs. the plane beach

In this section, the features of tsunamis propagating around a conical island are further compared to the features of landslide-generated tsunamis on a plane beach (see §3.3). To perform this comparison, beach slope and landslide characteristic parameters are kept equal, i.e. $s = 1/3\,, \sigma = 0.37\,\mathrm{m}$, $\lambda = \sigma/2$ in both geometries; landslide is half-submerged in its initial position in both cases. The island geometry is the same of table 5.1, the half-submergence condition requires the landslide centroid position at $r'_s = r'_0 = 2.07\,\mathrm{m}$. Figure 5.12$(a)$ and figure 5.12(b) show the time series of the free-surface runup (expression 5.3.22) in non-dimensional variables at the shoreline points $1S = (r_0, 20.6^\circ)$ and $2S = (r_0, 60.2^\circ)$ respectively, while figure 5.12(c) and figure 5.12(d) show the free-surface elevation time series in the far field (expression 5.3.7) at the offshore points $1O = (b, 0^\circ)$ and $2O = (2b, 0^\circ)$ respectively. As the landslide motion begins, water

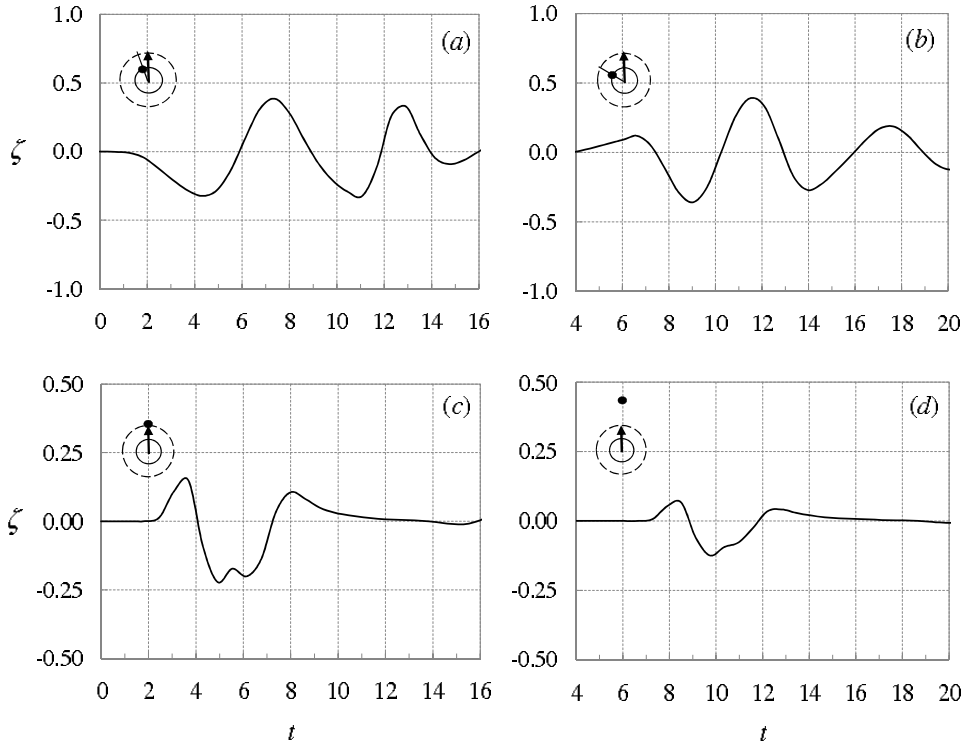

FIGURE 5.12: Time series in non-dimensional variables for a half-submerged landslide ($r_s = r_0$). Subplot (a) refers to the shoreline point $1S$ located at $(r_0, \theta = 20.6°)$, subplot (b) refers to $2S$ at $(r_0, \theta = 60.2°)$, subplot (c) to the far-field point $1O$ at $(b, 0°)$ and finally subplot (d) refers to point $2O$ at $(2b, 0°)$. Modes $n = 0$–9 have been considered. In each of the subplots, a plant view of the island is sketched on the top left corner. Here, the solid line (–) represents the island wet contour, while the dashed line (– –) represents the island bottom radius. The arrow indicates where the slide enters the water and the filled circle specifies the position of the relevant point.

is pushed ahead and a leading elevation wave travelling offshore is generated, quickly reaching the two points $1O$ at $r = b$ (figure 5.12c) and $2O$ at $r = 2b$ (figure 5.12d) in the far field. Note also the strong attenuation experienced by the leading wave crest while travelling from point $1O$ to point $2O$. In the meantime, a deep depression wave occurs just behind the slide. As a result, at point $1S$ on the shoreline close to the origin the first incoming wave has a trough, followed by a large crest generated by the elastic rebound (see figure 5.12a). The maximum runup is reached by the first crest, then oscillations decay in time, the free-surface elevation eventually reaching the unperturbed position. At point $2S$ on the shore far from the origin the first wave has instead a small crest, followed by a larger trough (see figure 5.12b), i.e. the first incoming perturbation is still a positive N-wave. Note that the maximum runup here is reached by the second incoming wave, which is followed in turn by a tail of smaller-amplitude waves. The fact that at large distances from the slide the largest wave is shifted towards the middle of the group is also a feature of tsunamis propagating along a plane beach. As demonstrated numerically by Lynett and Liu (2005), experimentally by Di Risio et al. (2009a) and then analytically in §3.3, this characteristic is due to the excitation of edge-wave modes trapped along the straight coast. The occurrence of such a phenomenon around the shoreline of the conical island suggests that edge-wave components of the water motion can be partially trapped along the coast also in a round geometry. Let us demonstrate

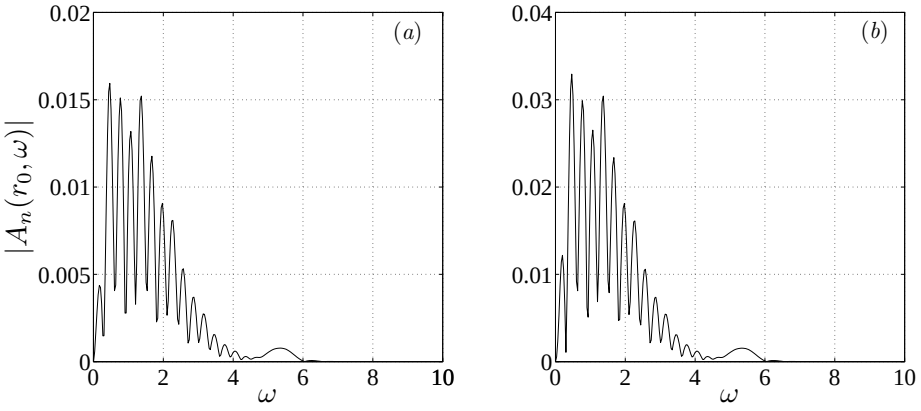

FIGURE 5.13: Plots of $|A_n(r_0,\omega)|$ versus frequency ω for the geometry used in the experiments of Di Risio et al. (2009b). Modal orders are: (a) $n=0$, (b) $n=1$.

this feature analytically by looking at expression (5.3.22) for the runup $\zeta(r_0,\theta,t)$. This is obtained for each of the angular modal components by integrating with respect to $\omega \in \mathbb{R}$ the form $\mathrm{e}^{-\mathrm{i}\omega t}$, representing a simple harmonic oscillation in time, multiplied by the forcing factor $A_n(r_0,\omega)$, expression (5.3.23). The latter physically represents the amplitude of each wave component in the frequency domain. Figure 5.13 shows the fast decay of $|A_n(r_0,\omega)|$ for increasing ω, so that the effective domain of integration of (5.3.22) is restricted only to smaller ω, for each of the angular modal components. Therefore only the lowest frequencies concur in determining the magnitude of the free-surface runup at the shoreline. Now, recalling condition (5.1.12), the lowest frequencies experience the strongest exponential attenuation as r increases towards infinity (see also Meyer, 1971; Mei et al., 2005): the relevant wave components are almost trapped around the shoreline, resembling the edge-wave modes. Hence the free-surface runup, expression (5.3.22), can be regarded almost as a sum of edge-wave like modes, for which the largest wave is always shifted towards the middle of the group (see Sammarco and Renzi, 2008).

Are then any practical differences between the wave fields generated around a conical island and along a plane beach? A direct comparison of the relevant runup time series shows them. The bold dashed lines in figure 5.14(a,b) show the free-surface runup time series at points $y' = 0.72\,\mathrm{m}$ ($y = y'/\sigma = 2.05$, corresponding to $1S$) and $y' = 2.175\,\mathrm{m}$ ($y = y'/\sigma = 5.88$, corresponding to $2S$) along the shoreline of a plane beach, obtained via the analytical model of §3. Here the beach slope $s = 1/3$ is the same as that of the island flanks. The characteristic parameters of the slide, σ and λ do not vary too, as anticipated above. In the same figure 5.14(a,b) the time series at points $1S$ and $2S$ of the conical island, already depicted in figure 5.12(a,b), are reported again for easiness of comparison, in bold lines. Note that at both points $1S$ and $2S$ the maximum runup (and minimum drawdown) of the first incoming waves is larger in the plane beach than in the conical island, even if the characteristic parameters of the slide are the same in both the geometries. This feature is again consequence of the fact that perfect wave trapping is possible only in a straight geometry. While on the plane beach energy is all trapped along the coast, due to the propagation of edge waves along the shoreline, in the circular geometry of the conical island perfect trapping is not possible. All frequencies, even the smallest ones, leak some amount of energy to infinity, resulting

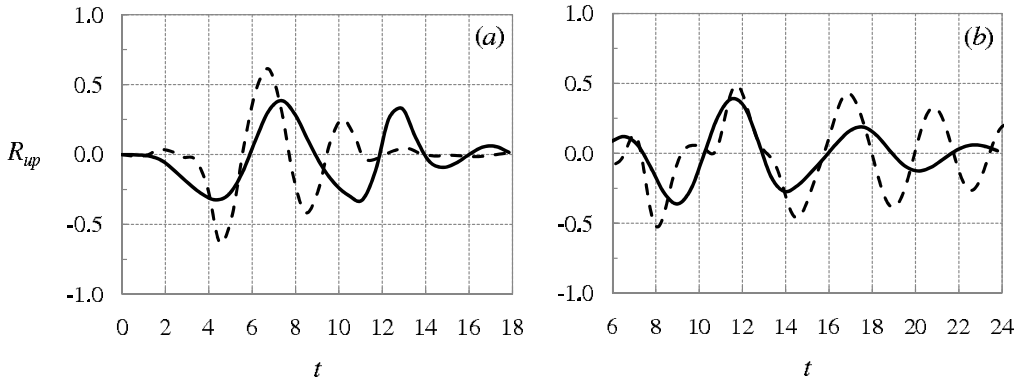

FIGURE 5.14: Free-surface elevation at points: (a) $y = 2.05$ (corresponding to 1S) and (b) $y = 5.88$ (corresponding to 2S) for the plane-beach geometry (bold dashed line) and the conical island (bold line).

in attenuation of the maximum wave height around the coast. This crucial result has been also shown to occur in the experiments of Di Risio et al. (2009b).

Chapter 6

Conclusions

This study concerned several aspects of the generation and propagation of landslide tsunamis in different oceanographic topographies, i.e. an indefinite plane beach, a plane beach connecting to a flat continental platform and a conical island.

An analytical forced two-horizontal-dimension (2HD) model has been developed to analyse the distinguishing physical features of landslide-induced tsunamis along a straight coast. After a short transient immediately following the landslide generation, the wave motion starts to be trapped at the shoreline and finally only transient longshore travelling edge waves are present. Longer waves travel faster and are followed by a tail of shorter waves, while new crests are created. Unlike transient waves generated and propagating in water of constant depth, for landslide-induced tsunamis along a sloping beach the larger waves are not in the front of the wavetrain, but are shifted toward the middle of it. Parametric analysis shows the dependence of the tsunami runup on the landslide shape, initial position and velocity. The higher the slide initial position on the incline, the larger the generated runup. Moving the initial position of the slide closer to water produces the double effect of decreasing the runup and enhancing the dispersive behaviour of the wave field. Experimental comparison shows the validity of the model in reproducing the physical behaviour of the system. Finally, the accuracy of homogeneous initial-value models in reproducing landslide-generated tsunamis is discussed. Since no analytical demonstration of the validity of this approach seems to exist, usage of such simplified models is advised only for quick runup assessment.

An analytical forced 2HD model has been developed to analyse the distinguishing features of landslide tsunamis on a semi-plane beach. The solution obtained via the method of separation of variables only allows the existence of trapped wave modes propagating along the coast. For very large values of the horizontal length of the slope, the free surface elevation matches the solution obtained for an infinite sloping beach, where all the eigenmodes are trapped. For a finite horizontal length of the slope, the free-surface elevation is the sum of an evanescent component, fast decaying with time, and an oscillatory component travelling along the shoreline, as it was the case for the plane beach. Despite the presence of the constant depth region would suggest the occurrence of a leading wave propagating offshore, no wave is propagated offshore and all energy is trapped along the coastline.

An analytical forced two-horizontal-dimension model has been developed to analyse

the distinguishing features of landslide tsunamis propagating around a conical island -continental shelf system. Two fields of wave motion are defined, the near field, i.e. the inner zone with variable depth, and the far field, i.e. the outer zone with constant depth. The long wave equation is solved in each of the two fields separately. The free-surface elevation in the whole domain is then found by matching at the common boundary the solutions for the two fields. As many other linear-system responses to transient excitations, the free-surface elevation in each field is given by integrating the solution of the homogeneous wave equation multiplied by the forcing factor proper to the field and dependent on the characteristics of the slide. The resulting perturbation of the free surface is made by transient waves propagating to infinity and transient local waves almost trapped. The occurrence of a leading elevation wave travelling offshore at large times is shown, its amplitude decaying as $O(t^{-1/2})$, i.e. faster than the leading Airy wave generated by a transient disturbance in a two-dimensional ocean of constant depth. Experimental comparison shows the validity of the model in reproducing the overall fluid behaviour. The tsunami generation mechanism is analysed for a subaerial slide. Just after the landslide has entered the water, the first perturbation leaves the origin as a positive N-wave. The wave profile near the generation zone resembles that of tsunamis along a plane beach. The free-surface runup at the shoreline induced by a half-submerged slide has been also investigated. Near the landslide the maximum runup is reached by the first crest of the incoming wave train, while far from the generation zone the highest wave is always shifted towards the middle of the incoming group. This is due to the excitation of edge-wave like components of small frequency, for which the energy is almost trapped along the shore. However, unlike tsunamis propagating along an indefinite plane beach, where edge-wave energy is all trapped along the shoreline, tsunamis around a conical island propagate energy also in the offshore direction. As a consequence, the waves travelling along the shoreline of a conical island are characterised by smaller runup than those generated by a similar landslide along a plane beach with the same slope.

Appendix A

Kummer's equation

A.1 General solution

Kummer's equation in its general form is (see Abramowitz and Stegun, 1972)

$$\xi X_{\xi\xi} + (\beta - \xi) X_\xi - \alpha X = 0, \tag{A.1.1}$$

where α and β are real numbers. (A.1.1) has a regular singular point at $\xi = 0$ and an irregular singular point at $\xi = \infty$. Let the two coefficients be

$$\alpha = \frac{1}{2}\left(1 - \frac{\omega^2}{k}\right), \quad \beta = 1, \tag{A.1.2}$$

so that (A.1.1) becomes

$$\xi X_{\xi\xi} + (1 - \xi) X_\xi - \frac{1}{2}\left(1 - \frac{\omega^2}{k}\right) X = 0. \tag{A.1.3}$$

As seen in section , this equation describes the behaviour of linear water waves propagating along a constant slope. We will now employ the Frobenius' method of power series to find the two independent solutions of (A.1.1) about the regular singular point $\xi = 0$. Let us assume

$$X(\xi) = \sum_{m=0}^{\infty} a_m \xi^{(m+\rho)}, \tag{A.1.4}$$

with ρ and a_m being respectively the index and the coefficients of the Frobenius expansion (A.1.4), still unknown. Substitution of the series expansion (A.1.4) into the Kummer equation (A.1.1) gives

$$\sum_{m=0}^{\infty}(m+\rho)(m+\rho-1)a_m\xi^{(m+\rho-2)} + (1-\xi)\sum_{m=0}^{\infty}(m+\rho)a_m\xi^{(m+\rho-2)} +$$
$$-\left(\frac{1}{2} - \frac{\omega^2}{2k}\right)\sum_{m=0}^{\infty} a_m \xi^{(m+\rho-1)} = 0.$$

With some simple algebraic manipulation of the power series, the latter expression can be finally written as

$$\rho^2 a_0 \xi^{\rho-2} + \sum_{m=0}^{\infty}\left[(m+\rho+1)^2 a_{m+1} - a_m(m+\rho+\alpha)\right]\xi^{m+\rho-1} \tag{A.1.5}$$

where the term α (A.1.2) is used for simplicity. Equation (A.1.5) is a polynomial expression which involves powers of ξ. For (A.1.5) to be satisfied we must require that the coefficients of each power of ξ are zero. Starting from the lowest power $\xi^{\rho-2}$ we obtain the indicial equation

$$a_0\rho^2 = 0.$$

Setting $a_0 \neq 0$ to avoid trivial solutions, the two indexes of the indicial equation are $\rho_1 = \rho_2 = 0$ and coincide. According to Frobenius' theory, in this case only one independent solution of (A.1.3) has the sought form (A.1.4). The remaining one has instead logarithmic terms and can be found only via further investigation (see Bender and Orzsag, 1978). Back to the first independent solution (A.1.4), setting to zero the coefficients of $\xi^{m+\rho-1}$ gives

$$a_{m+1}(\rho, k, \omega) = a_m \frac{m+\rho+\alpha}{(m+\rho+1)^2}. \tag{A.1.6}$$

Finally substituting $\rho = 0$ into (A.1.6), we obtain the following recurring relation for the coefficients $a_m(\omega) = a_m(k, \omega)$

$$a_{m+1} = a_m \frac{m+\alpha}{(m+1)^2}, \tag{A.1.7}$$

having set the arbitrary parameter $a_0 = 1$. From (A.1.7), note that

$$\frac{a_{m+1}}{a_m} \simeq \frac{m}{(m+1)^2} \to 0 \text{ as } m \to \infty$$

and the power series solution (A.1.4) with coefficients (A.1.7) converges in all the physical domain $\xi \in (0, \infty)$. Finally we seek an explicit expression of the series coefficients a_m. Starting from $m = 0$ and then increasing the index, (A.1.7) gives

$$\begin{aligned} a_1 &= \alpha, \\ a_2 &= \frac{\alpha\,(1+\alpha)}{4} \\ &\dots \\ a_m &= \frac{(\alpha)_m}{(m!)^2}, \end{aligned} \tag{A.1.8}$$

where the parameter α is still defined by (A.1.2) and

$$(\alpha)_m = \alpha\,(\alpha+1)\,(\alpha+2)\dots(\alpha+m-1)\,.$$

The Kummer function of first kind is therefore

$$M(\xi, \alpha) = X(\xi) = \sum_{m=0}^{\infty} a_m(\omega)\xi^m, \tag{A.1.9}$$

with the a_m given by (A.1.8).

Since the indicial equation has double zero roots $\rho^2 = 0$, the second independent solution of (A.1.3) contains logarithmic terms. As demonstrated by Bender and Orzsag (1978), its general form can be expressed as

$$X(\xi) = \ln\xi \sum_{m=0}^{\infty} b_m\xi^m + \sum_{m=0}^{\infty} c_m\xi^m. \tag{A.1.10}$$

By substituting this form into the governing equation (A.1.3) and following the same passages as above, it can be shown that the b_m and c_m must satisfy the following relations respectively

$$b_m = \frac{-1}{\Gamma(\alpha)}\, a_m, \tag{A.1.11}$$

$$c_m = \frac{-1}{\Gamma(\alpha)} \sum_{p=0}^{\infty} \frac{(\alpha)_p}{(p!)^2} \left[\psi(\alpha+p) - 2\psi(1+p)\right], \tag{A.1.12}$$

where $\psi(z) = \Gamma'(z)/\Gamma(z)$ and Γ is the gamma function. With these results, (A.1.10) can be re-written in its final form, i.e. the Kummer function of second kind and parameter α:

$$U(\xi,\alpha) = \frac{-1}{\Gamma(\alpha)} \left[\ln \xi\, M(\xi,\alpha) + \sum_{m=0}^{\infty} c_m \xi^m\right]. \tag{A.1.13}$$

Finally, the general solution of the Kummer equation is the linear combination of the two independent ones, respectively (A.1.9) and (A.1.13)

$$X(\xi) = AM(\xi,\alpha) + BU(\xi,\alpha). \tag{A.1.14}$$

A.2 Boundary conditions

In most physical applications, the solution (A.1.13) of the Kummer equation (A.1.1) is required to satisfy some basic boundary conditions, i.e. to be bounded as $\xi \to 0$ and to vanish as $\xi \to \infty$. For perturbations propagating along a plane beach, these boundary conditions are (see section 3.1.1)

$$|X(0)| < +\infty, \tag{A.2.1}$$

$$\lim_{\xi\to\infty} \mathrm{e}^{-\xi/2} X(\xi) = 0. \tag{A.2.2}$$

Due to the logarithmic singularity of $U(\xi,\alpha)$ as $\xi \to \infty$, condition (A.2.1) is satisfied only if $B = 0$. Hence we are left with $X(\xi) = AM(\xi,\alpha)$, which must satisfy the b.c. (A.2.2). To further investigate this condition, we employ the asymptotic form of $M(\xi,\alpha)$ for large argument (see Abramowitz and Stegun, 1972)

$$M(\xi,\alpha) \simeq \frac{1}{\Gamma(\alpha)}\, \mathrm{e}^{\xi}\, \xi^{\alpha-1}, \quad \xi \to \infty. \tag{A.2.3}$$

With this asymptotic expression, (A.2.2) can be re-written as

$$\lim_{\xi\to\infty} \frac{1}{\Gamma(\alpha)}\, \mathrm{e}^{\xi/2} \xi^{\alpha-1} = 0, \tag{A.2.4}$$

which is verified only if

$$\Gamma(\alpha) = \infty.$$

The latter condition is satisfied for

$$\alpha = \frac{1}{2}\left(1 - \frac{\omega^2}{k}\right) = 0, -1, -2 \ldots \tag{A.2.5}$$

i.e.

$$\omega = \omega_n = \sqrt{k\,(2n+1)}, \quad n = 0, 1, 2, \ldots \tag{A.2.6}$$

which defines the motion eigenfrequencies. Therefore each of

$$X_n = M(\xi, \alpha_n),\ n = 0, 1, 2, \ldots$$

is a solution of the governing equation (A.1.3), provided that the α_n satisfy the eigenvalue condition (A.2.5), in other terms

$$\alpha_n = -n, \quad n = 0, 1, 2, \ldots$$

Also, for these special values of the parameter α, the series coefficients a_{mn}(A.1.8) of the series expansion (A.1.4) become

$$\begin{aligned} a_{1\,n} &= -n \\ a_{2\,n} &= \frac{-n(1-n)}{4} \\ &\ldots \end{aligned} \tag{A.2.7}$$

$$a_{m\,n} = \frac{(-1)^m}{m!} \begin{pmatrix} n \\ n-m \end{pmatrix} \tag{A.2.8}$$

where $n = 0, 1, 2 \ldots$, $m \leq n$ and

$$\begin{pmatrix} n \\ p \end{pmatrix} = \frac{n!}{p!(n-p)!} \quad \text{if} \quad 0 \leq p \leq n,$$

$$\begin{pmatrix} n \\ p \end{pmatrix} = 0 \quad \text{if} \quad p < 0 \quad \text{or} \quad p > n$$

is the binomial coefficient. Note that (A.2.8) implies also

$$a_{(n+1)\,n} = 0,$$

being

$$\begin{pmatrix} n \\ n-(n+1) \end{pmatrix} = \begin{pmatrix} n \\ -1 \end{pmatrix} = 0 \quad .$$

Therefore, thanks to the recurrence relation (A.1.7), we obtain

$$a_{m\,n} = 0, \quad m = n+1, n+2, \ldots \tag{A.2.9}$$

In the series expansion (A.1.4) only the first n terms survive, i.e. $M(\xi, \alpha_n)$ is a polynomial of degree n, namely the Laguerre polynomial of order n

$$L_n(\xi) = \sum_{m=0}^{n} (-1)^m \begin{pmatrix} n \\ n-m \end{pmatrix} \frac{\xi^m}{m!}. \tag{A.2.10}$$

In conclusion, the boundary value problem studied admits as eigenfunctions each of the Laguerre polynomials $L_n(\xi)$ (A.2.10) with the relevant eigenfrequency ω_n (A.2.6). As an example, the lower-order Laguerre polynomials are given by

$$\begin{aligned} n = 0 \qquad & L_0 = 1 \\ n = 1 \qquad & L_1(\xi) = 1 - \xi \\ n = 2 \qquad & L_2(\xi) = 1 - 2\xi + \tfrac{1}{2}\xi^2. \end{aligned}$$

Appendix B

Gauss-Laguerre integration

Let us consider a regular real function $f(z)$; the integral

$$\int_0^\infty \mathrm{e}^{-z} f(z)\,\mathrm{d}z \tag{B.0.1}$$

can be evaluated numerically via the Gauss-Laguerre integration formula

$$\int_0^\infty \mathrm{e}^{-z} f(z)\,\mathrm{d}z \simeq \sum_{i=1}^{m} w_i f(z_i), \tag{B.0.2}$$

as shown by Dahlquist and Björck (2008). In the latter expression, z_i is the i-th zero of the Laguerre polynomial of the m-th order, L_m and the w_i are weights evaluated as

$$w_i = \frac{1}{z_i \left[\frac{\mathrm{d}L_m}{\mathrm{d}z}(z_i)\right]^2}.$$

With these positions, expression (B.0.2) is exact if $f(x)$ is a polynomial of degree $2m-1$ or less.

Application to landslide tsunamis propagating along a semi-plane beach

We now apply the Gauss-Laguerre numerical integration to evaluate $\zeta = \zeta^o + \zeta^e$, where ζ^o (4.6.7) and ζ^e (4.6.10) are respectively the oscillatory and evanescent component of the free surface elevation, representing a tsunami propagating along a semi-plane beach. By making use of (4.6.7) and (4.6.10), ζ can be rewritten as

$$\zeta(x,y,t) = \int_0^\infty \mathrm{e}^{-kx} f_n(k,t)\,\mathrm{d}k, \tag{B.0.3}$$

where

$$f_n(k,t) = \frac{2}{\pi} \sum_{n=0}^{N(k)} X_n(2kx) \left\{ A_n \cos\omega_n t + B_n \sin\omega_n t + \omega_n \hat{s} \mathcal{M}^n \left[\mathrm{e}^{-(\rho-t)^2} \right] \right\} \cos ky$$

and the nomenclature is still that of §4.5. Now, to transform (B.0.3) into the general form (B.0.1) we should make a change of variable, i.e. $k = z/x$. However, this position

will generate a singularity at $x = 0$, i.e. when evaluating the free-surface elevation at the shoreline. To circumvent this singularity, we shall rewrite (B.0.3) as

$$\zeta(x, y, t) = \int_0^\infty \mathrm{e}^{-k(x+b)} \mathrm{e}^{kb} f_n(k, t)\, \mathrm{d}k, \tag{B.0.4}$$

where $b > 0$ is the non-dimensional horizontal length of the incline. Note that the position (B.0.4) does not modify the leading behaviour of the integrand, which is still convergent for large k. Let us now set

$$k = \frac{z}{x+b},$$

so that (B.0.4) becomes

$$\zeta(x, y, t) = \frac{1}{x+b} \int_0^\infty \mathrm{e}^{-z} \mathrm{e}^{zb/(x+b)} f_n\left(\frac{z}{x+b}, t\right) \mathrm{d}z,$$

which is in the form of (B.0.1). Hence application of the Gauss-Laguerre integration formula (B.0.2) to the latter yields

$$\zeta \simeq \frac{1}{x+b} \sum_{i=1}^{m} w_i\, \mathrm{e}^{z_i b/(x+b)} f_n\left(\frac{z_i}{x+b}, t\right), \tag{B.0.5}$$

where z_i is the i-th zero of the Laguerre polynomial L_m. Note that the approximation (B.0.5) is valid for all x in the fluid domain and does not produce any singularity at the shoreline $x = 0$. Finally, let us define

$$k_i = \frac{z_i}{x+b},$$

so that (B.0.5) becomes

$$\zeta \simeq \frac{1}{x+b} \sum_{i=1}^{m} A_i\, \mathrm{e}^{k_i b} f_n(k_i, t),$$

which the sought Gauss-Laguerre approximation for the numerical calculation of ζ.

Appendix C

Confluent Heun's equation

The confluent Heun equation (CHE) in its natural general form is (see Slavyanov, 1995)

$$R_{rr}(r) + \left(\sum_{i=1}^{2} \frac{A_i}{r - r_i} + E_0 \right) R_r(r) + \\ + \left(\sum_{i=1}^{2} \frac{C_i}{r - r_i} + \sum_{i=1}^{2} \frac{B_i}{(r - r_i)^2} + D_0 \right) R(r) = 0. \tag{C.0.1}$$

In the latter equation, $R(r) : \mathbb{R} \to \mathbb{C}$ is the dependent function, A_i, B_i, C_i $(i = 1, 2)$, D_0 and E_0 are given coefficients. The CHE has two regular singular points at $r = r_1$ and $r = r_2$, while $r = \infty$ is an irregular singular point.

Let the coefficients in (C.0.1) be as follows:

$$A_1 = A_2 = 1; \quad B_1 = D_0 = 0; \quad C_1 = \lambda^2, C_2 = 0; \quad B_2 = -n^2; \quad E_0 = 0,$$

with $n \in \mathbb{N}$ and $\lambda \in \mathbb{C}$. Also, set the two regular singular points respectively at $r_1 = r_0 > 0$ and $r_2 = 0$, while leaving the remaining irregular singularity at infinity. Finally, restrict the domain of interest to $r > r_0$. With these positions, (C.0.1) becomes

$$R_{n,rr} + \left(\frac{1}{r} + \frac{1}{r - r_0} \right) R_{n,r} + \left[\frac{\lambda^2}{r - r_0} - \frac{n^2}{r^2} \right] R_n = 0. \tag{C.0.2}$$

As seen in section §5.2, this equation describes the behaviour of the radial part $R(r)$ of the free-surface elevation $\zeta(r, \theta, t)$ around a conical island of radius r_0, λ representing the complex wave frequency and n the order of the angular modes.

C.1 Solution

To find the two independent solutions of the CHE (C.0.2), we shall use the following change of variables

$$\xi = 1 - \frac{r_0}{r}, \quad Z_n(\xi; \lambda) = R_n(r; \lambda) \tag{C.1.1}$$

first suggested by Zhang and Zhu (1994), who already solved (C.0.2), but only finding one of the two independent solutions. Note that Zhang and Zhu (1994) called their result "new", without explicitly referring to the theory of confluent Heun functions originally developed by Heun (1899) and then tuned by Slavyanov (1995). Here we

pursue a slightly different deduction of the solution, which eventually will enable us to investigate the asymptotic behaviour of the confluent Heun functions for large parameter λ. By using (C.1.1) the regular singular point at $r = r_0$ is mapped to $\xi = 0$, while the irregular singularity at infinity is mapped to $\xi = 1$ and (C.0.2) becomes

$$Z_{n,\xi\xi} + \frac{p(\xi)}{\xi} Z_{n,\xi} + \frac{q(\xi)}{\xi^2} Z_n = 0, \tag{C.1.2}$$

where

$$p(\xi) = 1\,, \quad q(\xi) = \frac{\lambda^2 r_0 \xi - n^2 \xi^2 (1-\xi)}{(1-\xi)^3}. \tag{C.1.3}$$

We shall now employ the Frobenius' method of power series to find the two independent solutions of (C.1.2) about the regular singular point $\xi = 0$. Let us assume

$$Z(\xi;\lambda) = \xi^\rho \sum_{m=0}^{\infty} a_{nm}(\rho;\lambda)\xi^m, \tag{C.1.4}$$

with ρ and a_{nm} being respectively the index and the coefficients of the Frobenius expansion (C.1.4), still unknown. Also, since both the polynomials $p(\xi)$ and $q(\xi)$ are analytic at $\xi = 0$, they can be expanded in Taylor series about the origin:

$$\left\{ \begin{array}{c} p(\xi) \\ q(\xi) \end{array} \right\} = \sum_{k=0}^{\infty} \left\{ \begin{array}{c} p_k \\ q_k \end{array} \right\} \xi^k\,, \quad \left\{ \begin{array}{c} p_k \\ q_k \end{array} \right\} = \left\{ \begin{array}{c} 0 \\ -n^2(k-1) + \frac{\lambda^2 r_0}{2}\left(k + k^2\right) \end{array} \right\}, \tag{C.1.5}$$

$k \geq 1$, with $p_0 = 1$ and $q_0 = 0$. Substitution of both the series expansions (C.1.4) and (C.1.5) into (C.1.2) gives

$$\begin{aligned} \sum_{m=0}^{\infty} (m+\rho)(m+\rho-1) a_{nm} \xi^{(m+\rho-2)} \quad &+ \quad \sum_{m,k=0}^{\infty} p_k\, \xi^k (m+\rho) a_{nm} \xi^{(m+\rho-2)} + \\ &+ \quad \sum_{m,k=0}^{\infty} q_k\, \xi^k a_{nm} \xi^{(k+\rho-2)} = 0, \end{aligned} \tag{C.1.6}$$

where ρ and the a_{nm} are unknown. Equation (C.1.6) is a polynomial expression which involves powers of ξ. For (C.1.6) to be satisfied $\forall\, \xi \in (0,1)$, we must require that the coefficients of each power of ξ are zero. Starting from the lowest power $\xi^{\rho-2}$ (obtained with $m = k = 0$) we have

$$a_{n0} \left[\rho^2 + (p_0 - 1)\,\rho + q_0\right] = 0, \tag{C.1.7}$$

which is the indicial equation. Setting the arbitrary parameter $a_{n0} = 1$, the roots ρ_1, ρ_2 of the indicial equation (C.1.7) give the two indexes of the series expansion (C.1.4). With $p_0 = 1$ and $q_0 = 0$, (C.1.7) simply becomes $\rho^2 = 0$. Hence $\rho_1 = \rho_2 = 0$ are two coinciding indexes. According to Frobenius' theory, in this case only one independent solution of (C.1.2) has the sought form (C.1.4). The other solution has instead logarithmic terms and can be obtained only via further investigation (see Bender and Orzsag, 1978). Back to the first independent solution (C.1.4), the unknown terms $a_{nm}(\rho;\lambda)$ are to be found by setting to zero the remaining coefficients of the polynomial expression (C.1.6). Hence we get:

$$a_{nm}(\rho;\lambda) = \frac{1}{(m+\rho)^2} \sum_{k=1}^{m} a_{n,m-k}(\rho) \left[n^2(k-1) - \frac{\lambda^2 r_0}{2}\left(k + k^2\right)\right], \; m = 1, 2, \ldots \tag{C.1.8}$$

Then by substituting $\rho = 0$ in the latter relations we get the sought expression for the coefficients $a_{nm}(\lambda) = a_{nm}(\rho = 0; \lambda)$ of the series expansion (C.1.4):

$$a_{nm}(\lambda) = \frac{1}{m^2} \sum_{k=1}^{m} a_{n,m-k} \left[n^2(k-1) - \frac{\lambda^2 r_0}{2} \left(k + k^2\right) \right], \; m = 1, 2, \ldots \tag{C.1.9}$$

so that the first independent solution of the transformed equation (C.1.2) is

$$Z_n(\xi; \lambda) = \sum_{m=0}^{\infty} a_{nm}(\lambda)\, \xi^m \,, \tag{C.1.10}$$

with the a_{nm} given by (C.1.9). The Confluent Heun function of first kind and order n in terms of r (recall C.1.1) is

$$Hc_n^{(1)}(r/r_0; \lambda) \equiv Z_n(\xi; \lambda) = \sum_{m=0}^{\infty} a_{nm}(\lambda) \left(1 - \frac{r_0}{r}\right)^m , \tag{C.1.11}$$

and it represents the first independent solution of the governing equation (C.0.2). As done in section §1, the parametric dependence on the radius r_0 is further omitted for the sake of brevity. The series solution (C.1.11) has been checked numerically against the result of Zhang and Zhu (1994) showing perfect agreement. The second independent solution can now be found by differentiating the Frobenius series (C.1.4) with respect to the index ρ. In so doing, define the shorthand notation

$$L\cdot = (\cdot)_{\xi\xi} + \frac{p(\xi)}{\xi}(\cdot)_{\xi} + \frac{q(\xi)}{\xi^2}(\cdot),$$

such that (C.1.2) can be rewritten as $LZ(\xi; \lambda) = 0$. The general Frobenius expansion (C.1.4) satisfies

$$LZ(\xi; \lambda) = a_{n0}\, \xi^{\rho-2}\, \rho^2. \tag{C.1.12}$$

Indeed, by setting $\rho = 0$, the right hand of the latter expression vanishes and the polynomial expression (C.1.6) is obtained again, leading back to the first independent solution. However, differentiating (C.1.12) with respect to the index ρ and then substituting $\rho = 0$ yield

$$L\left[\left.\frac{\partial Z}{\partial \rho}\right|_{\rho=0} \right] = 0. \tag{C.1.13}$$

Therefore

$$\left.\frac{\partial Z}{\partial \rho}\right|_{\rho=0} = \ln(\xi) \sum_{m=0}^{\infty} a_{nm}(\lambda)\xi^m + \sum_{m=0}^{\infty} b_{nm}(\lambda)\xi^m$$

is also an independent solution of (C.1.2). The series coefficients

$$b_{nm}(\lambda) = \left.\frac{\partial a_{nm}(\rho; \lambda)}{\partial \rho}\right|_{\rho=0}$$

must satisfy the following relationship in order to be a solution of (C.1.13)

$$b_{nm}(\lambda) = \frac{1}{m^2} \sum_{k=1}^{m} b_{m-k} \left[n^2(k-1) - \frac{\lambda^2 r_0}{2} \left(k + k^2\right) \right] - \frac{2}{m}\, a_{nm}(\lambda)\,, \quad m = 1, 2, \ldots \tag{C.1.14}$$

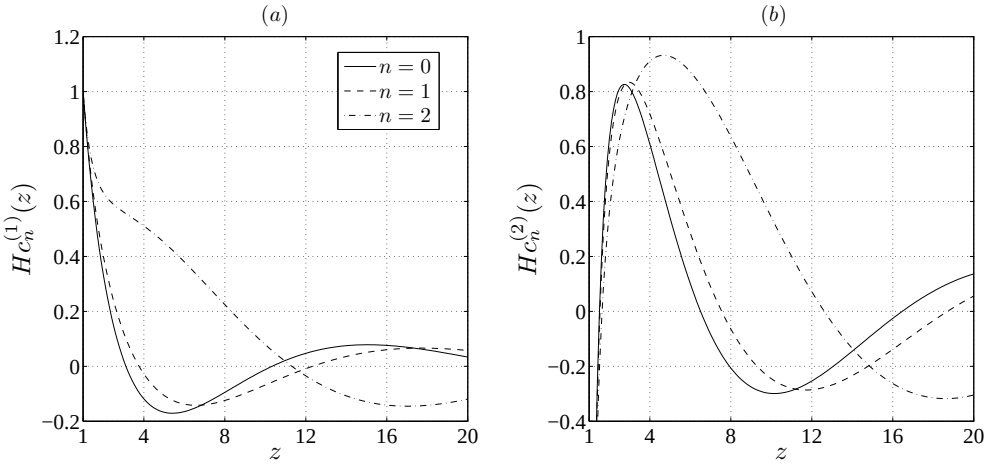

FIGURE C.1: Confluent Heun functions of the first kind $Hc_n^{(1)}$ (a) and of the second kind $Hc_n^{(2)}$ (b) for the first modes. Parameters are: $\omega = 1$, $r_0 = 1$. Note that $Hc_n^{(1)}(r_0) = 1$ and $Hc_n^{(2)}(z) \to -\infty$ as $z \to r_0$.

with $b_{n0} = 0$ and the a_{nm} given by (C.1.9). Back to the original variable r via the transforms (C.1.1), the second independent solution to (C.0.2) is then the Confluent Heun function of second kind and order n

$$Hc_n^{(2)}(r;\lambda) = \ln\left(1 - \frac{r_0}{r}\right) \sum_{m=0}^{\infty} a_{nm}(\lambda) \left(1 - \frac{r_0}{r}\right)^m + \sum_{m=0}^{\infty} b_{nm}(\lambda) \left(1 - \frac{r_0}{r}\right)^m. \quad \text{(C.1.15)}$$

The general solution of (C.0.2) is the linear combination of the two independent ones, respectively (C.1.11) and (C.1.15):

$$R_n(r;\lambda) = \alpha_n \, Hc_n^{(1)}(r;\lambda) + \beta_n \, Hc_n^{(2)}(r;\lambda).$$

The variations of $Hc_n^{(1)}$ and $Hc_n^{(2)}$ for the first modes are plotted in figure C.1.

C.2 Wronskian

Let us rewrite the confluent Heun equation (C.0.2) in the Sturm-Liouville form

$$\frac{\mathrm{d}}{\mathrm{d}r}\left(hrR_{n,r}\right) + \left[(\mathrm{i}\omega)^2 r - \frac{n^2 h}{r}\right] R_n = 0, \quad \text{(C.2.1)}$$

where $h = r - r_0$, $\omega = \mathrm{i}\lambda$. The two linearly independent solutions of (C.2.1), $R_n^{(1)} = Hc_n^{(1)}(r;\mathrm{i}\omega)$ and $R_n^{(2)} = Hc_n^{(2)}(r;\mathrm{i}\omega)$ satisfy then

$$\frac{\mathrm{d}}{\mathrm{d}r}\left(hrR_{n,r}^{(1)}\right) + \left[(\mathrm{i}\omega)^2 r - \frac{n^2 h}{r}\right] R_n^{(1)} = 0$$

and

$$\frac{\mathrm{d}}{\mathrm{d}r}\left(hrR_{n,r}^{(2)}\right) + \left[(\mathrm{i}\omega)^2 r - \frac{n^2 h}{r}\right] R_n^{(2)} = 0$$

respectively. Now multiplying the first of the latter equations by $R_n^{(2)}$, the second one by $R_n^{(1)}$ and then subtracting the two results, we get

$$\frac{\mathrm{d}}{\mathrm{d}r}\left(hrR_{n,r}^{(1)}R^{(2)} - hrR_{n,r}^{(2)}R_n^{(1)}\right) = 0.$$

Integration of this differential equation with respect to r provides

$$R_n^{(1)}R_{n,r}^{(2)} - R_{n,r}^{(1)}R_n^{(2)} = -\frac{A}{r(r-r_0)}, \tag{C.2.2}$$

where the left-side term is indeed the Wronskian $W\left[R_n^{(1)}, R_n^{(2)}\right]$ of the two independent solutions. The integration constant A can be found by directly evaluating the Wronskian W as r tends to r_0. For $r \to r_0$ the behaviour of the two functions $R_n^{(1)} = Hc_n^{(1)}(r;\mathrm{i}\omega)$ and $R_n^{(2)} = Hc_n^{(2)}(r;\mathrm{i}\omega)$ is defined by truncating the series solutions (C.1.11) and (C.1.15) respectively to terms of order $O(1-r_0/r)$. This yields

$$R_n^{(1)} = Hc_n^{(1)}(r;\mathrm{i}\omega) \simeq 1 + \omega^2 r_0\left(1 - \frac{r_0}{r}\right)$$

for the first solution and

$$R_n^{(2)} = Hc_n^{(2)}(r;\mathrm{i}\omega) \simeq \ \ln\left(1-\frac{r_0}{r}\right)\left[1+\omega^2 r_0\left(1-\frac{r_0}{r}\right)\right] - 2\omega^2 r_0\left(1-\frac{r_0}{r}\right)$$

for the second solution. Derivatives $R_{n,r}^{(1)}$ and $R_{n,r}^{(2)}$ for $r \to r_0$ can be evaluated by differentiating the above expressions with respect to r. Then equation (C.2.2) becomes

$$W = \frac{r_0}{r(r-r_0)} + \omega^4\frac{r_0^3}{r^3}(r-r_0) = -\frac{A}{r_0\,(r-r_0)},$$

which in the limit for $r \to r_0$ yields $A = -r_0$, i.e.

$$W\left[Hc_n^{(1)}(r;\mathrm{i}\omega), Hc_n^{(2)}(r;\mathrm{i}\omega)\right] = W(r) = \frac{r_0}{r(r-r_0)}. \tag{C.2.3}$$

C.3 Asymptotic behaviour for large parameter $\lambda = \mathrm{i}\omega$

Consider the confluent Heun equation (C.0.2), whose independent solutions are the two confluent Heun functions $Hc_n^{(1)}(r;\lambda)$ and $Hc_n^{(2)}(r;\lambda)$ of first and second kind respectively. Now let the parameter $\lambda = \mathrm{i}\omega$, with $\omega \in \mathbb{C}$. Then, the $a_{nm}(\lambda = \mathrm{i}\omega)$ are

$$a_{n,0} = 1, \quad a_{n,1} = \omega^2 r_0, \quad a_{n,2} = \tfrac{1}{4}\,\omega^4 r_0^2 + \tfrac{3}{4}\,\omega^2 r_0 + \tfrac{1}{4}\,n^2$$
$$a_{n,3} = \tfrac{1}{36}\,\omega^6 r_0^3 + \tfrac{5}{12}\,\omega^4 r_0^2 + \left(\tfrac{5}{36}\,n^2 + \tfrac{2}{3}\right)\omega^2 r_0 + \tfrac{2}{9}\,n^2.$$

For very large ω we retain only the higher order terms in the preceding expansions, thus getting the following approximated behaviour for the a_{nm}:

$$a_{nm} \simeq \frac{\left(\omega\sqrt{r_0}\right)^{2m}}{(m!)^2}, \quad m = 1, 2, \ldots \tag{C.3.1}$$

Therefore, to the crudest approximation,

$$Hc_n^{(1)}(r;\mathrm{i}\omega) \simeq \sum_{m=0}^{\infty}\frac{(x/2)^{2m}}{(m!)^2} = I_0(x)$$

where $x = 2\omega\sqrt{r_0(1-r_0/r)}$ and $I_0(x)$ is the modified Bessel function of first kind and order zero. Hence, for large ω

$$Hc_n^{(1)}(r;\mathrm{i}\omega) \simeq I_0\left[2\omega\sqrt{r_0\left(1-\frac{r_0}{r}\right)}\right]. \tag{C.3.2}$$

The second independent solution of the CHE $Hc_n^{(2)}$ has coefficients b_{nm} given by (C.1.14), which letting $\lambda = \mathrm{i}\omega$ and $\omega \to \infty$ can be approximated by

$$b_{n,0} = 0, \quad b_{n,m} \simeq -2\left(1+\frac{1}{2}+\frac{1}{3}+\cdots+\frac{1}{m}\right)\frac{1}{(m!)^2}\left(\omega\sqrt{r_0}\right)^{2m}, \quad m = 1,2,\ldots \tag{C.3.3}$$

Therefore to the crudest approximation for $\omega \to \infty$, recalling (C.1.15) and (C.3.2), we obtain

$$\begin{aligned} Hc_n^{(2)}(r;\mathrm{i}\omega) \simeq 2\Bigg\{\ln\left(\tfrac{x}{2\omega\sqrt{r_0}}\right)I_0(x) - \Bigg[\tfrac{x^2}{4} + \left(1+\tfrac{1}{2}\right)\tfrac{1}{(2!)^2}\left(\tfrac{x^2}{4}\right)^2 + \\ + \left(1+\tfrac{1}{2}+\tfrac{1}{3}\right)\tfrac{\left(x^2/4\right)^3}{(3!)^2} + \ldots\Bigg]\Bigg\}, \end{aligned} \tag{C.3.4}$$

with

$$x = 2\omega\sqrt{r_0\left(1-\frac{r_0}{r}\right)}.$$

Now, the terms inside the square brackets of the latter equation can be further expressed as

$$\frac{x^2}{4} + \left(1+\frac{1}{2}\right)\frac{1}{(2!)^2}\left(\frac{x^2}{4}\right)^2 + \cdots = K_0(x) + \left[\ln\left(\frac{x}{2}\right)+\gamma\right]I_0(x),$$

with $\gamma = 0.577\ldots$ and K_0 the modified Bessel function of second kind and order zero (see Abramowitz and Stegun, 1972). Hence expression (C.3.4) can be simplified as

$$\begin{aligned} Hc_n^{(2)}(r;\mathrm{i}\omega) \simeq 2\Bigg\{I_0\left[2\omega\sqrt{r_0\left(1-\tfrac{r_0}{r}\right)}\right]\left[\ln\left(\tfrac{1}{\omega\sqrt{r_0}}\right)-\gamma\right] + \\ - K_0\left[2\omega\sqrt{r_0\left(1-\tfrac{r_0}{r}\right)}\right]\Bigg\}, \end{aligned} \tag{C.3.5}$$

for large $\omega \in \mathbb{C}$. Moreover, in the complex half-plane $|\arg(\omega)| < \pi/2$, $K_0 \to 0$ for large ω. The asymptotic expansion (C.3.5) can be further approximated to the leading behaviour

$$Hc_n^{(2)}(r;\mathrm{i}\omega) \simeq -2I_0\left[2\omega\sqrt{r_0\left(1-\frac{r_0}{r}\right)}\right]\ln\left(\omega\sqrt{r_0}\right). \tag{C.3.6}$$

for large ω, with $|\arg(\omega)| < \pi/2$.

C.4 Behaviour for small parameter λ

The behaviour of the confluent Heun functions for small λ can be obtained by keeping only the first term in the relevant series expansions, with the argument r/r_0 regarded as a parameter. Hence the confluent Heun function of the first kind (C.1.11) becomes

$$Hc_n^{(1)}(r;\lambda) \simeq Hc_n^{(1)}(r;0) + O(\lambda^2), \tag{C.4.1}$$

while

$$Hc_n^{(2)}(r;\lambda) \simeq Hc_n^{(2)}(r;0) + O(\lambda^2), \tag{C.4.2}$$

is the approximation of the confluent Heun function of second kind (C.1.15). Asymptotic expansions of derivatives for small λ are defined accordingly, giving respectively

$$Hc_{n,r}^{(1)}(r;\lambda) \simeq Hc_{n,r}^{(1)}(r;0) + O(\lambda^2)$$

and

$$Hc_{n,r}^{(2)}(r;\lambda) \simeq Hc_{n,r}^{(2)}(r;0) + O(\lambda^2).$$

Appendix D

Complex integrals evaluation

D.1 Evaluation of the inner integral of (5.3.1)

Consider the integral in the far field

$$\int_{c-\mathrm{i}\infty}^{c+\mathrm{i}\infty} f_n(\omega)\mathrm{e}^{\omega t}\mathrm{d}\omega, \tag{D.1.1}$$

where

$$f_n(\omega) = \frac{F_n(\rho;\omega)Hc_n^{(1)}(\rho;\mathrm{i}\omega)K_n(\omega r/\sqrt{h_b})}{\Delta_n^{(1)}(\omega)}. \tag{D.1.2}$$

Here $\rho \in (r_0, b)$ and $r \in (b, \infty)$ are regarded as parameters, the forcing function F_n is given by (5.2.17) and the denominator $\Delta_n^{(1)}$ by (5.2.27). c is a positive real constant. A branch cut on the negative real axis is introduced to avoid multivaluedness of K_n (see Abramowitz and Stegun, 1972).

For $t < 0$, take a large semicircular contour C_R on the half-plane

$$\Omega = \{\omega \in \mathbb{C} : |\arg(\omega)| < \pi/2, \omega \neq 0\},$$

to form the closed circuit Γ, as depicted in figure D.1 . Hence

$$\int_{c-\mathrm{i}\infty}^{c+\mathrm{i}\infty} f_n(\omega)\mathrm{e}^{\omega t}\mathrm{d}\omega = \oint_{\Gamma} f_n\mathrm{e}^{\omega t}\mathrm{d}\omega - \int_{C_R} f_n\mathrm{e}^{\omega t}\mathrm{d}\omega. \tag{D.1.3}$$

Note that in the complex domain Ω each of the functions at the numerator of f_n, expression (D.1.2), are entire functions of ω (K_n has a pole at $\omega = 0 \notin \Omega$). The denominator $\Delta_n^{(1)}$ (5.2.27) of the integrand f_n has no zeros in the same complex domain, as shown in figure D.2(a,b). Since no poles are found for f_n,

$$\oint_{\Gamma} f_n\mathrm{e}^{\omega t} = 0,$$

as a result of Cauchy's theorem. On the large semicircular contour C_R the function F_n (5.2.17) at the numerator of the integrand f_n (5.3.2) can be expanded for large ω as

$$F_n(\rho;\omega) \simeq -2\Pi_n (r - r_s),$$

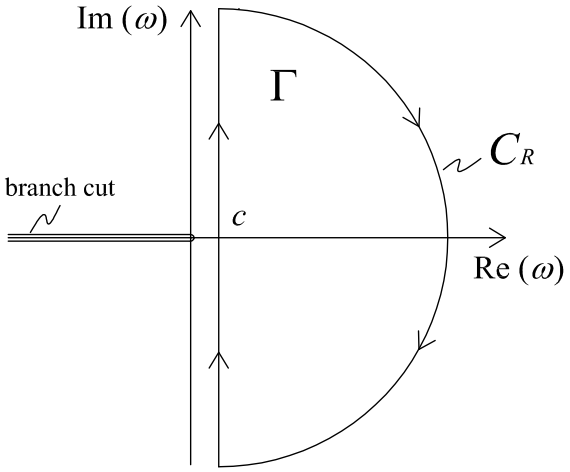

FIGURE D.1: Integration contour Γ for $t < 0$ and the semi-circular contour C_R.

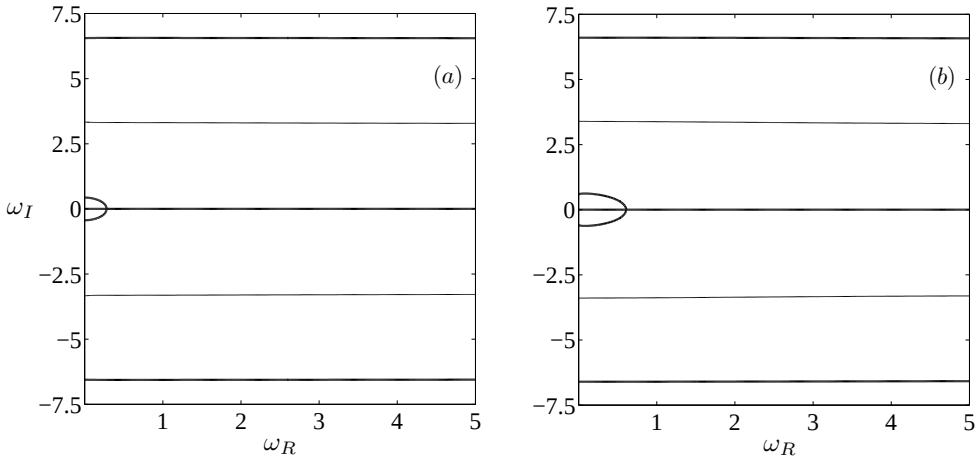

FIGURE D.2: Contour plots of the curves $\mathrm{Re}\left\{\Delta_n^{(1)}(\omega)\right\} = 0$ (solid line) and $\mathrm{Im}\left\{\Delta_n^{(1)}(\omega)\right\} = 0$ (bold line) in the complex $\omega = \omega_R + \mathrm{i}\omega_I$ plane, for modal order $n = 0$ (a) and $n = 1$ (b). Parameters are: $r_0 = 11.82$, $b = 25.43$. Complex zeros of $\Delta_n^{(1)}$, expression (5.2.27), occur at the points of intersection of the two curves $\mathrm{Re}\left\{\Delta_n^{(1)}\right\} = 0$ and $\mathrm{Im}\left\{\Delta_n^{(1)}\right\} = 0$. Note that no point of intersection is found in the domain considered.

i.e. a constant, having used the approximation $\mathrm{erf}(-x) \simeq -1 + \mathrm{e}^{-x^2}/\sqrt{\pi}x$ for large x. Also, recall the asymptotic expression (C.3.2)

$$Hc_n^{(1)}(r; \mathrm{i}\omega) \simeq I_0\left(2\omega\sqrt{r_0(1 - r_0/r)}\right),$$

as shown in appendix C.3. Finally, the modified Bessel functions of first and second kind can be approximated to the leading order by

$$I_n(x) \simeq \frac{\mathrm{e}^{\,x}}{\sqrt{2\pi x}}, \quad \text{if } |\arg(x)| < \frac{\pi}{2}$$

and

$$K_n(x) \simeq \frac{\mathrm{e}^{-x}}{\sqrt{\frac{2}{\pi}\,x}}, \quad \text{if } |\arg(x)| < \frac{3}{2}\pi$$

respectively (see Abramowitz and Stegun, 1972). By substituting the asymptotic expansions of F_n, $Hc_n^{(1)}$, I_n and K_n for large ω into the integrand function $f_n(\omega)$ (D.1.2), we get the leading behaviour of f_n for large ω:

$$f_n(\omega) \simeq \frac{\mathrm{e}^{-(\alpha\omega+\beta)}}{\omega}, \tag{D.1.4}$$

where

$$\alpha = 2\sqrt{r_0}\left(\sqrt{1 - \frac{r_0}{b}} - \sqrt{1 - \frac{r_0}{\rho}}\right) \tag{D.1.5}$$

and

$$\beta = h_b^{-1/2}(r - b) \tag{D.1.6}$$

are constant for fixed ρ and r. Since $\rho \in (r_0, b)$ and $r \in (b, \infty)$, both the terms α (D.1.5) and β (D.1.6) are positive. Now let us substitute $\omega = R\mathrm{e}^{\mathrm{i}\vartheta}$, $|\vartheta| < \pi/2$ inside (D.1.4); since

$$\mathrm{Re}\,\{\omega\} = R\cos\vartheta > 0,$$

the asymptotic expansion (D.1.4) on the large semicircular contour C_R is a negative exponential of R. As a result $|f_n| \to 0$ in the limit $R \to \infty$. The application of the Jordan's lemma gives then

$$\int_{C_R} f_n \mathrm{e}^{\omega t}\mathrm{d}\omega = 0,$$

so that

$$\int_{c-\mathrm{i}\infty}^{c+\mathrm{i}\infty} f_n(\omega)\mathrm{e}^{\omega t}\mathrm{d}\omega = 0$$

for $t < 0$.

For $t > 0$, consider the new integration path $\Gamma \subseteq \Omega$ shown in figure D.3. As above, we may write

$$\int_{c-\mathrm{i}\infty}^{c+\mathrm{i}\infty} f_n(\omega)\mathrm{e}^{\omega t}\mathrm{d}\omega = \left(\oint_\Gamma - \int_{\Gamma^+} - \int_{\Gamma^-} - \int_{\Gamma_\epsilon}\right) f_n(\omega)\mathrm{e}^{\omega t}\mathrm{d}\omega, \tag{D.1.7}$$

where the straight lines Γ^+ and Γ^- are parallel to the real axis at $\mathrm{Im}\,\{\omega\} = \pm\infty$ respectively, and the line Γ_ϵ lies just on the right of the imaginary axis, with $\epsilon \ll 1$

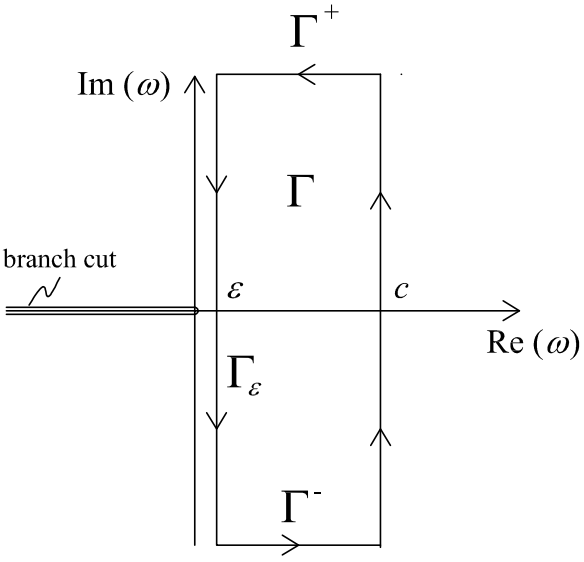

FIGURE D.3: Integration contour Γ for $t > 0$.

(see figure D.3); $f_n(\omega)$ is still given by (D.1.2). As seen above, the integrand f_n has no poles for $\omega \in \Omega$. Hence application of the Cauchy theorem to the first integral gives

$$\oint_{\Gamma} f_n(\omega) \mathrm{e}^{\omega t} \mathrm{d}\omega = 0.$$

Now, as ϵ approaches zero, the second integral on the straight line Γ^+ can be written as

$$\int_{\Gamma^+} f_n(\omega) \mathrm{e}^{\omega t} \mathrm{d}\omega = \lim_{\delta \to \infty} \int_c^{\epsilon} f_n(s + \mathrm{i}\delta) \mathrm{e}^{(s+\mathrm{i}\delta)t} \mathrm{d}s = \lim_{\delta \to \infty} \mathrm{e}^{-\beta + \mathrm{i}\delta(t-\alpha)} \int_c^{\epsilon} \frac{\mathrm{e}^{s(t-\alpha)}}{s + \mathrm{i}\delta} \mathrm{d}s = 0, \tag{D.1.8}$$

having used the asymptotic formula (D.1.4) for f_n. Analogous considerations can be made on the third integral in (D.1.7), yielding

$$\int_{\Gamma^-} f_n(\omega) \mathrm{e}^{\omega t} = 0.$$

Expression (D.1.7) becomes

$$\int_{c-\mathrm{i}\infty}^{c+\mathrm{i}\infty} f_n(\omega) \mathrm{e}^{\omega t} \mathrm{d}\omega = \int_{\epsilon-\mathrm{i}\infty}^{\epsilon+\mathrm{i}\infty} f_n(\omega) \mathrm{e}^{\omega t} \mathrm{d}\omega.$$

Consider the transform

$$\omega = \mathrm{e}^{\mathrm{i}\pi/2} s, \tag{D.1.9}$$

which is a rotation of -90 degrees about the origin. The latter integral equation becomes then

$$\int_{c-\mathrm{i}\infty}^{c+\mathrm{i}\infty} f_n(\omega) \mathrm{e}^{\omega t} \mathrm{d}\omega = \mathrm{i} \int_{-\infty-\mathrm{i}\epsilon}^{+\infty-\mathrm{i}\epsilon} f_n(\mathrm{i}s) \mathrm{e}^{\mathrm{i}st} \mathrm{d}s \doteq \mathrm{i}\, L_n(s). \tag{D.1.10}$$

In the limit $\epsilon \to 0$, the new integration path becomes slightly deformed due to the presence of the pole for K_n at $\omega = 0$. The branch cut is now placed on the positive

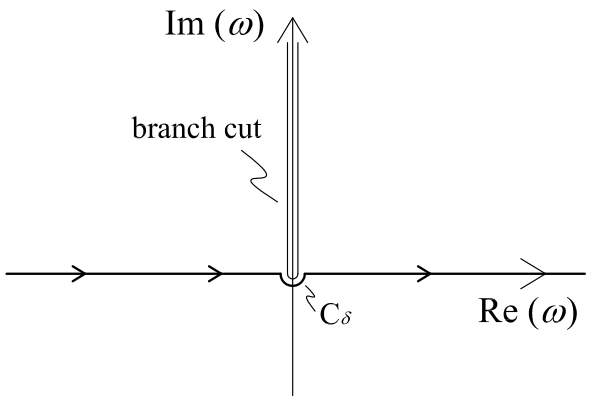

FIGURE D.4: Integration path (bold line) for (D.1.10). Note that the presence of the pole for K_n at $\omega = 0$ induces a deformation of the path, generating the small semicircle C_δ.

imaginary axis after having applied the transform (D.1.9)(see figure D.4). Hence we obtain

$$L_n(s) = \int_{-\infty-\mathrm{i}\epsilon}^{+\infty-\mathrm{i}\epsilon} f_n(\mathrm{i}s)\mathrm{e}^{\mathrm{i}st}\mathrm{d}s = \left(\int_{-\infty}^{0} + \int_{0}^{\infty} + \int_{C_\delta}\right) f_n(\mathrm{i}s)\,\mathrm{e}^{\mathrm{i}st}\mathrm{d}s, \tag{D.1.11}$$

C_δ being a small semi-circle of radius $\delta \ll 1$ surrounding the origin of the complex plane, as depicted in figure D.4. To evaluate the integral on the semi-cricle C_δ, consider

$$f_n(\mathrm{i}s) = \frac{F_n(\rho;\mathrm{i}s)Hc_n^{(1)}(\rho;s)K_n(\mathrm{i}sr/\sqrt{h_b})}{\Delta_n^{(1)}(\mathrm{i}s)}, \tag{D.1.12}$$

as $s \to 0$. The forcing term F_n (5.2.17) at the numerator of (D.1.12) can be approximated as

$$F_n(\rho;\mathrm{i}s) \simeq -2\,(\rho - r_s)\,\mathrm{e}^{-(\rho-r_s)^2}$$

for small s, ρ being still regarded as a parameter; the asymptotic expansion of the modified Bessel functions of second kind is instead

$$\left\{ \begin{array}{c} K_0(x) \\ K_n(x) \end{array} \right\} \simeq \left\{ \begin{array}{c} -\ln(x) \\ \frac{1}{2}(n-1)!\left(\frac{x}{2}\right)^{-n} \end{array} \right\}$$

for small argument $x \in \mathbb{C}$ and $n = 1, 2, \ldots$ (see Abramowitz and Stegun, 1972). Finally, the confluent Heun function of first kind can be expanded for small parameter s as shown in appendix C.4 , yielding

$$Hc_n^{(1)}(r;s) \simeq Hc_n^{(1)}(r;0) + O(s^2),$$

where the first expansion term is a finite value depending on the parameter $r/r_0 \in (1,\infty)$. The derivative of the confluent Heun function of the first kind $Hc_{n,r}^{(1)}$ is defined accordingly

$$Hc_{n,r}^{(1)}(r;s) \simeq Hc_{n,r}^{(1)}(r;0) + O(s^2).$$

Substituting the approximated forms for the forcing function F_n, the modified Bessel function K_n and the confluent Heun function $Hc_n^{(1)}$ into both the numerator and the denominator $\Delta_n^{(1)}(\mathrm{i}s)$ of (D.1.12) yields

$$f_0(\mathrm{i}s) \simeq 2b\,(\rho - r_s)\,\mathrm{e}^{-(\rho-r_s)^2}\ln\left(\frac{\mathrm{i}sr}{\sqrt{h_b}}\right) \tag{D.1.13}$$

for $n = 0$ and

$$f_n(\mathrm{i}s) \simeq \frac{Hc_n^{(1)}(\rho;0)\left(\frac{b}{r}\right)^n\left[-2\left(\rho - r_s\right)\mathrm{e}^{-(\rho-r_s)^2}\right]}{\frac{n}{b}Hc_n^{(1)}(b;0) + Hc_{n,r}^{(1)}(b;0)} = O(1) \tag{D.1.14}$$

for $n = 1, 2, \ldots$, $s \ll 1$. Note that in (D.1.13) and (D.1.14) r and ρ are to be regarded as parameters. With the approximated forms (D.1.13) and (D.1.14) the integral on the semi-circle C_δ (third of D.1.11) becomes

$$\int_{C_\delta} f_0(\mathrm{i}s)\mathrm{e}^{\mathrm{i}st}\mathrm{d}s \simeq 2b\left(\rho - r_s\right)\mathrm{e}^{-(\rho-r_s)^2}\int_{C_\delta}\ln\left(\frac{\mathrm{i}sr}{\sqrt{h_b}}\right)\mathrm{d}s \tag{D.1.15}$$

for $n = 0$ and

$$\int_{C_\delta} f_n(\mathrm{i}s)\mathrm{e}^{\mathrm{i}st}\mathrm{d}s \simeq \int_{C_\delta} O(1)\mathrm{d}s \tag{D.1.16}$$

for $n = 1, 2, \ldots$ respectively. Making use of the parametric transform $s = \delta\mathrm{e}^{\mathrm{i}\phi}$, $\phi \in (-\pi, 0)$, and letting $\delta \to 0$ yield

$$\int_{C_\delta} f_0(\mathrm{i}s)\mathrm{e}^{\mathrm{i}st}\mathrm{d}s \propto \delta\int_{-\pi}^{0}\ln\left(\mathrm{i}\,\delta\mathrm{e}^{\mathrm{i}\phi}\right)\mathrm{e}^{\mathrm{i}\phi}\mathrm{d}\phi \to 0$$

for (D.1.15) and

$$\int_{C_\delta} f_n(\mathrm{i}s)\mathrm{e}^{\mathrm{i}st}\mathrm{d}s \propto \delta\int_{-\pi}^{0} O(1)\mathrm{e}^{\mathrm{i}\phi}\mathrm{d}\phi \to 0$$

for (D.1.16). Hence the integral form (D.1.11) simplifies into

$$L_n(s) = \int_{-\infty}^{\infty} f_n(\mathrm{i}s)\mathrm{e}^{\mathrm{i}st}\mathrm{d}s,$$

and the Laplace integral (D.1.10) becomes

$$\int_{c-\mathrm{i}\infty}^{c+\mathrm{i}\infty} f_n(\omega)\mathrm{e}^{\omega t}\mathrm{d}\omega = \mathrm{i}\,L_n(s) = \mathrm{i}\int_{-\infty}^{\infty} f_n(\mathrm{i}s)\mathrm{e}^{\mathrm{i}st}\mathrm{d}s.$$

D.2 Evaluation of the integral (5.3.14)

Consider the complex integral

$$\int_{c-\mathrm{i}\infty}^{c+\mathrm{i}\infty} f_{jn}(\rho,\omega)\mathrm{d}\omega, \quad j = 1, 2$$

where

$$f_{1n}(\rho,\omega) = F_n(\rho;\omega)\left[Hc_n^{(1)}(\rho;\mathrm{i}\omega)\frac{\Delta_n^{(2)}(\omega)}{\Delta_n^{(1)}(\omega)} - Hc_n^{(2)}(\rho;\mathrm{i}\omega)\right]Hc_n^{(1)}(r;\mathrm{i}\omega)$$

and

$$f_{2n}(\rho,\omega) = F_n(\rho;\omega)\left[Hc_n^{(1)}(\rho;\mathrm{i}\omega)Hc_n^{(2)}(r;\mathrm{i}\omega) - Hc_n^{(2)}(\rho;\mathrm{i}\omega)Hc_n^{(1)}(r;\mathrm{i}\omega)\right].$$

In the latter expressions, F_n is the forcing function (5.2.17), while $\Delta_n^{(1,2)}$ are given by (5.2.27); ρ and r are fixed parameters.

For $t < 0$, take the large semicircular contour C_R depicted in figure D.1. Hence

$$\int_{c-\mathrm{i}\infty}^{c+\mathrm{i}\infty} f_{jn}(\rho,\omega)\mathrm{d}\omega = \oint_\Gamma f_{jn}\mathrm{e}^{\omega t}\mathrm{d}\omega - \int_{C_R} f_{jn}\mathrm{e}^{\omega t}\mathrm{d}\omega,$$

where Γ is the closed circuit represented in figure D.1. Since both f_{jn}, $j = 1, 2$ are entire functions of $\omega \in \Omega$, again

$$\oint_\Gamma f_{jn}\mathrm{e}^{\omega t}\mathrm{d}\omega = 0$$

by application of the Cauchy theorem. Furthermore, repeating the same algebra of the previous section, it is straightforward to show that $|f_{jn}(\rho,\omega)| \to 0$ as $|\omega| \to \infty$. As a consequence of the Jordan lemma,

$$\int_{C_R} f_{jn}(\rho,\omega)\mathrm{e}^{\omega t} = 0$$

and

$$\int_{c-\mathrm{i}\infty}^{c+\mathrm{i}\infty} f_{jn}(\omega)\mathrm{e}^{\omega t}\mathrm{d}\omega = 0, \quad j = 1, 2$$

for $t < 0$.

For $t > 0$, consider again the closed circuit shown in figure D.3. As seen before

$$\int_{c-\mathrm{i}\infty}^{c+\mathrm{i}\infty} f_{jn}\mathrm{e}^{\omega t}\mathrm{d}\omega = \left(\oint_\Gamma - \int_{\Gamma^+} - \int_{\Gamma^-} - \int_{\Gamma_\epsilon}\right) f_{jn}(\omega)\mathrm{e}^{\omega t}\mathrm{d}\omega, \tag{D.2.1}$$

where Γ^+ and Γ^- are two straight lines parallel to the real axis at $\Im\{\omega\} = \pm\infty$ respectively, and the line Γ_ϵ lies just on the right of the imaginary axis, with $\epsilon \ll 1$ (see figure D.3). Again, since the f_{jn} are entire functions of $\omega \in \Omega$, application of the Jordan lemma gives

$$\oint_\Gamma f_{jn}\,\mathrm{e}^{\omega t}\mathrm{d}\omega = 0.$$

Using the same argument of section §3.1, it is immediate to show that

$$\int_{\Gamma^{(+,-)}} f_{jn}\,\mathrm{e}^{\omega t}\mathrm{d}\omega = \lim_{\delta\to\infty}\int_{(c,\epsilon)}^{(\epsilon,c)} f_{jn}(s(+,-)\mathrm{i}\delta)\,\mathrm{e}^{(s(+,-)\mathrm{i}\delta)t}\mathrm{d}s = 0.$$

Therefore we are only left with

$$\int_{c-\mathrm{i}\infty}^{c+\mathrm{i}\infty} f_{jn}\,\mathrm{e}^{\omega t}\mathrm{d}\omega = \int_{\epsilon-\mathrm{i}\infty}^{\epsilon+\mathrm{i}\infty} f_{jn}\,\mathrm{e}^{\omega t}\mathrm{d}\omega,$$

$\epsilon \ll 1$. With the change of variable $s = \mathrm{e}^{\mathrm{i}\pi/2}\omega$, the latter integral equation becomes

$$\int_{c-\mathrm{i}\infty}^{c+\mathrm{i}\infty} f_{jn}\,\mathrm{e}^{\omega t}\mathrm{d}\omega = \mathrm{i}\int_{-\infty-\mathrm{i}\epsilon}^{\infty-\mathrm{i}\epsilon} f_{jn}(\mathrm{i}s)\,\mathrm{e}^{\mathrm{i}st}\mathrm{d}s \doteq \mathrm{i}L_{jn}(s), \tag{D.2.2}$$

where the new integration path is slightly below the real s axis. Letting $\epsilon \to 0$, the integrals $L_{jn}(s)$ are evaluated again on the deformed contour shown in figure D.4, thus yielding

$$L_{jn}(s) = \left(\int_{-\infty}^{\infty} + \int_{C_\delta}\right) f_{jn}\mathrm{e}^{st}\mathrm{d}s,$$

where C_δ is the semi-circular path of radius $\delta \ll 1$ (see again figure D.4). Consider the two integrand functions

$$f_{1n}(\rho, \mathrm{i}s) = F_n(\rho; \mathrm{i}s) \left[Hc_n^{(1)}(\rho; s) \frac{\Delta_n^{(2)}(\mathrm{i}s)}{\Delta_n^{(1)}(\mathrm{i}s)} - Hc_n^{(2)}(\rho; s) \right] Hc_n^{(1)}(r; s)$$

and

$$f_{2n}(\rho, \mathrm{i}s) = F_n(\rho, \mathrm{i}s) \Big[Hc_n^{(1)}(\rho; \mathrm{i}s)\, Hc_n^{(2)}(r; s) + \\ -Hc_n^{(2)}(\rho; s)\, Hc_n^{(1)}(r; s) \Big].$$

With the limiting forms for F_n, K_n, $Hc_n^{(1)}$ and $Hc_n^{(2)}$ already used in the previous subsection, it is immediate to show that

$$|f_{jn}(\mathrm{i}s)| = O(1),\ j = 1, 2, \ldots,$$

as s tends to zero. Once again $\int_{C_\delta} f_{jn} \mathrm{e}^{\mathrm{i}st} \mathrm{d}s = 0$ on the small semicircle C_δ. Hence (D.2.2) can be rewritten as

$$\int_{c-\mathrm{i}\infty}^{c+\mathrm{i}\infty} f_{jn}\, \mathrm{e}^{\omega t} \mathrm{d}\omega = \mathrm{i} L_{jn}(\rho) = \mathrm{i} \int_{-\infty}^{\infty} f_{jn}(\rho, \mathrm{i}s) \mathrm{e}^{\mathrm{i}st} \mathrm{d}s, \tag{D.2.3}$$

with f_{jn},$j = 1, 2$, given by (5.3.12) and (5.3.13) respectively.

Bibliography

M. Abramowitz and I.A. Stegun. *Handbook of Mathematical Functions*, volume 55 of *Applied Mathematics Series*. Nat. Bureau of Standards, 1972.

J.-P. Bardet, C.E. Synolakis, H.L. Davies, F. Imamura, and E.A. Okal. Landslide tsunamis: recent findings and research directions. *Pure and Appl. Geoph.*, 160:1793–1809, 2003.

C.M. Bender and S.A. Orzsag. *Advanced mathematical methods for scientists and engineers*. Mc Graw Hill, 1978.

H. J. Bruins, J.A. MacGillivray, C.E. Synolakis, C. Benjamini, J. Keller, H.J. Kisch, A. Klgel, and J. van der Plicht. Geoarchaeological tsunami deposits at Palaikastro (Crete) and the Late Minoan IA eruption of Santorini. *J. Archeological Science*, 35 (1):191–212, 2008.

G. F. Carrier and H. Wu, T.-R.and Yeh. Tsunami run-up and draw-down on a plane beach. *J. Fluid Mech.*, 475:79–99, 2003.

H. Cheng. *Advanced Analytic Methods in Applied Mathematics, Science and Engineering*. LuBan press, 2007.

G.D. Dahlquist and À Björck. *Numerical Methods in Scientific Computing*, volume I. SIAM, USA, 2008.

M. Di Risio and P. Sammarco. Analytical modeling of landslide generated waves. *Journal of Waterway, Port, Coastal and Ocean Engineering*, 134(1):143–159, 2008.

M. Di Risio, G. Bellotti, A. Panizzo, and P. De Girolamo. Three-dimensional experiments on landslide generated waves at a sloping coast. *Coastal Engineering*, 2009a. Submitted for publication.

M. Di Risio, P. De Girolamo, G. Bellotti, A. Panizzo, F. Aristodemo, M. Molfetta, and A.F. Petrillo. Landslide-generated tsunamis runup at the coast of a conical island: new physical model experiments. *J. Geophys. Res.*, 114(C01009), 2009b.

K. Fujima, D. Yuliadi, C. Goto, K. Hayashi, and T. Shigemura. Characteristics of long waves trapped by conical island. *Coastal Engineering in Japan*, 38(2):111–132, 1995.

R.T. Guza and R.E. Davis. Excitation of edge waves by waves incident on a beach. *J Geopys Res*, 79:1285–1291, 1974.

K. Heun. Zur Theorie der Riemann'schen Functionen zweiter Ordnung mit vier Verzweigungspunkten. *Mathematische Annalen*, 33:191, 1899.

U. Kanoglu and C.E. Synolakis. Long wave runup on piecewise linear topographies. *J. Fluid Mech.*, 374:1–28, 1998.

C.C. Lautenbacher. Gravity wave refraction by islands. *J. Fluid Mech.*, 41(3):655–672, 1970.

P. L.-F. Liu, P. Lynett, and C.E. Synolakis. Analytical solutions for forced long waves on a sloping beach. , 478, 101109. *J. Fluid Mech.*, 478:101–109, 2003.

P. L.-F. Liu, T.-R. Wu, F. Raichlen, C. E. Synolakis, and J. C. Borrero. Runup and rundown generated by three-dimensional sliding masses. *J. Fluid Mech.*, 536:107–144, 2005.

P.L.-F. Liu, Y.-S. Cho, M.J. Briggs, U. Kanoglu, and C.E. Synolakis. Runup of solitary waves on a circular island. *J. Fluid Mech.*, 302:259–285, 1995.

M.S. Longuet-Higgins. On the trapping of wave energy round islands. *J. Fluid Mech.*, 29(4):781–821, 1967.

P. Lynett and P.F. Liu. A numerical study of the runup generated by three-dimensional landslides. *Journal of Geophysical Research*, 110(C003006), 2005.

C.C. Mei. *Mathematical analysis in engineering.* Cambridge University Press, 1997.

C.C. Mei, M. Stiassnie, and D. K.-P. Yue. *Theory and applications of ocean surface waves.* World Scientific, 2005.

R.E. Meyer. Resonance of unbounded water bodies. In W. H. Reid, editor, *Mathematical Problems in the Geophisical Sciences*, volume 13 of *Lectures in Applied Mathematics.* AMS, 1971.

A. Panizzo, P. De Girolamo, and A. Petaccia. Forecasting impulse waves generated by subaerial landslides. *J. of Geophys. Res.*, 110(C12), 2005.

W.H. Press, S.A. Teukolsky, W.T. Vetterling, and B.P. Flannery. *Numerical Recipes in Fortran 77.* Cambridge University Press, 1986.

P. Sammarco and E. Renzi. Landslide tsunamis propagating along a plane beach. *Journal of Fluid Mechanics*, 598:107–119, 2008.

S. Yu. Slavyanov. Confluent heun equation. In A. Ronveaux, editor, *Heun's Differential Equation.* Oxford Science Publications, 1995.

R. Smith and T. Sprinks. Scattering of surface waves by a conical island. *J. Fluid Mech.*, 72(2):373–384, 1975.

W. Summerfield. Circular islands as resonators of long-wave energy. *Philosophical transactions of the Royal Society of London. Series A.*, 272:361–402, 1971.

C.E. Synolakis. Europe's tsunami of inaction against tsunamis. *Wall Street Journal Europe*, Nov, 5 2008.

C.E. Synolakis, E.N. Bernard, V.V. Titov, U. Kanoglu, and F.I. Gonzalez. Validation and verification of tsunami numerical models. *Pure Appl. Geophys.*, 165(11–12): 2197–2228, 2008.

D.R. Tappin, P. Watts, G.M. McMurtry, Y. Lafoy, and T. Matsumoto. Prediction of slump generated tsunamis: the July 17th 1998 Papua New Guinea event. *Science of Tsunami hazards*, 4:222–238, 2002.

S. Tinti and C. Vannini. Tsunami trapping near circular islands. *Pure and Applied Geophysics*, 144(3/4):595–619, 1995.

S. Tinti, A. Maramai, A. Armigliato, L. Graziani, A. Mannucci, G. Pagnoni, and F. Zaniboni. Observations of physical effects from tsunamis of December 30, 2002 at Stromboli volcano, southern Italy. *Bulletin of Volcanology*, 68(5):450–461, 2005.

E.O. Tuck and L.S. Hwang. Long wave generation on a sloping beach. *J. Fluid Mech.*, 51:449–461, 1972.

P. Watts. *Water waves generated by underwater landslides*. PhD thesis, California Institute of Technology, 1997.

P. Watts, S. T. Grilli, J. T. Kirby, G. J. Fryer, and D. R. Tappin. Landslide tsunami case studies using a boussinesq model and a fully nonlinear tsunami generation model. *Nat. Hazar. and Earth Syst. Sci.*, 3:391–402, 2003.

P. Watts, S. T. Grilli, D. R. Tappin, and G. J. Fryer. Tsunami generation by submarine mass failure. ii: predictive equations and case studies. *J. Wat., Port, Coas. and Oc. Eng*, Nov–Dec 2005.

R.L. Wiegel. Laboratory studies of gravity waves generated by the movement of a submarine body. *Trans. Am. Geophys. Union*, pages 759–774, 1955.

H. Yeh, P.L.-F. Liu, M. Briggs, and C.E. Synolakis. Tsunami catastrophe in babi island. *Nature*, 372:6503–6508, 1994.

Y. Zhang and S. Zhu. New solutions for the propagation of long water waves over variable depth. *J. Fluid Mech.*, 278:391–406, 1994.